O Pânico do Último Minuto

André Luiz de Amorim

Orientador:

Prof. Dr. Roberto Cid Fernandes Jr.

• • •

Universidade Federal de Santa Catarina
Centro de Ciências Físicas e Matemáticas
Programa de Pós-Graduação em Física

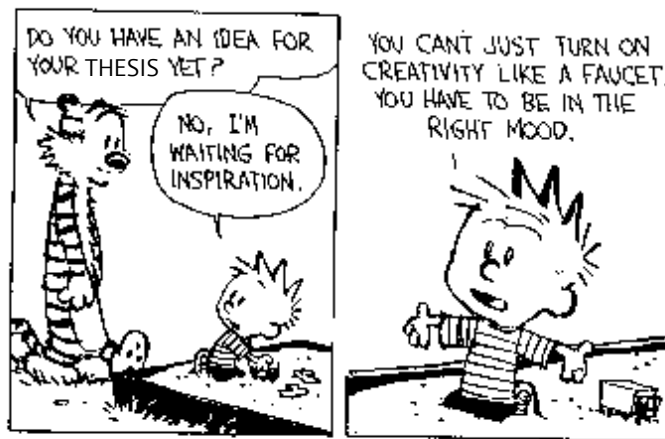Florianópolis (SC) – 30 de julho de 2015

Dedica.

Agradecimentos

Agradece.

Resumo

A figura a seguir resume esta tese.

Abstract

We developed a method for recovering and analysing the stellar populations of the different morphological components of galaxies using integral spectroscopy data. Using the software Imfit, wrapped in Python, we perform the decomposition of a sample of 53 candidate S0 galaxies from the CALIFA Survey into a Sérsic bulge and an exponential disk. The decomposition is made wavelength-wise, so that at the end we get the bulge and disk spectra for each pixel. The morphological parameters (R_e, n, P.A. and ϵ for bulge, h, P.A. and ϵ for disk) in most cases depends linearly on the wavelength, at least for wavelengths > 4000 Å. Using the decomposed spectra from two galaxies from the sample (NGC 1375 and NGC 7194), we apply a stellar population synthesis using STARLIGHT, in order to recover the stellar populations of bulge and disk. In both cases we recover an old bulge and an intermediate aged disk. We also obtain a weak but positive stellar age gradient for the bulges and no measurable gradient for the disks.

Sumário

Lista de Figuras

Capítulo 1

Introdução

1.1 Espectroscopia de campo integral

Na última década presenciamos uma proliferação de surveys de imageamento e espectroscopia. Surveys como o SDSS (York et al. 2000), ALHAMBRA (Moles et al. 2008) e COSMOS (Scoville et al. 2007), para citar alguns exemplos, permitem explorar a distribuição espectral de energia (SED[1]) de centenas de milhares a milhões de galáxias. Entretanto, da forma como estes surveys são executados, há sempre um compromisso entre a resolução espacial e a espectral. As imagens obtidas pelo SDSS têm um boa resolução espacial, mas mapeiam a SED de forma grosseira, com apenas 5 filtros de banda larga (*ugriz*). Já os espectros obtidos pelo mesmo survey possuem uma excelente resolução e cobertura espectral, mas obtém o espectro integrado da região central das galáxias.

O melhor dos dois mundos pode ser alcançado com instrumentos que fazem espectroscopia de campo integral (IFS[2]). Instrumentos que realizam este tipo de espectroscopia consistem em geral de um amontoado de fibras óticas, as quais alimentam um espectrógrafo comum. Assim, depois de um processo relativamente complicado de redução de dados, obtém-se espectros espacialmente resolvidos com uma boa resolução espectral e espacial. O survey CALIFA (*Calar Alto Legacy Integral Field Area survey*[3]) está utilizando o instrumento PMAS/PPAK do observatório Calar Alto para obter IFS de 600 galáxias (Sánchez et al. 2012). Destas, 100 já estão disponíveis no primeiro *Data Release* (Husemann et al. 2013, DR1), afirmando o caráter de legado deste survey.[FIXME] (atualizar pro DR2)

---

[1] *Spectral Energy Distribution.*

[2] *Integral Field Spectroscopy.*

[3] http://www.caha.es/CALIFA/

Quando completado, o CALIFA terá obtido da ordem de 10^6 espectros, quase o mesmo que o SDSS. Porém, este não será apenas mais um survey espectroscópico. A riqueza do CALIFA está nas informações espacialmente resolvidas, em uma amostra representativa do universo local ($0.005 < z < 0.03$, limitada em diâmetro angular) cobrindo a distribuição de galáxias no diagrama cor–magnitude da nuvem azul à sequência vermelha, amostrando galáxias todos os tipos morfológicos (espirais, elípticas, irregulares e até mesmo alguns sistemas em interação).

[TODO] Comparar califa com outros surveuy que vem. (Manga, sami).

Comparado a outros *surveys* já realizados, como o Altas3D (Cappellari et al. 2011) ou o *Disk Mass Survey* (DMS) (Bershady et al. 2010), o CALIFA cobre uma faixa muito maior de tipos morfológicos e massas. Outros *surveys* que estão em andamento são o SAMI (Croom et al. 2012; Bryant et al. 2015) e o MaNGA (Bundy et al. 2015). Estes também buscam obter uma amostra grande de galáxias, até maior do que a do CALIFA. Entretanto, a vantagem do CALIFA está na cobertura e amostragem espacial, observando uma maior porção de cada galáxia com mais riqueza de detalhes.

1.2 Síntese de população estelar espacialmente resolvida

Os espectros espacialmente resolvidos do CALIFA podem ser descritos como um cubo de dados, com as duas primeiras dimensões sendo a posição x e y (ascensão reta e declinação) e a terceira sendo o comprimento de onda. Nestes cubos, planos com comprimento de onda constante são imagens, enquanto "fatias" definidas por um par (x, y) constante são espectros. Pode-se tratar estes espectros individualmente, embora na verdade, nos cubos do CALIFA os pixels vizinhos estão correlacionados devido ao *seeing* do céu e ao processo de observação. Há a queda na relação sinal/ruído (S/N) nas regiões mais afastadas do núcleo da galáxia, onde o brilho superficial é muito menor. Algumas galáxias possuem outros objetos "intrusos" que precisam ser mascarados. Linhas telúricas[4] também precisam ser mascaradas. Assim, em geral, é necessário um preprocessamento visando manter um S/N mínimo e garantir um espectro livre de contaminação. Os detalhes sobre o preprocessamento utilizado neste trabalho estão descritos na seção 3 do Apêndice B.1.

Um aspecto importante do preprocessamento utilizado é que o cubo de dados é dividido em zonas de Voronoi, onde regiões com baixo S/N são combinadas formando efetivamente "pixels

---

[4]Linhas de absorção causadas pela atmosfera.

maiores". Desta forma, o cubo original é transformado numa matriz de zonas e comprimento de onda, onde fatias de zona constante são espectros. Com isso, os espectros, e as máscaras e erros que os acompanham, estão prontos para serem usados pelo próximo passo.

A síntese de população estelar consiste em obter a história de formação estelar (SFH) de uma galáxia utilizando modelos de população estelar simples (SSP). Ajusta-se o espectro de uma galáxia como a soma de espectros de SSPs com idades e composições químicas distintas (levando em conta a atenuação por poeira). O resultado é um vetor de frações de luz e massa destas SSPs, que podem ser facilmente convertidos a uma SFH conforme a prescrição de Asari et al. (2007). O programa utilizado é o STARLIGHT, desenvolvido por Cid Fernandes et al. (2005).

Passamos todos os espectros das zonas pelo STARLIGHT, obtendo o resultado da síntese como um arquivo de síntese separado para cada zona. Entretanto, para visualizar ou mesmo tentar entender estes resultados, é preciso organizar e converter estes arquivos para um formato mais adequado.

1.3   O nascimento do PyCASSO

Todo o descrito anteriormente forma o alicerce deste presente trabalho. Porém, dada a grande quantidade de dados espalhados em diversos formatos, a análise dos resultados da síntese de populações estelares para uma determinada galáxia pode se tornar um grande e complexo quebra-cabeças computacional. Trabalhar com todas as galáxias do *survey* fica virtualmente impossível desta forma. Assim, da necessidade de manipular os resultados da síntese dos cubos de dados das galáxias do CALIFA, nasceu o software PyCASSO.

PyCASSO (*Python CALIFA* STARLIGHT *Synthesis Organizer*) é um software desenvolvido em Python com o objetivo de organizar gerenciar os dados produzidos pelo STARLIGHT com base nos dados do CALIFA. O survey CALIFA é apresentado no Capítulo 2, que também discute os softwares QBICK e STARLIGHT, ferramentas básicas em nossa análise doe cubos de dados. O Capítulo 3 apresenta a documentação do PyCASSO, e em seguida discute os artigos publicados que o utilizam intensivamente.

1.4   Decomposição morfológica de galáxias

[TODO] detalhar mais aqui, ainda não tá legal. O Capitulo 4 apresenta um beabá sobre morfologia.

[TODO] Caracterização ds PSF no Capítulo 5. Explicar a importância de fazer isso pro survey.

Como aplicação científica do PyCASSO, o Capítulo 8 trata da síntese espectral das componentes morfológicas (bojo e disco) de uma galáxia, obtidas no conforme foi descrito no Capítulo 7. Estas componentes são armazenadas em cubos de dados, e são tratados exatamente da mesma forma que uma galáxia. Seus espectros são passados pelo starlight, resultando em cubos de síntese espectral. Os dados da síntese das componentes foram comparados com a síntese da galáxia original, utilizando o programa PyCASSO. **[TODO]** O que resultou?

Capítulo 2

Síntese de populações estelares em espectroscopia de campo integral

2.1   O *survey* CALIFA

O *Centro Astronómico Hispano Alemán* (CAHA) se localiza na *Sierra de los Filabres*, na Comunidade Autônoma de Andaluzia, Espanha. Ele é operado pelo *Max-Planck-Institut für Astronomie* (MPIA), em Heidelberg, Alemanha, e pelo *Instituto de Astrofísica de Andalucía* (IAA/CSIC), em Granada, Espanha. O *survey* CALIFA foi agraciado com 210 noites pelo Comitê Executivo do Calar Alto, espalhadas por 6 semestres, iniciando em junho de 2010 (na prática, as observações se estenderam até o final de 2014). O instrumento utilizado foi a Unidade de Campo Integral PPAK[1] (Kelz et al. 2006), do Espectrógrafo PMAS[2] (Roth et al. 2005; Roth et al. 2010), no telescópio de 3,5 m do CAHA.

A intenção do *survey* é caracterizar a população local de galáxias, que pode ser resumida nos seguintes aspectos científicos principais (Sánchez et al. 2012):

- Amostra cobrindo uma fração substancial da função de luminosidade.

- Amostra grande o suficiente para obter conclusões com uma estatística significativa para todas as classes de galáxias do survey.

- Caracterização das galáxias sobre toda a sua extensão, evitando bias de abertura.

---

[1][**TODO**] PPAK footnote
[2][**TODO**] PMAS footnote

Figura 2.1: [TODO]: Esquema do instrumento PMAS/PPAK, de Kelz et al. (2006).

- Medição de mecanismos de ionização do gás: formação estelar, choques, AGN.

- Medição de abundâncias de oxigênio e nitrogênio no gás ionizado (regiões H II).

- Medição de propriedades de populações estelares: idades, razões massa-luminosidade, metalicidades e (de forma limitada) padrões de abundâncias.

- Medição de cinemática galática em gás em estrelas, campos de velocidade para todas as galáxias e dispersão de velocidades para as mais massivas.

A arquitetura do *survey* foi então desenhada levando em conta os requerimentos acima, junto com as limitações instrumentais e de tempo disponível. Ela está descrita nas seções a seguir.

2.1.1   Instrumentação

À época do início do CALIFA, o PPAK/PMAS era o instrumento de sua classe com o tamanho de campo, $> 1\,\mathrm{arcmin}^2$. Ele consiste em um maço de 331 fibras ópticas cobrindo o campo de observação, direcionado a um espectrógrafo de fenda longa que espalha a luz sobre um detector CCD[3]. A Figura 2.1 ilustra a montagem esquemática do instrumento. Desta forma, de cada fibra se obtém um espectro. Através de um programa de computador, os espectros podem ser reorganizados de modo a formar um cubo de dados, onde há duas dimensões espaciais

---

[3][TODO] footnote CCD

e uma dimensão espectral. Todavia, pode-se notar na Figura 2.1 que as fibras não cobrem totalmente o campo de observação. Na verdade, apenas em torno de 60% da luz proveniente do campo cai dentro das fibras. O restante se perde nos espaços entre elas. Para mitigar este problema, observa-se o campo várias vezes, deslocando o telescópio uma fração de em spaxel em diversas direções, e reconstruindo o cubo de dados utilizando uma técnica é chamada *dithering*.

A estratégia inicial do *survey* foi observar todos os objetos utilizando duas configurações diferentes e complementares do instrumento. A primeira, utilizando a grade de difração V500, com resolução $\Delta\lambda/\lambda \approx 850$ em $\lambda = 5000\,\text{Å}$ e uma largura a meia altura FWHM $\approx 6\,\text{Å}$, cobre a maior faixa espectral possível, tal que as linhas [O II] $\lambda 3727$ e [O II] $\lambda 6731$ sejam observadas para todos os objetos da amostra. A segunda, utilizando a grade de difração V1200, com resolução $\Delta\lambda/\lambda \approx 1650$ em $\lambda = 4500\,\text{Å}$ e uma largura a meia altura FWHM $\approx 2,7\,\text{Å}$, cobrindo a faixa azul do espectro, incluindo a descontinuidade de Balmer ($\approx$ 4000–4400 Å), Hδ, Hγ e [O III] $\lambda 4363$. Estas duas configurações são chamadas daqui em diante de V500 e V1200 respectivamente. **[TODO]** Vignetting, COMBO.

2.1.2 Amostra

A amostra obtida pelo CALIFA deve satisfazer os requerimentos científicos descritos anteriormente, levando em conta as limitações técnicas e instrumentais. Assim, uma amostra foi inicialmente selecionada a partir do catálogo DR7 do *SDSS* (Abazajian et al. 2009), garantindo a disponibilidade de imagens de boa qualidade em bandas múltiplas bandas espectrais, e em muitos casos, espectros nucleares. Sobre esta amostra inicial foram feitos cortes referentes ao tamanho aparente e o *redshift* da galáxia. O tamanho aparente da galáxia deve ser compatível com o instrumento, escolheu-se limitar a amostra em diâmetro da isofota de brilho superficial $25\,\text{mag/arcsec}^2$ (D_{25}), tal que $45'' < D_{25} < 80''$ na banda *r* do *SDSS*. O *redshift* deve ser $0,005 < z < 0,03$. O resultado é uma amostra de 939 galáxias, denominada *amostra mãe*, descrita e estudada em detalhes por Walcher et al. (2014). O conteúdo da amostra, junto com tabelas auxiliares, está disponível no *website* do CALIFA[4]. A amostra final observada deve conter aproximadamente 2/3 da amostra mãe, em torno de 600 galáxias, a serem selecionadas conforme a visibilidade, num padrão quase aleatório.

[TODO] falar da Figura 2.2.

---

[4]`http://www.caha.es/CALIFA/`

Figura 2.2: **[TODO]**: Caracterização da amostra do CALIFA. CMD e mapa do céu de Sánchez et al. (2012).

2.1.3 *Data Releases*

A primeira liberação pública de dados (em inglês, *data release*), denominado DR1 (Husemann et al. 2013), ocorreu em outubro de 2013**[FIXME]**. Foram escolhidas 100 galáxias nas duas configurações, V500 e V1200, que passaram por um controle de qualidade do *survey*, num total de 200 cubos de dados. As características da amostra do DR1 reproduzem bem as da amostra mãe, dentro do que é esperado estatisticamente para uma amostra menor. Massas derivadas da síntese de populações estelares foram usadas para caracterizar a amostra do DR1, como pode ser visto no painel superior da Figura 2.3.

O *data release* seguinte, DR2 (García-Benito et al. 2015), dobra a quantidade de cubos de dados, com 200 galáxias nas duas configurações. Todos os cubos de dados do DR2 foram reduzidos com uma versão aprimorada do *pipeline***[FIXME]**, apresentando melhor calibração espectrofotométrica**[FIXME]**, registro de imagem e resolução espacial. Da mesma forma que para o DR1, a massa das galáxias derivadas de síntese de populações estelares foi utilizada para caracterizar a amostra do DR2 (painel inferior da Figura 2.3). A PSF[5] típica dos cubos de dados (Figura 2.4) do *survey* foi determinada utilizando as mesmas técnicas de ajuste de imagem apresentadas no Capítulo 7. Mais detalhes sobre a medição da PSF no Capítulo 5.

[TODO] Encerramento do survey, data release final.

---

[5]**[TODO]** PSF footnote

Figura 2.3: [TODO]: Distribuição de massa das galáxias no DR1 e no DR2 do CA-LIFA. Reproduzido dos artigos de apresentação do DR1 (Husemann et al. 2013, figura 6) e DR2 (García-Benito et al. 2015, figura 7).

Figura 2.4: [TODO]: Caracterização da PSF do CALIFA DR2. Reproduzido do artigos de apresentação do DR2 (García-Benito et al. 2015, figura 13).

2.2 Síntese de população estelar

2.2.1 QBICK

O programa, desenvolvido por Rubén García Benito para fazer o mascaramento e tesselagem dos cubos de dados descrito a seguir, foi chamado de QBICK. Para mais detalhes sobre o processo completo, ver o artigo por Cid Fernandes et al. (2013b), disponível no Apêndice B.1.

É preciso preparar os espectros para passarem pelo STARLIGHT. Isto envolve principalmente remover medidas não confiáveis, além de deixar todos os espectros e cubos de dados num formato comum, para executar o STARLIGHT em modo *pipeline*. Antes de tudo, todos os *spaxels* que contêm luz não proveniente da galáxia, como estrelas de campo ou galáxias de fundo, foram mascarados. Também foram mascarados artefatos da observação e regioes de baixo sinal-ruído. Este é um procedimento quase artesanal, e necessita de um bom par de vistas humanas bem treinadas. Para um *survey* do porte do CALIFA, com cerca de 600 galáxias, isto ainda é factível. Após o mascaramento espacial, foram mascaradas as linhas espectrais causadas pela atmosfera terrestre. Os espectros foram em seguida postos no referencial de repouso utilizando o *redshift* obtido pela *pipeline*, medido nos $5''$ centrais da galáxia. Foi escolhida uma janela espectral de 5590 a 5680 Å para fazer a medida do sinal-ruído dos espectros. Espectros com sinal-ruído baixo, em geral nas regiões menos brilhantes da galáxia, podem gerar resultados espúrios no STARLIGHT. Estes espectros foram combinados de modo a obter um melhor sinal-ruído utilizando uma técnica conhecida como de tesselagem de Voronoi. Foi escolhido um sinal-ruído de 20 como alvo para o agrupamento dos spaxels. O código utilizado para a tesselagem de Voronoi foi implementado por Cappellari & Copin (2003) e modificado para levar em conta erros correlacionados.

2.2.2 STARLIGHT

O STARLIGHT é um código de síntese espectral desenvolvido por Cid Fernandes et al. (2005). Nele, o espectro observado de uma galáxia é modelado como uma combinação linear de espectros de uma base, um modelo de atenuação por poeira, e efeitos conemáticos (*redshift* e dispersão gaussiana de velocidades). Esta base em geral é composta de uma biblioteca de populações estelares simples (SSP[6]), formando uma grade de idades e metalicidades. O STARLIGHT busca neste espaço de parâmetros (que pode ser imenso, com quase 300 dimensões no

---

[6]Uma SSP consiste num conjunto de estrelas formadas ao mesmo tempo com a mesma metalicidade.

Figura 2.5: [TODO]: Exemplo de saída do QBICK.

caso do presente estudo) qual conjunto de frações de luz, atenuação e cinemática que melhor ajustam o espectro observado, que toma a forma

$$F_\lambda^{\text{modelo}} = \sum_{j=1}^{N_\star} F_\lambda^\star(t_j, Z_j) 10^{-0.4 A_\lambda} \otimes G(v_\star, \sigma_\star)$$

Nesta equação, $F_\lambda^{\text{modelo}}$ é o fluxo em cada comprimento de onda. O termo $10^{-0.4 A_\lambda}$ corrige o espectro pelo efeito de atenuação interestelar, que pode ser por exemplo do tipo (Cardelli et al. 1989, CCM) ou (Calzetti et al. 1994, CAL). $G(v_\star, \sigma_\star)$ denota uma função gaussiana (centrada em $v_\star$ e com dispersão $\sigma\star$) utilizada para modelar os efeitos da cinemática estelar. Na prática a equação acima é implementada após um procedimento de normalização a um comprimento de onda de referência λ_N:

$$F_\lambda^{\text{modelo}} = F_{\lambda_N} \sum_{j=1}^{N_\star} x_j b_\lambda^\star(t_j, Z_j) 10^{-0.4(A_\lambda - A_{\lambda_N})} \otimes G(v_\star, \sigma_\star)$$

onde $b_\lambda^\star(t_j, Z_j) \equiv F_\lambda^\star(t_j, Z_j) / F_{\lambda_N}^\star(t_j, Z_j)$ denota o espectro do elemento j da base normalizado a seu valor em λ_N. A dada elemento j corresponde uma idade t_j e uma metalicidade Z_j, e a importância de cada elemento na soma total é dada pelo peso x_j. O conjunto $\{x_j, i = 1, 2, \ldots, N_\star\}$ é chamado vetor de população ($\vec{x}$) da galáxia considerada.

O melhor ajuste é escolhido minimizando a equação

$$\chi^2 = \sum_\lambda \left[(F_\lambda^{\mathrm{observado}} - F_\lambda^{\mathrm{modelo}})w_\lambda \right]^2$$

onde o peso w_λ é definido como o inverso do erro em $F_\lambda^{observado}$.

Os espectros da base provêm de modelos de síntese evolutiva de populações estelares. A maior parte dos resultados publicados do sᴛᴀʀʟɪɢʜᴛ usa os modelos de Bruzual & Charlot (2003, BC03). Em particular, em seus estudos de galáxias do SDSS o grupo da UFSC normalmente usa uma base composta de 150 SSPs cobrindo 25 idades (entre 10^6 e $1,8 \times 10^{10}$ anos) e 6 metalicidades (entre 1/200 e 2,5 solar; vide Mateus et al 2006). A Figura 2.6 mostra o ajuste feito para uma galáxia do *SDSS* utilizando esta base. A extinção é modelada com uma lei de avermelhamento de CCM. [!!CARDELI CLAYTON & MATHIS]^[FIXME]

Neste trabalho usamos modelos mais atualizados de espectros de SSPs, extraídos dos modelos de Granada (Gonzalez Delgado et al. 2005, para idades até 63 Ma) e os do projeto MILES (Vazdekis et al. 2010). No total esta nova base contém 235 elementos cobrindo idades de 0,001 a 14 Gyr, e $\log Z/Z_\odot$ de -2.3 a $+0.33$. Para mais detalhes ver GD14 e GD15.

A aplicação imediata do resultado do sᴛᴀʀʟɪɢʜᴛ é a remoção do contínuo estelar para medir com maior precisão as linhas de emissão provenientes do gás, não incluídas no modelo. É possível também estudar o vetor de população $\vec{x}$, que representa a fração de luz proveniente de cada população estelar da base. De forma alternativa, pode-se utilizar o vetor de fração de massa $\vec{\mu}$, que se relaciona ao $\vec{x}$ através da relação massa–luminosidade de cada elemento da base. Individualmente os componentes x_j e μ_j dos vetores não são confiáveis, pois há muita degenerescência nos elementos da base (referência CF05?). Porém, a informação contida nos vetores pode ser condensada, gerando medidas físicas galáxia, como a taxa de formação estelar, a idade estelar média e a metalicidade estelar média, os dois últimos ponderados por luminosidade ($\vec{x}$) ou massa ($\vec{\mu}$), por exemplo. Estas medidas são muito mais robustas, como demonstrado por Cid Fernandes et al. (2013a).

Esta técnica foi utilizada em diversos artigos. Em particular a colaboração SEAGal (*Semi Empirical Analysis of Galaxies*), liderada pela UFSC, aplicou o sᴛᴀʀʟɪɢʜᴛ a todos 926246 espectros de galáxias do Data Release 7 do *SDSS*. As propriedades físicas derivadas desta análise de populações estelares, junto com as medidas de linhas de emissão, foram disponibilizadas como um banco de dados no *website* `http://www.starlight.ufsc.br/`.

Os resultados foram utilizados em estudos varrendo desde a história de formação estelar de galáxias (Asari et al 2007) a efeitos ambientais (Mateus 2007) e a origem de linhas de
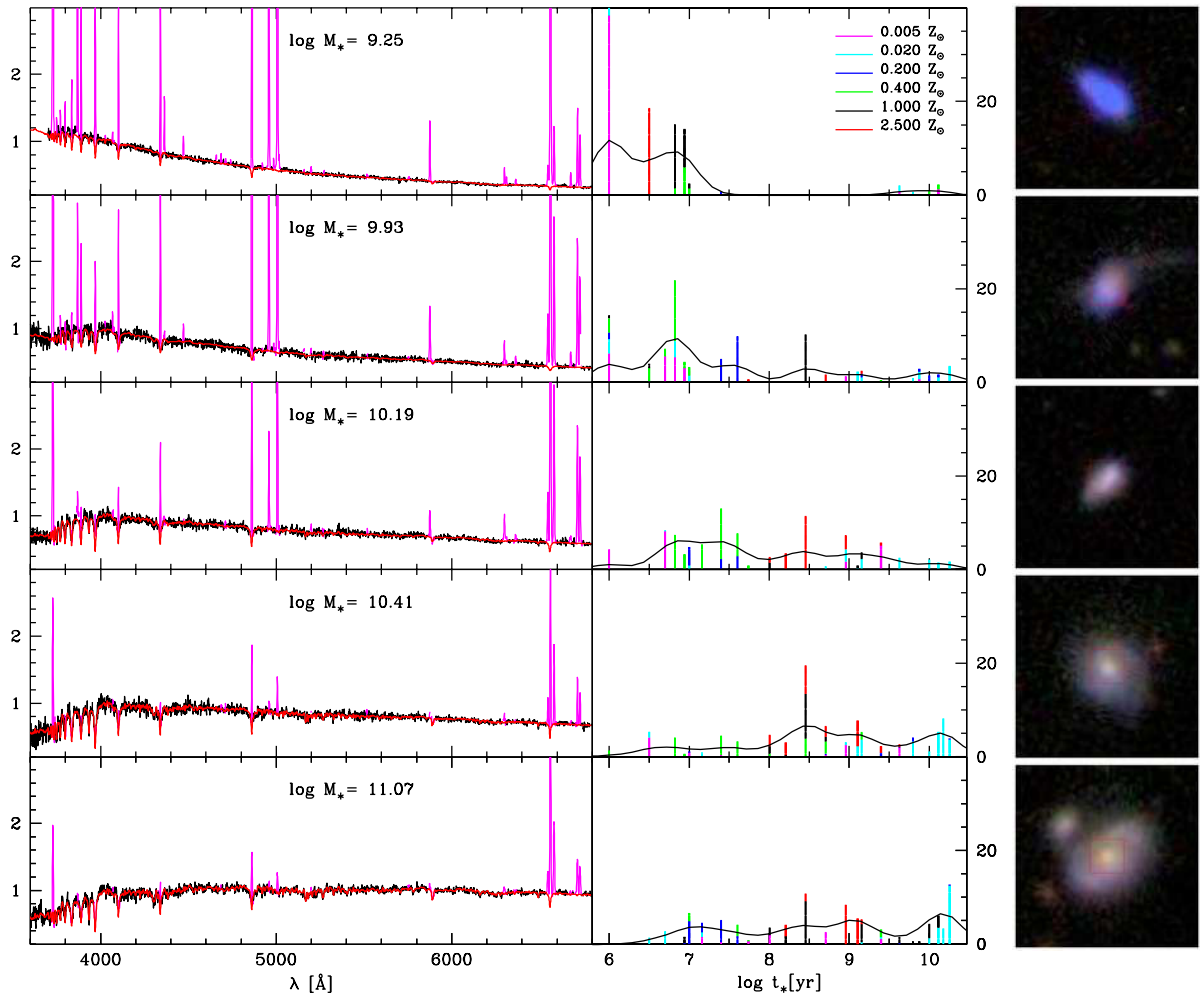
Figura 2.6: Exemplos de ajuste de espectros de galáxias com o STARLIGHT (Asari et al. 2007). À esquerda, espectros observados (preto), espectros modelados (vermelho), com regiões mascaradas em magenta. No meio, a fração da luz associada à cada uma das 25 idades das SSPs usadas na síntese, com a curva representando a versão suavizada do histórico de formação estelar. À direita, imagens do *SDSS* correspondentes às galáxias.

emissão de galáxias "aposentadas"(Stasinska 2008, CF11). Além desses, pesquisadores em todo o mundo produziram artigos (Bian et al. 2006; Liang et al. 2007; Peeples et al. 2009; Lara-López et al. 2009, 2010, para citar alguns) independentes baseados nesse banco de dados.

Em todos esses estudos, cada galáxia é representada por apenas um espectro. A extensão desse tipo de estudo a dados IFU parece trivial, e em certa medida o é se considerarmos o espectro de cada zona (ou spaxel) como o espectro de uma galáxia inteira. No entanto, para tirar máximo proveito da informação sobre populações estelares e sua distribuição espacial é necessária uma ferramenta que organize os resultados do STARLIGHT para um dado cubo de dados. Dessa necessidade nasceu a plataforma PyCASSO, assunto do próximo capítulo.

Capítulo 3

PyCASSO

A fim de agilizar o desenvolvimento de ferramentas de manipulação de cubos de dados do CALIFA. Este "kit de ferramentas" foi chamado de PyCASSO (Python CALIFA STARLIGHT Synthesis Organizer). PyCASSO foi desenvolvido em Pyton e é, a grosso modo, composto de três partes.

Conversor de tabelas. Com ele se pode converter a saída do STARLIGHT (arquivos ASCII para cada pixel de cada galáxia) para cubos de dados nos formatos FITS e HDF5, de forma a otimizar o acesso aos dados. Uma galáxia leva tipicamente 2 minutos para ser carregada em memória usando arquivos texto. Este tempo se reduz para menos de um segundo usando arquivo FITS. Há outra otimização para acessar dados de várias galáxias simultaneamente, utilizando o formato HDF5. Neste caso a carga dos dados em disco para a memória é "preguiçosa", quer dizer, é feita somente quando os dados são efetivamente acessados.

Camada de entrada e saída. Os arquivos FITS e HDF5 foram montados de forma a serem facilmente acessados em qualquer ambiente. Ainda assim, há uma camada de abstração de armazenamento, onde as várias matrizes e cubos são acessadas com nomes próprios (por exemplo, `popx`,que designa a fração de luz distribuída pelas populações estelares), de forma a ser possível programar ferramentas de análise sem precisar se preocupar com as características de cada formato de armazenamento.

Camada de análise. Como foi mencionado na Seção 1.2, o resultado da síntese consiste em cubos indexados por zona. Os dados ficam armazenados no disco desta forma. Porém, na grande maioria das vezes se está interessado na informação espacialmente resolvida. Esta camada implementa uma rotina de conversão da notação de zonas para (x, y). Boa parte das propriedades da síntese, como luminosidade, massa, atenuação por poeira, e idade estelar, já

estão implementadas. Estes cubos espacialmente resolvidos são calculados dinamicamente, quer dizer, não ocupam memória do sistema até que sejam acessados. Existem outras rotinas para calcular geometria, perfis radiais e azimutais, e raio de escala. Outras rotinas podem ser adicionadas facilmente[1].

Este software está sendo utilizado pelo grupo de populações estelares da colaboração do CALIFA, do qual o autor faz parte. No total são aproximadamente 10 pessoas utilizando este software. Foram publicados 4 artigos que utilizam extensivamente PyCASSO, apresentados na Seção 3.2, e 2 que utilizaram algum dado resultante de forma indireta (Husemann et al. 2013; Iglesias-Páramo et al. 2013).[FIXME] (atualizar lista)

3.1   A ferramenta de manipulação de cubos de dados Py-CASSO

PyCASSO é uma biblioteca desenvolvida em Python. Porém uma biblioteca não é nada sem uma boa documentação. Aqui se apresenta de forma breve das capacidades do PyCASSO. A documentação completa se encontra no Apêndice A.

O trabalho com a variedade e quantidade de dados gerados pela síntese espectral de IFS tem em geral um caráter fortemente exploratório. Frequentemente não se sabe exatamente o que se está buscando, e o trabalho do programador/cientista consiste em desenhar gráficos, realizar cálculos, determinar operações ou filtros nos dados com base nestes gráficos e cálculos, desenhar novamente, e assim sucessivamente. Assim se escolheu a linguagem Python, que possui ferramentas adequadas à programação exploratória[2], como o `IPython`[3] e o `matplotlib`[4]. Foi feito um esforço para que o acesso aos dados de cada galáxia fosse feito de forma simples e direta, um exemplo de código pode ser visto na Figura 3.1.

Para algumas operações, como o cálculo da idade estelar média feito na Figura 3.1, pode-se utilizar apenas o resultado para as zonas. Neste caso, a idade estelar média é calculada usando a expressão $\langle \log t \rangle_L^{gal} = \sum_z \langle \log t \rangle_{L,z} L_z / \sum_z L_z$, onde L_z é a luminosidade de cada zona e $\langle \log t \rangle_{L,z}$ é a idade estelar média de cada zona. Entretanto, para tirar vantagem das informações espaciais, é preciso converter as propriedades da notação de zona para imagem. Por exemplo,

---

[1]Há um estudo de PCA (análise de componentes principais) sendo desenvolvido por outro estudante na UFSC, por exemplo.

[2]Além de estar se tornando uma espécie de *lingua franca* na Astrofísica computacional.

[3]http://ipython.org/

[4]http://matplotlib.org/

```python
# Carregar arquivo FITS com os dados.
from pycasso import fitsQ3DataCube
K = fitsQ3DataCube('K0001_synthesis_suffix.fits')

# Acessar a idade media ponderada pela luminosidade.
at = K.at_flux__z

# Calcular a idade media da galaxia.
at_total = (at * K.Lobn__z).sum() / K.Lobn__z.sum()
print 'Idade media da galaxia: %.2f' % at_total
```

Figura 3.1: Exemplo de acesso aos dados. Todas as propriedades estão disponíveis diretamente pelo nome, inclusive utilizando a função auto-completar da maioria dos ambientes de desenvolvimento Python.

```python
# Carregar arquivo FITS com os dados.
from pycasso import fitsQ3DataCube
K = fitsQ3DataCube('K0001_synthesis_suffix.fits')

# Converter zonas para imagem.
at_image = K.zoneToYX(K.at_flux__z, extensive=False)

# Desenhar o mapa.
import matplotlib.pyplot as plt
plt.imshow(at_image)
plt.colorbar()
```

Figura 3.2: Programa para desenhar o mapa de idade estelar média ponderada pela luminosidade.

o programa na Figura 3.2 calcula a idade estelar média espacialmente resolvida[5], e em seguida desenha um gráfico da imagem gerada (Figura 3.3).

Enquanto um mapa é uma forma muito boa de visualizar informações em duas dimensões, há vezes em que uma visualização resumida é mais adequada. Galáxias em geral têm simetria aproximadamente axial, logo poder medir perfil radial das propriedades das galáxias é fundamental para estudá-las. Com PyCASSO, o cálculo do perfil radial é bastante simples, como pode ser visto no programa na Figura 3.4, que calcula o perfil radial da idade estelar média. O resultado está na Figura 3.5.

---

[5]O mapa de idade já está previamente calculado, disponível através da propriedade `at_flux__yx`. Esta conversão é feita explicitamente aqui para ilustrar como a conversão pode ser feita para qualquer propriedade.
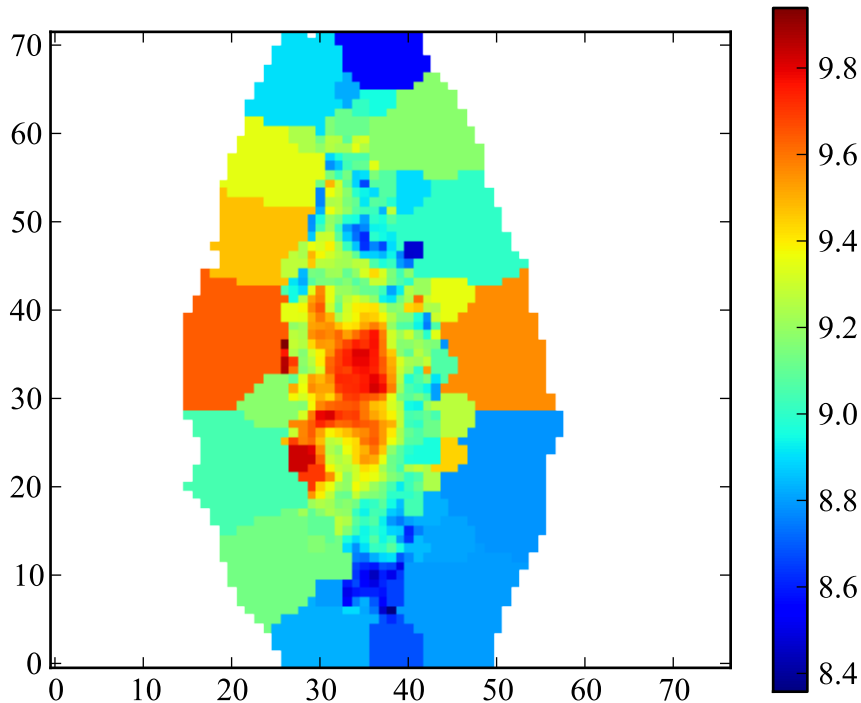
Figura 3.3: Mapa de idade estelar média ponderada pela luminosidade da galáxia IC 5376, desenhado pelo programa da Figura 3.2.

```python
# Carregar arquivo FITS com os dados.
from pycasso import fitsQ3DataCube
K = fitsQ3DataCube('K0001_synthesis_suffix.fits')

# Converter zonas para imagem.
at_image = K.zoneToYX(K.at_flux__z, extensive=False)

# Calcular o perfil radial.
bins = np.arange(0, 26, 1)
bin_center = (bins[1:] + bins[:-1]) / 2.0
at_rad = K.radialProfile(at_image, bins, rad_scale=1.0)

# Desenhar o perfil radial.
import matplotlib.pyplot as plt
plt.plot(bin_center, at_rad)
```

Figura 3.4: Programa para desenhar o perfil radial da idade estelar média ponderada pela luminosidade.
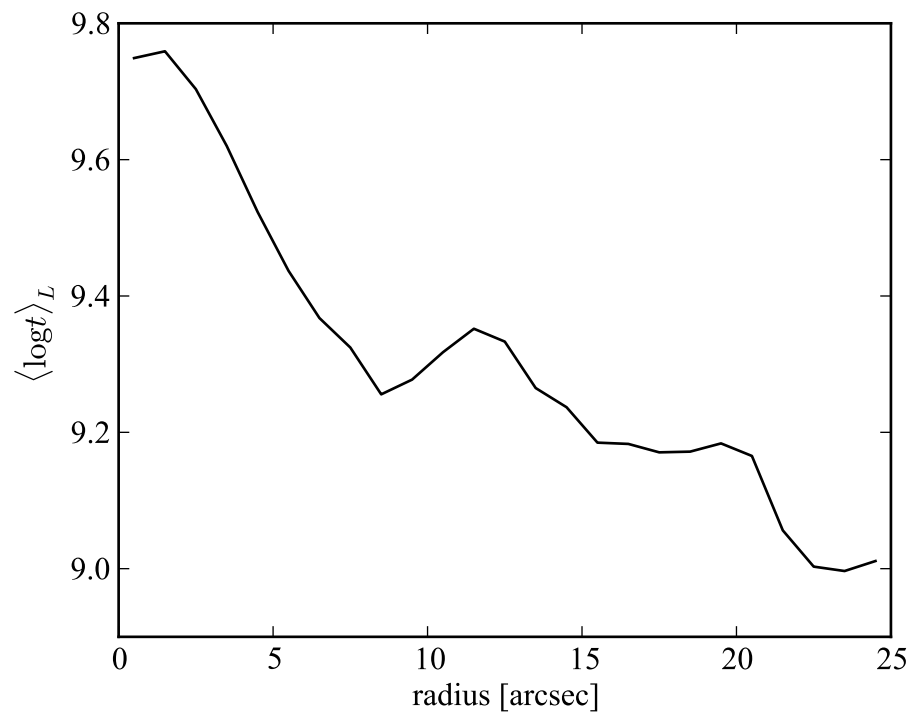
Figura 3.5: Perfil radial da idade estelar média ponderada pela luminosidade da galáxia IC 5376, desenhado pelo programa da Figura 3.4.

Esta é só uma pequena demonstração das ferramentas existentes no PyCASSO. Também é possível trabalhar com espectros, calcular perfis azimutais, lidar com pixels mascarados, entre outras coisas. Tudo isto está descrito em detalhes no manual do programa (Apêndice A).

3.2   Artigos publicados

Nesta seção discute-se os artigos onde se utilizou PyCASSO, e o autor teve uma colaboração importante. Além destes artigos, Husemann et al. (2013), no artigo apresentando o primeiro *data release*, utiliza as massas estelares determinadas pelo STARLIGHT e disponibilizadas pelo PyCASSO **[TODO]**: Figuras **??** e 2.4. **[TODO]**: DR2, Letter da Rosa, outro paper da Rosa.

3.2.1   Artigo: *Resolving galaxies in time and space. I. Applying STAR-LIGHT to CALIFA datacubes*

Este artigo por Cid Fernandes et al. (2013b) descreve todo o processo de síntese espectral dos cubos de dados do CALIFA, mencionados no Capítulo 1, e serve como uma demonstração da capacidade do PyCASSO. O artigo está reproduzido na íntegra no Apêndice B.1. O preprocessamento dos cubos de espectros é feito através do programa QBICK, desenvolvido por Rubén Garcia Benito especialmente para o CALIFA, mas é genérico o bastante para ser usado em outros cubos de dados. Após explicar em detalhes todos os passos envolvidos desde o preprocessamento, passando pela descrição do STARLIGHT até a importação dos dados pelo PyCASSO, o artigo apresenta um caso de estudo com a galáxia NGC 2916.

As Figuras 3.6 e 3.7 mostram mapas de propriedades físicas obtidas pela síntese espectral. Propriedades como a massa (Figura 3.6d) e luminosidade (Figuras 3.6a e 3.6c) são quantidades extensivas, e são proporcionais à escala. Já a atenuação por poeira (Figura 3.6b), idade e metalicidade estelar são quantidades intensivas, independentes de escala. Na prática isto significa que as quantidades extensivas podem ser divididas entre os pixels que compõem uma zona, enquanto as intensivas são uma propriedade comum à todos os pixels desta zona. Esta diferença pode ser notada nas zonas mais externas dos mapas, onde aparecem platôs na quantidades intensivas. As quantidades extensivas passam por um processo apelidado de "dezonificação"[FIXME], descrito na Seção 3.1.

Um dos desafios de se trabalhar com cubos multidimensionais é como visualizar esta informação. Uma alternativa é comprimir determinadas dimensões. Para ilustrar esta capacidade
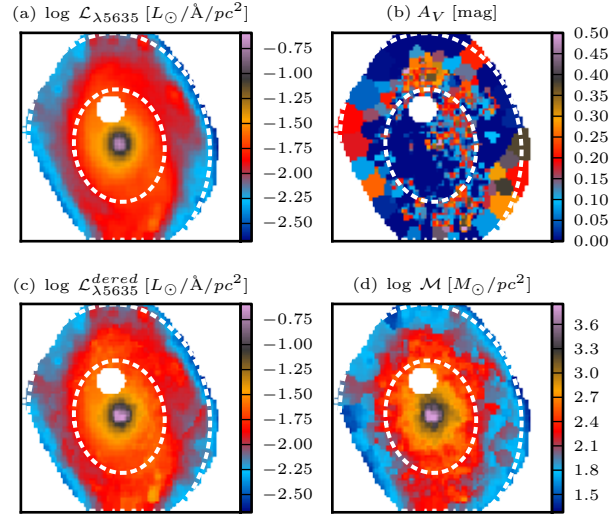
Figura 3.6: Propriedades físicas espacialmente resolvidas para a galáxia NGC 2916. (a) Luminosidade em 5635 Å por unidade de área. (b) Atenuação por poeira na banda *V*. (c) Luminosidade em 5635 Å por unidade de área, corrigido de extinção. (d) Desidade superficial de massa estelar. Retirado de (Cid Fernandes et al. 2013b, figura 4), Apêndice B.1.
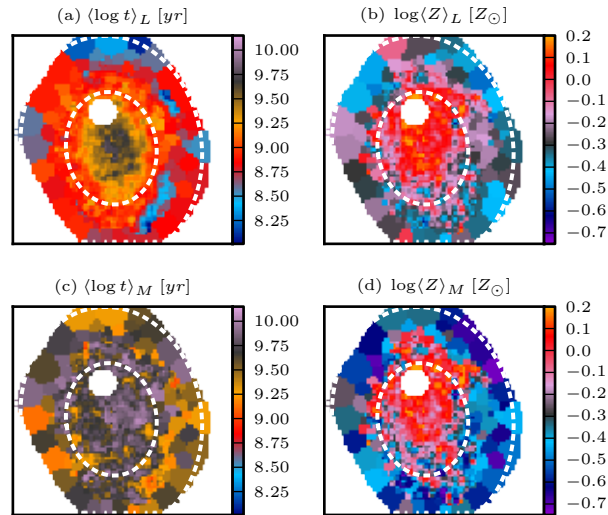
Figura 3.7: Idade e metalicidade estelar média, espacialmente resolvidas, para a galáxia NGC 2916. (a) Idade estelar média pesada pela luminosidade. (b) metalicidade estelar média pesada pela luminosidade. (c) Idade estelar média pesada pela massa. (d) metalicidade estelar média pesada pela massa. Retirado de (Cid Fernandes et al. 2013b, figura 6), Apêndice B.1.
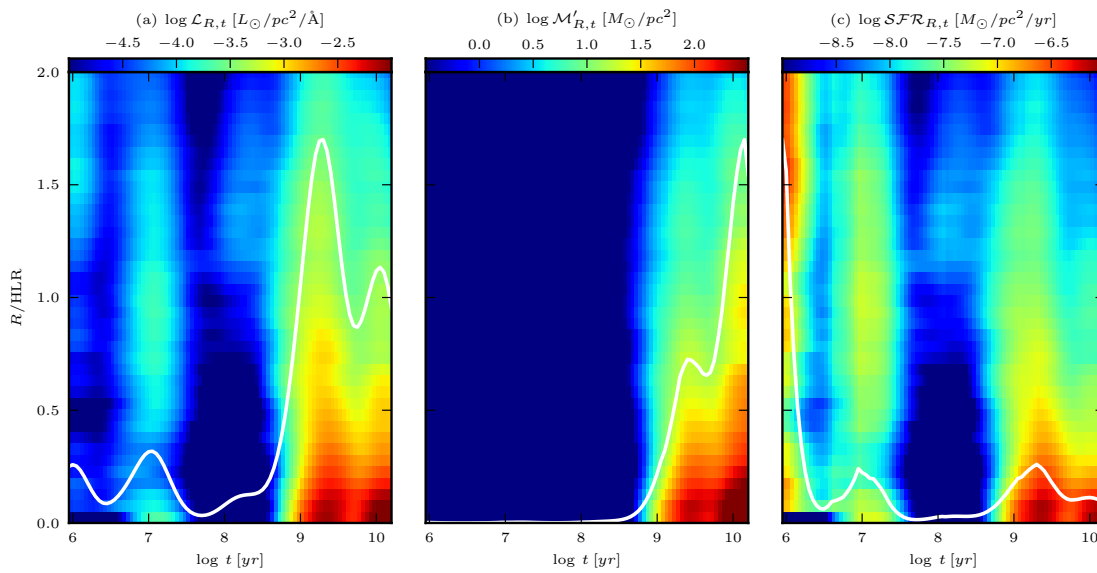
Figura 3.8: Diagramas $R \times t$ para luz, massa e taxa de formação estelar (SFR). (a) Luminosidade em 5635 Å por unidade de área. (b) Massa transformada em estrelas por unidade de área. (c) Taxa de formação estelar por unidade de área. A linha sólida representa o gráfico colapsado na direção vertical, apenas para ilustrar a variação temporal das quantidades mapeadas. Retirado de (Cid Fernandes et al. 2013b, figura 12), Apêndice B.1.

do PyCASSO, a Figura 3.8 mostra diagramas de luz, massa e taxa de formação estelar (SFR) em função do tempo, onde as dimensões *x* e *y* foram transformadas em distância radial. Diagramas como este, junto com perfis 1-D radiais e temporais ajudam a visualizar e interpretar o resultado da síntese espectral, oferecendo novas ferramentas para estudar a estrutura e evolução de galáxias.

3.2.2 Artigo: *Resolving galaxies in time and space: II: Uncertainties in the spectral synthesis of datacubes*

Uma crítica bastante comum aos métodos de ajuste é que eles não provêm a incerteza associada aos valores ajustados. A forma mais simples de determinar esta incerteza é refazer o ajuste várias vezes, perturbando as medidas reproduzindo de forma realista os erros. Este artigo por Cid Fernandes et al. (2013a) investiga a incerteza nos ajustes feitos no artigo discutido na seção anterior. O artigo está reproduzido na íntegra no Apêndice B.2.

Quando se injeta erros aleatórios, obtém-se incertezas de ~ 0.08 dex em idades e metalicidades pesadas pela luminosidade, e de ~ 0.15 dex quando pesadas pela massa. A massa estelar teve uma incerteza de ~ 0.08 dex, e A_V de ~ 0.06 mag. Injetando erros sistemáticos em cor[6] os erros são similares, exceto para A_V, que recebe um desvio sistemático de +0.05 mag e um erro de ~ 0.16 mag.

Embora haja uma incerteza considerável analisando-se as propriedades da galáxia pixel a pixel, os perfis radiais em geral são bastante robustos. Propriedades diretas como a luminosidade, massa, idade e metalicidade estelar, quando vistas em perfil radial (Figura 3.9) mantém o mesmo formato com pouca dispersão, exceto nas regiões mais afastadas do núcleo, onde há poucas zonas. Na verdade, qualquer forma de média espacial que envolva pixels (ou zonas) suficientes deverá levar a uma diminuição na incerteza.

O artigo também explora os efeitos da escolha da base de SSPs nos resultados do ajuste. Em geral, bases diferentes levam a resultados consistentes. Pode-se ver na Figura 3.10 que a idade estelar média ponderada pela luminosidade, a atenuação e a massa estelar inicial têm uma concordância muito boa entre as bases. As metalicidades médias mostram uma correlação, mas com uma dispersão muito grande, certamente devido a diferenças nas trajetórias evolucionárias dos modelos, poucos valores de metalicidade na base, e diferenças na metalicidade máxima da base. A incerteza nestas propriedades mencionadas acima é cerca de 2 vezes maior do que as calculadas adicionando ruído aleatório. Claramente a escolha de uma base

---

[6]Adicionando componentes lineares em comprimento de onda, a fim de emular uma má calibração de fluxo.
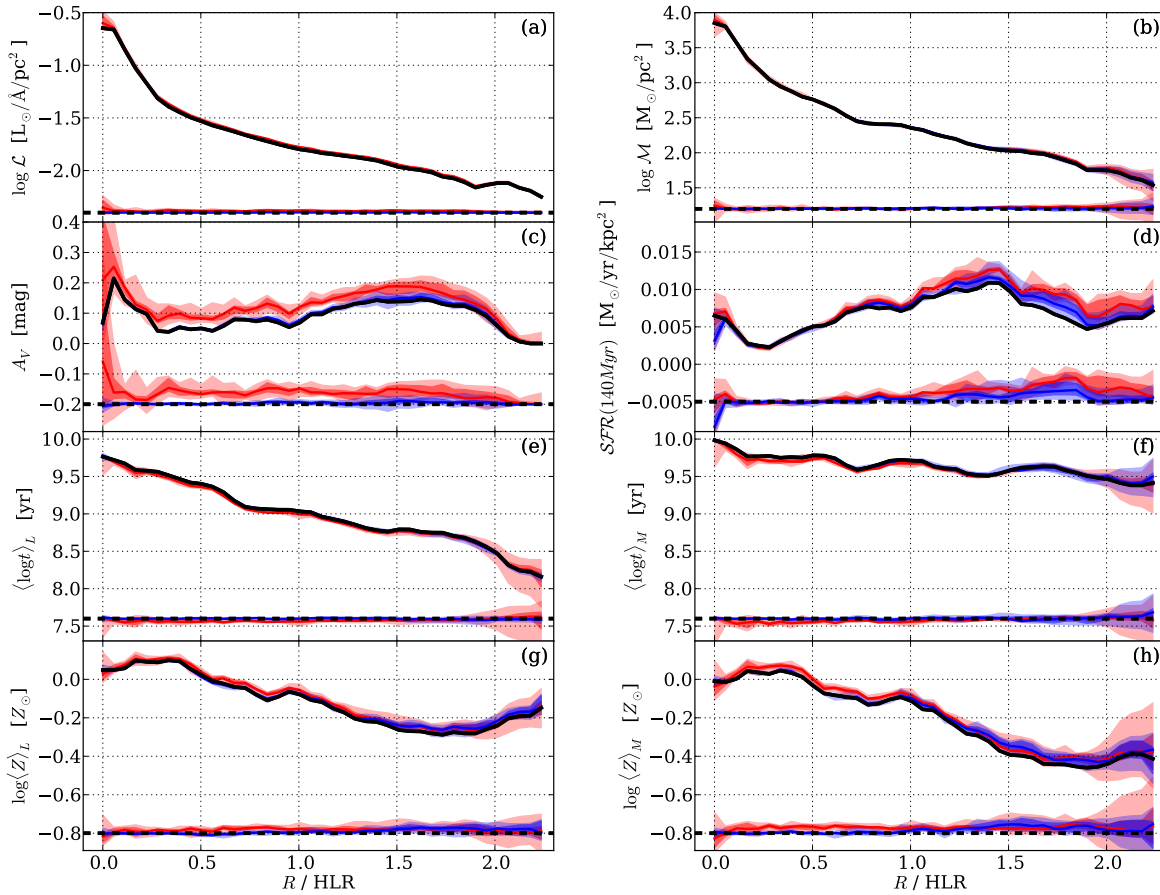
Figura 3.9: Incerteza nos perfis radiais de algumas propriedades. (a) Luminosidade superficial a 5635 Å, corrigida de extinção. (b) Densidade superficial de massa. (c) Atenuação na banda *V*. (d) Taxa de formação estelar (últimos 140 Myr) por unidade de área. (e) Idade estelar média ponderada pela luminosidade. (f) Idade estelar média ponderada pela massa. (g) Metalicidade estelar média ponderada pela luminosidade. (h) Metalicidade estelar média ponderada pela massa. As linhas em preto marcam a solução original. Em faixas azuis e vermelhas, as distribuições das realizações com ruído aleatório, e sistemático em cor, respectivamente. A diferença entre as simulações e o original está desenhada abaixo de cada painel, com o zero marcado pela linha tracejada. Retirado de (Cid Fernandes et al. 2013a, figura 4), Apêndice B.2.
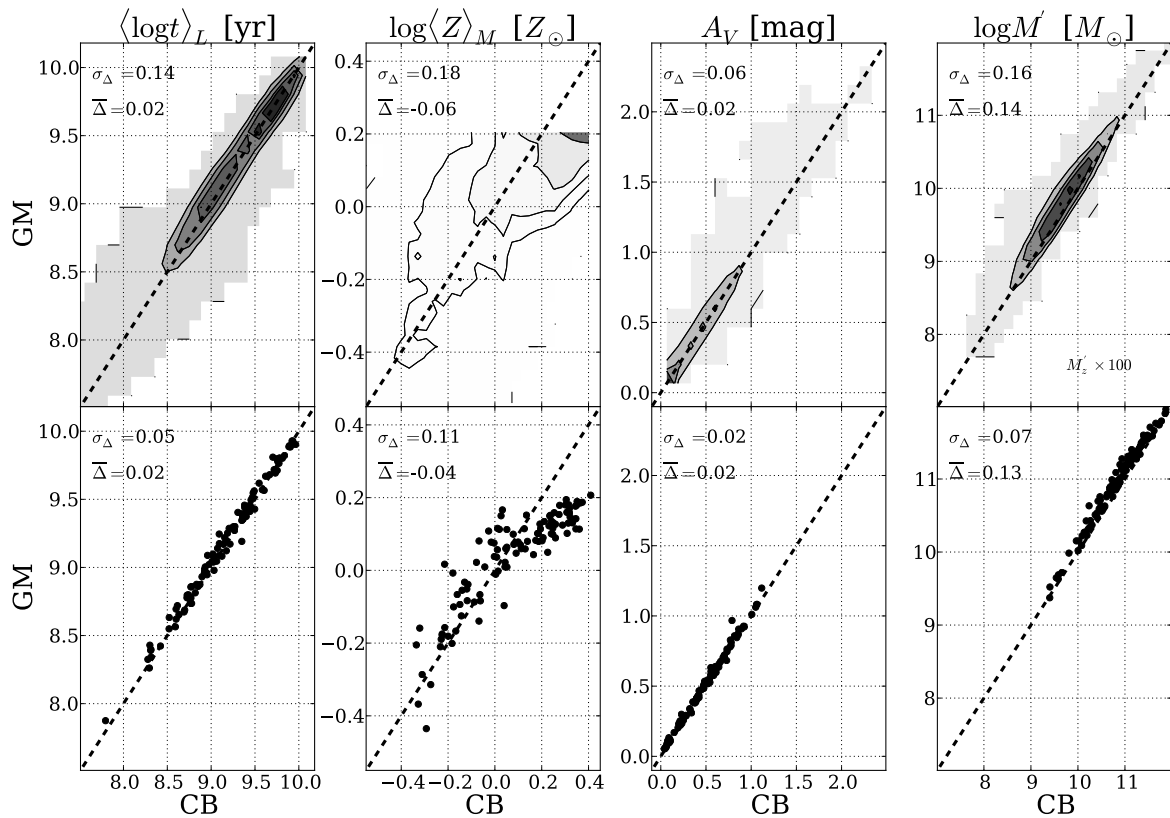
Figura 3.10: Comparação de propriedades obtidas com o ajuste utilizando as bases GM (eixo vertical) CB (eixo horizontal). Os painéis superiores mostram um histograma 2-D com contornos para propriedades de cada pixel de 107 galáxias do CALIFA. Da esquerda para a direita: idade estelar ponderada pela luminosidade, metalicidade estelar ponderada pela massa, atenuação na banda *V*, massa estelar inicial. Os painéis inferiores mostram a distribuição das mesmas propriedades, porém calculadas para o espectro integradas das galáxias. Retirado de (Cid Fernandes et al. 2013a, figura 9), Apêndice B.2.
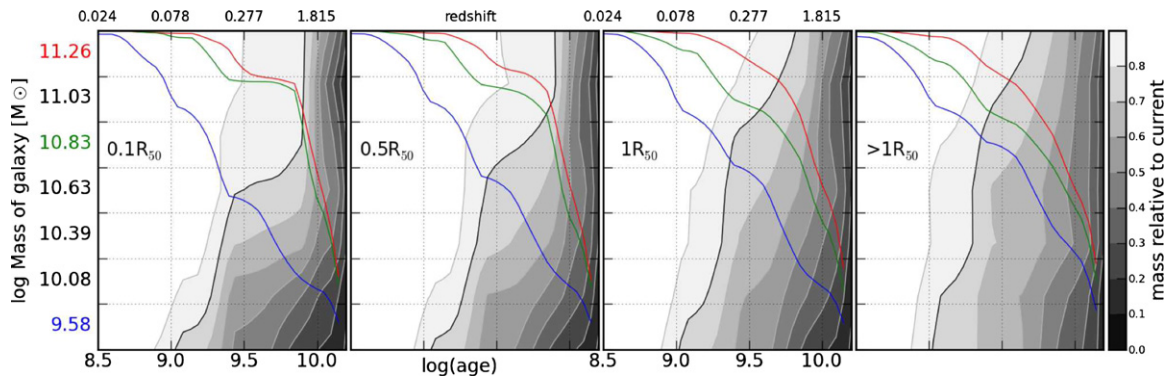
Figura 3.11: Crescimento de massa estelar de dentro para fora. As 105 galáxias foram separadas em grupos de 15, em massa, formando os *bins* do eixo vertical. Os painéis mostram o crescimento da massa em escala de cinza, normalizado, em função do tempo e da massa das galáxias. O contorno em preto marca 80%. Da direita para a esquerda se vê as regiões em raio $r < 0{,}1\,R_{50}$, $0{,}1 < r \le 0{,}5\,R_{50}$, $0{,}5 < r \le 1\,R_{50}$ e $r > 1\,R_{50}$. Para facilitar a visualização da forma da variação temporal, as linhas azuis, verdes e vermelhas em cada painel mostram um corte horizontal nos *bins* inferior, intermediário e superior, com escala de 0 a 1. Retirado de (Pérez et al. 2013, figura 9), Apêndice B.3.

adequada é de grande importância para a análise.

3.2.3   Artigo: *The Evolution of Galaxies Resolved in Space and Time: A View of Inside-out Growth from the CALIFA Survey*

Em Pérez et al. (2013) se estuda o crescimento de dentro para fora de 105 galáxias do CA-LIFA. O estudo se baseia na síntese espectral com o STARLIGHT, e segue exatamente a mesma prescrição de Cid Fernandes et al. (2013b), descrita na Seção 3.2.1. O artigo está reproduzido na íntegra no Apêndice B.3.

Galáxias vêm em todos os tamanhos. Para determinar o crescimento, as distâncias são normalizadas em utilizando o raio onde a luminosidade cumulativa (em 5635 Å) alcança 50% da luminosidade total da galáxia, denominado R_{50}. As galáxias da amostra são separadas em *bins* com 15 galáxias cada, segundo a sua massa. O crescimento em massa em função do tempo é calculado para cada pixel de cada galáxia e somado em cada *bin* de massa.

A Figura 3.11 ilustra o crescimento de massa em anéis crescentes em raio ($0{,}1\,R_{50}$, $0{,}5\,R_{50}$, $1\,R_{50}$ e $> 1\,R_{50}$.). Em cada painel, o tempo passa da direita para a esquerda, e a massa estelar, normalizada, cresce desde zero (direita, em preto) até 1 (esquerda, em branco). Se

vê claramente que galáxias menos massivas, na parte inferior dos *bins*, têm um crescimento gradual mais ou menos constante em todos os raios. As galáxias mais massivas, a parte superior dos *bins*, apresentam um crescimento muito rápido nas regiões centrais, enquanto as regiões externas crescem mais gradualmente. As linhas azul, verde e vermelha, em cada painel, representam cortes horizontais no *bin* de mais baixa massa, no intermediário e no de mais alta massa, respectivamente, para facilitar a visualização. A mudança de regime ocorre em $\log M\star = 10,83$, ou seja, uma massa de $\sim 7 \times 10^{10}\ M_\odot$. O autor cita vários estudos que indicam esta faixa como uma "massa especial", onde a taxa de formação estelar alcança valores altos muito rapidamente. De qualquer forma, esta é uma evidência observacional de algo que já se suspeita há muito tempo: que as galáxias massivas se formaram de dentro para fora.

3.2.4 Artigo: *The star formation history of CALIFA galaxies: Radial structures*

O artigo por González Delgado et al. (2013) faz um estudo detalhado da estrutura radial de diversas propriedades de 107 galáxias do CALIFA. O artigo está reproduzido na íntegra no Apêndice B.4. Um dos resultados mais importantes é que a densidade superficial de massa estelar e idade estelar média ponderada por luminosidade, medidas a $1\,R_{50}$, são representativos das médias da galáxia como um todo. A Figura 3.12 mostra a correlação entre os valores em três raios distintos e o global para a idade estelar média ponderada pela luminosidade (esquerda) e a densidade superficial de massa estelar (centro). Valores a $1\,R_{50}$, marcado como HLR (*Half Light Radius*) nas figuras, coincidem em geral com a média global da galáxia. Ainda na mesma figura pode-se ver a correlação entre a densidade superficial de massa estelar média da galáxia e a massa estelar total da galáxia. Este resultado está de acordo com Kauffmann et al. (2003), usando a amostra do SDSS.

O raio contendo metade da massa estelar (HMR, *Half Mass Radius*) é em média 20% menor que R_{50} (HLR). A razão entre HMR e HLR tem correlação com a massa total da galáxia e o tipo morfológico. Na Figura 3.13 pode-se ver que a relação HMR/HLR diminui com a massa estelar para galáxias com massa menor que $10^{11}\ M_\odot$, enquanto permanece constante para galáxias mais massivas. Um comportamento similar ocorre com o tipo morfológico: em galáxias com disco a relação HMR/HLR diminui com a massa, e em galáxias esferoidais a relação é aproximadamente constante.

Para galáxias esferoidais, o gradiente de idade depende mais da massa estelar total da galáxia do que da densidade superficial de massa estelar, que, conforme o painel inferior esquerdo
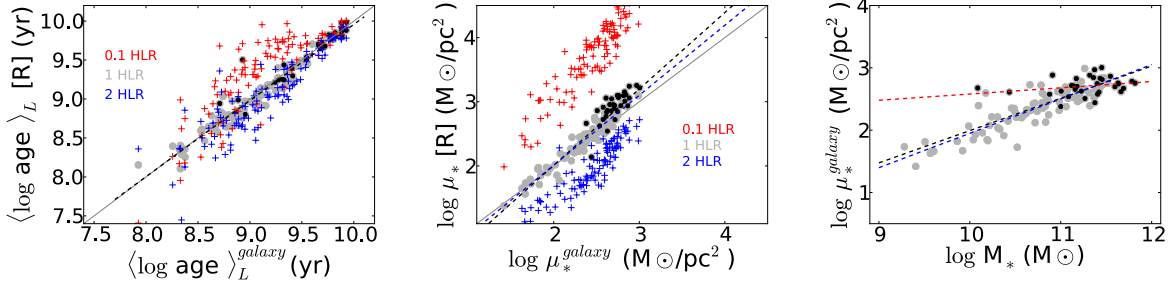
Figura 3.12: (esquerda) Correlação entre a idade estelar média ponderada pela luminosidade em $1\,R_{50}$ (círculos cinza), $0{,}1\,R_{50}$ (cruzes azuis), $2\,R_{50}$ (cruzes vermelhas) e a média da galáxia. Pontos em preto marcam galáxias esferoidais, com $C \geq 2{,}8$. (centro) O mesmo gráfico para a densidade superficial de massa estelar. (direita) Correlação entre a densidade superficial de massa média da galáxia e a massa estelar total da galáxia. As linhas tracejadas mostram o ajuste linear total (preto), apenas discos (azul), e apenas para esferoidais (vermelho). Retirado de (González Delgado et al. 2013, figura 6), Apêndice B.4.
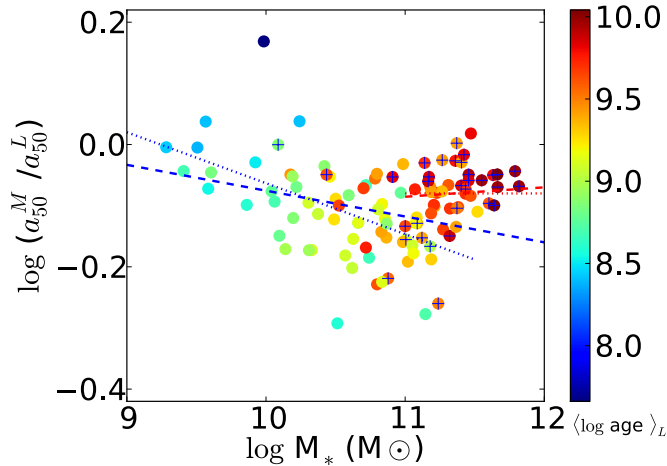
Figura 3.13: Relação entre a_{50}^M/a_{50}^L e a massa estelar total. A cor dos pontos reflete a idade estelar média ponderada pela luminosidade, em $0{,}5\,a_{50}^L$. Galáxias com índice de concentração $C \geq 2{,}8$ estão marcadas com uma cruz. A linha azul mostra o ajuste linear para galáxias com massa estelar Retirado de (González Delgado et al. 2013, figura 10), Apêndice B.4.
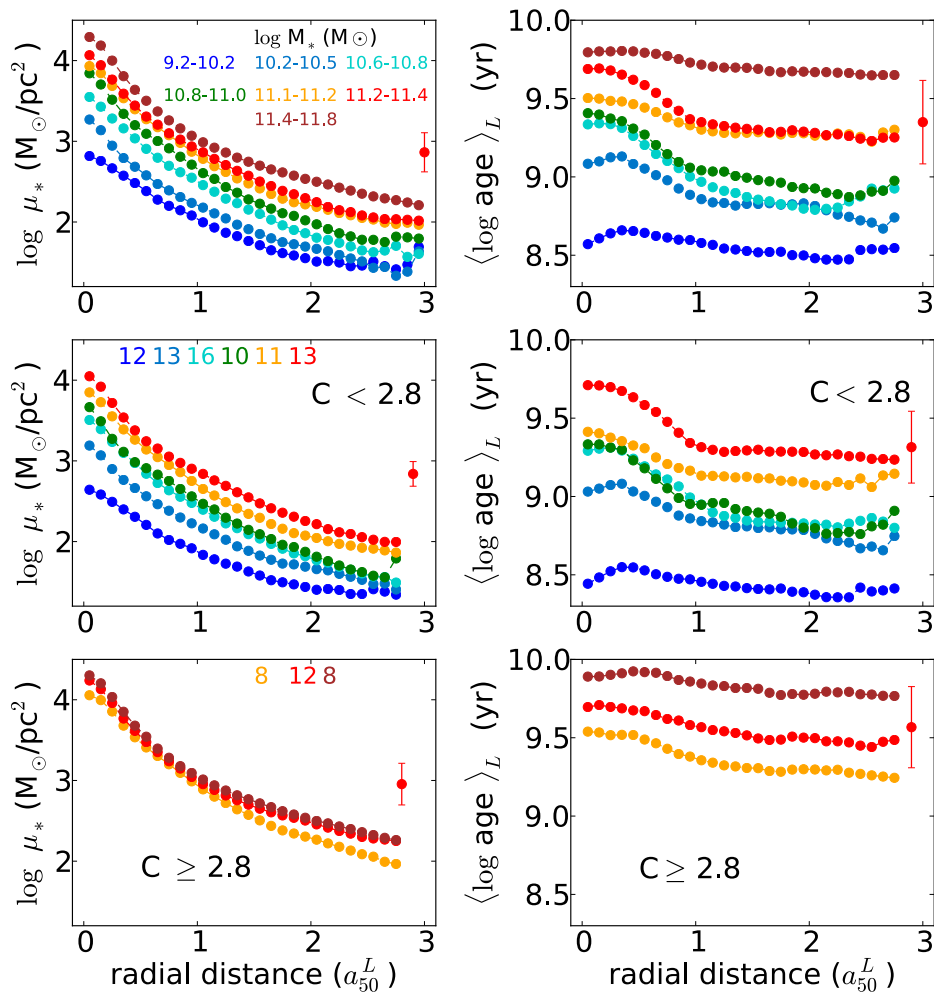
Figura 3.14: Perfis radiais da densidade superficial de massa estelar (esquerda) e idade estelar média ponderada pela luminosidade (direita), para *bins* de massa estelar contendo 15 galáxias cada. (cima) Todas as galáxias. Os *bins* em massa estão codificados em cores. (meio) Galáxias dominadas por disco. (baixo) Galáxias esferoidais ($C \geq 2,8$). Retirado de (González Delgado et al. 2013, figura 13), Apêndice B.4.

da Figura 3.14, é aproximadamente constante. A massa total da galáxia é a propriedade mais fundamental para galáxias esferoidais, enquanto a densidade superficial de massa é mais importante para as galáxias com disco.

Capítulo 4

Morfologia de galáxias

A descoberta das formas das galáxias, e a sua separação em classes segundo a sua morfologia, somente se tornou uma ciência séria quando *surveys* fotográficos extensos começaram a ser realizados (Sandage et al. 1975). Pode-se considerar o ano de 1845 como um marco inicial no estudo da forma das galáxias, quando Lord Rosse, observando com o telescópio refletor de 72 polegadas no Castelo de Birr, descobriu estruturas espirais em M51 (Galáxia do Redemoinho, no catálogo de Messier). À época, pouco se sabia sobre a natureza das "nebulosas espirais" e os esquemas de classificação eram puramente descritivos como o de Wolf (1908), mostrado na Figura 4.1. Knox-Shaw (1915), entre outros, chamou a atenção para nebulosas sem braços espirais, que viriam a ser chamadas mais tarde de elípticas. Curtis (1918) foi o primeiro a identificar espirais com barra. Em meados de 1940 já se havia descoberto a maioria dos tipos mais comuns das "nebulosas extragaláticas", termo que já começava a cair em desuso em favor do nome mais glamouroso, segundo o próprio Hubble (1936): "galáxias".
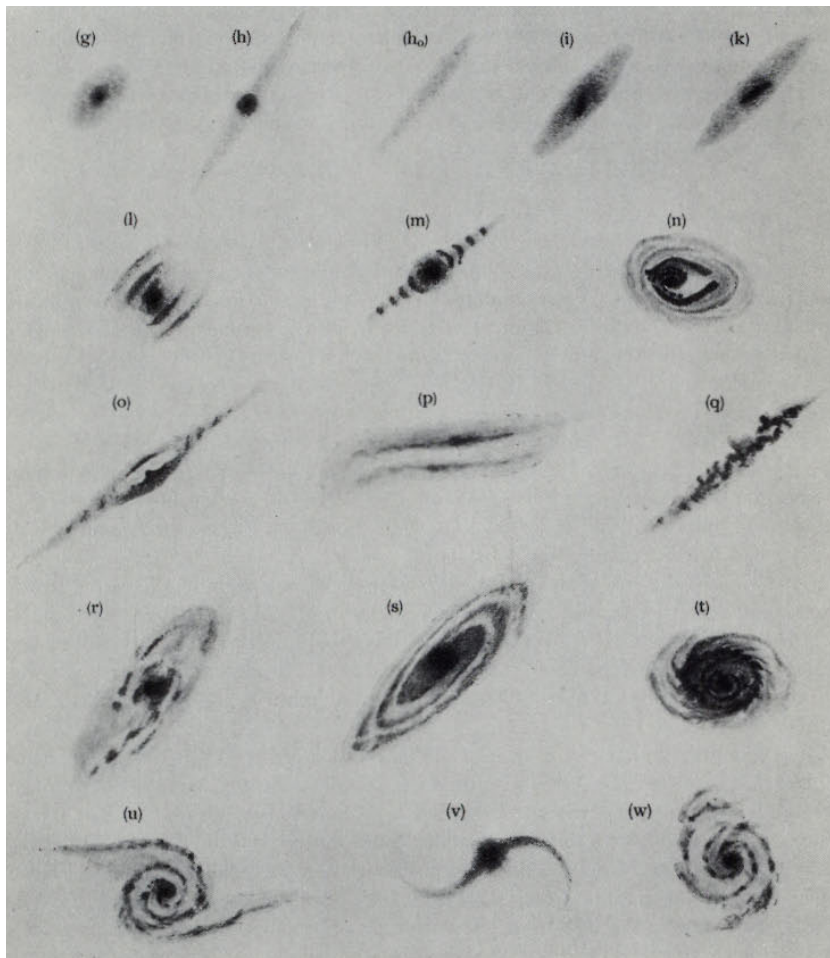
Figura 4.1: Sistema de classificação descritivo de nebulosas por Wolf (1908), apresentava também nebulosas galáticas (na primeira linha, que foi removida). Reproduzido de Sandage et al. (1975).

4.1 Classificação de Hubble

O primeiro sistema amplamente utilizado de classificação de galáxias segundo a sua morfologia foi o de Hubble (1926). Neste sistema, as galáxias são separadas nas classes elíptica, espiral, espiral com barra e irregular. As elípticas são classificadas segundo o seu formato, desde esférico até mais alongado. As espirais são classificadas conforme o tamanho relativo do bojo e as características dos braços (quantidade, grau de espiralamento e granularidade). A forma final de classificação de Hubble é frequentemente ilustrada pelo "diagrama diapasão", apresentado na Figura 4.2, do clássico *The Realm of the Nebulae* de Hubble (1936), e atualizado (incluindo a classe S0 na intersecção dos ramos das espirais) por Sandage et al. (1975).

O sistema de Hubble parece ser mais do que um simples "catálogo botânico" de galáxias. Muitas das propriedades observadas das galáxias, como índices de cor, tipo espectral e densidade de hidrogênio gasoso, variam sistematicamente na sequência de formas. De algum modo, parece haver algo de fundamental escondido nesta classificação baseada apenas na forma, que talvez indique uma relação com as condições iniciais e subsequente evolução temporal das galáxias (Sandage et al. 1975). Estas correlações fizeram com que, durante muito tempo, a sequência de Hubble fosse considerada uma sequência evolutiva, onde as galáxias eram inicialmente elípticas, passavam a ser lenticulares e depois espirais. Isto sobrevive até
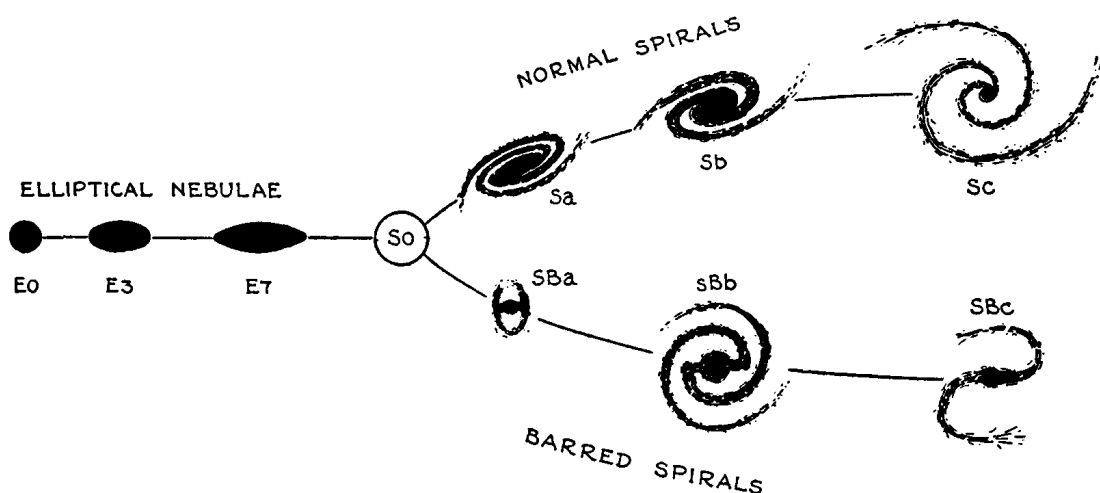
Figura 4.2: Sistema de classificação de Hubble (1936), também conhecido como "diagrama diapasão de Hubble". Foi atualizado por Sandage et al. (1975) para incluir a classe S0 na intersecção dos ramos das espirais.

hoje na nomenclatura "*early type*" (tipo jovem) para elípticas e lenticulares, e "*late type*" (tipo tardio) para espirais e irregulares. Entretanto, Hubble (1927) enfatizou desde o início que a classificação era puramente empírica, e que interpretações de natureza evolutiva deveriam ser tomadas com cautela.

4.2 Componentes estruturais

Os sistemas de classificação descritos na seção anterior são baseados em inspeção visual, com natureza evidentemente qualitativa. Levando tal forma de classificação a um extremo, como o projeto *GalaxyZoo* (Lintott et al. 2008; Willett et al. 2013), chega-se a conclusões estatísticas, mas ainda não se obtém medidas quantitativas de objetos individuais. Para descrever mais precisamente a estrutura de uma galáxia, normalmente é necessário decompô-la em sub-estruturas. Estas sub-estruturas são em geral modeladas como funções analíticas, as quais permitem derivar medidas quantitativas. De forma simplificada, podemos considerar que galáxias são compostas de duas componentes principais: bojo e disco. Os próprios discos podem conter barras, braços espirais, anéis e halos, para citar algumas sub-componentes mais comuns.

4.2.1 Bojos e discos

Do ponto de vista fotométrico (medindo o perfil de brilho superficial), galáxias lenticulares (S0) e espirais *early type* (Sa-Sb) podem ser bem descritas como uma combinação de duas componentes: um bojo e um disco. Neste modelo, o disco é delgado enquanto o bojo é quase esférico (embora haja casos em que ele seja um elipsóide triaxial), ambos observados projetados no plano do céu.

Levando em consideração apenas o perfil de brilho superficial, a separação em componentes baseado no aspecto visual parecer arbitrária. Afinal, pode-se inventar algum modelo empírico onde uma só componente descreva as imagens observadas tão bem quanto a soma de um bojo e um disco. Porém, estas componentes parecem ter outras propriedades distintas, como índices de cores, conteúdo de gás e poeira, cinemática e populações estelares, o que confere uma certa confiança no conjunto de componentes escolhido.

King (1966) descreve um modelo derivado para aglomerados globulares, assumindo velocidades estelares isotérmicas e isotrópicas. Muito embora este modelo tenha motivações

físicas, não possui uma forma funcional simples. Leis como as de Hubble-Reynolds (Binney & Tremaine 2011, equação 2.55) e de Vaucouleurs (1948, 1977), mesmo sendo puramente empíricas, descrevem bem bojos de galáxias. Suas formas funcionais são:

$$I(r) = \frac{I_0}{\left[1 + (r/r_H)^2\right]} \qquad \text{(Hubble-Reynolds)}$$

$$I(r) = I_e \exp\left\{-7{,}67\left[\left(\frac{r}{r_e}\right)^{1/4} - 1\right]\right\} \qquad \text{(de Vaucouleurs)}$$

Os termos r_e e r_H são os parâmetros de escala radial, I_0 é o brilho para $r = 0$ na lei de Hubble-Reynolds e I_e é o brilho para $r = r_e$ na lei de de Vaucouleurs. Estas formas funcionais se ajustam bem à maioria dos bojos e galáxias elípticas. Para sistemas que não são esféricos, deve-se ainda introduzir uma elipticidade e uma orientação. Adicionalmente, a elipticidade e a orientação podem variar com o raio.

Discos, por outro lado, são facilmente modelados como um perfil exponencial (Freeman 1970) dado por

$$I(r) = I_0 \exp\left(\frac{r}{h}\right),$$

com h sendo o parâmetro de escala radial, e I_0 o brilho em $r = 0$.

Sérsic (1963) mostra que os perfis de de Vaucouleurs e exponencial podem ser tomados como casos particulares da equação

$$I(r) = I_e \exp\left\{-b_n\left[\left(\frac{a}{r_e}\right)^{1/n} - 1\right]\right\},$$

que ficou conhecida como "lei de Sérsic". Aqui, o parâmetro n é o índice de concentração, também chamado de "índice de Sérsic", que pode variar continuamente. A Figura 4.3 mostra alguns exemplos. Com $n = 1$ obtém-se uma lei exponencial (linha azul), e com $n = 4$ a lei de de Vaucouleurs (linha vermelha). A maioria dos bojos de espriais e galáxias elípticas podem ter seus perfis de brilho ajustados com índices de Sérsic na faixa de $1 < n < 10$. Valores maiores de n mudam muito pouco a forma da curva. O parâmetro b_n está definido em função de n, ver a seção 6.1.5 de Erwin (2015).

É preciso ter em mente que estas leis são empíricas, e dependem do bom senso de escolher o perfil (ou conjunto de perfis) certo para a galáxia em questão. Tentar ajustar um modelo ina-propriado a uma galáxia pode levar a conclusões equivocadas, embora o ajuste possa parecer
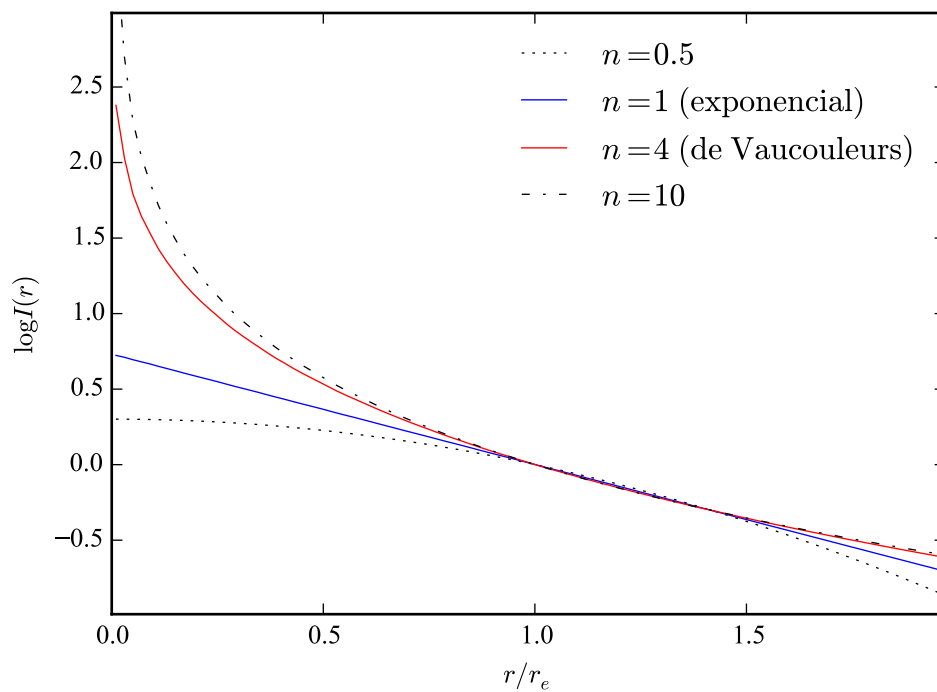
Figura 4.3: Perfis empíricos de Sérsic. O índice n controla a concentração do perfil. Com $n = 1$ obtém-se um perfil exponencial (azul), e com $n = 4$ um perfil de de Vaucoulerus (vermelho). Outros valores de n são mostrados em linhas descontínuas.

bem sucedido.

4.2.2   Dependência dos modelos com o comprimento de onda

Tudo o que se discutiu sobre classificação de galáxias quanto a sua forma, até agora, levou em conta imagens feitas no banda óptica do espectro. Basta olhar umas poucas galáxias em infravermelho ou ultravioleta para verificar que a forma de uma galáxia pode mudar dramaticamente dependendo do comprimento de onda em que se observa. Bojos normalmente desaparecem em ultravioleta por possuírem poucas estrelas jovens. Já em infravermelho, os bojos tendem a dominar, e discos podem ter uma forma bastante diferente por conta da menor profundidade óptica das estruturas de poeira. Claramente há uma dependência da morfologia das galáxias com o comprimento de onda.

Kelvin et al. (2012) utilizou imagens de galáxias do projeto GAMA (Driver et al. 2009) em 9 bandas espectrais, do óptico (Abazajian et al. 2009, bandas *ugriz* do DR7) ao infravermelho (Lawrence et al. 2007, bandas *YJHK* do UKIDSS), para ajustar perfis de Sérsic a > 160.000 galáxias, encontrando gradientes leves no índice de Sérsic em função do comprimento de onda. Os ajustes para cada comprimento de onda foram feitos individualmente. O projeto MegaMorph (Häußler et al. 2013) faz o mesmo de uma forma um pouco mais refinada. Utilizando as bandas fotométricas do SDSS, eles ajustam a variação dos parâmetros morfológicos através de um polinômio (Vika et al. 2013, Figura 4.4). Todos os comprimentos de onda são ajustados de uma vez. Aí se pode ver que em grande escala (em comprimento de onda), há galáxias com um comportamento linear (ou até razoavelmente constante) em r_e. Nestes casos, utilizar um modelo linear em função do comprimento de onda, segundo os autores, melhora a qualidade do ajuste.

Além de efeitos causados pelo método de ajuste, como má escolha do modelo, mudança no sinal-ruído nas várias bandas espectrais, ou mínimos locais, parece haver motivos reais para levar a sério a variação dos parâmetros morfológicos. Populações estelares diferentes emitem mais intensamente em comprimentos de onda distintos, com populações mais jovens dominando em comprimentos de onda menores. Isto parece causar um leve gradiente no índice de Sérsic em galáxias *early type* (La Barbera & de Carvalho 2009). Poeira parece afetar a medida do tamanho e forma de discos (Möllenhoff et al. 2006). O conteúdo e a distribuição de poeira e pode variar significativamente de galáxia a galáxia, dificultando uma conclusão global sobre o seu efeito nos parâmetros morfológicos.

Johnston et al. (2012) obtiveram espectros de fenda longa de galáxias lenticulares (S0),
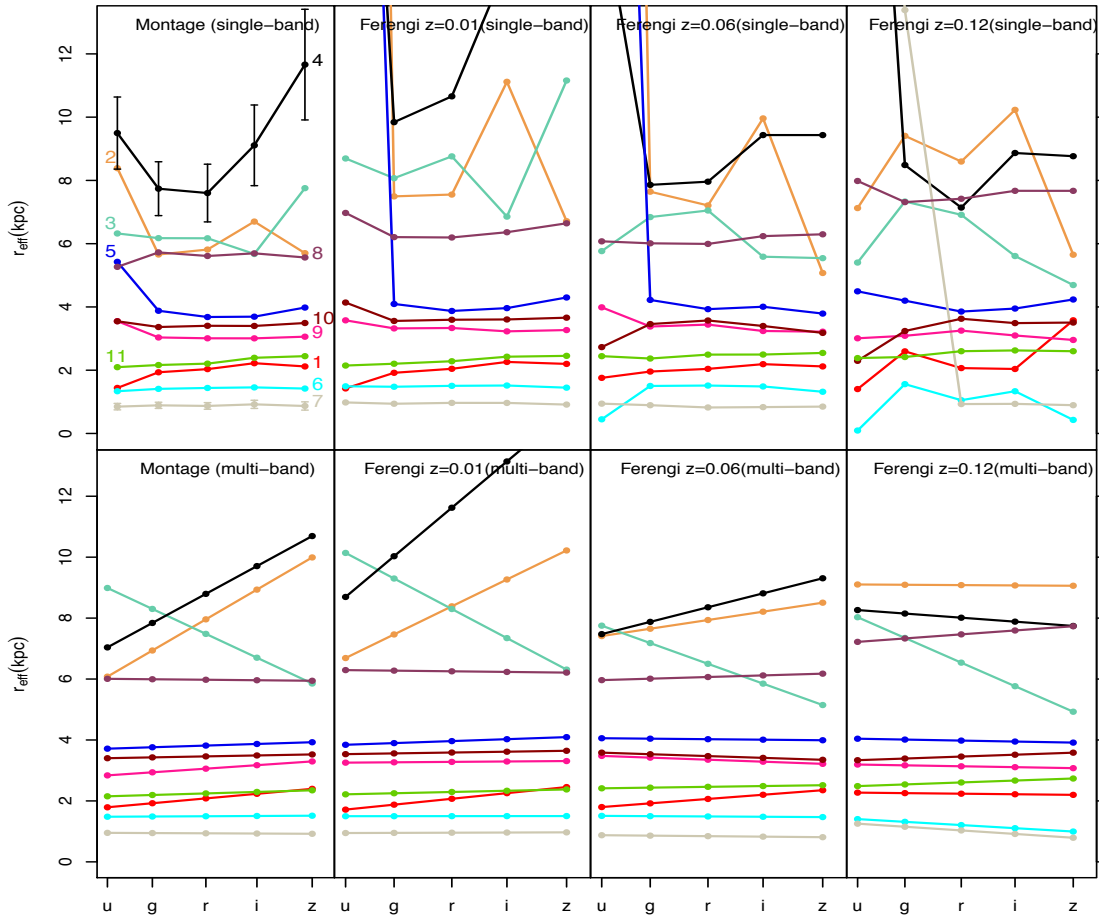
Figura 4.4: Ajuste morfológico de 11 galáxias, utilizando as bandas fotométricas do SDSS. Os gráficos mostram o raio efetivo (r_e neste trabalho) ajustado livremente a cada banda (painéis superiores), e com uma dependência linear em comprimento de onda (painéis inferiores). À esquerda estão os ajustes com as imagens originais, as colunas seguintes são para imagens com *redshift* artificiais. Retirado de Vika et al. (2013).
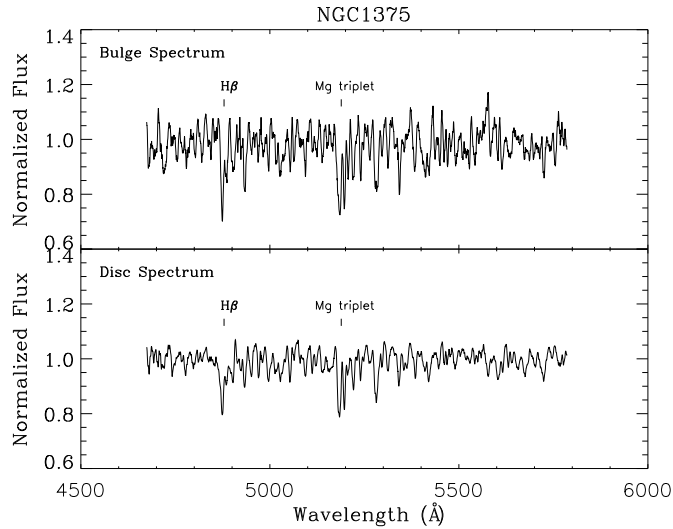
Figura 4.5: Espectros unidimensionais de bojo (acima) e disco (abaixo) de NGC 1375. É possível reconhecer a linha espectral Hβ e o tripleto de magnésio, em absorção. Retirado de Johnston et al. (2012).
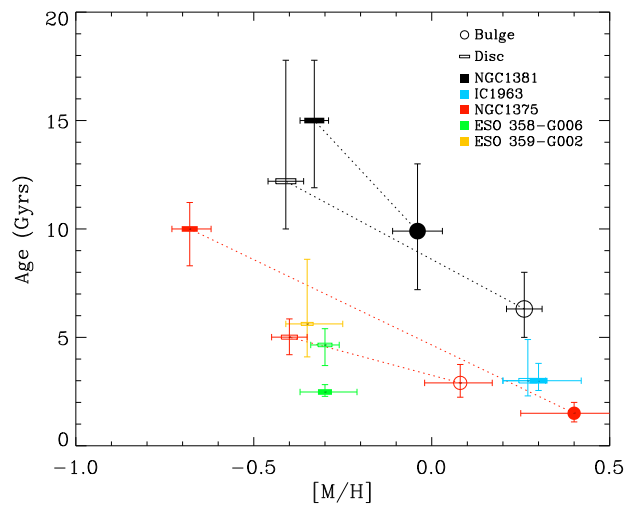
Figura 4.6: Idade (eixo vertical) e metalicidade (eixo horizontal) estelares de bojos (marcadores redondos) e discos (marcadores retangulares) de uma amostra de galáxias S0 observadas com espectrógrafo de fenda longa. As linhas pontilhadas ligam componentes de uma mesma galáxia. Retirado de Johnston et al. (2012).

gerando assim perfis de brilho das galáxias para cada comprimento de onda. Ajustando um perfil de de Vaucouleurs e um exponencial ao perfil de brilho de cada uma das galáxias (em ambos os lados), eles obtém os espectros separados de cada um dos seus dois componentes morfológicos, como mostrado na Figura 4.5. Com os espectros, pode-se tentar entender que populações estelares compõe o bojo e o disco destes galáxias. Os autores estimam a idade e a mtelicidade estelar das componentes utilizando a intensidade da linha Hβ e do tripleto de magnésio, comparando com uma grade de modelos sintéticos de populações estelares. A conclusão que chegam é que os bojos são sistematicamente mais jovens e mais metálicos do que os discos (Figura 4.6). Inspirado neste estudo, o Capítulo 7 descreve a decomposição de espectros de galáxias em espectros de bojos e discos, mas utilizando cubos de dados do CALIFA.

4.2.3   Ajuste de modelos

Utiliza-se geralmente algoritmos de minimização para encontrar os modelos que melhor ajustam o perfil de brilho de uma galáxia. A abordagem usual é baseada no princípio de máxima verossimilhança ($\mathcal{L}$). Se a estatística das medidas é gaussiana (que é aproximadamente verdade na maioria das imagens astronômicas relevantes ao ajuste de modelos), o logarítmo da verossimilhança se assemelha à familiar soma de χ^2(Erwin 2015, seção 4.1.2). Isto significa que o problema passa a ser a minimização da equação

$$-2\ln\mathcal{L} = \chi^2 = \sum_i^N \frac{(d_i - m_i)^2}{\sigma_i^2},$$

onde d_i é o valor medido, m_i é o valor do modelo, e σ_i é o erro gaussiano na medida. O modo como se procura o mínimo χ^2 vai depender de como se aborda o problema.

A Figura 4.7 mostra um exemplo de ajuste de bojo e disco em um perfil de brilho unidimensional. Pode-se fazer o ajuste diretamente na imagem, em duas dimensões (Figura 4.8), utilizando modelos com perfis elipsoidais. Independente da escolha do modelo, há um aspecto importante do ajuste da morfologia que foi negligenciado até agora: efeitos instrumentais e atmosféricos. Estes efeitos são representados pela figura da PSF (*Point Spread Function*), tratada em detalhes no Capítulo 5. A grosso modo, levar em conta a PSF significa considerar que a luz que atinge determinada posição no detector não é proveniente apenas de uma região pontual no céu, e sim de uma região extensa que depende dos instrumentos e da tubulência atmosférica. Efetivamente, objetos pontuais tornam-se "borrões" na imagem observada.
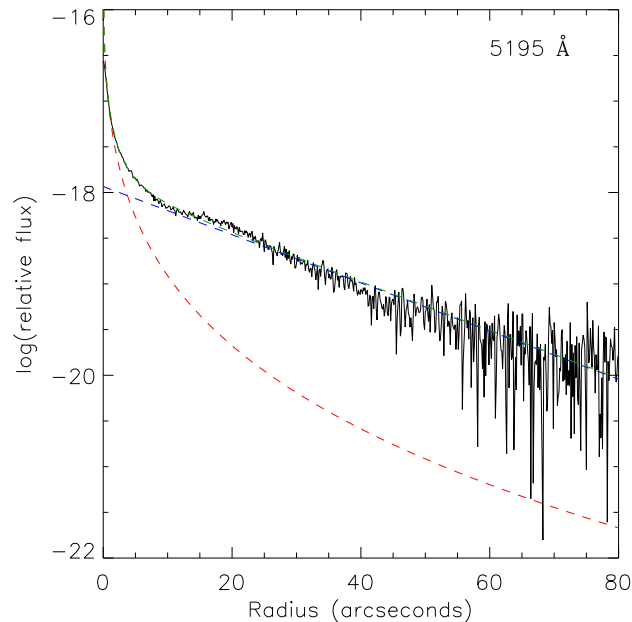
Figura 4.7: Ajuste morfológico em uma dimensão, utilizando modelos de bojo e disco. A linha preta mostra o perfil de brilho da galáxia NGC 1375 em 5195 Å, obtido através de espectroscopia de fenda longa. Em azul um perfil exponencial e em vermelho um perfil de De Vaucouleurs (Sérsic com $n = 4$), que somados são o melhor ajuste, em verde. Retirado de Johnston et al. (2012).

Figura 4.8: [TODO] Ajuste morfológico em duas dimensões, feito de alguma forma com GALFIT (Peng et al. 2002). Procurar uma figura melhor.

Pode-se evitar tocar neste ponto quando se faz o ajuste em uma dimensão. Se as dimensões da PSF forem muito menores do que as da galáxia, e esta tiver uma imagem suave, a forma da galáxia muda muito pouco devido à PSF, exceto exatamente sobre o núcleo. Isto é especialmente problemático em *early types*, onde um perfil de Sérsic pode gerar um pico de várias ordens de magnitude, concentrado em uns poucos em *pixels*. A forma mais simples de se escapar da PSF, em uma dimensão, é "varrê-la para baixo do tapete", isto é, não tentar ajustar pontos muito próximos ao núcleo (mascarando alguns segundos de arco, dependendo do tamanho da PSF). O ajuste de um perfil de Sérsic pode ficar comprometido em casos onde a PSF é muito grande e se descarta uma fração considerável do bojo.

Em duas dimensões o mais adequado é adotar a PSF como parte do problema. Uma boa caracterização da PSF é crucial para se obter resultados satisfatórios no ajuste. Mas, trabalhar com a PSF traz um custo computacional enorme, uma vez que é preciso efetuar um cálculo de convolução (ver Seção 5.1) cada vez que se avalia o modelo para um determinado conjunto de parâmetros. O problema de minimização, que já é de natureza não-linear para modelos de componentes de galáxia, tona-se ainda mais complicado.

Diversos algoritmos foram desenvolvidos para tratar do problema de minimização não-linear. O método Levenberg-Marquardt (Levenberg 1944; Marquardt 1963, daqui em diante L-M), com sua busca através do gradiente no espaço de parâmetros, tem a vantagem de ser muito rápido. Mas, sua própria natureza de gradiente faz com que seja necessário um bom "chute inicial", com a possibilidade de ficar preso em mínimos locais. Pode-se reduzir a chance de ser pêgo em mínimos locais utilizando algoritmos mais complexos, como o Nelder-Mead *simplex* (Nelder & Mead 1965, daqui em diante N-M). A desvantagem é que conforme se vai aumentando a complexidade do algoritmo, o tempo necessário para encontrar o mínimo tende a crescer drasticamente. De qualquer modo, tanto o L-M quanto o N-M sofrem de um problema comum: é preciso especificar um valor inicial, e o algoritmo segue um ou mais caminhos até encontrar o mínimo. O algoritmo de Metropolis (Metropolis et al. 1953; Saha & Williams 1994) adota uma abordagem Bayesiana, e o problema de minimização se torna análogo a um problema de mecânica estatística[FIXME], onde se vai baixando a temperatura até encontrar o estado de menor energia. São necessários apenas os limites do espaço de parâmetros, uma grande vantagem em casos onde não se sabe de antemão o modelo aproximado. Novamente troca-se velocidade por robustez, este algoritmo é significativamente mais lento do que L-M e N-M. *Differential Evolution* (Storn & Price 1997, daqui em diante DE) aborda o problema de forma completamente distinta. Nele, a busca através do espaço de parâmetros é feita com uma população de modelos. Os modelos sofrem "mutações" e "recombinações" em cada iteração, e somente os modelos que se saem melhor são mantidos. Algoritmos desta

natureza são chamados genéticos. Como o algoritmo de Metropolis, apenas são necessários os limites do espaço de parâmetros. Outra vantagem é que é muito mais improvável que este algoritmo fique preso num mínimo local do que o L-M, o N-M ou mesmo o de Metropolis. Tudo isto cobra um grande preço: ele é o algoritmo mais lento considerado aqui, cerca de duas ordens de magnitude mais lento do que o L-M.

Existem diversas ferramentas utilizadas em astrofísica que implementam algum destes algoritmos para fazer o ajuste de modelos em imagens. Vale citar, por exemplo, GALFIT3 (Peng et al. 2010) e GASP2D (Méndez-Abreu et al. 2008) utilizando L-M, BUDDA (de Souza et al. 2004) utilizando N-M, GIM2D (Simard et al. 2002) utilizando o algoritmo de Metropolis, e IMFIT[1] Erwin (2015), que utiliza L-M, N-M ou DE. O programa escolhido para o presente trabalho foi o IMFIT, em grande parte por ter seu código livre, e também por ter sido desenvolvido tendo em mente a facilidade de modificação. Entretanto, como a versão original foi feita em forma de um programa executado em linha de comando, não é muito prático utilizá-la em seu formato original para implementar as tarefas deste trabalho.

Foi feita uma versão modificada do IMFIT em forma de biblioteca dinâmica, com um envelope de código**[FIXME]** para ser acessado em Python. Esta biblioteca foi chamada python-imfit[2], e expõe**[FIXME]** praticamente toda a funcionalidade do IMFIT, utilizando *arrays* numéricos do Python. Esta biblioteca é bastante genérica, e pode ser utilizada para qualquer aplicação de ajuste de imagem. Contudo, o mais importante é que a manipulação de modelos e o ajuste para múltiplas imagens deixa de ser um exercício tedioso de organização de *shell scripts***[FIXME]**, passando a ser um programa de computador propriamente dito, com toda a maquinaria do Python a sua disposição. O programa resultante, que faz a decomposição em bojo e disco em um cubo de dados do CALIFA, é apresentado no Capítulo 7.

---

[1] `http://www.mpe.mpg.de/~erwin/code/imfit/index.html`
[2] `https://github.com/streeto/python-imfit`

Capítulo 5

Caracterizando a PSF do CALIFA

5.1 Efeitos instrumentais e atmosféricos

A PSF (sigla para *Point Spread Function*, em inglês) descreve a resposta de um sistema de imageamento a uma fonte pontual. Observando uma fonte pontual no infinito, que emite no comprimento de onda λ com uma lente ideal de diâmetro de abertura D, obtém-se uma imagem de diâmetro (em radianos) $\theta \approx 1{,}22\frac{\lambda}{D}$. Esta imagem, conhecida como Disco de Airy, é a figura de interferência causada por uma abertura circular, e limita a resolução espacial teórica que se pode obter com um telescópio de uma dada abertura. Isto vale para desde telescópios e câmeras pequenos, até telescópios espaciais.

Para um telescópio suficientemente grande, na superfície terrestre, a figura de difração torna-se desprezível se comparada ao efeito causado pela turbulência atmosférica, conhecida como *seeing*. Telescópios com diâmetro a partir de $\sim 20\,\mathrm{cm}$ já têm sua resolução espacial (no óptico) limitada pelo *seeing*[1]. O modelo de Kolmogorov, baseado em estudos de turbulência e desenvolvido por Tatarskii (1961), descreve como as frentes de onda são perturbadas durante a passagem por células de turbulência atmosférica. Uma excelente revisão sobre a teoria da PSF é feita por Racine (1996). O perfil de Kolmogorov é dado pela transformada de Bessel da função de transferência de modulação atmosférica dado pelo modelo de Kolmogorov, e fica definido em função de uma integral sem forma fechada, devendo ser resolvida numericamente. Costuma-se utilizar formas funcionais que se aproximam do perfil de Kolmogorov. Gaussianas são usadas muito frequentemente, mesmo não sendo adequadas. O perfil de Moffat (1969) se ajusta bem ao perfil de Kolmogorov numa faixa de ~ 7 magnitudes em brilho superficial, muito

---

[1]Desconsiderando telescópios que aplicam técnicas de óptica adaptativa, que não fazem parte do escopo deste trabalho.
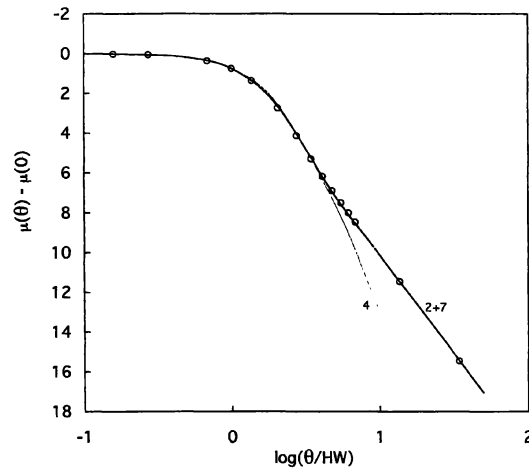
Figura 5.1: Ajuste de perfil de Moffat (linhas sólidas) ao modelo de PSF de Kolmogorov (círculos abertos). A linha fina, é um perfil de Moffat com $\beta = 4$, e a linha espessa é a soma de dois perfis de Moffat, com $\beta = 7$ (80 % do fluxo) e $\beta = 2$ (20 % do fluxo). Retirado de Racine (1996).

além do que a maioria dos casos de uso requer, e tem uma forma bastante simples, dada por

$$I(r) = \frac{I_0}{\left[1 + \left(\frac{r}{\alpha} \right)^2 \right]^\beta}, \quad \alpha = \frac{\text{FWHM}}{2 \sqrt{2^{1/\beta} - 1}}.$$

Dois parâmetros controlam a forma da PSF neste perfil: a largura a meia altura (FWHM) e o índice β, que controla a intensidade das "asas" da PSF. Com $\beta \to \infty$, o perfil de Moffat torna-se uma gaussiana. O melhor ajuste ao perfil de Kolmogorov se obtém quando $\beta = 4$ (Figura 5.1).

Se a PSF é constante em todo o campo, seu efeito na imagem pode ser calculado como a convolução entre a imagem da PSF e a imagem original. Isto tem um custo computacional extremamente elevado, especialmente quando se utiliza algum procedimento iterativo como um ajuste de modelo. Uma convolução, em cálculo numérico, significa calcular uma integral em duas dimensões para cada *pixel*, ou seja, escala com $O(n^2)$. Um truque bastante comum é utilizar transformadas de Fourier para simplificar este cálculo e transformá-lo num algoritmo que escala com $O(n \log n)$. Se I é a imagem original e I^{PSF} a imagem da PSF, a imagem final I^* é dada por

$$I^* = I \otimes I^{\text{PSF}}.$$

Aplicando a transformada de Fourier,

$$\mathcal{F}\{I^*\} = \mathcal{F}\{I \otimes I^{\mathrm{PSF}}\}$$
$$= \mathcal{F}\{I\} \cdot \mathcal{F}\{I^{\mathrm{PSF}}\},$$

ou seja, troca-se uma convolução por uma multiplicação. Para obter a imagem final, basta aplicar a transformada de Fourier inversa sobre o produto. A transformada de Fourier da PSF é sempre a mesma, logo a cada iteração apenas duas integrais numéricas em duas dimensões são necessárias: a transformada da imagem original e a transformada inversa para a imagem final. O ganho é tão significativo que praticamente todos os programas de ajuste de imagens astronômicas utilizam transformadas de Fourier para convoluir a imagem.

5.2 Medindo a PSF

Para determinar as caraterísticas da PSF, idealmente é preciso observar um objeto pontual brilhante, em várias regiões do campo do detector, e com as mesmas condições atmosféricas que as observações. Raramente estas condições são preenchidas, mesmo para fotometria CCD com campos muito grandes. Assim, conhecer a PSF em instrumentos IFU não é uma tarefa trivial. Ainda há o fato de que as imagens são reconstruídas através de técnicas de *dithering* (ver Seção 2.1.1), e dependendo o algoritmo utilizado, a PSF pode nem sequer ser analítica. Entretanto, é preciso de algum modo obter uma aproximação da forma da PSF para poder modelar a morfologia de uma galáxia (Capítulo 4), especialmente o seu bojo. O procedimento descrito a seguir é mais um esforço para entender a PSF e poder realizar a decomposição morfológica do que um estudo aprofundado sobre o tema.

Para o CALIFA, observar campos estelares para caracterizar a PSF significaria a redução no número de galáxias na amostra final do *survey*. Dadas as restrições de tempo de telescópio e de significância estatística da amostra, além do fato de a PSF não ser fundamental para os casos científicos alvo do *survey*, estas observações não foram realizadas. Porém, sendo um *survey* espectroscópico, o CALIFA necessita de observações de "velas padrão" para calibrar o fluxo das galáxias. Foram observadas 45 estrelas para este fim. Estas estrelas foram obsevadas no centro no campo de observação do instrumento, com um tempo de exposição muito menor do que o das galáxias (120 s contra 900 s). Esta amostra foi denominada "estrelas de calibração". Alternativamente, pode-se procurar estrelas que apareçam na frente das galáxias do *survey*. Neste caso a vantagem é que as estrelas têm o mesmo tempo de exposição das galáxias, e são observadas nas mesmas condições atmosféricas. Porém, não se encontra estas estrelas

Perfil de Moffat com $\beta = 4$ para feige67 @ 20120616 (config. V500 em 4949 Å)
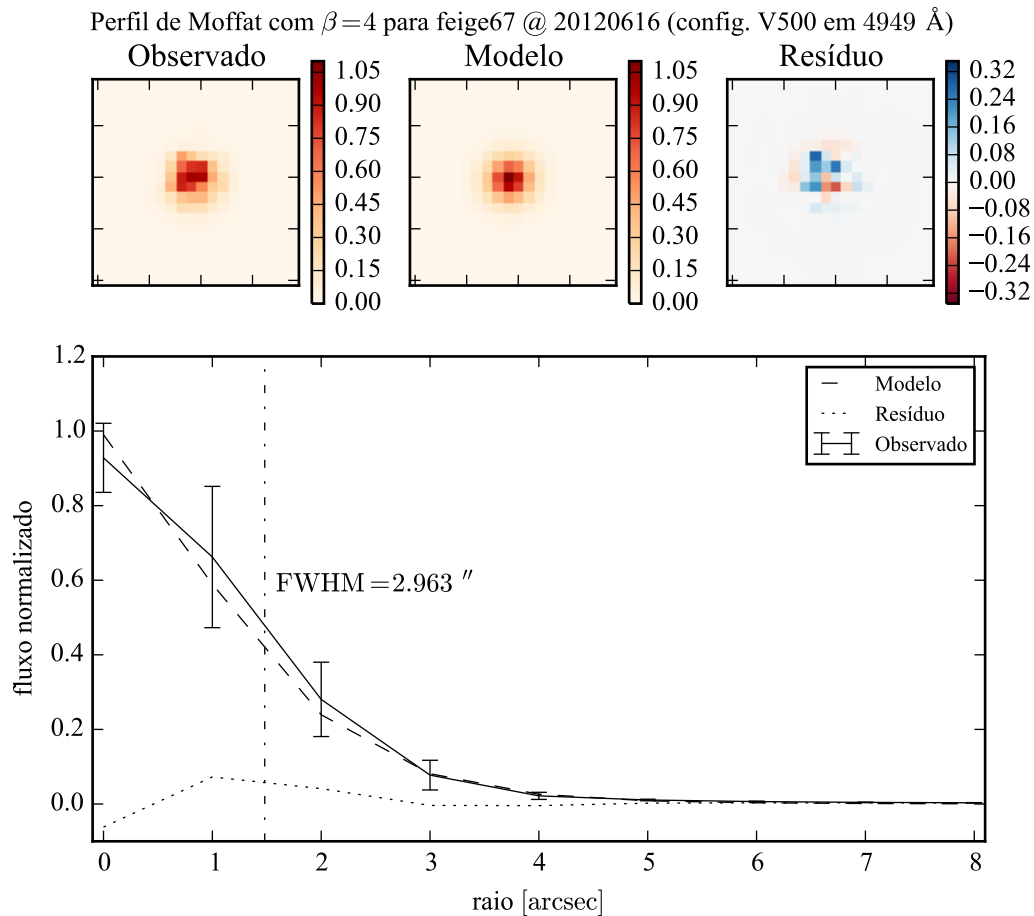
Figura 5.2: Exemplo de ajuste de PSF para a estrela de calibração Feige67, observada em 16/06/2012, com a cofiguração V500. O modelo ajustado foi um perfil de Moffat elipsoidal com $\beta = 4$. Nos painéis superiores estão imagens do fluxo observado numa caixa de 400 Å centrada em 4949 Å, do modelo ajustado e do resíduo do ajuste. No painel inferior mostra-se o perfil de brilho radial médio: observado (linha sólida, onde as barras de erro são 1σ da média), modelo (linha tracejada, e a linha traço-ponto marca a largura a meia altura FWHM = 2,963 $''$) e resíduo (linha pontilhada).

intrometidas em todos os cubos, logo obter uma PSF para cada um deles está descartado. Outro problema em potencial é que elas em geral, por construção do *survey*, são fracas e se localizam na periferia do campo de observação. Esta amostra foi denominada "estrelas de campo", com 9 estrelas suficientemente brilhantes escolhidas em cubos de galáxias *early type*. As duas amostras de estrelas reaproveitadas foram usadas para caracterizar a PSF do CALIFA com o procedimento descrito a seguir.

O modelo utilizado foi um perfil de Moffat 2-d elipsoidal, com $\beta = 4$, conforme visto na

Perfil de Moffat - estrelas de calibração
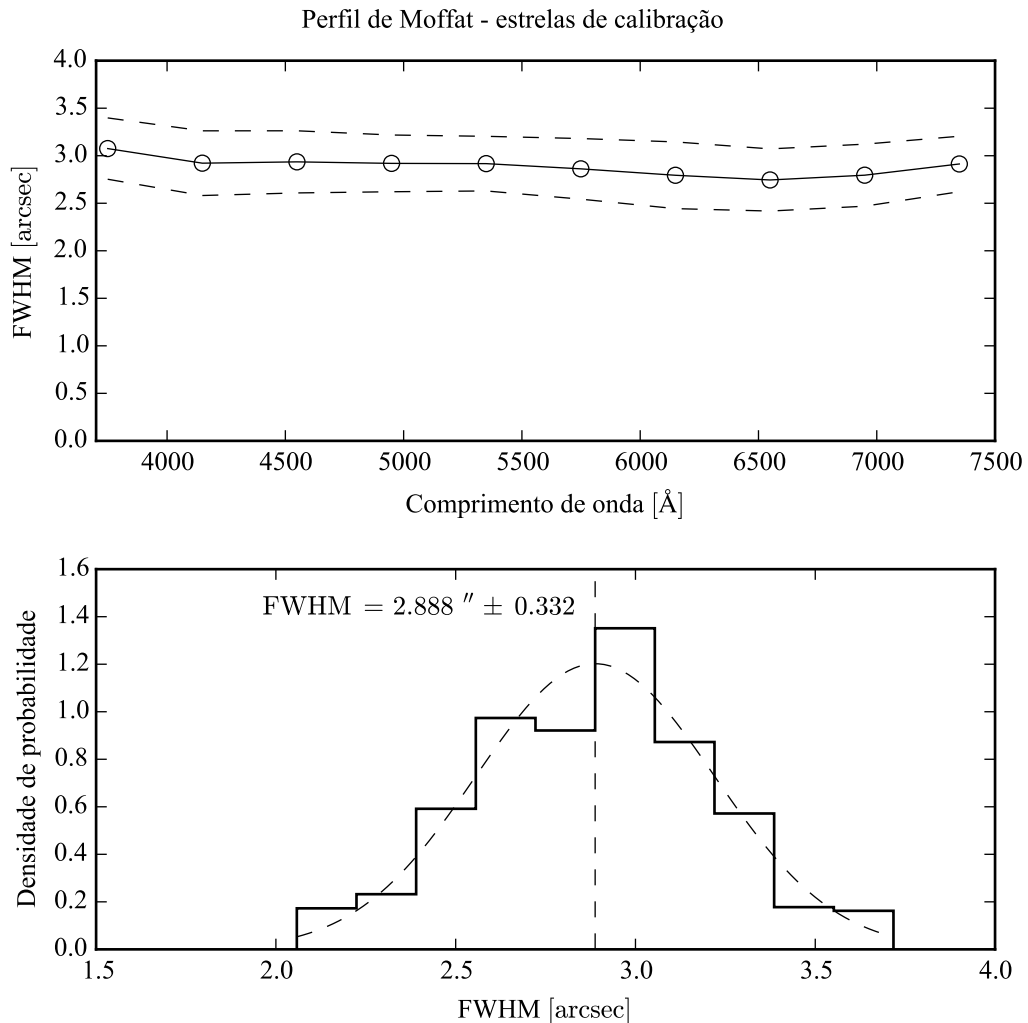
Figura 5.3: PSF do CALIFA modelada como um perfil de Moffat com $\beta = 4$, utilizando 45 estrelas de calibração. *Acima*: FWHM da PSF em função do comprimento de onda (caixas de 400 Å). As linhas tracejadas indicam a distribuição em 1 σ. *Abaixo*: Histograma da FWHM da PSF, ponderado pela verossimilhança do modelo em todos os comprimento de onda de todas as estrelas, com FWHM = 2,888±0,332 ″.

Seção 5.1. Os cubos foram combinados em caixas de 400 Å de largura, gerando 10 imagens de fluxo e incerteza para cada estrela. Estas imagens foram ajustadas aos modelos através de um programa desenvolvido utilizando a biblioteca PYTHON-IMFIT[2]. O resultado do ajuste são os parâmetros do perfil de Moffat e a estatística χ^2 do melhor modelo. A Figura 5.2 ilustra o ajuste feito para uma estrela de calibração, numa faixa espectral próxima a 5000 Å.

---

[2]PYTHON-IMFIT é uma biblioteca baseada no programa IMFIT de Erwin (2015), a mesma utilizada no programa de decomposição morfológica, ver Seção 4.2.2.

Este procedimento foi realizado para as 45 estrelas de calibração, e o resultado pode ser visto na Figura 5.3. Praticamente não há dependência da PSF com o comprimento de onda, como se pode verificar no painel superior da figura. Na mesma figura, no painel inferior, mostra-se um histograma ponderado pela verossimilhança ($e^{-\chi^2/2}$) de todos os ajustes (todas as estrelas em todas as caixas de comprimento de onda). Desta distribuição obtém-se uma largura a meia altura média de FWHM = 2,888 ± 0,332 ″. A elipticidade ($\epsilon = 1 - b/a$) média encontrada é de $\epsilon = 0,097 \pm 0,065$, ou seja, a PSF é praticamente circular. A incerteza nos dois casos representa o desvio padrão ($1\,\sigma$) da média ponderada. O mesmo vale para todas as incertezas obtidas no resto desta seção.

O mesmo procedimento foi realizado para as 9 estrelas de campo, presentes nos cubos de galáxias do *survey* e normalmente mascaradas por não serem de interesse no estudo do espectro das galáxias. As estrelas desta amostra estão na frente de galáxias com simetria axial (elípticas e S0). Dado um cubo de uma galáxia, recortou-se 7 *spaxels* ao redor da estrela, gerando dois cubos: um da galáxia, com a estrela mascarada, e outro da estrela. Neste ponto o cubo da estrela ainda está contaminado pela luz da galáxia. Então, considerando que a galáxia tem simetria axial, calculou-se um perfil de brilho radial médio da galáxia (ver Seção 3.1, Figura 3.5), para cada comprimento de onda. Com este perfil, é possível estimar quanto a galáxia está contribuindo para a luz de cada *spaxel* do cubo da estrela, pois a distância de cada *spaxel* ao centro da galáxia é conhecido. Criou-se assim um cubo de "luz de fundo" para a mesma região que contém a estrela. Subtraindo o cubo de fundo do cubo da estrela, obteve-se um cubo com apenas a luz proveniente da estrela. Este cubo foi então analisado da mesma forma que os cubos de estrelas de calibração, com os resultados mostrados na Figura 5.4. Da mesma forma, não há dependência da FWHM da PSF com o comprimento de onda, com FWHM = 2,564 ± 0,354 ″ e elipticidade $\epsilon = 0,093 \pm 0,059$.

Há uma diferença considerável no valor obtido para a FWHM da PSF nos dois casos, embora eles estejam a cerca de $1\,\sigma$ de separação. Isto poderia indicar uma diferença sistemática entre a PSF das estrelas de calibração e a PSF das estrelas de campo. Todavia, observando atentamente o histograma de FWHM das estrelas de campo (painel inferior da Figura 5.4), pode-se notar que a distribuição possui um excesso próximo a 2,8 ″. Isso parece indicar que a FWHM da PSF das estrelas de campo é em geral maior do que o estimado pela média ponderada, já que a distribuição se desvia de uma gaussiana. Isto, aliado ao fato de que o tamanho da amostra de estrelas de calibração (45) é maior do que o das estrelas de campo (9), fez com que se escolhesse a medida da primeira amostra como a mais confiável.

Já com os valores de elipticidade (ϵ) obtidos nos dois casos, os semieixos maior e menor da FWHM estão dentro da faixa de $1\,\sigma$ um do outro. E em ambos os casos, ϵ é muito próximo
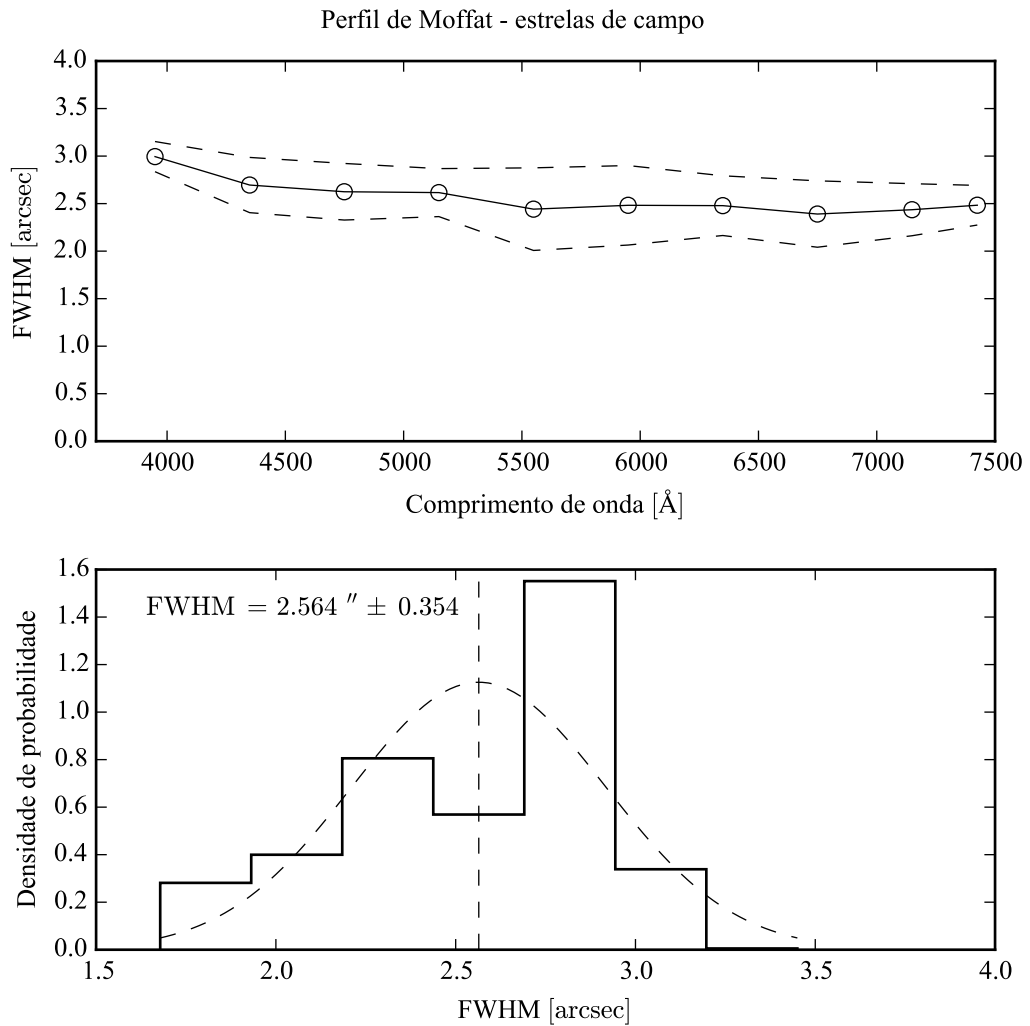
Figura 5.4: PSF do CALIFA modelada como um perfil de Moffat com $\beta = 4$, utilizando 9 estrelas de campo, na frente das galáxias observadas. *Acima*: FWHM da PSF em função do comprimento de onda (caixas de 400 Å). As linhas tracejadas indicam a distribuição em 1 σ. *Abaixo*: Histograma da FWHM da PSF, ponderada pela verossimilhança do modelo em todos os comprimentos de onda de todas as estrelas, com FWHM = 2,564 ± 0,354 ″.

a zero, dentro da incerteza. Levar a elipticidade em conta seria adicionar uma complexidade desnecessária (e possivelmente artificial) ao modelo de PSF.

Assim, a PSF adotada neste trabalho é um perfil de Moffat com simetria axial, $\beta = 4$ e FWHM $= 2,9 \pm 0,3''$. Este foi o mesmo procedimento para fazer a caracterização da PSF publicada no DR2 do CALIFA (García-Benito et al. 2015), mas com uma diferença. Naquele caso, modelou-se tanto FWHM quanto β, obtendo-se FWHM $= 2,39 \pm 0,26''$ e $\beta = 1,73 \pm 0,11$. A diferença está basicamente em qual região da PSF se está interessado. Por uma questão geométrica, há mais *pixels* longe do centro do perfil, o que acaba causando mais peso destas regiões periféricas no modelo escolhido pelo ajuste (ver as barras de erro cada vez menores com a distância, na Figura 5.2, que são a grosso modo inversamente proporcionais ao peso). Porém, na maioria destes *pixels* periféricos o fluxo proveniente da estrela já está submerso no ruído, achatando o perfil (isto é, diminuindo β). O ajuste resultante é então pior nas regiões centrais, com peso menor. No caso do ajuste morfológico de uma galáxia, isto pode causar problemas na determinação dos parâmetros do bojo. Assim, optou-se por refazer a análise ds PSF para esta tese com β fixo.

Capítulo 6

Testes da decomposição morfológica espectral

6.1 Construindo uma galáxia

6.2 Dependência do ajuste com a PSF

6.3 Teste antigo (só pra referência, apagar depois!)

Para determinar se o método de decomposição funciona (ou melhor, se ele falha mesmo para o caso mais básico), foi desenhado um exercício bastante simples. Dado um conjunto de parâmetros morfológicos arbitrários, foi montado um cubo de espectros de uma galáxia sintética composta de um bojo velho (utilizando uma SSP de $12\,Gyr$) e um disco jovem (utilizando uma SSP de $3\,Gyr$). Os espectros de base para o bojo e o disco podem ser vistos na Figura 6.1. Após gerar os cubos de dados de espectros, foi adicionado um ruído gaussiano de 10%. Executando a decomposição neste cubo de dados simulado, deveria-se encontrar valores para os parâmetros próximos aos escolhidos no início. A Figura 6.2 mostra a comparação dos parâmetros obtidos com os iniciais. Os valores ajustados (linhas sólidas) estão de acordo com o valor inicial, levando em conta o erro injetado nos espectros. É necessário repetir este teste com configurações mais complexas, a fim de determinar as limitações do método.
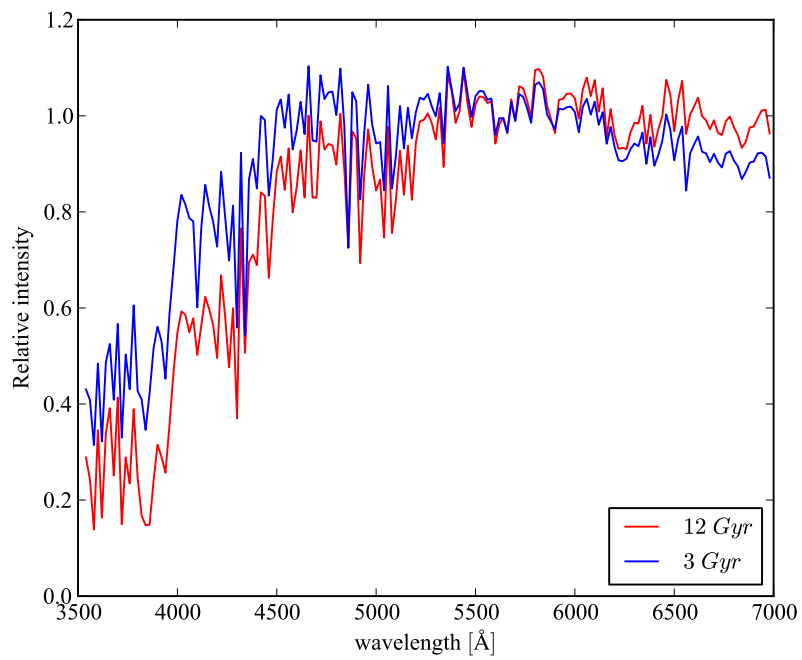
Figura 6.1: Espectros de base para o teste de decomposição.
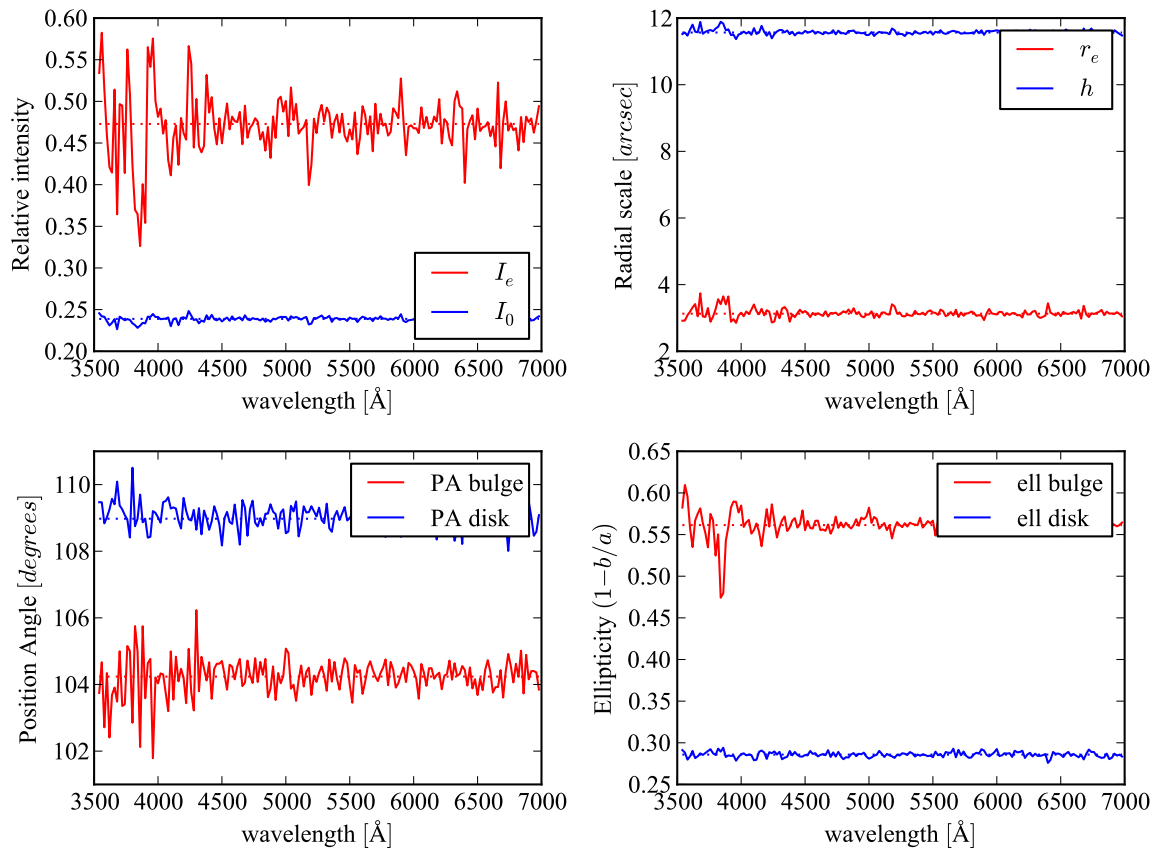
Figura 6.2: Parâmetros obtidos com o teste de decomposição. Em tracejado são os parâmetros originais, em linhas sólidas os ajustes. Os parâmetros do bojo estão em vermelho e os do disco em azul. O índice de Sérsic (*n*) foi mantido constante e igual a 4.

Capítulo 7

Decomposição bojo-disco de IFS de galáxias

7.1 Seleção da amostra

[TODO]: Amostra selecionada usando como critério: Candidata a S0 (descrever a tabela de morfologia do CALIFA) e baixa inclinação (b/a > 0.6).

[TODO]: Limpando a amostra. Ajustes iterativos de uma banda espectral, e inspeção visual (primeira limpeza). Ajuste completo, e segunda inspeção visual.

[TODO]: Criar tabela da amostra. Marcar quais foram vetadas em qual passo, e escrever o motivo – dust lane, bad fit, etc.

7.2 Decomposição espectral

[TODO] Revisar esta seção. Neste trabalho trata-se apenas de galáxias com disco e esferoidais. Galáxias esferoidais seguem em geral um perfil de Sérsic, conforme a equação

$$I(r) = I_e \exp\left\{-b_n\left[\left(\frac{a}{r_e}\right)^{1/n} - 1\right]\right\}.$$

Já galáxias de tipo disco são bem modeladas por um perfil exponencial, dado por

$$I(r) = I_0 \exp(-r/h).$$

Uma galáxia pode ser bem descrita como a soma de um disco exponencial e um bojo com perfil de Sérsic. Através de um algoritmo de ajuste de funções, pode-se determinar, dado o perfil de brilho de uma galáxia, qual combinação de valores para os parâmetros livres (neste caso, I_e, r_e, n, I_0 e h) melhor reproduz o perfil de brilho da galáxia. O mesmo princípio foi então aplicado aos cubos de dados de IFS do CALIFA. Diferente de do método de Johnston et al., foram ajustadas imagens a cada comprimento de onda, utilizando um programa baseado na versão modificada do Imfit, conforme a Seção **??**. A decomposição é realizada sobre os espectros sintéticos[FIXME], provenientes de uma síntese realizada anteriormente, sobre os dados originais. A motivação para isto é bastante simples: evitar efeitos de linhas de emissão. Estas seriam outra fonte de incerteza no ajuste morfológico, dado que em geral estão relacionadas a regiões de formação estelar e núcleos ativos, que não necessariamente seguem o mesmo perfil que o bojo ou o disco. Como este trabalho é experimental, estas complicações foram deixadas de lado, neste momento.

[TODO]: Explicar melhor o método de decomposição.

Os resultados apresentados aqui devem ser tomados com cuidado. O ajuste é feito sem fazer hipótese alguma sobre como os parâmetros morfológicos variam a cada comprimento de onda.

7.3 Resultado

[TODO]: Refazer todo o que vem a seguir.

A discussão a seguir refere-se à decomposição feita sobre os cubos de dados da galáxia UGC 10695 (Figura 7.1). A decomposição foi feita utilizando a seguinte configuração:

- Todos os pixels originais, sem agrupar em zonas de Voronoi.

- Espectros sintéticos provenientes de uma síntese executada anteriormente.

- Ajuste de todos os parâmetros livres: I_e, r_e, n, I_0, h e a geometria da elipse[1].

---

[1]A geometria da elipse é definida pelo ângulo de posição (*P.A.*) e a elipticidade $(1 - b/a)$.
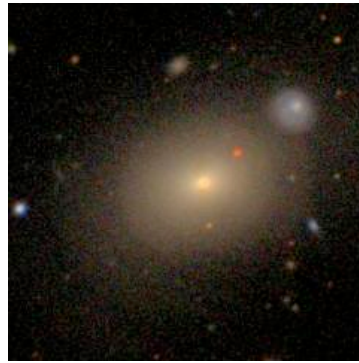
Figura 7.1: Montagem RGB da galáxia UGC 10695, do SDSS.

- Convolução com uma PSF[2] gaussiana de largura a meia altura de 2,4 ", medida numa estrela presente no campo observado.

Na Figura 7.2 pode-se ver os parâmetros obtidos no ajuste morfológico. Em comprimentos de onda menores que 4000 Å o ajuste sai um pouco ruidoso, provavelmente devido à má calibração dos espectros do CALIFA nesta região. Nas outras regiões os parâmetros tendem a variar suavemente, embora haja variações locais próximas às linhas de absorção. Em especial, o ângulo de posição do bojo e do disco, e o centro dos dois modelos, são praticamente constantes.

A Figura 7.3 permite uma visualização bidimensional dos modelos em 5635 Å, e uma comparação com a imagem original neste comprimento de onda. O resíduo é mostrado no painel inferior direito. Ali se observa efeitos de borda próximo às regiões externas mascaradas, além de um artefato no núcleo, provavelmente devido à forma da PSF. Outra forma de visualizar a qualidade do ajuste é através do perfil radial. A Figura 7.4 mostra o perfil radial em intervalos de aproximadamente 100 Å. Ali se vê que o disco e o bojo estão bem modelados, e que o ajuste é muito bom (o modelo é marcado com uma linha preta pontilhada, e a sua maior parte fica sob a linha preta sólida, o perfil original).

Os espectros obtidos são geralmente bem comportados. Um exemplo, a 5" do núcleo, pode ser visto no painel superior da Figura 7.5. O espectro de resíduo apresenta poucos artefatos. Nos painéis inferiores estão os parâmetros de intensidade (I_e e I_0) e de escala (r_e e h), para comparação.

---

[2] *Point Spread Function*, a distribuição que representa a forma que uma fonte pontual aparece na imagem.
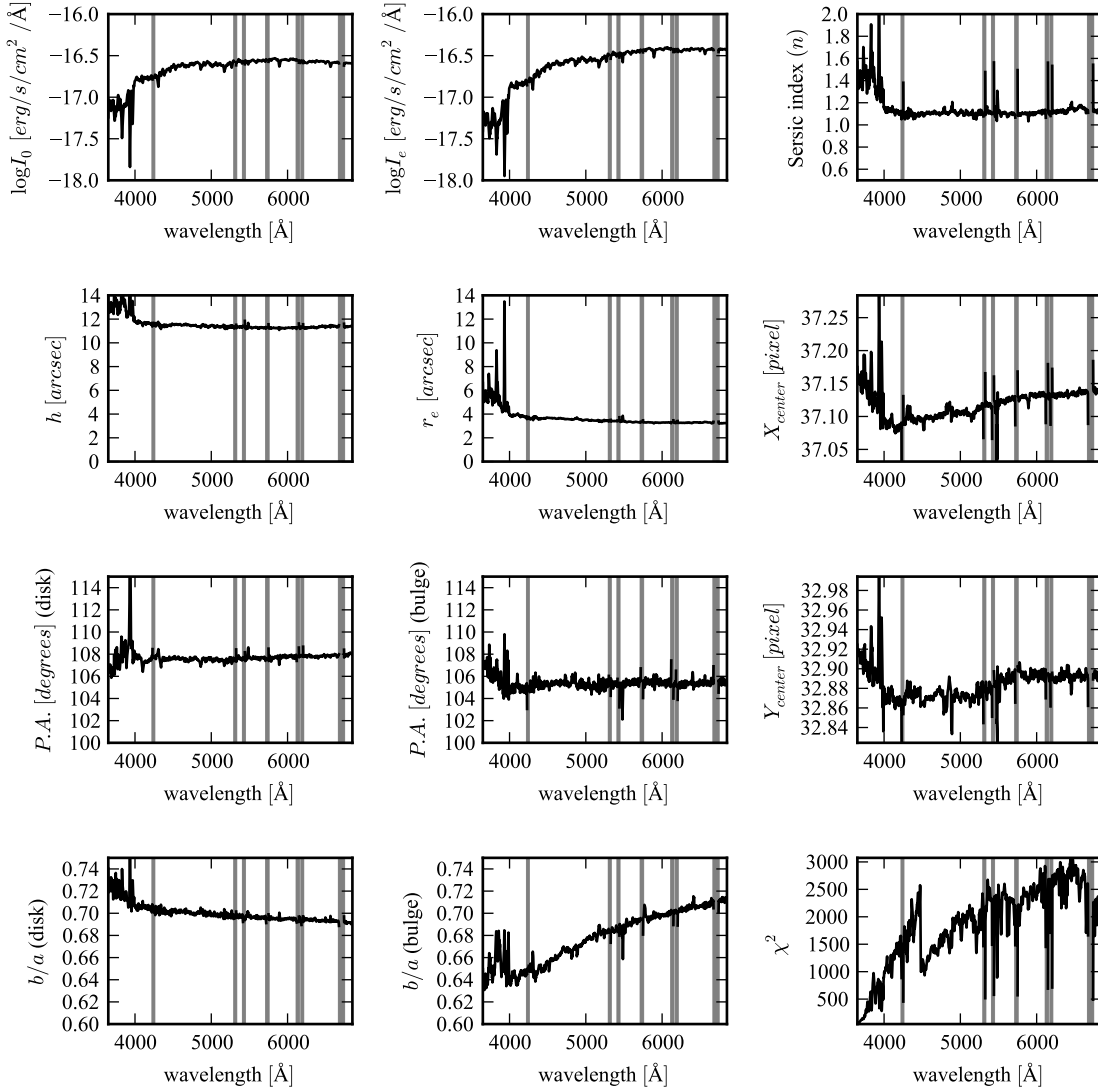
Figura 7.2: Parâmetros morfológicos obtidos no ajuste de UGC 10695. Nos painéis à esquerda estão os parâmetros para o disco. Nos painéis ao centro, e no painel superior à direita, estãos os parâmetros do bojo. Ainda na coluna da direita há os painéis da posição do centro dos modelos e o χ^2 do ajuste.
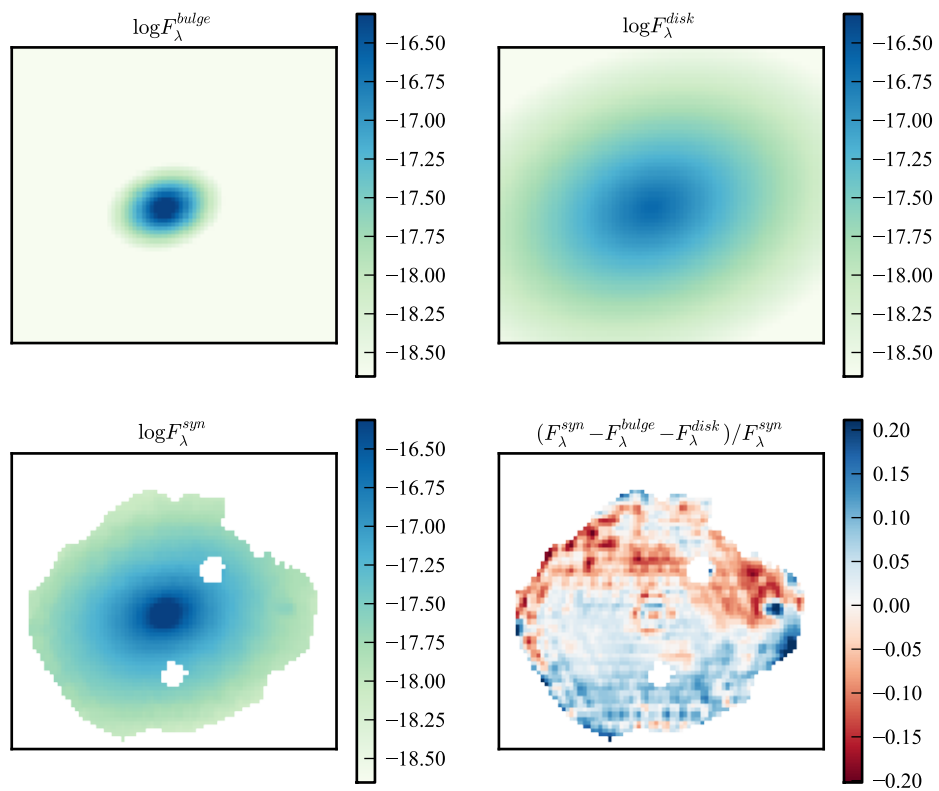
Figura 7.3: Visualização 2-D da decomposição morfológica. Nos painéis superiores os modelos de bojo e disco em 5635 Å. No painel inferior à esquerda, a imagem original. No painel inferior à direita, o resíduo do ajuste, normalizado pela imagem original.
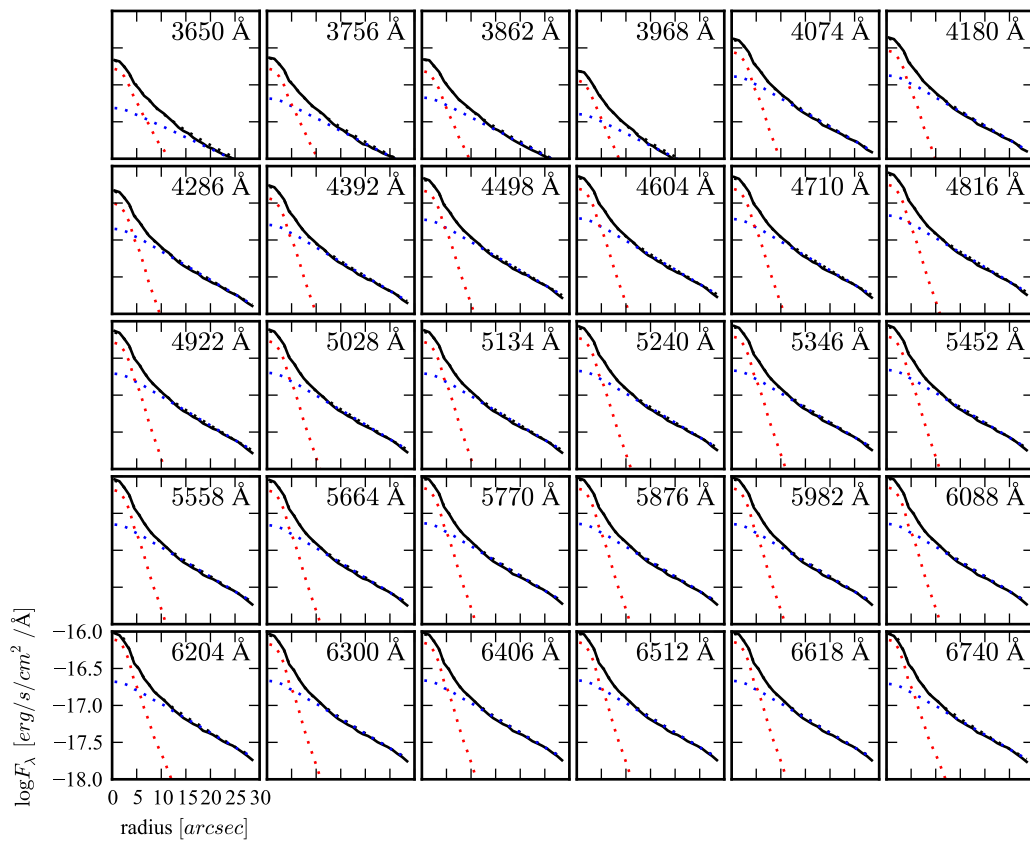
Figura 7.4: Perfis radias da decomposição em função do comprimento de onda.
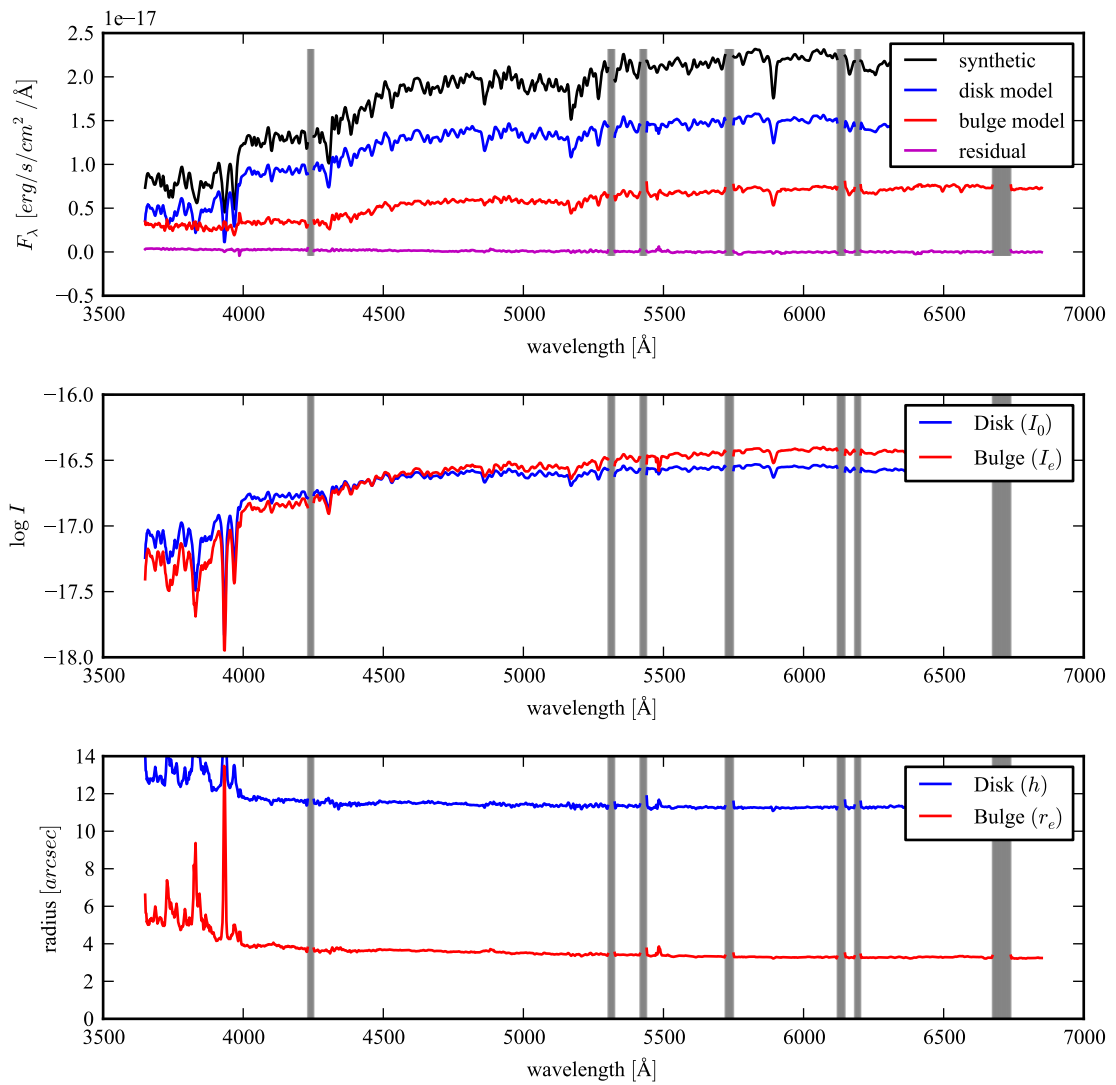
Figura 7.5: Espectro decomposto a 5" do núcleo.

Capítulo 8

Estudo das populações estelares

8.1 Section 1

[TODO]: Movido do capítulo de decomposição. Ainda tem que refazer, só está aqui pra referência.

Os cubos espectrais resultantes para bojo e disco foram passados pelo STARLIGHT como se fossem galáxias separadas, resultando em dois cubos de síntese extras para a galáxia UGC 10695. O perfil radial de algumas propriedades físicas são mostradas na Figura 8.1. O perfil de densidade superficial de massa estelar é semelhante ao perfil de luminosidade, porém com um bojo mais acentuado. Isto sugere um bojo velho (com maior razão massa/luminosidade) e massivo. Como o bojo domina em luz e massa nas regiões centrais, também é de se esperar que as propriedades pesadas por massa e luz (idade e metalicidade) da galáxia original sejam mais próximas do valor do bojo nesta região. O mesmo ocorre nas regiões externas, onde o disco domina, as propriedades da galáxia refletem os valores do disco. Ou seja, o resultado é consistente.

A interpretação do perfil radial de A_V requer um pouco mais de cuidado. Em geral se esperaria que o disco contivesse mais poeira do que o bojo. Entretanto, uma inspeção visual na Figura 7.1 mostra estruturas como anéis concêntricos, o que pode indicar que a galáxia está sofrendo ou sofreu interação (a pequena galáxia a nordeste na imagem pode ser o culpado). Neste caso é possível que a poeira não esteja distribuída como normalmente se espera, mas isto é apenas especulação.

O histórico de formação estelar é mostrado na Figura 8.2. Aqui se vê um bojo (painel
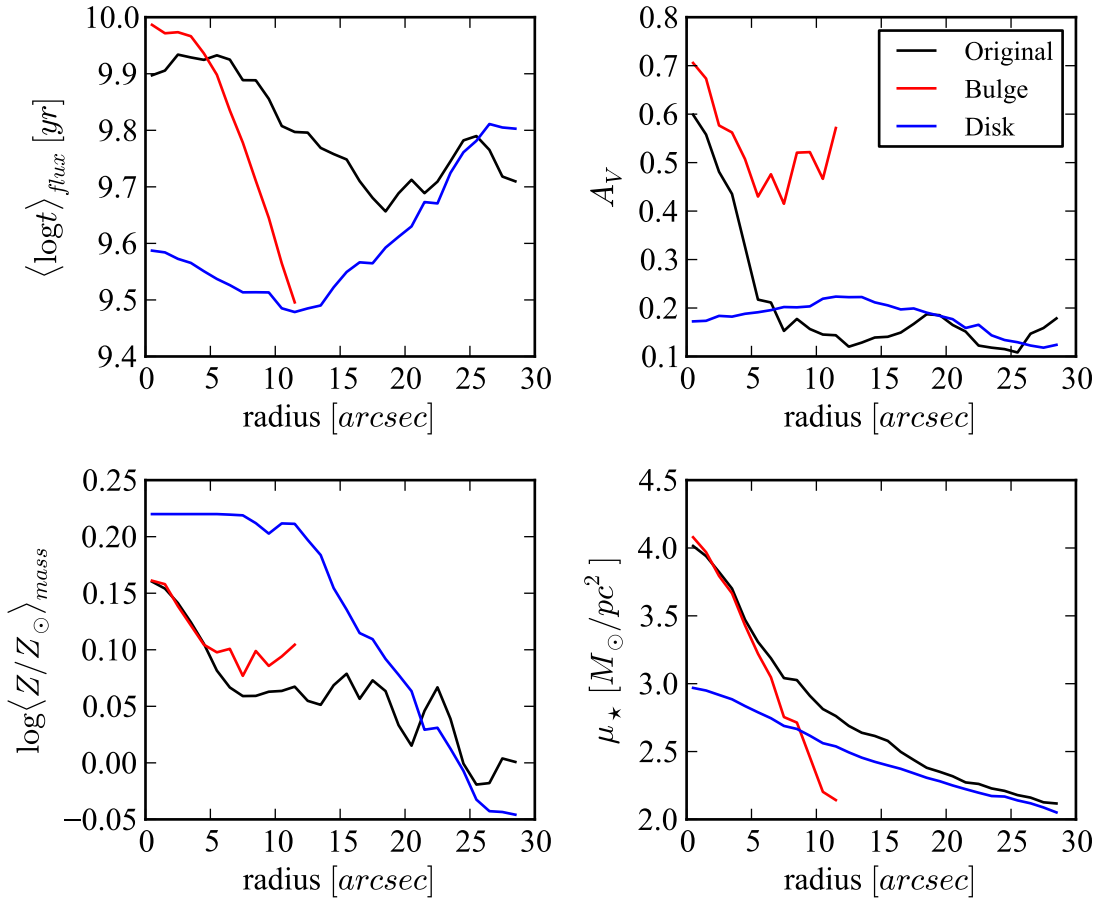
Figura 8.1: Perfil radial das propriedades físicas do bojo (vermelho), disco (azul), e original (preto). (cima, esquerda) Idade estelar média ponderada pela luminosidade. (baixo, esquerda) Metalicidade estelar média ponderada pela massa estelar. (cima, direita) Atenuação por poeira, na banda *V*. (baixo, direita) Desidade superficial de massa estelar. O Bojo vai somente até 12", que corresponde a $3\,R_{50}$.

central) sendo formado por um surto de formação estelar antigo e concentrado, com um episódio de formação estelar recente. Isto é consistente com um cenário de interação. O disco se constrói de forma mais ou menos uniforme até menos de 10^9 anos atrás, porem não apresenta formação estelar recente significativa na mesma época que o bojo.

Através da decomposição morfológica realizada neste trabalho, foram obtidos cubos de síntese espectral para o bojo e o disco de uma galáxia. As propriedades físicas destas componentes são a grosso modo compatíveis com o que se espera de um bojo e um disco. É preciso levar em conta, entretanto, que estes são resultados preliminares. Testes similares aos apresentados anteriormente, com simulações de galáxias com histórico de formação estelar mais
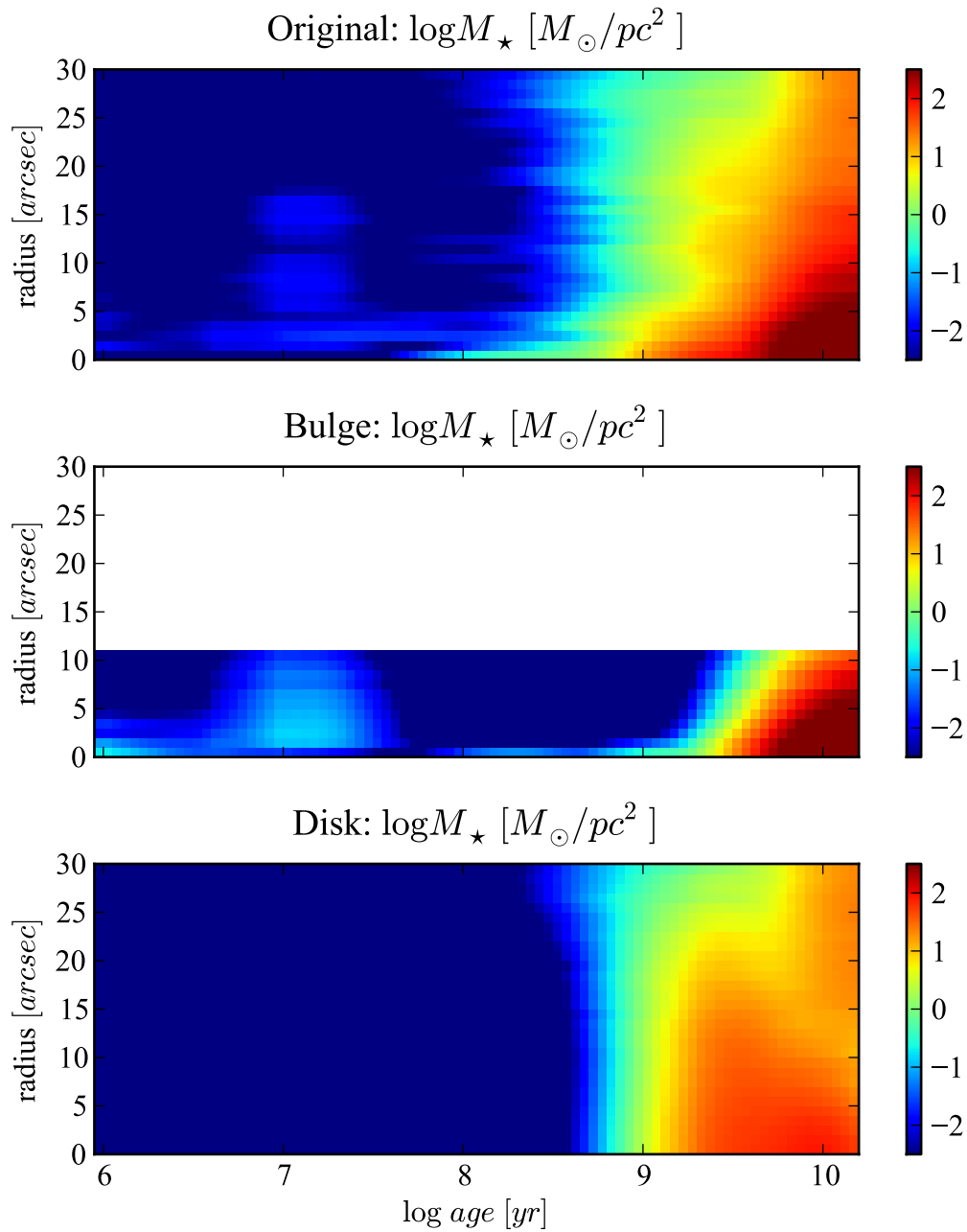
Figura 8.2: Histórico de formação estelar da galáxia original (cima), bojo (meio) e disco (baixo). Os gráficos mostram quanta massa por unidade de área foi transformada em estrelas, em cada *bin* de raio e idade. O Bojo vai somente até 12", que corresponde a $3\,R_{50}$.

realistas são fundamentais para determinar a confiabilidade do método.

Apêndice A

Manual do software PyCASSO

Versão impressa da documentação do software PyCASSO. Para uma melhor visualização e navegação entre as referências, acessar a versão completa deste manual se encontra no site:

`http://minerva.astro.ufsc.br/~andre/PyCASSO-0.9.3/`

Nota: a seção de referência foi removida por motivo de espaço.

PyCASSO Documentation
Release 0.9.3

André Luiz de Amorim

December 03, 2013

CONTENTS

INTRODUCTION

PyCASSO stands for Python CALIFA Stellar Synthesis Organizer, and its main objective is to help handling stellar synthesis datacubes produced by STARLIGHT[1] from integrated field spectra (IFS) produced by the CALIFA survey[2].

This manual serves two purposes: it is a reference for the data cubes API, and a guide to the usage pattern of PyCASSO. The examples, when possible, contain real world data and perform common tasks when dealing with IFS data.

The CALIFA data cubes were preprocessed using a tool called QBICK to obtain spectra with a minimum signal-to-noise ratio using Voronoi binning. PyCASSO and QBICK may merge in the future.

---

[1] http://astro.ufsc.br/starlight/
[2] http://califa.caha.es/

GETTING STARTED

2.1 Requirements

PyCASSO requires python 2.7. You also need these to use the data access modules.

- numpy/scipy
- pyfits
- h5py

These are probaby available at you python package manager. For example, in Mac OSX using macports, use these commands to install python 2.7 and the dependencies, and then select this as your default python installation.

```
$ sudo port install python27 py27-h5py py27-numpy py27-scipy py27-pyfits
$ sudo port select --set python python27
```

You will also need PySTARLIGHT[1]. The package is in the python package index[2], you may install it using easy_install or pip (*NOTE*: be sure that pip and easy_install are using the same python installation as you use for coding, or PySTARLIGHT will be installed at the wrong directory):

```
$ pip install PySTARLIGHT
```

or

```
$ easy_install PySTARLIGHT
```

If you want to create your own datasets, you'll also need atpy[3]. Refer to the site for installation instructions. In macports, install it using the command:

```
$ sudo port install py27-atpy
```

2.2 Stable version

The stable version of PyCASSO is 0.9.0[4]. Install using these commands:

```
$ tar xvzf PyCASSO-X.X.X.tar.gz
$ cd PyCASSO-X.X.X/
$ python setup.py install
```

---

[1]https://bitbucket.org/astro_ufsc/pystarlight
[2]https://pypi.python.org/pypi
[3]http://atpy.github.com/
[4]https://bitbucket.org/astro_ufsc/pycasso/get/PyCASSO-0.9.0.tar.gz

2.3 Development version

Development version is hosted in bitbucket. Note that the development version may be broken or have half-implemented features. If you are feeling brave, clone it from the mercurial repository:

```
$ hg clone https://bitbucket.org/astro_ufsc/pycasso
```

To install it, run the commands:

```
$ cd pycasso
$ python setup.py install
```

CREATING DATASETS

3.1 STARLIGHT data

The main objective of PyCASSO is to organize the access to the stellar synthesis data provided by STARLIGHT. If you are reading this I assume you have the following files:

- QBICK segmentation FITS file (A.K.A. zone file)

- Input spectra for STARLIGHT

- STARLIGHT output

It is important to have the name of the files following the rules:

- Input spectra must have the format: `KNNNN_MMMM_suffix` where `KNNNN` is the CALIFA number and `MMMM` is the zone ID. The suffix can be anything and will be ignored.

- There can be only one input file starting with each pair `KNNNN_MMMM` in the same directory. Use different directories for different runs. This limitation will be fixed in later releases.

- STARLIGHT output files must have the format: `KNNNN_MMMM_runID`. These files can be gzipped or bzipped, and the `.gz` or `.bz2` suffixes will be ignored.

3.2 The PyCASSO import tools

The import process is similar whether you want to use FITS or HDF5 files. Keep in mind that most of the effort will be towards the HDF5 storage, and the FITS support may be dropped in the future.

The import tools are `h5pycassoImport.py` and `pycassoImport.py` to import data to HDF5 and FITS, respectively. These scripts are located in the `tools` directory. Here is an example of a `h5pycassoImport.py` run:

```
$ h5pycassoImport.py --synthesis-dir=./sl_out/ --spectra-dir=./sl_in/ \
> --base=Bgsd01 --base-description='Granada 01' \
> --qbick-run=q027 --qbick-description='COMBO convex voronoi zones ver. 0.2.7' \
> --run-id=eBR_v20_q027.d13c512.ps3b.k1.mC.CCM.Bgsd01.v01 \
> --run-description='q027/Bgsd01 with default parameters' \
> --zone-file=K0001_eBR_v20_q035.d13c512-planes.fits \
> --database=qalifa-synthesis.h5 K0001
```

The arguments are the following:

- `--synthesis-dir`: Path to the synthesis output directory.

- `--spectra-dir`: Path to the synthesis input directory.

- `--base`: Identifier of the base used in the synthesis.

- `--base-description`: Description of the base used in the synthesis.

- `--qbick-run`: Identifier of the qbick run used in the synthesis.

- `--qbick-description`: Description of the qbick run used in the synthesis.

- `--run-id`: Identifier of the whole synthesis run.

- `--run-description`: Description of the whole synthesis run.

- `--zone-file`: Path to the FITS file containing the qbick planes.

- `--database`: Path to the HDF5 database file.

- `CALIFAID`: Califa name of the galaxy.

It is recommended to use a single database for everything.

The arguments for the FITS version are similar. For a complete list, run `h5pycassoImport.py --help` or `pycassoImport.py --help`.

For more information on the database structure, see PyCASSO data model[1].

---

[1] https://docs.google.com/document/d/1s3D8Ma-whWlZauMb9cMH7lISRrfpuzTh5Tkhbm-zbbA

USAGE

4.1 Listing synthesis runs

This section only applies to HDF5 datasets. If you are using the FITS format, you have one FITS file per galaxy per run.

Start a python shell. To list the synthesis runs present in the database *qalifa-synthesis.h5*, use the function `listRuns()` (page 49):

```
>>> from pycasso.h5datacube import
>>> listRuns('qalifa-synthesis.h5')
eBR_v20_q027.d13c512.ps3b.k1.mC.CCM.Bgsd01.v01
eBR_v20_q036.d13c512.ps03.k2.mC.CCM.Bgsd61
```

In this case, we have two runs, `'eBR_v20_q027.d13c512.ps3b.k1.mC.CCM.Bgsd01.v01'` and `'eBR_v20_q036.d13c512.ps03.k2.mC.CCM.Bgsd61'`. The other tools for listing the contents of a database are `listBases()` (page 49) and `listQbickRuns()` (page 49).

```
>>> listBases('qalifa-synthesis.h5')
Bgsd01 Bgsd61
>>> listQbickRuns('qalifa-synthesis.h5')
q027 q036
```

Now, we can search the runs that have specific bases or qbick runs using the keyword arguments `baseId` and `qbickRunId`. One can specify any one or both of these filter arguments.

```
>>> listRuns('qalifa-synthesis.h5', baseId='q036', qbickRunId='Bgsd61')
eBR_v20_q036.d13c512.ps03.k2.mC.CCM.Bgsd61
```

4.2 Loading galaxy data

To load the galaxy `'K0001'` (IC5376), in the run `'eBR_v20_q036.d13c512.ps03.k2.mC.CCM.Bgsd61'` from the database, do

```
>>> from pycasso.h5datacube import
>>> K = h5Q3DataCube('qalifa-synthesis.h5', \
'eBR_v20_q036.d13c512.ps03.k2.mC.CCM.Bgsd61', 'K0001')
```

The object `K` is a `h5Q3DataCube` (page 49). which implements `IQ3DataCube` (page 59). The latter defines high level algorithms like zone to spatial conversions and radial profiles, while the former contains the I/O related stuff. If you are using ipython, entering `K` followed by two tab keystrokes, you should see all the properties of the galaxy and all methods available to operate on those.

If you have FITS files with your data, please refer to *Loading from FITS files* (page 25).

4.2.1 Zone smoothing

The data from the galaxies are are binned in spatial regions called voronoi bins. There is a procedure called "dezonification" which converts the data from voronoi bins back to spatial coordinates. When doing so, one can use the surface brightness of the image of the galaxy as a hint to smooth some of the properties.

This is enabled by default. To disable it, set the keyword argument `smooth` to `False` when loading the galaxy.

```
>>> K = h5Q3DataCube('qalifa-synthesis.h5', \
'eBR_v20_q036.d13c512.ps03.k2.mC.CCM.Bgsd61', 'K0001', smooth=False)
```

For more information, see `getDezonificationWeight()` (page 59).

4.3 Displaying property images

In this section we explain how to obtain images of properties of the galaxy. Most of of the properties of interest are already calculated, see the section *Galaxy property list* (page 31).

Here we assume the galaxy is loaded as `K`. Now, all the data is stored as voronoi zones, but we really want to see the spatial distribution of the galaxy properties. `K` has a method for converting data from voronoi zones to images, the method `zoneToYX()` (page 59).

Let's see the property `popx` (page 54). It is a 3-dimensional array, containing the light fraction for every triplet (*age*, *metallicity*, *zone*).

```
>>> K.popx.shape (39, 4, 649) >>> K.N_age, K.N_met, K.N_zone (39, 4, 649)
```

Now, we want to see how this is distributed in the galaxy. The fraction of light in each population is the same in every pixel of a zone. So, we call `popx` an **intensive** property. To inform `zoneToYX()` (page 59) that the property is intensive, we set `extensive=False`.

```
>>> popx = K.zoneToYX(K.popx, extensive=False) >>> popx.shape (39, 4, 72, 77)
```

In this case, the resulting `popx` is 4-dimensional, where the zone dimension has been replaced by the (x,y) plane. Let's plot the young population (summing only the fractions for ages smaller than 1Gyr) as a function of the position in the galaxy plane.

```
>>> import matplotlib.pyplot as plt
>>> popY = popx[K.ageBase < 1e9].sum(axis=1).sum(axis=0)
>>> plt.imshow(popY, origin='lower', interpolation='nearest')
>>> cb = plt.colorbar()
>>> cb.set_label('[%]')
>>> plt.title('light fraction < 1 Gyr')
```
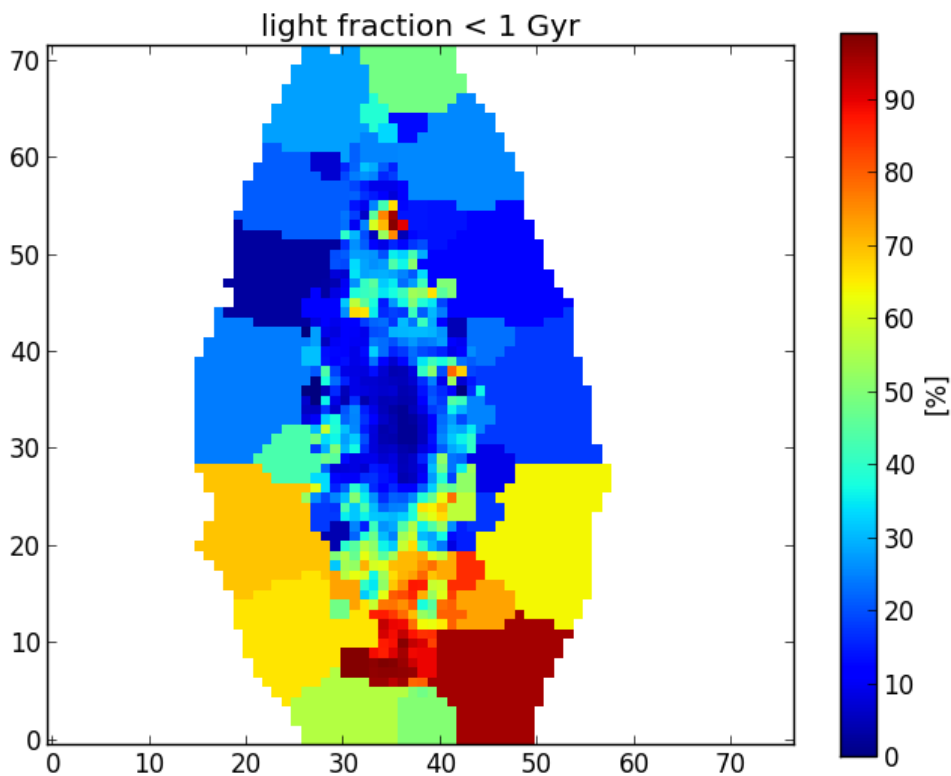
4.3.1 Masked pixels

The white pixels do not belong to any zone (*masked pixels*), and by default are set to `numpy.nan`. One might change the fill value for the masked pixels using the keyword `fill_value`. For example, to fill with zeros,

```
>>> popx_fill_zeros = K.zoneToYX(K.popx, extensive=False, fill_value=0.0)
```

It is recommended to use the fill values as `nan`, this way you know when you make a mistake and use values from regions where there's no data (`nan` is contagious, any operation containing a `nan` will yield `nan`).

4.3.2 Surface densities

When the property is extensive, such as mass or flux, it is more proper to work with surface densities of these properties, when working with images. The most easily acknowledged extensive properties are light and mass. The properties Lobn__z (page 73), Mini__z (page 74) and Mcor__z (page 74) are the total light and mass for the voronoi zones. When we convert these to images, setting `extensive=True`, the resulting image contains the surface density of these properties (for example, in units of $M_\odot/pc^2$).

```
>>> McorSD = K.zoneToYX(K.Mcor__z, extensive=True)
>>> plt.imshow(McorSD, origin='lower', interpolation='nearest')
>>> cb = plt.colorbar()
>>> cb.set_label('$[M_\odot / pc^2]$')
>>> plt.title('McorSD')
```
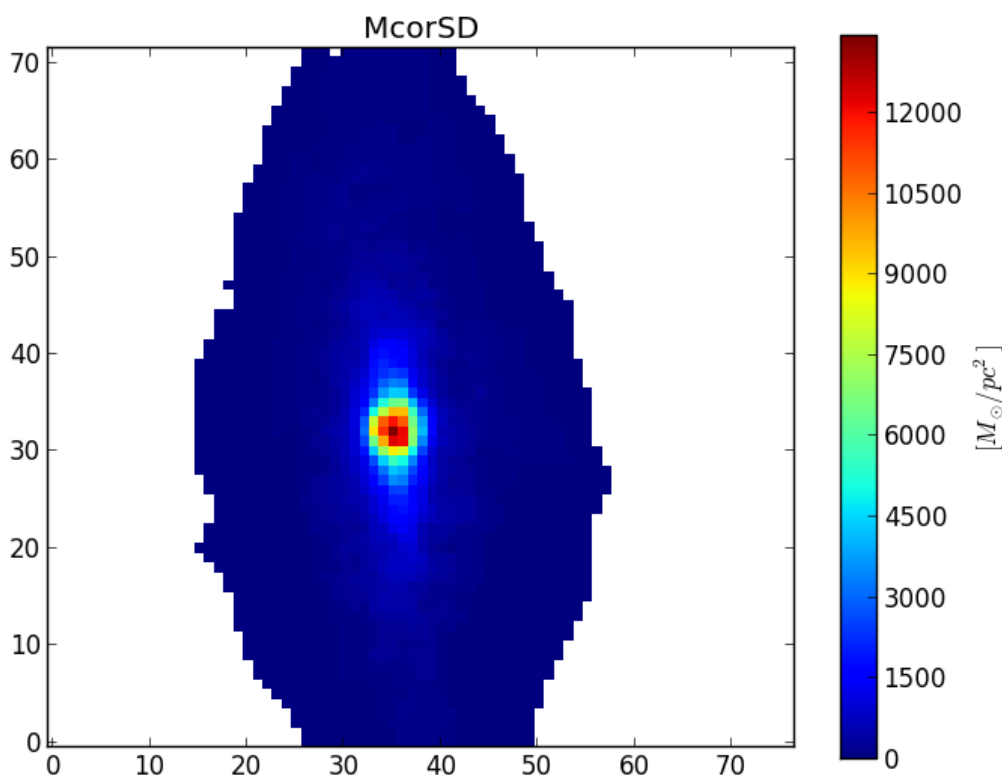
This is the same property as `McorSD__yx` (page 74), see the section below.

4.3.3 Predefined properties

The conversion from zones to images is perhaps the most common thing you wil ever use from PyCASSO. To make things easier (and less verbose), most of the properties already have been converted to images. These predefined properties take care of the extensiveness or intensiveness nature of the physical property, and return a surface density when suitable. The full list of propeties can be seen in the section *Galaxy property list* (page 31).

4.4 Radial and azimuthal profiles

Galaxy images are nice and all, but in the end you want to compare spatial information between galaxies, and it can not be done in a per pixel basis. One can think in polar coordinates and analyze only the radial variations of the properties. For this we have to think about what galaxy distances in these images really mean.

4.4.1 Image geometry

One fair approximation is to assume the galaxy has an axis-symmetric geometry. Therefore, if we see the galaxy as an elliptic shape, that is because of its inclination with respect to the line of sight. If we get all the points at a given distance `a` from the center of the galaxy, this will appear as an ellipse of semimajor axis equal to `a`.

To know the distace of each pixel to the center of the galaxy, we need to know the *ellipticity* (`ba` (page 51)) of the galaxy, defined as $\frac{b}{a}$ (ratio between semiminor and semimajor axes), and the *position angle* (`pa` (page 51), in radians, counter-clockwise from the X-axis) of the ellipse. These can be set using the method `setGeometry()` (page 60). The distance of each pixel is obtained using the property `pixelDistance__yx` (page 51).

```
>>> K.setGeometry(pa=45*np.pi/180.0, ba=0.75)
>>> dist = K.pixelDistance__yx
>>> plt.imshow(dist, origin='lower', interpolation='nearest')
>>> cb = plt.colorbar()
>>> cb.set_label('pixels')
>>> plt.title('Pixel distance')
```
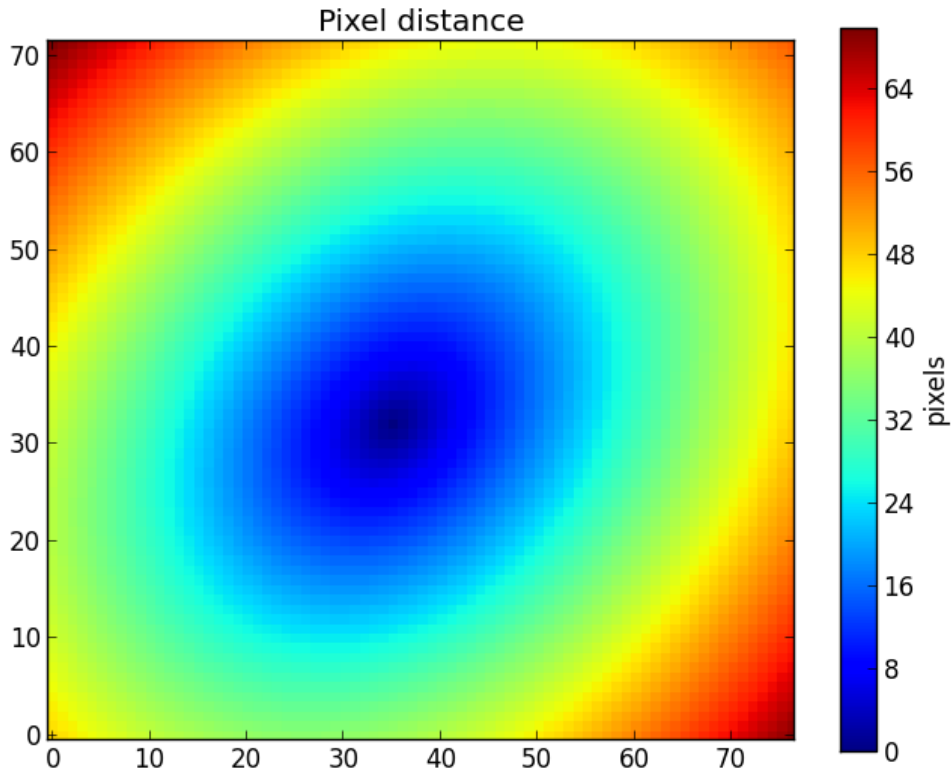

This example geometry clearly does not correspond to geometry of the galaxy, as seen in the previous figures. If we lack the values of `ba` and `pa` from other sources, we can use the method `getEllipseParams()` (page 68) to estimate these ellipse parameters using "Stokes' moments" of the flux (actually, we use `qSignal` (page 52)) as explained in the paper Sloan Digital Sky Survey: Early Data Release[1].

```
>>> pa, ba = K.getEllipseParams()
>>> K.setGeometry(pa, ba)
```

_____

[1]http://adsabs.harvard.edu/abs/2002AJ....123..485S
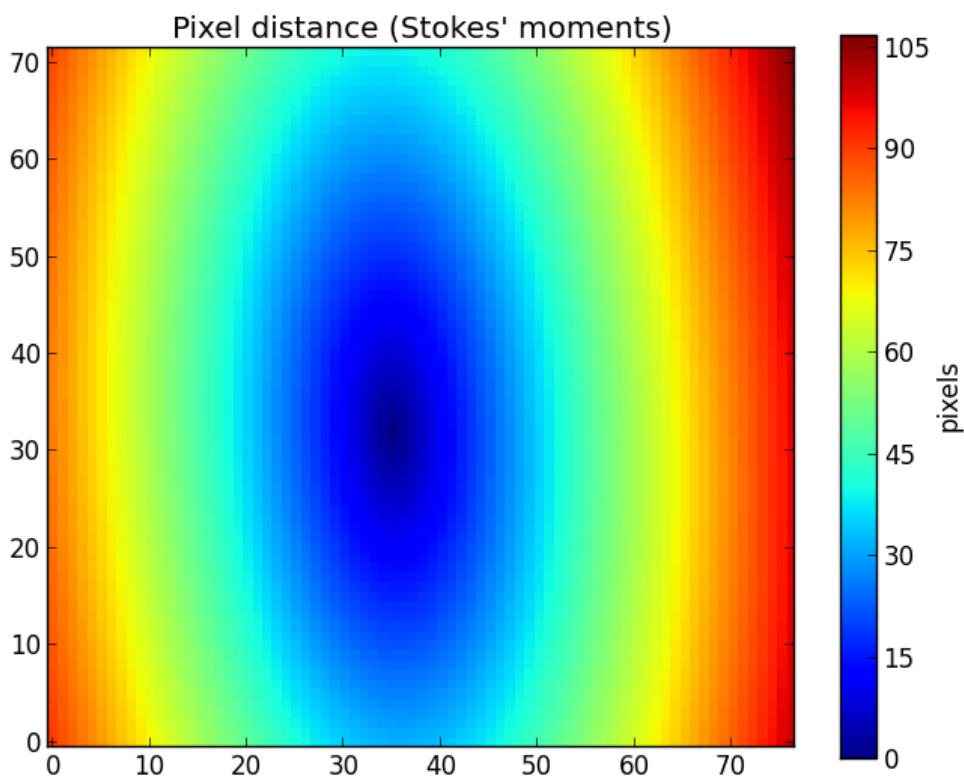
Now the distances match the geometry of the galaxy assuming it has an elliptical desitribution. Other parameters thar may be set by setGeometry() (page 60) are the *Half Light Radius* (see below) and the center of the galaxy, by using respectively the keyword parameters HLR_pix and center (a tuple containing x and y).

4.4.2 Galaxy scales

We also need to take into account that galaxies exist in all sizes and distances. This means that using pixels as a distance scale is not satisfactory. Thus we have to convert distances to a "natural scale" to compare the radial profiles of distinct galaxies.

We define the *Half Light Radius* (HLR_pix (page 50)) as the semimajor axis of the ellipse centered at the galaxy center containing half of the flux in a certain band. In PyCASSO, we use qSignal (page 52), which is the flux in the normalization window (5635).

The HLR is updated whenever setGeometry() (page 60) is called. One can explicitly set the HLR using the HLR_pix parameter, or let it be determined automatically. Note that the HLR depends heavily on the ellipse parameters.

- Circular

```
>>> K.setGeometry(pa=0.0, ba=1.0)
>>> K.HLR_pix
9.334798311419563
```

- Ellipse

```
>>> pa, ba = K.getEllipseParams()
>>> K.setGeometry(pa, ba)
>>> K.HLR_pix
12.878480006876336
```

```
>>> K.HLR_pc
2545.9657503507078
```

In the last line we show the HLR in parsecs (`HLR_pc` (page 50)), which may be handy sometimes. It is based on `HLR_pix` (page 50) and `parsecPerPixel` (page 50).

Alternatively, one can think in terms of other property as a half-scale. This is achieved using the method `getHalfRadius()` (page 69). One alternate scale commonly used is the mass. To calculate the Half Mass Radius (HMR) use the following:

```
>>> K.getHalfRadius(K.McorSD__yx)
7.612629351561292
```

The input for this method must be a 2-D image.

Note: This uses the same computation as the HLR.

4.4.3 Calculating the radial profile of a 2-D image

Now that we have a scale to measure things in radial distance, it is useful to have a radial profile of things. First, let's assume we have a 2-D image we want to get the radial profile, for instance, `at_flux__yx` (page 75). The method `radialProfile()` (page 63) receives a 2-D image of a given property, a set of radial bins, an optional radial scale (it uses HLR by default) and returns the average values of the pixels inside each bin. Think of it as a fancy histogram.

```
>>> HMR = K.getHalfRadius(K.McorSD__yx)
>>> bin_r = np.arange(0, 3+0.1, 0.1)
>>> bin_center = (bin_r[1:] + bin_r[:-1]) / 2.0
>>> at_flux__HLR = K.radialProfile(K.at_flux__yx, bin_r)
>>> at_flux__HMR = K.radialProfile(K.at_flux__yx, bin_r, rad_scale=HMR)
>>> plt.plot(bin_center, at_flux__HLR, '-k', label='HLR')
>>> plt.plot(bin_center, at_flux__HMR, '--k', label='HMR')
>>> plt.ylabel(r'$\langle \log t\rangle$')
>>> plt.xlabel(r'$R_{50}$')
>>> plt.title('Radial profile of the mean stellar age')
>>> plt.legend()
```
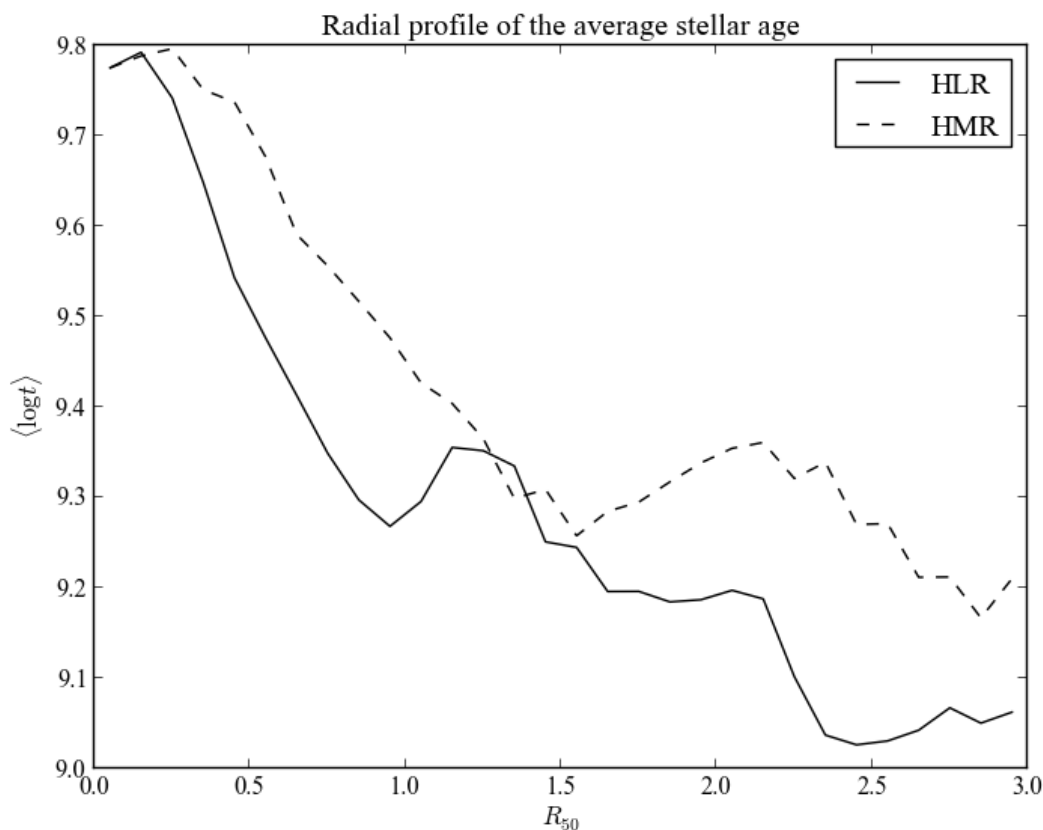
Now let's explain the procedure. `bin_r` represent the bin boundaries in which we want to calculate the mean value of the property. It is not suitable for plotting, as it contains one extra value (`len(bin_r) == len(at_flux__HLR) + 1`). So, we calculate the central points of the bins, `bin_center`. Then, we proceed to calculate the radial profile of `at_flux__yx`, which is the average log. of the age, weighted by flux. We do so using HLR and HMR as a distance scale. The mass is usually more concentrated in the center of the galaxy, so that in general `HMR < K.HLR_pix` and therefore the plots look similar, but stretched.

4.4.4 Calculating the radial profile of a N-D image

In the example above we compute the radial profile of a 2-D image. Now, the process is the same for higher-dimensional images. The presentation can be tricky, though. Let's see an example.

We have the surface distribution of mass in ages, `McorSD__tyx`, which is a 3-D array (age, y, x). One may be tempted to do a `for` loop for each age, but the method `radialProfile()` takes care of this, as it accepts properties with more than 2 dimensions, as long as the spatial dimensions are the rightmost (`[..., y, x]` in numpy slice notation). In this example, we want to plot a 2-D map of the mass as a function of radius and age. We will use the Half Light Radius as a radial scale, so we don't have to set the argument `rad_scale` as we did previously. We also don't need the bin centers, as the plot method used is fit for dealing with histogram-like data.

```
>>> bin_r = np.arange(0, 2.5+0.1, 0.1)
>>> McorSD__tyx = K.McorSD__tZyx.sum(axis=1)
>>> logMcorSD__tr = np.log10(K.radialProfile(McorSD__tyx, bin_r, mode='mean'))
>>> vmin = -2
>>> vmax = 4
>>> plt.pcolormesh(bin_r, K.logAgeBaseBins, logMcorSD__tr, vmin=-2, vmax=4)
>>> plt.colorbar()
>>> plt.ylim(K.logAgeBaseBins.min(), K.logAgeBaseBins.max())
>>> plt.ylabel(r'$\log t$')
>>> plt.xlabel(r'$R_{50}$')
>>> plt.title(r'$\log M_{cor} [M_\odot / pc^2]$')
```
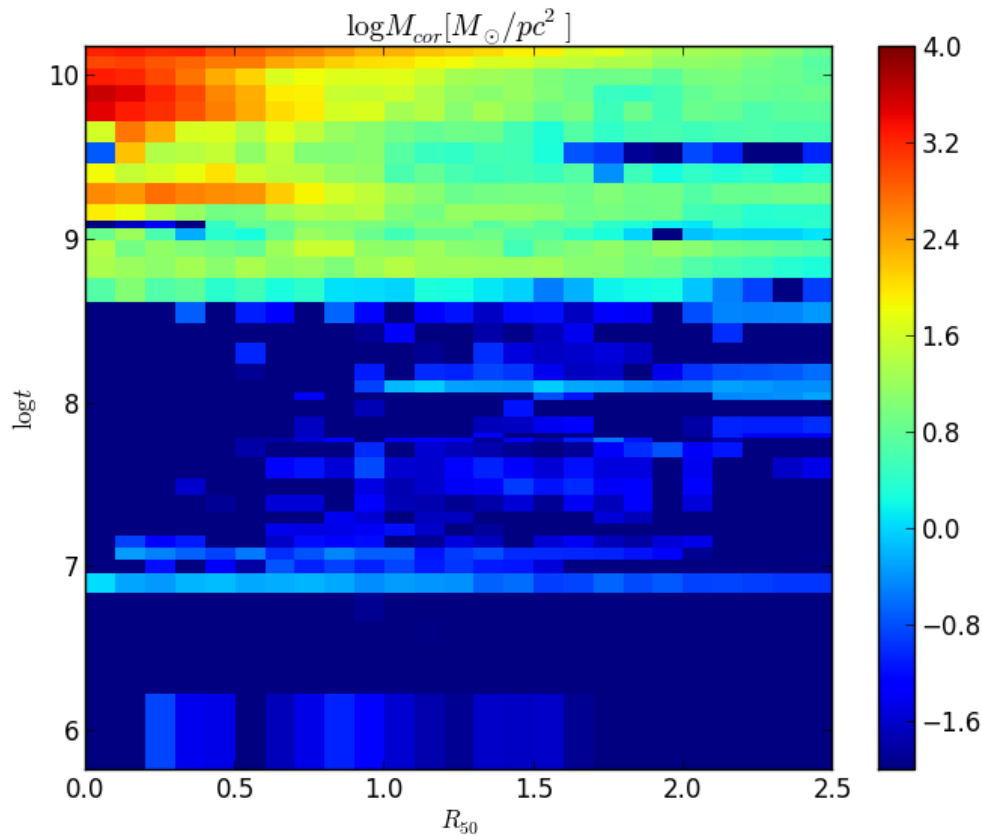
As we said, the :meth:pseudocolor method needs the bin edges, so we have to use the radial bin edges (provided by `bin_r`), and the age bin edges. The property called `logAgeBaseBins` returns the age bin edges in log space, see it's documentation for more details.

One can also compute the sum of the values (or the mean or median) inside a ring, using a pair of values as bins:

```
>>> Mcor_tot_ring = K.radialProfile(K.McorSD__yx, \
(0.5, 1.0), mode='sum') * K.parsecPerPixel**2
```

The rightmost term is the pixel area, to convert from surface density to absolute mass. The `mode` keyword indicates what to do inside the bins. By default, the mean is computed. The valid values for `mode` are:

- `'mean'`
- `'mean_exact'` (see below)
- `'sum'`
- `'median'`

If the number of pixels inside each radial bin is needed, the keyword argument `return_npts` may be set. In this case, the return value changes to a tuple containing the radial binnned property and the number of points in each bin.

```
>>> bin_r = np.arange(0, 2.5+0.1, 0.1)
>>> bin_center = (bin_r[1:] + bin_r[:-1]) / 2.0
>>> McorSD__r, npts = K.radialProfile(K.McorSD__yx, bin_r, return_npts=True)
>>> fig = plt.figure()
>>> plt.title('$M_{cor}$ and number of points')
>>> ax1 = fig.add_subplot(111)
>>> ax1.plot(bin_center, McorSD__r, '-k')
>>> ax1.set_xlabel(r'$R_{50}$')
>>> ax1.set_ylabel(r'$M_{cor} [M_\odot / pc^2]$ (solid)')
>>> ax2 = ax1.twinx()
```

```
>>> ax2.plot(bin_center, npts, '--k')
>>> ax2.set_ylabel(r'$N_{pts}$ (dashed)')
```
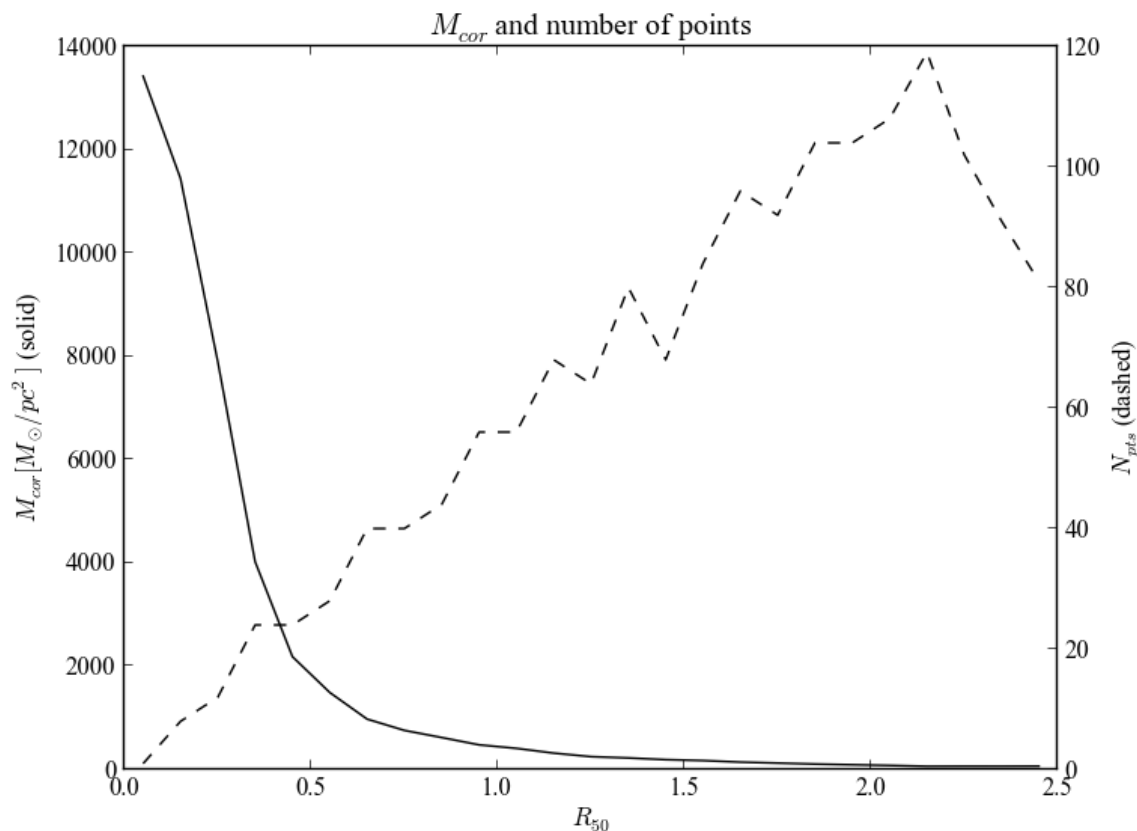

4.4.5 Radial profiles using exact apertures

All the radial profiles calculated above suffer from a "jagginess" caused by the discrete method of assigning pixels to the radial bins (see the dashed line from the image above). When pixels fall in the boundaries of the bins, the whole pixel gets assigned to one or the other bin, based onthe pixel center. Often this is harmless, but for small radii (or conversely, large pixels) this effect can be a problem. The solution in this case is to "split" the pixel between the bins, calculating the intersection of the bin boundaries and each pixel. Needless to say, this can be very slow. To use the exact apertures algorithm (shamelessly "stolen" from photutils[2]), change the `mode` parameter to `'mean_exact'`.

Here we can see a comparison between the exact and the discrete versions of the radial profile of the luminosity weighted mean stellar age.

```
>>> bin_r = np.arange(0, 2.5+0.1, 0.1)
>>> bin_center = (bin_r[1:] + bin_r[:-1]) / 2.0
>>> atflux, npts = K.radialProfile(K.at_flux__yx, bin_r, \
mode='mean', return_npts=True)
>>> atflux_ex, npts_ex = K.radialProfile(K.at_flux__yx, bin_r, \
mode='mean_exact', return_npts=True)
>>> fig = plt.figure()
>>> plt.title(r'$\langle \log t \rangle_L$ and number of points: discrete vs. exact')
>>> ax1 = fig.add_subplot(111)
>>> ax1.plot(bin_center, atflux, '-k', label='discrete')
>>> ax1.plot(bin_center, atflux_ex, '-r', label='exact')
>>> ax1.set_xlabel(r'$R_{50}$')
```

---

[2]https://github.com/astropy/photutils

```
>>> ax1.set_ylabel(r'$\langle \log t \rangle_L [yr]$ (solid)')
>>> plt.legend(loc='lower right')
>>> ax2.plot(bin_center, npts_ex, '--r')
>>> ax2 = ax1.twinx()
>>> ax2.plot(bin_center, npts, '--k')
>>> ax2.set_ylabel(r'$N_{pts}$ (dashed)')
```
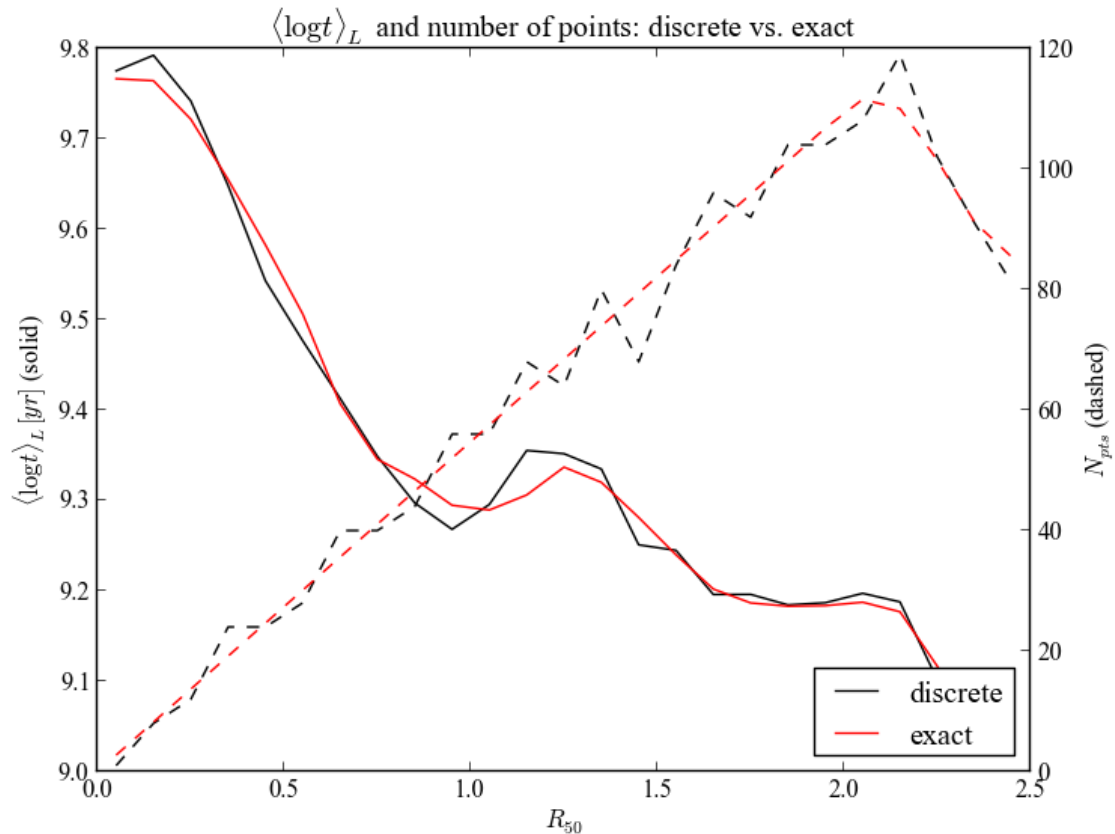

The bin area (dashed lines, right vertical axis) is much smoother when using the 'mean_exact' algorithm (in red), compared to the discrete 'mean' version (in black). As you can see, the age radial profile (solid lines, left vertical axis) becomes less noisy.

4.4.6 Azimuthal and radial profile of a N-D image

Still more generic than radialProfile() (page 63) is azimuthalProfileNd() (page 66). It adds the capability of azimuthal profiles, based on the angles associated with each pixel. This angle is accessible using pixelAngle__yx (page 51), in radians. The method getPixelAngle() (page 69) allows one to get the angle in degrees, or to get an arbitrary ellipse geometry, much like getPixelDistance() (page 68).
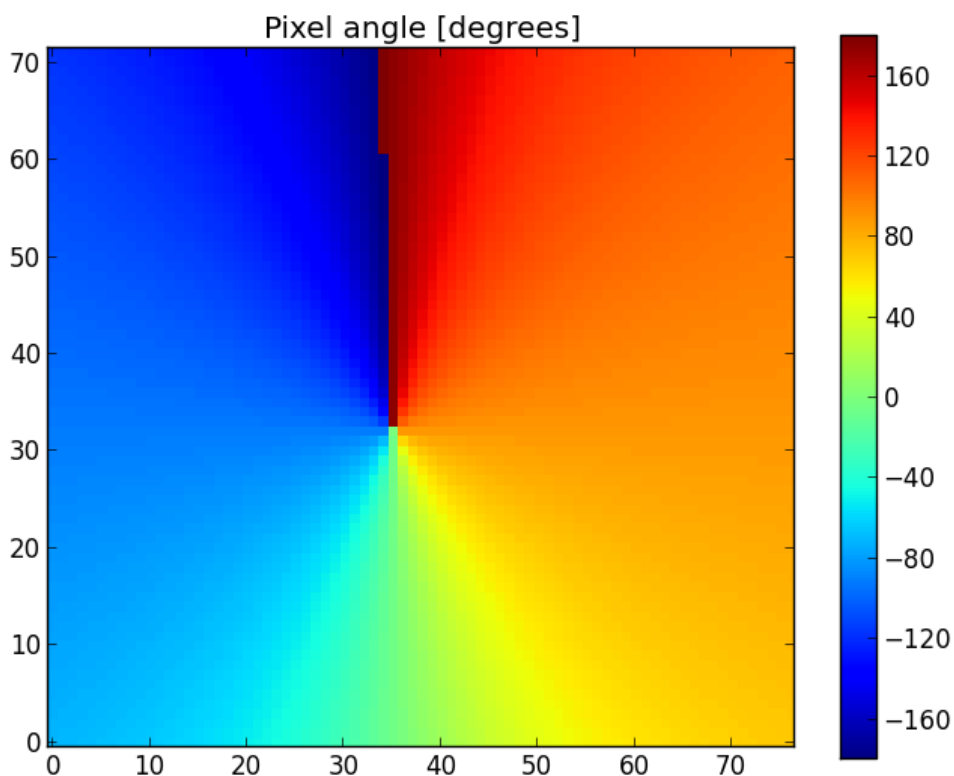
In PyCASSO the pixel angle is defined as the counter-clockwise angle between the pixel and the semimajor axis, taking the ellipse distortion into account. Please look at `getPixelAngle()` (page 69) for more details.

In the example below, we calculate the azimuthal profile of the log. age, averaged in flux, inside three rings between 0.5, 1.0, 1.5 and 2.0 HLR.

```
>>> bin_a = np.linspace(-np.pi, np.pi, 21)
>>> bin_a_center_deg = (bin_a[1:] + bin_a[:-1]) / 2.0 * 180 / np.pi
>>> bin_r = np.array((0.5, 1.0, 1.5, 2.0))
>>> at_flux__ar = K.azimuthalProfileNd(K.at_flux__yx, bin_a, bin_r)
>>> plt.plot(bin_a_center_deg, at_flux__ar[:,0], '-r', label='0.5 > r(HLR) > 1.0')
>>> plt.plot(bin_a_center_deg, at_flux__ar[:,1], '-g', label='1.0 > r(HLR) > 1.5')
>>> plt.plot(bin_a_center_deg, at_flux__ar[:,2], '-b', label='1.5 > r(HLR) > 2.0')
>>> plt.title('Azimuthal profile of mean stellar age')
>>> plt.ylabel(r'$\langle \log t \rangle_L$')
>>> plt.xlabel(r'$\theta\ [degrees]$')
>>> plt.legend()
```
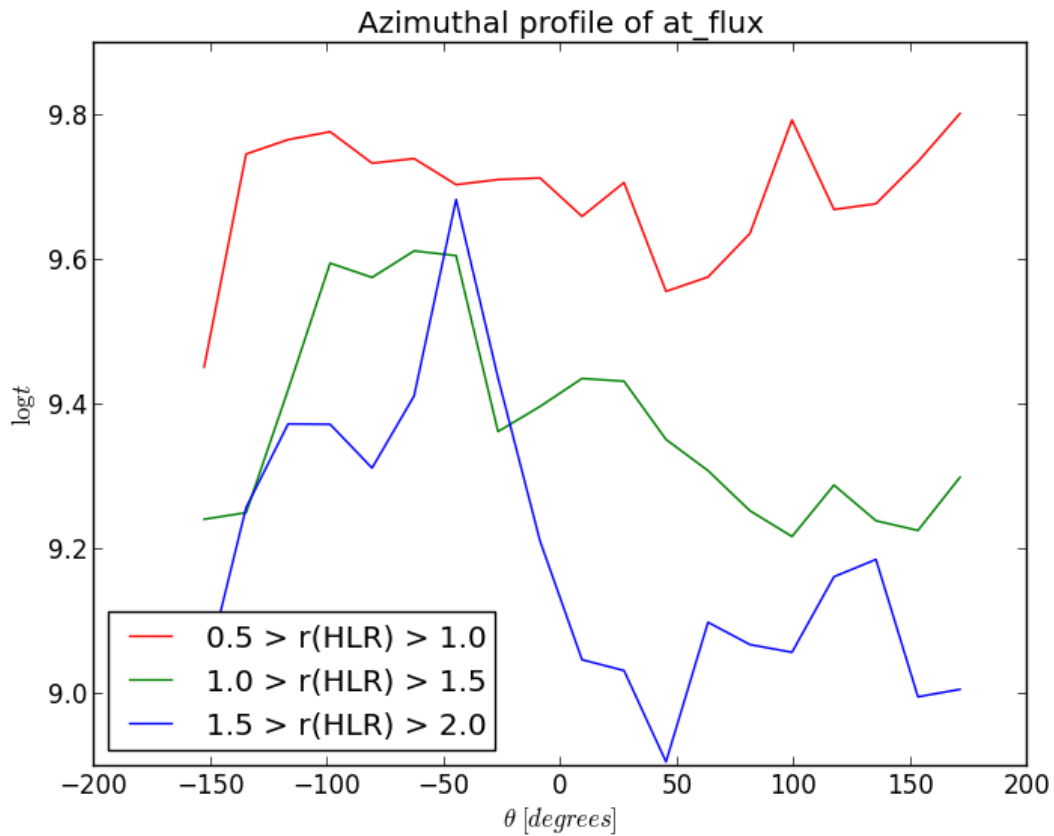
4.5 Filling missing data

The example galaxy used above does not have any masked foreground or background objects. This is not always the case. For example, galaxy K0277 (NGC2916) has a foreground star near it's center, which was masked in the analysis pipeline.
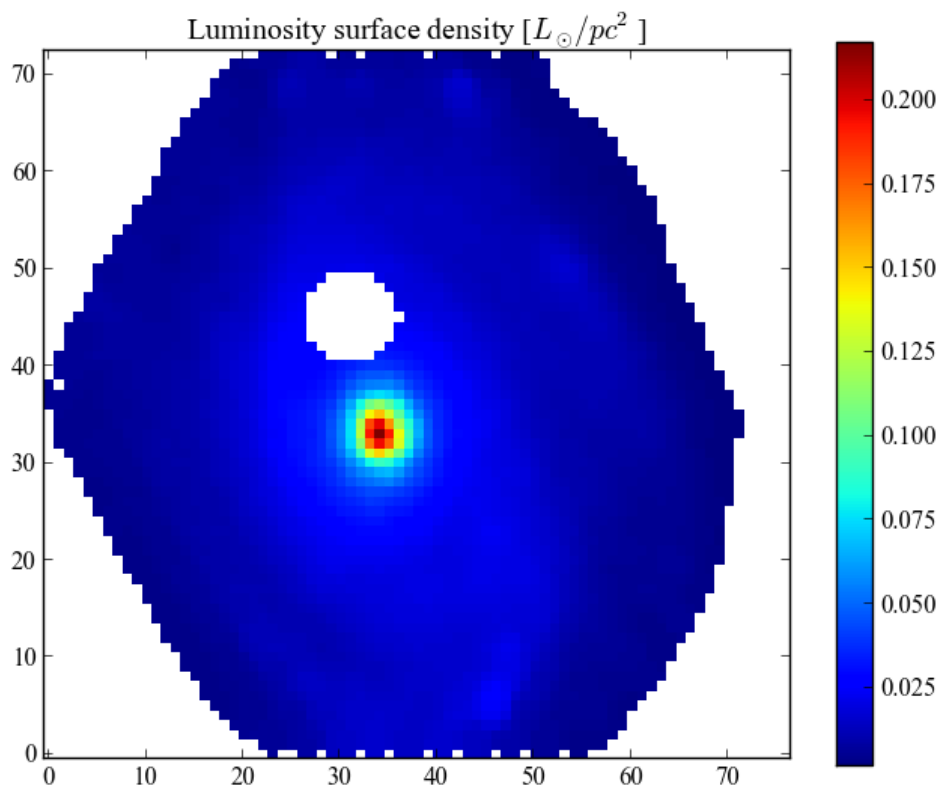
This impacts some measurements like the total mass of the galaxy or the cumulative radial curves. The latter can have a big effect in properties like the half light radius. To take the hollow areas into account, we can use the method `fillImage()` (page 67). By default, it takes a property as input, calculates its radial profile and interpolates the missing data from the radial profile. This assumes the user already called `setGeometry()` (page 60) with proper values. Alternatively, one can calculate a radial profile and use it as parameter when filling, see the documentation. Also, there's two modes of filling: `'hollow'` and `'convex'`. The first one only fills the hollow pixels, while the second fills the complete convex hull of the image (that is, fills the edges making the image "roundy"). Here's the same image as above, filling the convex hull.
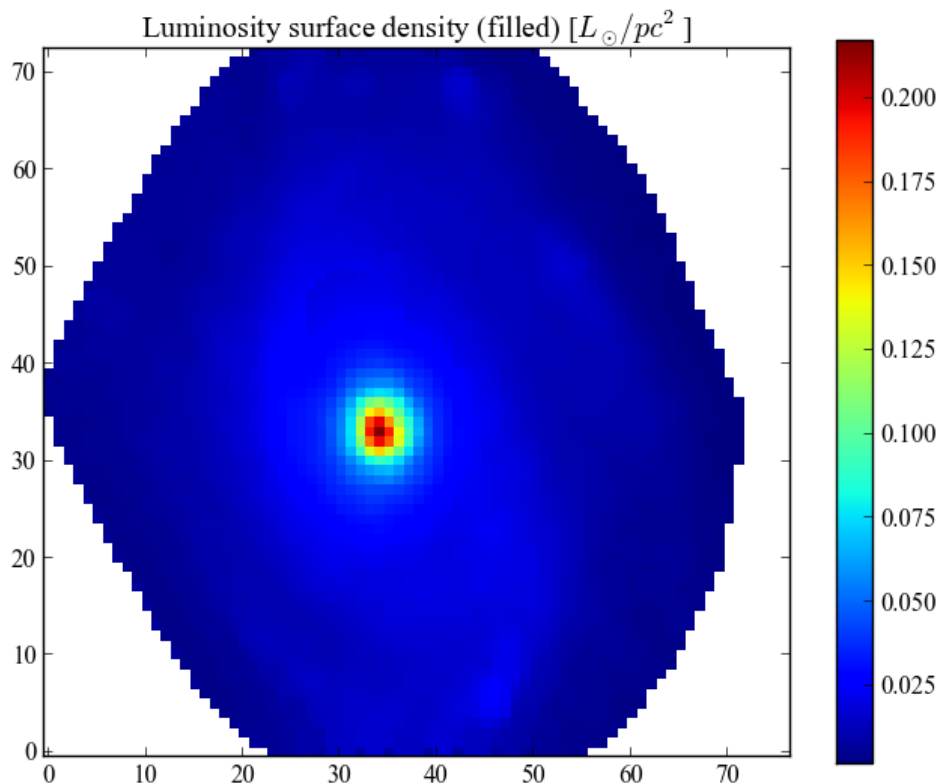
Note the barely visible artifact in the filled areas. As an example, let's compare the values of the half light radius with and without filling. We will calculate the filling by hand to illustrate the usage. The methods getHalfRadius() (page 69) and getHLR_pix() (page 70) have a `fill` parameter, which when set to True, will perform the filling automatically.

```
>>> pa, ba = K.getEllipseParams()
>>> K.setGeometry(pa, ba)
>>> LobnSD_fill, mask = K.fillImage(K.LobnSD__yx, mode='hollow')
>>> K.getHalfRadius(LobnSD_fill, mask=mask)
19.43191121094409
>>> K.getHalfRadius(K.LobnSD__yx)
19.991108029801655
```

If one does not fill the hollow areas, the computed half light radius will be overestimated (in this case, by about 0.5 pixel, but it can be worse). The same applies to the total mass or luminosity of the galaxy.

4.6 Working with spectra

PyCASSO handles the stellar synthesis results from IFS data. One of the products of the stellar synthesis is a synthetic spetrum of each pixel (f_syn__lyx (page 77)), containing only the stellar contribution to the light. The observed spectra (f_obs__lyx (page 76)), errors (f_err__lyx (page 77)) and flags (f_flag__lyx (page 76)) are also available. Using these, one can easily, for example, obtain the residual spectra and measure emission lines.

```
>>> f_syn_nuc = K.f_syn__lyx[:, K.y0, K.x0]
>>> f_obs_nuc = K.f_obs__lyx[:, K.y0, K.x0]
>>> f_flag_nuc = K.f_flag__lyx[:, K.y0, K.x0]
>>> mask = f_flag_nuc < 1.0
>>> ax1 = plt.subplot(211)
```

```
>>> ax1.plot(K.l_obs[mask], f_obs_nuc[mask], '-k', label='Obs.')
>>> ax1.plot(K.l_obs[mask], f_syn_nuc[mask], '-r', label='Syn.')
>>> ax1.set_xlabel(r'wavelength $[\AA]$')
>>> ax1.set_ylabel(r'Flux $[erg / s / cm^2 / \AA]$')
>>> ax1.set_title('Spectra')
>>> ax1.legend()
>>> ax2 = plt.subplot(212)
>>> ax2.plot(K.l_obs[mask], f_obs_nuc[mask] - f_syn_nuc[mask], '-k')
>>> ax2.set_xlabel(r'wavelength $[\AA]$')
>>> ax2.set_ylabel(r'Flux $[erg / s / cm^2 / \AA]$')
>>> ax2.set_title('Residual')
```
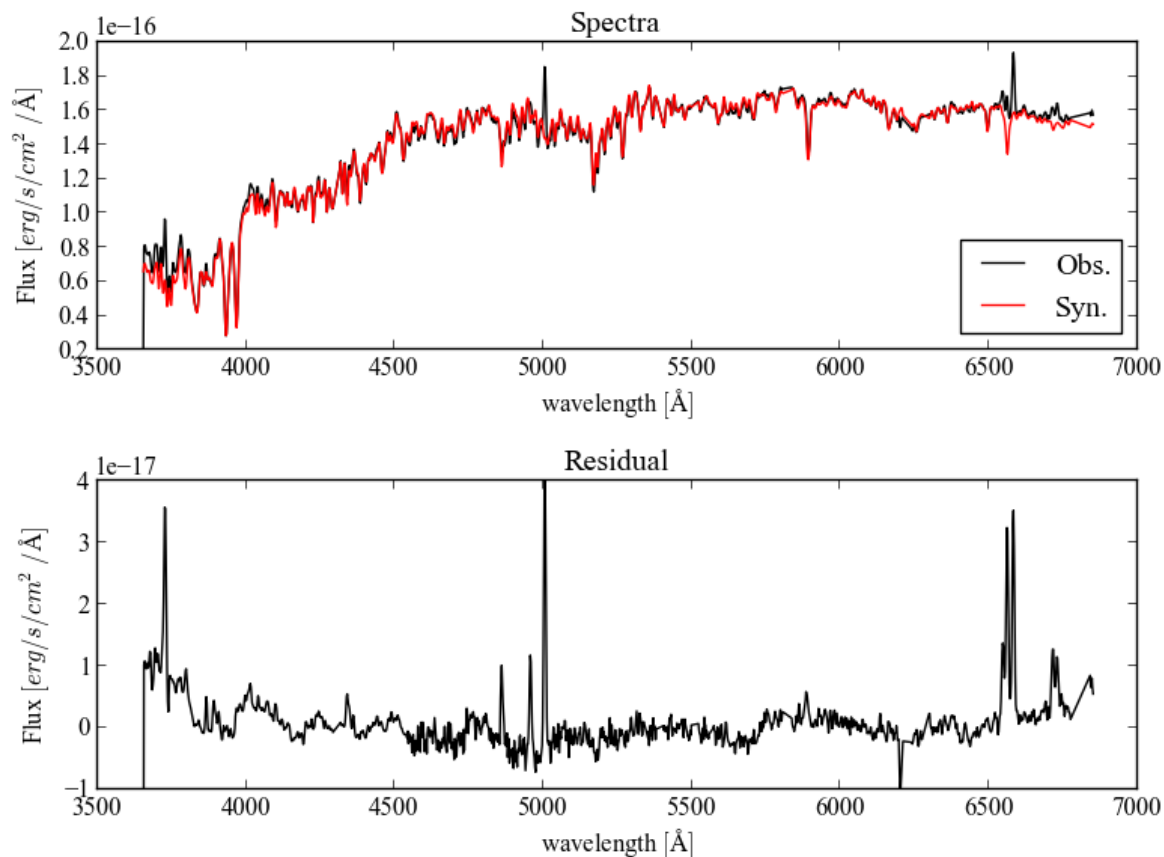
Notice the emission lines are more evident in the residual. Thus using PyCASSO it is possible to analyze the spatially resolved spectral features like the $D_n(4000)$ and Lick indices.

4.7 Integrated properties

In addition to the spatially stellar synthesis, we performed the stellar synthesis in the integrated spectra of the galaxies. This was one can check if the sum of the parts is equal to the whole. In general the properties in integrated form contain the prefix `integrated_`. Please take a look at the section *Galaxy property list* (page 31). Let's take a look in the mass of the galaxy.

```
>>> K.integrated_Mcor / 1e10
6.4588941491889695
>>> (K.McorSD__yx * K.parsecPerPixel**2).sum() / 1e10
6.7011924815290183
>>> K.integrated_Mcor / (K.McorSD__yx * K.parsecPerPixel**2).sum()
0.9638425051947227
```

That is, the total mass of the galaxy, calculated using the stellar synthesis of the integrated spectra

(`integrated_Mcor`) is 4% smaller than the sum of the masses of the pixels, calculated in the same way.

LEGACY API

5.1 Loading from FITS files

The process of loading data for a galaxy in a FITS file is similar to the HDF5 one. The main difference is that you only have to specify the path to the file. One should use sensible file names in this case. Using the same example, let's load the data from the file 'K0001_synthesis_eBR_v20_q036.d13c512.ps03.k2.mC.CCM.Bgsd61.fits'.

```
>>> from pycasso.fitsdatacube import fitsQ3DataCube
>>> K = fitsQ3DataCube('K0001_synthesis_eBR_v20_q036.d13c512.ps03.k2.mC.CCM.Bgsd61.fits')
```

The object K is a fitsQ3DataCube, whick quacks almost exactly like a h5Q3DataCube (page 49), except for the dynamic loading of data present in the HDF5 implementation. Your script should work just like before.

5.2 Using very old scripts

There were several prototype versions of PyCASSO containing features which were abandoned, or renamed, or had changes in functionality. The class Q3DataCube (page 26) is meant to be a backwards compatibility layer for older scripts that used these features.

The main use for the old API is to convert from zone to XY notation, and produce radial profiles using the older dialect.

```
>>> from califa.Q3DataCube import Q3DataCube
>>> K = Q3DataCube('K0001_synthesis_eBR_v20_q036.d13c512.ps03.k2.mC.CCM.Bgsd61.fits')
>>> zyx = K.getZoneToYXTensor(extensive=True, dezonification=True)
>>> LobnSD__yx = np.tensordot(K.Lobn__z, zyx, (0, 0))
>>> ryx, bin_r, bin_area = K.getYXToRadialBinsTensor(d_r=0.1, \
rad_bin_ini=0.0, rad_bin_fin=2.5)
>>> LobnSD__r = np.tensordot(LobnSD__yx, ryx, [(0, 1), (1, 2)])
>>> plt.plot(bin_r, LobnSD__r, '-k')
>>> plt.xlim(0, 2.5)
>>> plt.xlabel(r'$R_{50}$')
>>> plt.ylabel(r'$L_\odot / pc^2$')
>>> plt.title('Radial profile of luminosity using old API')
```
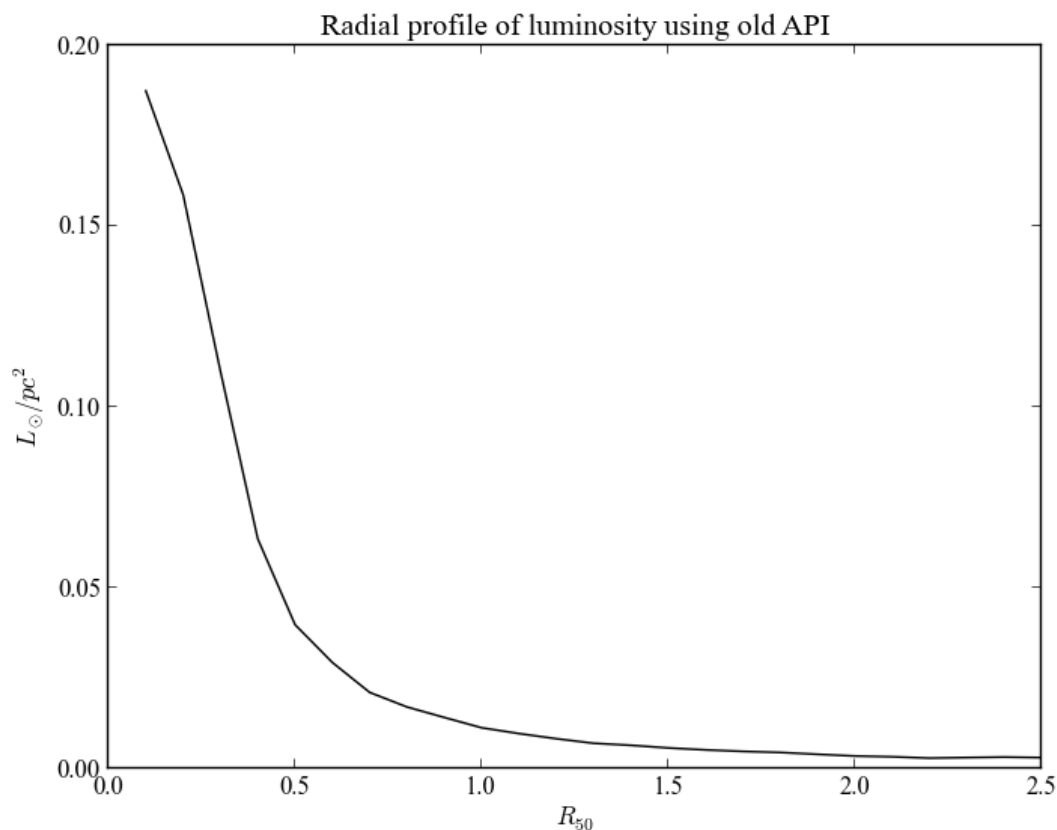
All that could be easily attained using the methods `zoneToYX()` (page 59) and `radialProfile()` (page 63) without the hassle intermediary matrices and the order of the dimensions in tensordot.

5.3 Old API reference

class `califa.Q3DataCube.`**`Q3DataCube`**(*synthesisFile*, *circularProfile=True*, *runId=None*, *califaId=None*, *smoothDezonification=True*)

    `getZoneToYXTensor`(*extensive=True*, *dezonification=True*)

        Returns a tensor to transform from zone notation to spatial notation, with shape (zone, y, x). The normalization of the pixels can take into account the area of the zones or the luminosity weigth, using the following parameters:

        Parameters **extensive** : boolean

            A.K.A. "normalize by zone area". Use surface density when calculating the transformation from zone to spatial coordinates.

        dezonification : boolean

            Use image at 5650AA to weight pixels in the zones. This is used only when `extensive=True`.

        Returns **zoneToYX** : 3-D array

            The transform tensor, shape (nZones, y, x).

    See Also:

    `getYXToRadialBinsTensor` (page 27), `getZoneToRadialBinsTensor` (page 27)

Examples

To transform a cube named mycube, with axes (age, zone), into a cube with axes (age, y, x), one can perform the operation

```
>>> K = Q3DataCube(filename)
>>> zyx = K.getZoneToYXTensor()
>>> numpy.tensordot(mycube, zyx, (1, 0))
```

where 1 is the number of the zone axis in `mycube`, and 0 is the zone axis number in `zyx`.

getYXToRadialBinsTensor(*d_r*, *rad_bin_ini=0*, *rad_bin_fin=None*, *use_HLR_units=True*, *normalize_area=True*)
Compute a tensor that transforms an array from zone binning notation to radial binning notation. Given the radial profile for this galaxy, this method calculates a tensor similar to the `zonesToYXTensor`, it transforms an image from spatial coordinates (x,y) to a radial profile.

> **Parameters**   **d_r** : float
>
>> Radial step of the rings, in units of HLR.
>>
>> **rad_bin_ini** : float, defaults to 0.0
>>
>>> Initial value for rad bins, in units of HLR.
>>>
>>> **rad_bin_fin** : float, defaults to infinity
>>>
>>>> Final value for rad bins, in units of HLR.
>>>>
>>>> **use_HLR_units** : boolean
>>>>
>>>>> If True, use the bins in HLR units. If False, use pixels.
>>>>>
>>>>> **normalize_area** : boolean
>>>>>
>>>>>> If True, divide the tensor by the bin area.
>
> **Returns**   **YXToRad** : array, shape (rad. bins, y, x).
>
>> The transform tensor.
>>
>> **bin_R** : array of float
>>
>>> Radial bin outer edges.
>>>
>>> **bin_area** : array of float
>>>
>>>> Radial bin area, in pixels.

See Also:

`getZoneToRadialBinsTensor` (page 27), `getZoneToYXTensor` (page 26)

Examples

```
>>> c = Q3DataCube(file)
>>> yxToRad, bins, unused = c.getYXToRadialBinsTensor(d_r=0.2)
```

`c.LobnSD__yx` is the luminosity surface desity in each pixel. Compute the radial profile of the average luminosity surface density.

```
>>> radProf__R = np.tensordot(Lobn_tot__yx, yxToRad, [(0,1),(1,2)])
>>> plot(bins, radProf__R)
```

getZoneToRadialBinsTensor(*d_r*, *rad_bin_ini=0*, *rad_bin_fin=None*, *use_HLR_units=True*, *extensive=True*, *dezonification=False*)
Return a tensor that transforms an array from zone binning notation to radial binning notation. Given the radial profile for this galaxy, this method calculates a tensor similar to the `zonesToYXTensor`, it transforms an image from spatial coordinates (x,y) to a radial profile.

5.3. Old API reference   **27**

Parameters   **d_r** : float

     Radial step of the rings, in units of HLR_pix.

     rad_bin_ini : float, defaults to 0.0

       Initial value for rad bins, in units of HLR_pix.

     rad_bin_fin : float, defaults to infinity

       Final value for rad bins, in units of HLR_pix.

     use_HLR_units : boolean

       If True, use the bins in HLR units. If False, use pixels.

     extensive : boolean

       Use surface density when calculating the transformation from zone to spatial coordinates.

     dezonification : boolean

       Use image at 5650AA to weight pixels in the zones.

Returns   **YXToRad** : array, shape (y, x, zone)

     The transform tensor.

     bin_R : array of float

       Radial bin outer edges.

     bin_area : array of float

       Radial bin area, in pixels.

See Also:

`getYXToRadialBinsTensor` (page 27), `getZoneToYXTensor` (page 26)

Examples

```
>>> c = Q3DataCube(file)
>>> zoneToRad, bins, unused = c.getZoneToRadialBinsTensor(d_r=0.2)
```

`c.popx` is luminosity fraction per zone. `c.popx.shape` is (ageBase, metBase, zone). Get the flux per unit area (?) for each zone.

```
>>> Lobn = c.popx / 100.0 * c.Lobs_norm
```

Total luminosity in each zone.

```
>>> Lobn_tot = Lobn.sum(axis=1).sum(axis=0)
>>> radProf = np.tensordot(Lobn_tot, zoneToRad, (1,1))
>>> plot(bins, radProf)
```

findHLR_pix_CID()

     TODO: Deprecated findHLR_pix_CID(). Find the half light radius using the image at 5650 Angstrom. Using radial bins of 1 pixel, calculate the cumulative sum of luminosity. The HLR is the radius where the cum. sum reaches 50% of its peak value.

     Returns   **HLR** : float

       The half light radius, in pixels.

See Also:

`setGeometry`

Notes

This value should be close to $dfrac{HLR_{circular}}{sqrt{b/a}}$.

GALAXY PROPERTY LIST

These are most of the attributes for a galaxy. Refer to section *Full data access API* (page 49) for a complete (and very long) list.

Some properties have a suffix like `__tZyx`. This is a mnemonic to the dimensions of the property. The dimensions are as following:

- `t`: age - `N_age` (page 50)

- `Z` (capital): metallicity - `N_met` (page 50)

- `z` (small): zone - `N_zone` (page 50)

- `y`: Y-position - `N_y` (page 50)

- `x`: X-position - `N_x` (page 50)

- `l`: wavelength - `Nl_obs` (page 50)

6.1 Base

`h5Q3DataCube.`**`ageBase`**
 Ages of the base.

 •Units: $[Yr]$

 •Shape: `(N_zone)`

`h5Q3DataCube.`**`metBase`**
 Metalicities of the base.

 •Units: dimensionless

 •Shape: `(N_zone)`

`h5Q3DataCube.`**`Mstars`**
 Fraction of the initial stellar mass for a given population that is still trapped inside stars.

 •Units: dimensionless

 •Shape: `(N_age, N_met)`

`h5Q3DataCube.`**`fbase_norm`**
 TODO: Add description of cubes.

6.2 qbick planes

`h5Q3DataCube.`**`qSignal`**
 Signal at wavelength WINDOWSN.

•Units: $[erg/s/cm^2/\overset{\circ}{A}]$

•Shape: `(N_y, N_x)`

h5Q3DataCube.**qNoise**
    TODO: Add description of cubes.

h5Q3DataCube.**qSn**
    S/N at wavelength WINDOWSN.

•Units: dimensionless

•Shape: `(N_y, N_x)`

h5Q3DataCube.**qSignalUnmasked**
    Image at wavelength WINDOWSN (quick, not masked).

•Units: $[erg/s/cm^2/\overset{\circ}{A}]$

•Shape: `(N_y, N_x)`

h5Q3DataCube.**qNoiseUnmasked**
    TODO: Add description of qNoiseUnmasked.

h5Q3DataCube.**qPipeNoise**
    TODO: Add description of qPipeNoise.

h5Q3DataCube.**qMask**
    Boolean image mask used for data.

•Units: bool

•Shape: `(N_y, N_x)`

h5Q3DataCube.**qZones**
    Voronoi/segmentation zones (bins).

•Units: index

•Shape: `(N_y, N_x)`

h5Q3DataCube.**qZonesSn**
    S/N in Voronoi zones.

•Units: dimensionless

•Shape: `(N_y, N_x)`

h5Q3DataCube.**qZonesNoise**
    Noise (RMS) in Voronoi zones.

•Units: $[erg/s/cm^2/\overset{\circ}{A}]$

•Shape: `(N_y, N_x)`

h5Q3DataCube.**qFlagRatio**
    Ratio of flags in window at wavelength WINDOWSN

•Units: $[\%]$

•Shape: `(N_y, N_x)`

h5Q3DataCube.**qZonesSnOrig**
    S/N in Voronoi zones (unresampled, beta).

•Units: dimensionless

•Shape: `(N_y, N_x)`

h5Q3DataCube.**qZonesNoiseOrig**
    Noise (RMS) in Voronoi zones (unresampled, beta).

•Units: $[erg/s/cm^2/\overset{\circ}{A}]$

•Shape: `(N_y, N_x)`

h5Q3DataCube.**qSegmentationSn**
    Voronoi program output S/N.

•Units: dimensionless

•Shape: `(N_y, N_x)`

h5Q3DataCube.**qPipeNoiseOrig**
    Noise image derived from formal errors (unresampled).

•Units: $[erg/s/cm^2/\overset{\circ}{A}]$

•Shape: `(N_y, N_x)`

h5Q3DataCube.**qPipeZonesNoiseOrig**
    Noise image derived from formal errors in Voronoi zones (unresampled).

•Units: $[erg/s/cm^2/\overset{\circ}{A}]$

•Shape: `(N_y, N_x)`

h5Q3DataCube.**qSpatialMask**
    TODO: Add description of qSpatialMask.

h5Q3DataCube.**qSnMask**
    TODO: Add description of qSnMask.

h5Q3DataCube.**qFilledMask**
    TODO: Add description of qFilledMask.

h5Q3DataCube.**qConvexHull**
    Convex hull of data mask.

•Units: bool

•Shape: `(N-y, N_x)`

h5Q3DataCube.**qHollowPixels**
    Masked (bad) pixels inside the data mask.

•Units: bool

•Shape: `(N-y, N_x)`

6.3 Population

6.3.1 Zone

h5Q3DataCube.**popx**
    Light fractions for each population, in voronoi zones.

•   –Units: $[\%]$

•Shape: `(N_age, N_met, N_zone)`

h5Q3DataCube.**popmu_ini**
    Initial mass fractions for each population, in voronoi zones.

•Units: $[\%]$

•Shape: `(N_age, N_met, N_zone)`

h5Q3DataCube.**popmu_cor**
    Current mass fractions for each population, in voronoi zones.

•Units: [%]

•Shape: (N_age, N_met, N_zone)

h5Q3DataCube.**popAV_tot**
    Extinction for each population, in voronoi zones.

•Units: $[mag]$

•Shape: (N_age, N_met, N_zone)

h5Q3DataCube.**Lobs_norm**
    Luminosity density in norm window, in voronoi zones.

•Units: $[L_\odot/\overset{\circ}{A}]$

•Shape: (N_zone)

h5Q3DataCube.**Mini_tot**
    Initial mass for each population, in voronoi zones.

•Units: $[M_\odot]$

•Shape: (N_zone)

h5Q3DataCube.**Mcor_tot**
    Current mass for each population, in voronoi zones.

•Units: $[M_\odot]$

•Shape: (N_zone)

6.3.2 Spatially resolved

h5Q3DataCube.**popx__tZyx**
    Spatially resolved light fractions for each population.

•Units: [%]

•Shape: (N_age, N_met, N_y, N_x)

h5Q3DataCube.**popmu_ini__tZyx**
    Spatially resolved initial mass fractions for each population.

•Units: [%]

•Shape: (N_age, N_met, N_y, N_x)

h5Q3DataCube.**popmu_cor__tZyx**
    Spatially resolved corrected mass fractions for each population.

•Units: [%]

•Shape: (N_age, N_met, N_y, N_x)

h5Q3DataCube.**popAV_tot__tZyx**
    Spatially resolved extinction by dust for each population.

•Units: $[mag]$

•Shape: (N_age, N_met, N_y, N_x)

6.3.3 Integrated

h5Q3DataCube.**integrated_popmu_ini**
    Current mass fractions for each population, in integrated spectrum.

•Units: [%]

> •Shape: `(N_age, N_met)`

h5Q3DataCube.**integrated_popmu_cor**
> Current mass fractions for each population, in integrated spectrum.

> > •Units: $[\%]$

> > •Shape: `(N_age, N_met)`

h5Q3DataCube.**integrated_popAV_tot**
> Extinction by dust for each population, in integrated spectrum.

> > •Units: $[mag]$

> > •Shape: `(N_age, N_met)`

6.4 Physical properties

See also `HLR_pix` (page 50), `HLR_pc` (page 50) and `q_norm` (page 50).

6.4.1 Zone

h5Q3DataCube.**Mini__tZz**
> Initial mass of each population, in voronoi zones.

> > •Units: $[M_\odot]$

> > •Shape: `(N_age, N_met, N_zone)`

h5Q3DataCube.**Mcor__tZz**
> Current mass of each population, in voronoi zones.

> > •Units: $[M_\odot]$

> > •Shape: `(N_age, N_met, N_zone)`

h5Q3DataCube.**Lobn__tZz**
> Luminosity of each population in normalization window, in voronoi zones.

> > •Units: $[L_\odot]$

> > •Shape: `(N_age, N_met, N_zone)`

h5Q3DataCube.**DeRed_Lobn__tZz**
> "Dereddened" luminosity of each population in normalization window, in voronoi zones.

> > •Units: $[L_\odot]$

> > •Shape: `(N_age, N_met, N_zone)`

h5Q3DataCube.**Mini__z**
> Initial mass, in voronoi zones.

> > •Units: $[M_\odot]$

> > •Shape: `(N_age, N_met, N_zone)`

h5Q3DataCube.**Mcor__z**
> Current mass, in voronoi zones.

> > •Units: $[M_\odot]$

> > •Shape: `(N_age, N_met, N_zone)`

h5Q3DataCube.**Lobn__z**
> Luminosity in normalization window, in voronoi zones.

> > •Units: $[L_\odot]$

•Shape: (N_zone)

h5Q3DataCube.**DeRed_Lobn__z**
"Dereddened" luminosity in normalization window, in voronoi zones.

•Units: $[L_\odot]$

•Shape: (N_zone)

h5Q3DataCube.**A_V**
Extinction by dust, in voronoi zones.

•Units: $[mag]$

•Shape: (N_zone)

h5Q3DataCube.**v_0**
Velocity displacement, in voronoi zones.

•Units: $[km/s]$

•Shape: (N_zone)

h5Q3DataCube.**v_d**
Velocity dispersion, in voronoi zones.

•Units: $[km/s]$

•Shape: (N_zone)

6.4.2 Spatially resolved

h5Q3DataCube.**MiniSD__tZyx**
Spatially resolved initial mass surface density of each population.

•Units: $[M_\odot/pc^2]$

•Shape: (N_age, N_met, N_y, N_x)

h5Q3DataCube.**McorSD__tZyx**
Spatially resolved current mass surface density of each population.

•Units: $[M_\odot/pc^2]$

•Shape: (N_age, N_met, N_y, N_x)

h5Q3DataCube.**LobnSD__tZyx**
Spatially resolved luminosity surface density of each population in normalization window.

•Units: $[L_\odot/pc^2]$

•Shape: (N_age, N_met, N_y, N_x)

h5Q3DataCube.**DeRed_LobnSD__tZyx**
Spatially resolved "dereddened" luminosity surface density of each population in normalization window.

•Units: $[L_\odot/pc^2]$

•Shape: (N_age, N_met, N_y, N_x)

h5Q3DataCube.**MiniSD__yx**
Spatially resolved initial mass surface density.

•Units: $[M_\odot/pc^2]$

•Shape: (N_y, N_x)

h5Q3DataCube.**McorSD__yx**
Spatially resolved current mass surface density.

•Units: $[M_\odot/pc^2]$

•Shape: `(N_y, N_x)`

h5Q3DataCube.**LobnSD__yx**
  Luminosity surface density of each population in normalization window.

  •Units: $[L_\odot/pc^2]$

  •Shape: `(N_y, N_x)`

h5Q3DataCube.**DeRed_LobnSD__yx**
  "Dereddened" luminosity surface density of each population in normalization window.

  •Units: $[L_\odot/pc^2]$

  •Shape: `(N_y, N_x)`

h5Q3DataCube.**M2L__yx**
  Spatially resolved mass to light ratio.

  •Units: $[M_\odot/L_\odot]$

  •Shape: `(N_y, N_x)`

h5Q3DataCube.**DeRed_M2L__yx**
  Spatially resolved "dereddened" mass to light ratio.

  •Units: $[M_\odot/L_\odot]$

  •Shape: `(N_y, N_x)`

h5Q3DataCube.**A_V__yx**
  Spatially resolved extinction by dust.

  •Units: $[mag]$

  •Shape: `(N_y, N_x)`

h5Q3DataCube.**v_0__yx**
  Spatially resolved velocity displacement.

  •Units: $[km/s]$

  •Shape: `(N_y, N_x)`

h5Q3DataCube.**v_d__yx**
  Spatially resolved velocity dispersion.

  •Units: $[km/s]$

  •Shape: `(N_y, N_x)`

h5Q3DataCube.**at_flux__yx**
  Spatially resolved, flux-weighted average log. age.

  •Units: $[\log Gyr]$

  •Shape: `(N_y, N_x)`

h5Q3DataCube.**at_mass__yx**
  Spatially resolved, mass-weighted average log. age.

  •Units: $[\log Gyr]$

  •Shape: `(N_y, N_x)`

h5Q3DataCube.**aZ_flux__yx**
  Spatially resolved, flux-weighted average metallicity.

  •Units: dimensionless

  •Shape: `(N_y, N_x)`

h5Q3DataCube.**aZ_mass__yx**
  Spatially resolved, mass-weighted average metallicity.

•Units: dimensionless

•Shape: `(N_y, N_x)`

6.4.3 Integrated

`h5Q3DataCube.`**`integrated_Lobn`**
  Luminosity in normalization window of the integrated spectrum.

  •Units: $[L_\odot]$

  •Type: float

`h5Q3DataCube.`**`integrated_Lobn__tZ`**
  Luminosity of each population in normalization window of the integrated spectrum.

  •Units: $[L_\odot]$

  •Shape: `(N_age, N_met)`

`h5Q3DataCube.`**`integrated_DeRed_Lobn`**
  "Dereddened" luminosity in normalization window of the integrated spectrum.

  •Units: $[L_\odot]$

  •Type: float

`h5Q3DataCube.`**`integrated_DeRed_Lobn__tZ`**

  "Dereddened" luminosity of each population in normalization window of the integrated spectrum.

  • Units: $[L_\odot]$

  • Shape: `(N_age, N_met)`

`h5Q3DataCube.`**`integrated_Mcor`**
  Current mass of the integrated spectrum.

  •Units: $[M_\odot]$

  •Type: float

`h5Q3DataCube.`**`integrated_Mcor__tZ`**
  Current mass of each population of the integrated spectrum.

  •Units: $[M_\odot]$

  •Shape: `(N_age, N_met)`

`h5Q3DataCube.`**`integrated_Mini`**
  Initial mass of the integrated spectrum.

  •Units: $[M_\odot]$

  •Type: float

`h5Q3DataCube.`**`integrated_Mini__tZ`**
  Initial mass of each population of the integrated spectrum.

  •Units: $[M_\odot]$

  •Shape: `(N_age, N_met)`

`h5Q3DataCube.`**`integrated_M2L`**
  Mass to light ratio of the integrated spectrum.

  •Units: $[M_\odot/L_\odot]$

  •Type: float

`h5Q3DataCube.`**`integrated_DeRed_M2L`**
  "Dereddened" mass to light ratio of the integrated spectrum.

•Units: $[M_\odot/L_\odot]$

•Type: float

h5Q3DataCube.**integrated_at_flux**
    Flux-weighted average log. age of the integrated spectrum.

•Units: $[\log Gyr]$

•Type: float

h5Q3DataCube.**integrated_at_mass**
    Mass-weighted average log. age of the integrated spectrum.

•Units: $[\log Gyr]$

•Type: float

h5Q3DataCube.**integrated_aZ_flux**
    Flux-weighted average metallicity of the integrated spectrum.

•Units: dimensionless

•Type: float

h5Q3DataCube.**integrated_aZ_mass**
    Mass-weighted average metallicity of the integrated spectrum.

•Units: dimensionless

•Type: float

6.5 Spectra

6.5.1 Zone

h5Q3DataCube.**l_obs**
    Wavelength array for the spectral.

•Units: $[\mathring{A}]$

•Shape: (Nl_obs)

h5Q3DataCube.**f_obs**
    Observed flux (input spectra for the synthesis), in voronoi zones.

•Units: $[erg/s/cm^2/\mathring{A}]$

•Shape: (Nl_obs, N_zone)

h5Q3DataCube.**f_err**
    Error in observed spetra, in voronoi zones.

•Units: $[erg/s/cm^2/\mathring{A}]$

•Shape: (Nl_obs, N_zone)

h5Q3DataCube.**f_flag**
    Flagged spaxels, in voronoi zones.

    FIXME: describe flags.

•Units: dimensionless

•Shape: (Nl_obs, N_zone)

h5Q3DataCube.**f_syn**
    Synthetic spectra, in voronoi zones.

• Units: $[erg/s/cm^2/\overset{\circ}{A}]$

• Shape: (Nl_obs, N_zone)

h5Q3DataCube.**f_wei**
> Weight of the spaxels in the input spectra. This is the weight actually used by the synthesis, after clipping, etc. Values for voronoi zones.

> FIXME: describe flags and weights.

>> • Units: dimensionless

>> • Shape: (Nl_obs, N_zone)

6.5.2 Spatially resolved

h5Q3DataCube.**f_obs__lyx**
> Spatially resolved observed flux (input spectra for the synthesis).

>> • Units: $[erg/s/cm^2/\overset{\circ}{A}]$

>> • Shape: (Nl_obs, N_y, N_x)

h5Q3DataCube.**f_err__lyx**
> Spatially resolved error in observed spetra.

>> • Units: $[erg/s/cm^2/\overset{\circ}{A}]$

>> • Shape: (Nl_obs, N_y, N_x)

h5Q3DataCube.**f_flag__lyx**
> Spatially resolved flagged spaxels.

> FIXME: describe flags.

>> • Units: dimensionless

>> • Shape: (Nl_obs, N_y, N_x)

h5Q3DataCube.**f_syn__lyx**
> Spatially resolved synthetic spectra.

>> • Units: $[erg/s/cm^2/\overset{\circ}{A}]$

>> • Shape: (Nl_obs, N_y, N_x)

h5Q3DataCube.**f_wei__lyx**
> Spatially resolved weight of the spaxels in the input spectra. This is the weight actually used by the synthesis, after clipping, etc.

> FIXME: describe flags and weights.

>> • Units: dimensionless

>> • Shape: (Nl_obs, N_y, N_x)

6.5.3 Integrated

h5Q3DataCube.**integrated_f_obs**
> Observed flux (input spectra for the synthesis), in integrated spectrum.

>> • Units: $[erg/s/cm^2/\overset{\circ}{A}]$

>> • Shape: (Nl_obs)

h5Q3DataCube.**integrated_f_err**
> Error in integrated observed spetrum.

- Units: $[erg/s/cm^2/\overset{\circ}{A}]$

- Shape: `(Nl_obs)`

h5Q3DataCube.**integrated_f_flag**
Flagged spaxels, in integrated spectrum.

FIXME: describe flags.

- Units: dimensionless

- Shape: `(Nl_obs)`

h5Q3DataCube.**integrated_f_syn**
Synthetic integrated spectrum.

- Units: $[erg/s/cm^2/\overset{\circ}{A}]$

- Shape: `(Nl_obs)`

h5Q3DataCube.**integrated_f_wei**
Weight of the spaxels in the integrated input spectra. This is the weight actually used by the synthesis, after clipping, etc.

FIXME: describe flags and weights.

- Units: dimensionless

- Shape: `(Nl_obs, N_y, N_x)`

6.6 Synthesis fit diagnostics

h5Q3DataCube.**adev**
Mean absolute relative deviation, in percent, only for the `Nl_eff` points actually used in the synthesis.

- Units: $[\%]$

- Shape: `(N_zone)`

h5Q3DataCube.**adevS**
From Cid @ 26/05/2012: Here's my request for pycasso reader: That it defines a new figure of merit analogous to `adev`, but which uses the synthetic flux in the denominator instead of the observed one. This is the `adevS__z` thing defined below in awful python. Why? Well, despite all our care there are still some non-flagged pixels with very low fluxes, which screws up adev, and this alternative definition fixes it.

Original code:

```python
>>> adevS__z = np.zeros((self.nZones))
>>> for i_z in np.arange(self.nZones):
>>>     _a = np.abs(self.f_obs[:,i_z] - self.f_syn[:,i_z]) / self.f_syn[:,i_z]
>>>     _b = _a[self.f_wei[:,i_z] > 0]
>>>     adevS__z[i_z] = 100.0 * _b.mean()
>>> return adevS__z
```

   Returns   aDevS : array of length (nZones)

h5Q3DataCube.**NOl_eff**
Number of OK wavelengths in input spectrum, in voronoi zones.

- Units: dimensionless

- Shape: `(N_zone)`

h5Q3DataCube.**Nglobal_steps**
Number of steps in spectral fitting, in voronoi zones.

- Units: dimensionless

•Shape: (N_zone)

`h5Q3DataCube.`**`chi2`**

χ^2/Nl_{eff} of the fit, in voronoi zones.

•Units: dimensionless

•Shape: (N_zone)

Apêndice B

Artigos publicados

B.1 Resolving galaxies in time and space. I. Applying STARLIGHT to CALIFA datacubes

Artigo por Cid Fernandes et al. (2013b) (doi:`10.1051/0004-6361/201220616`). Também disponível em *preprint* (`arXiv:1304.5788`).

Astronomy & Astrophysics

Resolving galaxies in time and space

I. Applying STARLIGHT to CALIFA datacubes

R. Cid Fernandes[1,2], E. Pérez[1], R. García Benito[1], R. M. González Delgado[1], A. L. de Amorim[2], S. F. Sánchez[1,3], B. Husemann[4], J. Falcón Barroso[5,6], P. Sánchez-Blázquez[7], C. J. Walcher[4], and D. Mast[1,3]

[1] Instituto de Astrofísica de Andalucía (CSIC), PO Box 3004, 18080 Granada, Spain
e-mail: cid@astro.ufsc.br
[2] Departamento de Física, Universidade Federal de Santa Catarina, PO Box 476, 88040-900, Florianópolis, SC, Brazil
[3] Centro Astronómico Hispano Alemán, Calar Alto, (CSIC-MPG), C/Jesús Durbán Remón 2-2, 04004 Almería, Spain
[4] Leibniz-Institut für Astrophysik Potsdam, innoFSPEC Potsdam, An der Sternwarte 16, 14482 Potsdam, Germany
[5] Instituto de Astrofísica de Canarias, Vía Lactea s/n, 38200 La Laguna, Tenerife, Spain
[6] Departamento de Astrofísica, Universidad de La Laguna, 38205 Tenerife, Spain
[7] Departamento de Física Teórica, Universidad Autónoma de Madrid, 28049 Madrid, Spain

Received 23 October 2012 / Accepted 16 April 2013

ABSTRACT

Aims. Fossil record methods based on spectral synthesis techniques have matured during the past decade, and their application to integrated galaxy spectra has fostered substantial advances in the understanding of galaxies and their evolution. Yet, because of the lack of spatial resolution, these studies are limited to a global view, providing no information about the internal physics of galaxies.
Methods. Motivated by the CALIFA survey, which is gathering integral field spectroscopy (IFS) over the full optical extent of 600 galaxies, we have developed an end-to-end pipeline that: (i) partitions the observed datacube into Voronoi zones in order to, when necessary and taking due account of correlated errors, increase the signal-to-noise ratio; (ii) extracts rest-framed spectra, including propagated errors and bad-pixel flags; (iii) feeds the spectra into the   spectral synthesis code; (iv) packs the results for all galaxy zones into a single FITS or HDF5 file; (v) performs a series of post-processing operations, including zone-to-pixel image reconstruction and unpacking the spectral and stellar population properties derived by   into multidimensional time, metallicity, and spatial coordinates. This paper provides an illustrated description of the whole pipeline and its many products. Using data for the nearby spiral NGC 2916 as a showcase, we go through each of the steps involved and present a series of ways of visualizing and analyzing this manifold. These include 2D maps of properties such as the velocity field, stellar extinction, mean ages and metallicities, mass surface densities, and star formation rates on different time scales and normalized in different ways, as well as 1D averages in the temporal and spatial dimensions, which lead to evolutionary curves and radial profiles of physical properties. Projections of the stellar light and mass growth onto radius-age diagrams are introduced as a means of visualizing galaxy evolution in time and space simultaneously, something which can also be achieved in 3D with snapshot cuts through the (x, y, t) cubes.
Results. The results vividly illustrate the richness both of the combination of IFS data with spectral synthesis and of the insights on galaxy physics provided by the variety of diagnostics and semi-empirical constraints obtained. Additionally, they give a glimpse of what is to come from CALIFA and future IFS surveys.

Key words. galaxies: general – galaxies: stellar content – galaxies: fundamental parameters

1. Introduction

Technology in the past decade has lead to massive surveys either in imaging or spectroscopy modes that have been very successful in providing information of the spectral energy distribution or central/integrated spectra for a large number of galaxies (e.g., 2dF, Folkes et al. 1999; SDSS, York et al. 2000; COMBO-17, Bell et al. 2004; ALHAMBRA, Moles et al. 2008; COSMOS, Ilbert et al. 2009). These data have allowed significant insight into the integrated properties of galaxies, as well as into the evolution of global quantities such as the mass assembly (Pérez-Gonzalez et al. 2008) and the star formation history (SFH) of the universe (Lilly et al. 1996; Madau et al. 1996). However, these surveys are limited in either spectral or spatial resolution. Imaging provides spatial information, but at the expense of coarse spectral coverage (typically broadband filters), limiting the amount of information on the stellar populations, and providing little or no information on the gas (emission lines)

or the kinematics of the galaxy. Surveys based on integrated spectra offer a richer list of diagnostics of the gaseous and stellar components but lack spatial resolution and suffer from aperture effects (one spectrum per object, centered at the nucleus and not covering the full galaxy). Moreover, integrated galaxy spectra do not allow, for example, the isolation of morphological components (bulge, disk, bars), the mapping of the effects of mergers, and the tracing of secular processes such as stellar migration and other features of galaxy formation and evolution, which can only be observationally tackled with a combination of imaging and spectroscopic capabilities.

The near future will see a proliferation of integral field spectroscopy (IFS) surveys, which will allow a detailed look at physics *within* galaxies, as opposed to the global view offered by integrated light surveys. The Calar Alto Legacy Integral Field Area survey (CALIFA) is a pioneer in this area (Sánchez et al. 2012), and others will follow soon, like SAMI (Croom et al. 2012), VENGA (Blanc et al. 2009), and MaNGA

(Bundy et al., in prep.). CALIFA is obtaining IFS for 600 nearby galaxies ($0.005 < z < 0.03$) of all types, mapping stellar populations, ionized gas and their kinematics across the full optical extent of the sources. The number of spectra to be generated is of the same order of the whole SDSS ($\sim 10^6$).

Clearly, however, these will not be "just another million galaxy spectra". Processed through the machinery of fossil record methods, which recover the history of a stellar system out of the information encoded in its spectrum (Walcher et al. 2011 and references therein), CALIFA will provide valuable and hitherto unavailable information on the spatially resolved SFH of galaxies. An example of what can be done was presented by Pérez et al. (2012), where we used data on the first 105 galaxies observed by CALIFA in conjunction with the spectral synthesis code   (Cid Fernandes et al. 2005) to study the spatially resolved mass assembly history of galaxies. We find that the inner parts of massive galaxies grow faster than the outer ones, a clear signature of inside-out growth, and that the relative growth rate depends on the stellar mass of the galaxy, with a maximum relative growth efficiency for intermediate masses ($\sim 7 \times 10^{10}\ M_\odot$).

The application of spectral synthesis methods to IFS datacubes opens new ways of studying galaxies and their evolution. In practice, however, this apparently simple extension of work done for spatially integrated spectra involves a series of technical details and methodological issues, as well as challenges in the visualization and representation of the results.

The purpose of this paper is to present a detailed account of all steps in the processing of CALIFA (x, y, λ) datacubes to the multidimensional products derived from the   analysis. We thus focus basically on methodology, leaving the exploration of results for subsequent studies. Paper II (Cid Fernandes et al. 2013) presents a thorough study of the uncertainties involved in these products, including the effects of random noise, spectral shape errors, and evolutionary synthesis models used in the analysis. Despite the emphasis on CALIFA and   , the issues discussed here and in Paper II are of direct interest to spectral synthesis analysis of IFS data in general.

The paper is organized as follows. Section 2 presents the data. Section 3 provides a detailed description of the preprocessing steps, which prepare the reduced data for a full spectral fitting analysis. Section 4 reviews the   code and the ingredients used in our analysis. It also introduces the PyCASSO pipeline, used to pack and analyze the results of the synthesis. Our main results are presented in Sect. 5, which uses the nearby spiral NGC 2916 (galaxy 277 in the CALIFA mother sample) as a showcase. This long section starts with considerations on how to evaluate the quality of the spectral fits, and then proceeds to the presentation of the synthesis products in different ways, including 2D maps of the stellar light and mass, extinction, mean ages and metallicities, and star formation rate maps on different time scales; 1D maps on either the spatial or temporal dimensions, and attempts to visualize the evolution of galaxies in time and space simultaneously. The emphasis is always on methodological issues, but the examples naturally illustrate the richness of the multidimensional products of this analysis. Finally, our results are summarized in Sect. 6.

2. Data

The goals, observational strategy and overall characteristics of the survey were described in Sánchez et al. (2012). In summary, CALIFA's mother sample comprises 939 galaxies in the $0.005-0.03$ redshift range, which is extracted from the SDSS imaging survey to span the full color−magnitude diagram down to $M_r < −18$ mag, with diameters selected to match the field of the IFU instrument ($\sim 1'$ in diameter). A thorough characterization of the sample will be presented in Walcher et al. (in prep). CALIFA will observe ~ 600 galaxies from this mother sample, applying purely visibility-based criteria at each observing night. The final sample will be representative of galaxies in the local universe, statistically significant, and well selected.

The data analyzed in this paper were reduced using the CALIFA pipeline version 1.3c, described in the Data Release 1 article (Husemann et al. 2013). Each galaxy is observed with PMAS (Roth et al. 2005, 2010) in the PPAK mode (Verheijen et al. 2004; Kelz et al. 2006) at the 3.5 m telescope of Calar Alto Observatory and with two grating setups: the V500, covering from ~ 3700 to 7500 Å at $FWHM \sim 6$ Å resolution, and the V1200 ($\sim 3650-4600$ Å, $FWHM \sim 2.3$ Å). The wide wavelength coverage of the V500 is ideal for our purposes, but the blue end of its spectra, which contains valuable stellar population tracers such as the 4000 Å break and high-order Balmer lines, is affected by vignetting over a non-negligible part of the field of view. To circumvent this problem we worked with a combination of the two gratings, whereby the data for $\lambda < 4600$ Å come from the V1200 (which does not suffer from this problem at this wavelength range) and the rest from the V500. The spectra were homogenized to the resolution of the V500.

For each galaxy the pipeline provides an (x, y, λ) cube with a final sampling of ($1'', 1'', 2$ Å). The cube comprises absolute calibrated flux densities at each spaxel (F_λ), corrected by Galactic extincion using the Schlegel et al. (1998) maps and the extinction law of Cardelli et al. (1989) law with $R_V = 3.1$. Besides fluxes, the reduced cubes contain carefully derived errors (ϵ_λ) and a bad-pixel flag (b_λ), which signals unreliable flux entries, due to bad columns, cosmic rays, and other artefacts (see Husemann et al. 2013, for details).

3. Pre-processing steps: from datacubes to STARLIGHT input

A series of pre-processing steps is applied to the reduced datacubes, with the general goal of extracting good quality spectra for a stellar population analysis with   or any other similar code. These are:

1. definition of a spatial mask;
2. outer signal-to-noise ratio (S/N) mask;
3. refinements of the b_λ (flag) and ϵ_λ (error) spectra;
4. rest framing;
5. spatial binning;
6. resampling in λ.

This section describes each of these operations.

3.1. Spatial masks

The first step is to mask out foreground stars, artefacts, and low S/N regions. As a starting point, candidate spurious sources are identified applying SExtractor (Bertin & Arnouts 1996) to the SDSS r-band image. The masked image is then matched to the CALIFA field of view using the WCS information available in the headers to reproject the SDSS masks to the scale, orientation, and pixel size of the CALIFA cubes. To improve upon this first approximation, we perform a visual inspection of each galaxy, correcting its mask interactively whenever necessary. For instance, we manually fixed a few unmasked pixels that remained

in the borders of each masked object (probably due to a combination of the slightly better PSF of the SDSS images and the accuracy of the CALIFA WCS information used in the matching). Also, in a number of cases we found that the initial mask included bright H regions, while in others very dim point-like sources can be distinguished in the SDSS image, but have no clear counterpart in the CALIFA image or spectra. In all cases, the masks were corrected by hand.

The resulting masks are free from spurious spaxels. Unlike the other operations described below, this step could not be fully automated. For the size of CALIFA, this is still a feasible, albeit laborius, task. A last step in defining the spatial mask is to impose a spectral quality threshold based on the S/N of the data. This step has been fully automated in the pipeline described next.

3.2. Flags, errors, and segmentation: the QBICK pipeline

The next steps (items ii to vi) were all packed in a fully automated package, , built specifically for CALIFA but sufficiently general to handle any FITS format to pre-process datacubes for a 3D spectral fitting analysis.

The b_λ flags produced by the reduction pipeline ($b_\lambda \equiv 0$ for good pixels and >0 for flagged ones) do a good job in identifying problematic pixels. For uniformity, we enforce $b_\lambda > 0$ around the strongest sky lines seen in the CALIFA data: HgI 4358 Å, HgI 5461 Å, OI 5577 Å, NaI D (around 5890 Å), OI-OH (6300 Å), OI 6364 Å, and the B-band atmospheric absorption (Sánchez et al. 2007). We have further set $b_\lambda > 0$ when the value of the error is very large (specifically, when $\epsilon_\lambda > 5F_\lambda$), but this is merely a cosmetic choice as these pixels would not influence the spectral fits anyway. Anomalously small ϵ_λ values, on the other hand, can have a disproportionately large weight on the analysis. In the very few cases where this happens, the pixels were flagged. These refinements are useful to circumvent potential problems in the spectral fitting analysis, specially when the whole data set is processed in "pipeline mode".

After these fixes all spectra are rest-framed using the redshift derived by the reduction pipeline for the central 5″ spectrum (Sánchez et al. 2012), which is included in the original headers. This step includes a $(1 + z)^3$ correction for the energy, time, and bandwidth changes with redshift.

We used the (rest wavelength) window between 5590 and 5680 Å to estimate a S/N, defining the signal as the mean flux and the noise as the detrended standard deviation[1] of F_λ, both excluding flagged pixels[2]. Regions outside the outer S/N = 5 iso-contour were added to the spatial mask and discarded from the analysis. In a few cases this threshold was lowered due to low surface brightness.

Figure 1b shows the 5635±45 Å image of CALIFA 277, after the final spatial mask. The hole above the nucleus corresponds to the foreground source seen in the SDSS image (panel a). The hexagonal pattern of the fiber bundle is clearly visible since in this example S/N > 5 over most of the field of view (panel c).

The 5635 Å image is also used to compute the galaxy's half light radius (HLR), adding up fluxes in spaxels sorted by distance to the nucleus and picking the radius at which half of the total flux is reached. For CALIFA 277, HLR = 17.9″. This

---

[1] The detrended standard deviation is the rms variation with respect to a linear fit, which is useful to remove the effect of the spectral slope in the window.

[2] Note that this is an apparently superfluous definition since we already have the noise spectrum. This "empirical" S/N is nevertheless useful, as explained in Sect. 3.3.
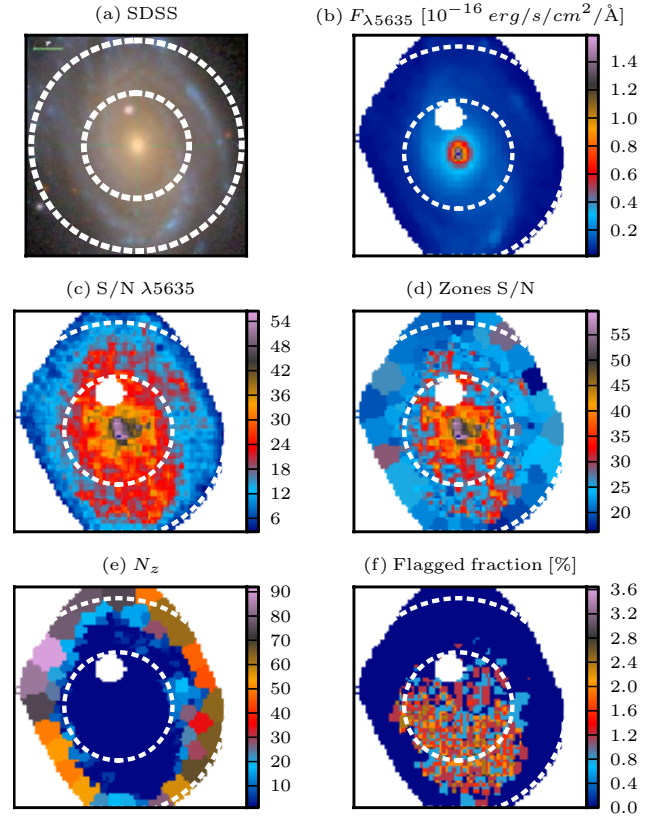
Fig. 1. a) SDSS stamp for NGC 2916 (CALIFA 277). As in other images throughout this paper, the circles mark $R = 1$ and 2 Half Light Radius (HLR). **b)** CALIFA image in the rest-frame 5635 ± 45 Å interval after applying the spatial mask. **c)** Map of the S/N at 5635 Å. **d)** S/N map after the Voronoi binning. **e)** Number of spaxels in each Voronoi zone. Note that no spatial binning ($N_z = 1$) was necessary throughout the inner ~1 HLR. **f)** Percentage of bad pixels in the 3800−6850 Å range. North is up and east is towards the left in all images.

datacube-based HLR may not be the ideal measure of the size of a galaxy, but it is the most convenient metric for the present analysis because it is based on the exact same data. In Fig. 1 and all images throughout this paper circles are drawn at $R = 1$ and 2 HLR to guide the eye.

The following step (item v in our list) consists of applying a segmentation structure to the data, grouping spaxels into spatial zones. All spaxels belonging to the same zone are assigned a common integer ID label, unique for each zone. stores the zone-to-xy tensor needed to map zones to pixels and vice-versa. In this paper we use spatial binning to increase the S/N for the spectral analysis. Other applications may prefer to group spaxels according to, say, morphology or emission-line oriented criteria. admits an externally provided segmentation map to allow for such choices.

The zoning scheme adopted here is based on the Voronoi tesselation technique, as implemented by Cappellari & Copin (2003), but with modifications to account for correlated errors (Sect. 3.3). The code is fed with the signal and noise images in the 5635 ± 45 Å range discussed above. The target S/N is set to 20. In practice, most individual spaxels inside 1 HLR satisfy this condition. Figure 1d shows the S/N map of CALIFA 277 after the spatial binning. For this galaxy, the 3649 non-masked spaxels were grouped into 1638 zones, the overwhelming majority (1527) of which are not binned at all. As seen in the map of the number of spaxels per zone (N_z, Fig. 1e), spatial binning

effectively starts at $R \sim 1$ HLR. Discounting the single spaxel zones, the median N_z is 10, but values up to 92 are reached in the outskirts.

Once the spatial binning map is defined, the flux, error, and flag spectra are computed for each zone. This operation must account for the flagged pixels. The total flux in zone z, which contains N_z spaxels whose fluxes are $F_{\lambda,k}$, is given by

$$F_{\lambda,z} = \frac{N_z}{\Phi_{\lambda,z}} \sum_{k=1}^{N_z} F_{\lambda,k} \phi_{\lambda,k}, \qquad (1)$$

where $\phi_{\lambda,k} = 0$ for flagged pixels ($b_{\lambda,k} > 0$) or 1 otherwise ($b_{\lambda,k} = 0$), and $\Phi_{\lambda,z} \equiv \sum \phi_{\lambda,k}$ is the number of useful spaxels at wavelength λ in the zone. The zone flux is thus N_z times the average flux over all non-flagged pixels. When none of the $F_{\lambda,k}$ fluxes are flagged, this equation simply sums all the fluxes in the zone, whereas when this is not the case, flagged entries are replaced by the average of non-flagged ones.

This scaling recipe is reasonable as long as the number of flagged pixels is not comparable to N_z. For example, in a zone of $N_z = 10$ spaxels, one would not like to take the resulting $F_{\lambda,z}$ seriously if eight of them are flagged. We chose to flag away entries whenever fewer than half of the spaxels in a zone have credible data at the given λ:

$$b_{\lambda,z} = \begin{cases} 0 & \text{if } \Phi_{\lambda,z} \geq N_z/2; \\ 1 & \text{if } \Phi_{\lambda,z} < N_z/2. \end{cases} \qquad (2)$$

For our example galaxy, the fraction of flagged pixels in the 3800−6850 Å interval used in the spectral synthesis analysis ranges from 5 to 8%, with a median of 6% (see Fig. 1f).

The computation of the error in $F_{\lambda,z}$ follows a recipe similar to Eq. (1), but adding in quadrature:

$$\epsilon_{\lambda,z}^2 = \beta_z^2 \frac{N_z}{\Phi_{\lambda,z}} \sum_{k=1}^{N_z} \epsilon_{\lambda,k}^2 \phi_{\lambda,k}, \qquad (3)$$

where β_z accounts for correlated errors (see below).

　also produces the total spatially integrated spectrum, following these same prescriptions. This is useful to compare the analysis of the whole to the sum of the analysis of the parts (which we do in Sect. 5.9).

Finally, all the spectra are resampled to 2 Å. The resulting zone spectra are stored in ASCII and/or FITS files, with flux, error, and flag columns necessary for a careful spectral analysis. All the quality control images produced in this process are packed in a single FITS file, along with the technical parameters adopted in the different steps (S/N clipping, segmentation map, etc.).

3.3. Spatial binning and correlated errors

As mentioned, the datacubes have a spatial sampling of $1'' \times 1''$. Because of the three-fold dithering pattern used in the observations, each spaxel has a varying contribution from a number of fibers. Since one fiber can contribute to more than one spaxel, the noise in a given spaxel is partially correlated with that of its neighbors. This implies that when spectra from adjacent spaxels are added together the noise in the resulting spectrum has to be calculated taking spatial covariances into account. As an extreme example, consider N_z completely correlated (i.e., ∼identical) spaxels in a zone. Clearly, co-adding their spectra would not result in the desired increase in the S/N as both signal
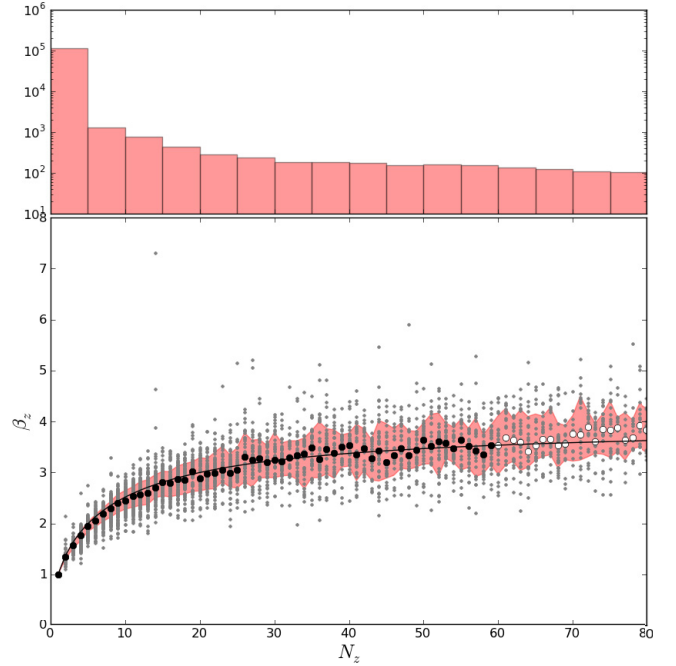
Fig. 2. Ratio of the measured over the idealized noise for Voronoi zones comprising N_z spaxels. The idealized noise is that derived under the assumption of uncorrelated errors, while the measured one is obtained from the detrended standard deviation of fluxes in a ±45 Å range around 5635 Å. Gray dots represent β_z values for 99267 spaxels from 109 galaxies. Circles show the median β_z for each N_z, and the solid line shows Eq. (4). *The top panel* shows the histogram of N_z values (notice the logarithmic scale).

and noise scale linearly with N_z. Unless told otherwise, however, the zoning algorithm assumes that the spaxels are independent and hence that the noise in the zone is given by $\sqrt{\sum \epsilon_k^2}$, resulting in an improvement of the S/N of the co-added spectrum by $\sim \sqrt{N_z}$, whereas in fact it has not changed at all[3].

An empirical correction was devised to account for the global behaviour of the spatial correlation of the signal in CALIFA data. We proceed by first defining initial Voronoi zones with the Cappellari & Copin (2003) algorithm. Because it assumes uncorrelated input, the code presumes the zone error is $\sqrt{\sum \epsilon_k^2}$. We then measure the "real" noise (e_z) in the resulting zone summed spectra from the (detrended) rms in the 5635 ± 45 Å range. The ratio of these two numbers, which we call β_z, is represented versus the number of spaxels in each zone in Fig. 2. Small grey dots are β_z values for the individual zones, and circles represent the median value computed at each N_z, while the shaded region represents the 16 to 84 percentiles. There are nearly 10^5 points in this plot, obtained from 244 196 spaxels in 109 galaxies (all those observed with the V500 and V1200 setups up to May 2012). The top panel shows the histogram of N_z.

The rise and flattening of the $\beta_z - N_z$ relation reflects the expected behavior. Zones with small N_z group adjacent and highly correlated spaxels, producing the initial rise of β_z. As farther apart spaxels are aggregated, the errors become less correlated, leading to the flattening observed. The scatter in the relation is

---

[3] ϵ_k denotes the noise in spaxel k, defined as the detrended rms in the same 5635 ± 45 Å range used to define the signal for spatial binning purposes.

likely related to the way the Voronoi algorithm assemble spaxels. Also, the three-fold dithering pattern is not completely uniform, so the amount of correlation is not exactly the same across the face of the fiber bundle. Still, the $\beta_z(N_z)$ relation portrayed in Fig. 2 is tight enough to derive an excellent statistical correction.

The solid line represents the fit of the following function:

$$\beta_z(N_z) = \left(\frac{15N_z}{15 + N_z - 1}\right)^{1/2}, \qquad (4)$$

where the fit was carried out considering only the filled circles. We can now apply this correction directly in the zoning code, replacing its idealized computation of the noise by

$$e_z = \beta_z(N_z)\sqrt{\sum_{k=1}^{N_z}\epsilon_k{}^2}, \qquad (5)$$

which accounts for the effects of spatially correlated errors. This correction was applied λ by λ (cf. Eq. (3)). An independently derived correction very similar to Eq. (4) is presented in Husemann et al. (2013).

While this scheme naturally leads to larger zones than those obtained under the (erroneous) hypothesis of independent spaxels, it ensures that the target S/N of 20 is actually achieved in all but the outermost zones (when the algorithm runs out of spaxels to bin). Typically, we obtain 1000 zones per galaxy.

4. STARLIGHT runs and PyCASSO

is a spectral synthesis code which combines the spectra from a base in order to match an observed spectrum O_λ. The search for an optimal model M_λ and the coefficients of the population vector x associated with the $N_\star$ base elements also allows for reddening, a velocity off-set $v_\star$, and a stellar velocity dispersion $\sigma_\star$. The code was first introduced in Cid Fernandes et al. (2004) and substantially optimized by Cid Fernandes et al. (2005). The code, didactic introductions and a user manual are available at www.starlight.ufsc.br. We are using a new and yet to be documented version of , but since most of the new features are not used in our analysis, the publicly available manual remains an accurate reference for the purposes of this paper.

The virtues and caveats of full spectral fits are discussed in a number of articles (e.g., Panter et al. 2003; Ocvirk et al. 2006; Cid Fernandes 2007; Tojeiro et al. 2007; McArthur et al. 2009; Sánchez-Blázquez et al. 2011). A general consensus in the field is that uncertainties in the results for individual objects average out for large statistical samples (Panter et al. 2007). With CALIFA, each galaxy is a statistical sample per se! Hence, even if the results for single spaxels (or zones) are not iron-clad, the overall trends should be robust (see Paper II for a detailed evaluation of the uncertainties in our   -based analysis of CALIFA data). It is also worth pointing out that despite the diversity of spectral synthesis methods, substantial changes in the results are more likely to come from revisions in the input data (as happened, for instance, with the recalibration of SDSS spectra between data releases 5 and 6) and from updates in the base models, the single most important ingredient in any spectral synthesis analysis.

The results reported in this paper rely on a spectral base of simple stellar populations (SSPs) comprising four metallicities, $Z = 0.2, 0.4, 1$, and $1, 5 Z_\odot$, and 39 ages between $t = 10^6$ and 1.4×10^{10} yr. This base (dubbed "*GM*" in Paper II) combines the Granada models of González Delgado et al. (2005) for

$t < 63$ Myr with those of Vazdekis et al. (2010; as updated by Falcón-Barroso et al. 2011) for larger ages. They are based on the Salpeter Initial Mass Function and the evolutionary tracks by Girardi et al. (2000), except for the youngest ages (≤ 3 Myr), which are based on Geneva tracks (Schaller et al. 1992; Schaerer et al. 1993a,b; Charbonnel et al. 1993). A comparison of results obtained with other bases and examples of the spectral fits are presented in Paper II.

The fits were carried out in the 3800−6850 Å interval. Reddening was modeled with the Cardelli et al. (1989) curve, with $R_V = 3.1$. As in Cid Fernandes et al. (2005), the main emission lines as well as the NaI D doublet (because of its sensitivity to ISM absorption) were masked. All runs were performed in the IAA-GRID, a network of computers which allows us to process 10^5 spectra in less than a day.

As documented in the user manual,   outputs a large array of quantities. In broad terms, these can be categorized as:

1. Input data: file names, configuration options, and other information provided either by the user explicitly or derived from the user-provided spectrum. Base-related data are also reported, including ages and metallicities of each component, the corresponding light-to-mass ratios (at the chosen normalization wavelength, λ_N), and a returned-mass correction factor.
2. Fit results: figures of merit (χ^2, $\overline{\Delta}$), kinematic parameters ($v_\star, \sigma_\star$), the V-band extinction (A_V), total stellar masses and luminosities, and population vectors, expressed in terms of light (x) and mass (μ) fractions.
3. Spectral data: the input (O_λ), best-model fit (M_λ), and weight spectra (w_λ, which equals ϵ_λ^{-1}, except for flagged, masked, and clipped pixels).

All these data are stored in a plain ASCII file, one for each fitted spectrum. The population vectors can be post-processed in a number of ways to obtain SFHs, compute the mass growth as a function of time, condense the results into first moments like the mean t and Z, etc. This scheme works fine for studies of independent objects, like SDSS galaxies or globular clusters.

IFS data, however, require a more structured level of organization, as it is cumbersome and inefficient to handle so many files separately. To handle datacubes we developed PyCASSO, which comprises three main parts:

1. A *writer* module, which packs the output of all   fits of the individual zones of a same galaxy into a single (FITS or HDF5) file. This file also contains all information generated during the pre-processing steps (Sect. 3), as well as information propagated from the original datacube.
2. A *reader* module, which reads this file and structures all the data in an easy to access and manipulate format.
3. A *post-processing* module, which performs a series of common operations, such as mapping any property from zones to pixels, resampling and smoothing the population vectors, computing growth functions, and averaging in spatial, time or metallicity dimensions. All these functionalities are conveniently wrapped as python packages, easily imported into the user's own analysis code.

PyCASSO will be the main workhorse behind a series of articles by our collaboration, so we dedicate the remainder of this paper to illustrating its main products.

5. Results

The Sb galaxy NGC 2916 (CALIFA 277) was chosen as a showcase. For the adopted distance of 56 Mpc, 1″ (=1 CALIFA spaxel) corresponds to 270 pc. With an r-band absolute magnitude of -21.17, $u - r = 2.18$ and $g - r = 0.54$ colors, and concentration index $C = 2.16$, NGC 2916 can be characterized as a blue-disk galaxy with an intermediate mass ($\sim 10^{11}$ $M_\odot$). Rudnick et al. (2000) have shown that the galaxy presents some degree of lopsidedness, indicating a weak interaction (possibly with its irregular satellite 5′ away, Gutiérrez et al. 2002) or a minor merger. Moorthy & Holtzman (2006) have obtained long-slit spectra and measured emission lines and Lick indices along the position angle PA $= -80°$. They found that the nuclear spectrum is well within the AGN wing of the [O]/Hβ vs. [N]/Hα diagram, in a location close to what is now accepted as borderline between Seyferts and LINERs (Kewley et al. 2006).

Our Voronoi binning of the CALIFA datacube produces $N = 1638$ zones. The corresponding $N + 1$ spectra (the $+1$ corresponding to the spatially integrated spectrum) were fitted with   and the results feed into PyCASSO. The following subsections describe how we handled the data and the products of the analysis.

5.1. Fit quality assessment

As with 1D spectra, the quality of the spectral fits should be examined before proceeding to interpretation of the results. This subsection describes some standard methods to do this, the caveats involved and strategies to circumvent them.

Figure 3a shows the map of the fit quality indicator

$$\overline{\Delta} = \frac{1}{N_\lambda^{\text{eff}}} \sum_\lambda \frac{|O_\lambda - M_\lambda|}{M_\lambda}, \tag{6}$$

where O_λ and M_λ are the observed and model spectra, respectively, and the sum is carried over the N_λ^{eff} wavelengths actually used in the fit, i.e., discarding masked, flagged, and clipped pixels[4]. For this galaxy $\overline{\Delta}$ spans the range between 1.0 and 5.6%, with a median value of 3.0%. It increases towards the outer regions, where the S/N is smaller (Fig. 1c). The $\chi^2 = \sum w_\lambda^2 (O_\lambda - M_\lambda)^2$ map (Fig. 3b) shows the opposite behavior, since the errors also increase outwards. Because of its non-explicit reliance on the (often hard to compute, if not altogether unavailable) ϵ_λ spectrum, and because of its easily grasped meaning, $\overline{\Delta}$ is a more useful figure of merit to assess fit quality.

Inspection of the highest $\overline{\Delta}$ spectra often reveals non-masked emission lines or artifacts, like imperfect masking of foreground sources, slightly misplaced b_λ flags, or O_λ values that should have been clipped by   but were not because of large ϵ_λ. We emphasize that such bugs are very rare in CALIFA. The median $\overline{\Delta}$ for the $\sim 10^5$ zone spectra analyzed so far is just 4% (corresponding to an equivalent S/N of 25), and in less than 2% of the cases $\overline{\Delta}$ exceeds 10%. This high rate of success is mainly due to the carefully derived errors and flags in the reduction pipeline and further refined in our pre-processing steps (Sect. 3).

---

[4] We note that Eq. (6) is nearly, but not exactly, identical to what is called "adev" in   's output, the difference being the use of M_λ instead of O_λ in the denominator. This avoids faulty (but not flagged) O_λ entries with very low flux affecting the statistics. This rarely occurs in CALIFA, and when it does the pixels invariably have large errors and so are irrelevant for the fit. They can, however, affect the value of $\overline{\Delta}$.
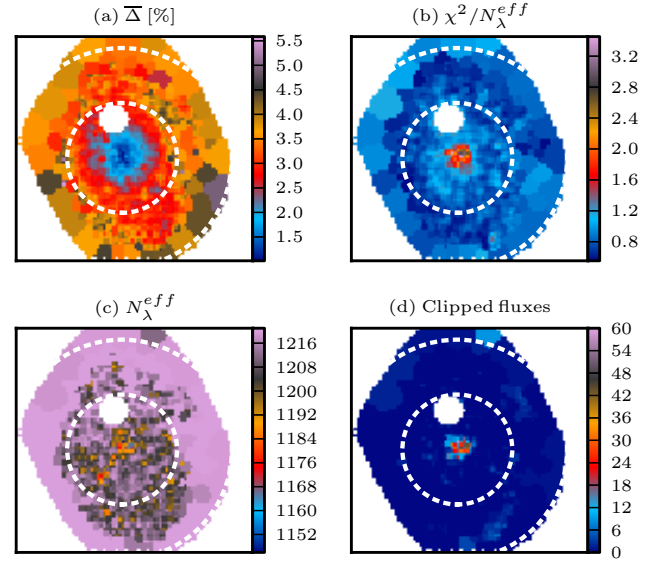
Fig. 3. Maps of spectral-fit quality indicators. **a)** Mean relative deviation $\overline{\Delta}$; **b)** χ^2 per fitted flux; **c)** number of fluxes used in the fit; and **d)** number of clipped fluxes.

One can use such maps to define spatial masks over which the spectral fits satisfy some quality threshold. Experiments with the whole data set suggest that a reasonable quality-control limit should be in the $\overline{\Delta} = 8$ to 10% range. Not surprisingly, the large residuals tend to be located in the outer regions of the galaxies. Generally speaking, results beyond 2–3 HLR should be interpreted with greater care. No $\overline{\Delta}$-based cut is needed for our example galaxy. For the benefit of   users, it is nevertheless worth making some further remarks on quality control.

5.1.1. Subtleties and caveats on quality control

In full spectral fitting methods, seemingly trivial operations like imposing a fit quality threshold often hide subtleties that can easily go unnoticed, particularly when processing tons of data. The paragraphs below (focused on   but extensible to other codes) review some of these.

First, one should distinguish cases where $\overline{\Delta}$ is large because of bad data from those where large residuals arise because of the user's failure to properly inform, through spectral masks (m_λ) or flags (b_λ), spectral regions that should be ignored in the fit. For instance, one can have an excellent spectrum of an HII region with several strong emission lines besides those included in a generic emission line mask feed into   , causing an artificially large $\overline{\Delta}$. Large velocity offsets can have a similar effect, as emission lines get shifted out of fixed m_λ windows. Similarly, sky residuals and other artefacts missed out by the b_λ flags lead to large $\overline{\Delta}$, even when the overall spectrum is good. In short, not everything that fails a blind quality control is actually bad.

The clipping options implemented in   help spot pixels that are too hard to fit and thus probably represent non-stellar or spurious features. Our fits use the "NSIGMA" clipping method and a conservative 4σ threshold, meaning that we only clip pixels when $|O_\lambda - M_\lambda| > 4\epsilon_\lambda$. Figure 3c maps the number of clipped points in CALIFA 277. One sees a peak in the central pixels, where the S/N is so high that our 4σ clipping does not forgive even small $O_\lambda - M_\lambda$ deviations (most often associated
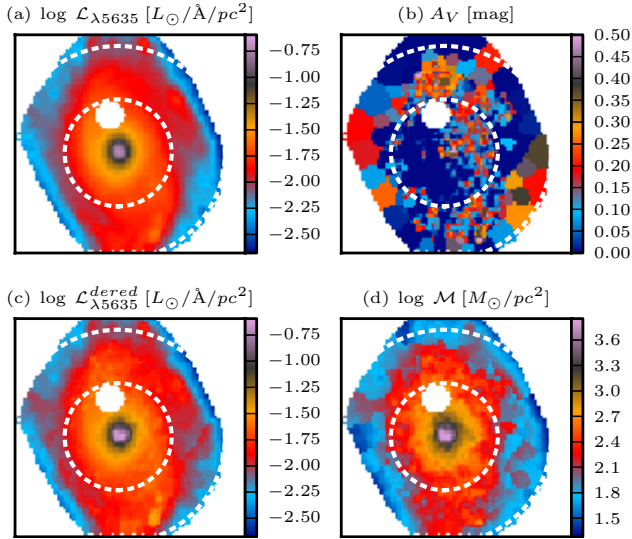
Fig. 4. **a)** Synthetic surface brightness at 5635 Å; **b)** stellar extinction map (A_V); **c)** dereddened $\mathcal{L}_{\lambda 5635}$ image; **d)** stellar mass surface density.

with problems with the base models rather than with the data). Elsewhere, very few pixels were clipped. The point to highlight here is that clipping only worked because we have a reliable ϵ_λ. Other clipping methods can be used when this is not the case, but in all cases the user should always carefully check the output, as it may easily happen that too many points are clipped.

Custom-made spectral masks also help. For instance, since Mateus et al. 2006), the   analysis of SDSS spectra employs individual masks constructed by searching for emission lines in the $O_\lambda - M_\lambda$ residual spectrum obtained from a first fit, and taking into consideration the local noise level. O_λ is then refitted with this tailor-made m_λ, circumventing some of the issues above. This refinement has not yet been implemented for CALIFA.

Errors, flags, and masks are, of course, secondary actors in any spectral synthesis analysis, but these general remarks illustrate that it is worthwhile to pay attention to them.

5.2. 2D maps: stellar light, mass, and extinction

One of the main products of spectral synthesis is to convert light to mass. Figure 4 illustrates the results for CALIFA 277. Its top-left panel shows the surface density of the luminosity at $\lambda_N = 5635$ Å, while the top-right panel show the derived extinction map. The dust corrected image and the mass surface density are also shown.

While the effects of the Voronoi binning are present in all panels, they are much more salient in the A_V map. This is because the light and mass images were *"dezonified"* by scaling the value at each xy spaxel by its fractional contribution to the total flux in a zone (z). For instance, for the mass surface density ($\mathcal{M}$) this operation reads

$$\mathcal{M}_{xy} = \frac{M_{xy}}{A_{xy}} = \frac{M_z}{A_z} \times w_{xyz}, \tag{7}$$

where A_{xy} (A_z) denotes the area in a spaxel (zone), and

$$w_{xyz} = \frac{F_{xy}}{\sum_{xy|z} F_{xy}}, \tag{8}$$

with F_{xy} as the mean flux in the 5635 ± 45 Å region, the same used in the Voronoi zoning (Sect. 3). This operation was applied
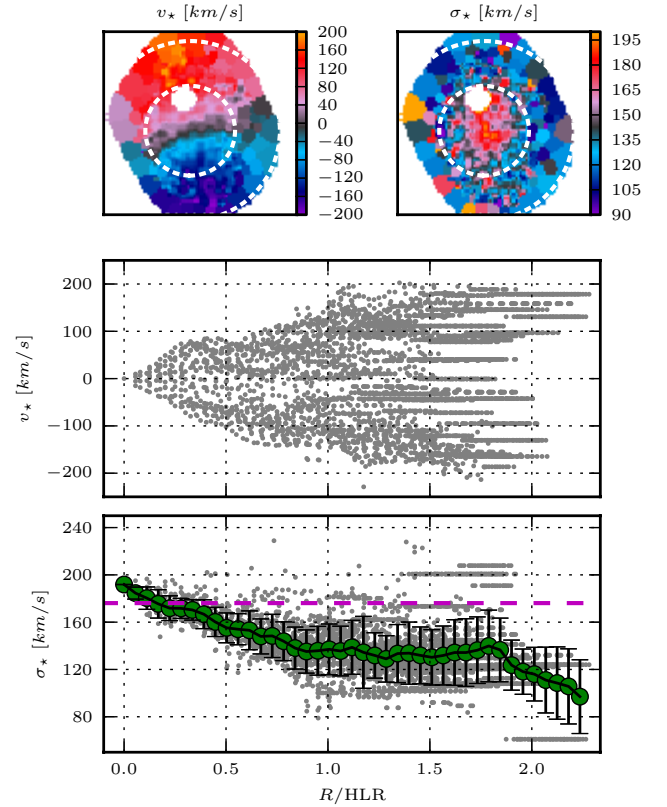
Fig. 5. Kinematical products of the spectral fitting. The $\sigma_\star$ values are *not* corrected for instrumental broadening, which dominates below 140 km s^{-1}. The horizontal stripes in the position-velocity and $\sigma_\star(R)$ panels correspond to Voronoi zones.

to luminosity and mass related quantities, producing somewhat smoother images than obtained with $w_{xyz} = 1$. Intensive properties (like A_V, mean ages, $\sigma_\star$), however, cannot be dezonified.

The stellar extinction map shows low values of A_V (of order 0.1−0.2 mag), with slight enhancements in the nuclear region and the arms. Overall, however, there is relatively little variation across the face of the galaxy (see also Fig. 10). The light and mass images have a similar structure, both showing the bulge at $R \lesssim 0.5$ HLR, and the disk beyond that. The spiral arms are less prominent in terms of mass than in light because of the higher L/M of stars in the arms.

The total stellar mass obtained from the sum of the zone masses is $M = 6.5 \times 10^{10}\ M_\odot$. This is the mass locked in stars nowadays. Counting also the mass returned by stars to the interstellar medium, $M' = 9.0 \times 10^{10}\ M_\odot$ were involved in star formation. These values ignore the mass in the masked region around the foreground star northeast of the nucleus. PyCASSO can fill in such holes with values estimated from (circular or elliptical) radial profiles. For CALIFA 277, this correction increases the masses quote above by 4%.

5.3. 2D maps: kinematics

Figure 5 shows the $v_\star$ and $\sigma_\star$ fields estimated by   , as well as a position-velocity diagram and a radially averaged $\sigma_\star$ profile. The $v_\star$ field indicates a projected rotation velocity of ~200 km s^{-1}. The V500 resolution prevents the determination of $\sigma_\star$ values below ~150 km s^{-1}, and the flat $\sigma_\star(R)$ profile beyond ~0.7 HLR reflects this resolution limit (we have not corrected the values for the instrumental resolution in this plot).
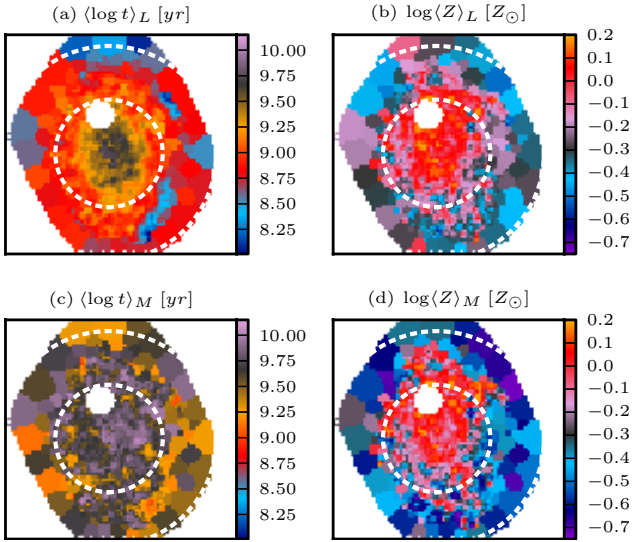
Fig. 6. Luminosity (*top*) and mass (*bottom*) weighted mean age (*left*) and metallicity (*right*) maps for CALIFA 277.

Only in the inner regions are the $\sigma_\star$ values reliable, reaching 200 km s^{-1} in the nucleus (equivalent to 140 km s^{-1} after correcting for instrumental broadening).

The kinematical information derived from our analysis will be superseded by studies based on the higher spectral resolution V1200 datacubes (Falcón-Barroso et al., in prep.). Eventually, one can envisage feeding the parameters derived from these more precise analyses back into the ⟨STARLIGHT⟩ fits (using its fixed-kinematics mode). In fact, this feedback may well turn out to improve our stellar population analysis, given the potential degeneracy between $\sigma_\star$ and Z (decreasing the former while increasing the latter has the same global effect of making metal lines deeper; Koleva et al. 2009; Sánchez-Blázquez et al. 2011).

5.4. 2D maps: mean ages and metallicities

The crudest way to quantify the SFH of a system is to compress the age and metallicity distributions encoded in the population vectors to their first moments. For this purpose we will use the following definitions:

$$\langle \log t \rangle_L = \sum_{t,Z} x_{tZ} \log t \qquad (9)$$

$$\langle Z \rangle_L = \sum_{t,Z} x_{tZ} Z, \qquad (10)$$

where x_{tZ} is the fraction of light at λ_N due to the base population with age t and metallicity Z. The mass-weighted versions of these indicators, $\langle \log t \rangle_M$ and $\langle Z \rangle_M$, are obtained by replacing x_{tZ} by the mass fraction μ_{tZ}.

Figure 6 shows the light and mass-weighted mean (log) age and metallicity maps. The $\langle \log t \rangle_L$ image shows a steady increase towards the center. Outside 1 HLR, traces of the spiral arms are noticeable as regions of lower age (as in the SDSS color image in Fig. 1a, the arms are brighter in the western half of the image). Because of the large weight of old populations, $\langle \log t \rangle_M$ spans a smaller dynamical range than $\langle \log t \rangle_L$, hence producing lower contrast maps, but the outwardly decreasing age is still visible. Negative gradients are also clearly present in metallicity, with indications of flattening within the bulge region. As in
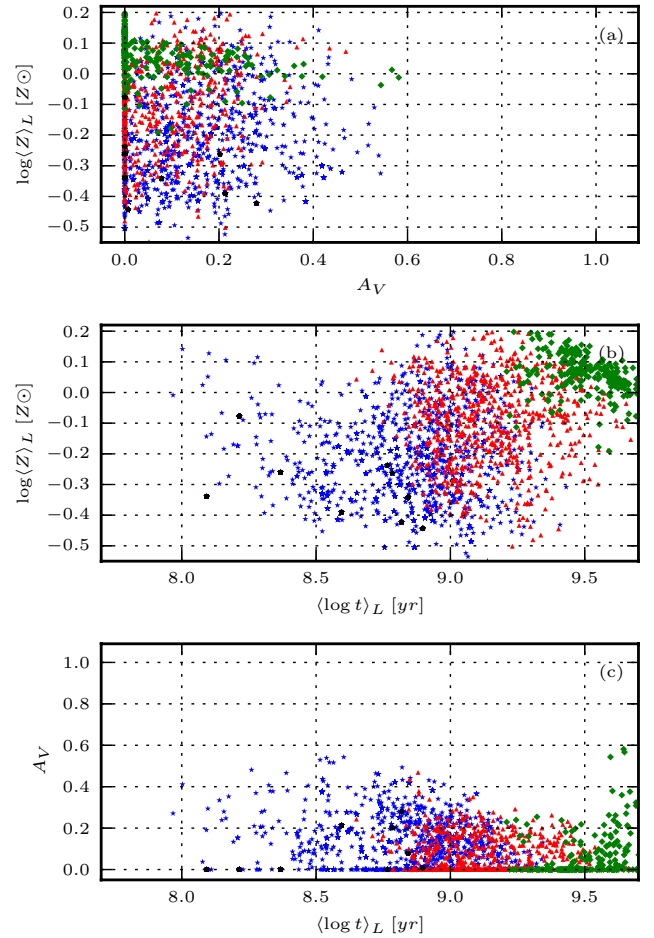
Fig. 7. Mean age versus mean metallicity versus extinction, coding zones by their distance to the nucleus. Green diamonds: $R < 0.5$ HLR. Red triangles: $0.5-1$ HLR. Blue stars: $1-2$ HLR. Black dots: > 2 HLR.

other 2D maps, the small-scale fluctuations towards the edges are at least in part due to the lower S/N.

The fact that t and Z grow in the same sense suggests that the results are not badly affected by the age-metallicity degeneracy. As shown by Sánchez-Blázquez et al. (2011), full spectral synthesis is much less sensitive to this than conventional index-based approaches. Figure 7 plots extinction versus mean age versus metallicity, the main properties involved in spectral synthesis. Points are color- and symbol-coded by their distance from the nucleus. One sees that the highest values of A_V are found for old central ($R < 0.5$ HLR) and young outer ($R > 1$ HLR) populations and that A_V bears no correlation with Z. The middle panel shows the positive $t-Z$ relation inferred from the 2D maps. Within 0.5 HLR (green diamonds), however, t anticorrelates with Z, most likely due to the age-metallicity degeneracy. The mean Z values in this central region straddle 1 and 1.5 $Z_\odot$, the two highest metallicities in our base.

5.5. 2D maps: x_Y, x_I, x_O

Population synthesis studies in the past found that a useful way to summarize the SFH is to condense the age distribution encoded in the population vector into age ranges. This strategy comes from a time when the analysis was based on equivalent widths and colors (Bica 1988; Bica et al. 1994; Cid Fernandes et al. 2001, 2003), but it was also applied to full spectral fits (Gonzalez Delgado et al. 2004).

(a) x_Y [%]

(b) x_I [%]

(c) x_O [%]
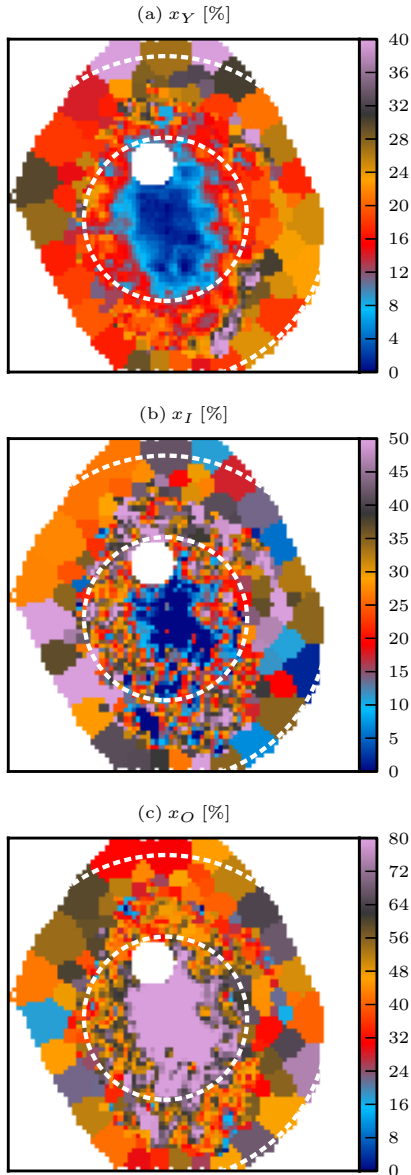
Fig. 8. Maps of the percentage contribution of young ($t < 0.14$ Gyr), intermediate age ($0.14-1.4$ Gyr), and old (>1.4 Gyr) stars to the observed light at 5635 Å.

Figure 8 presents images of the light fraction due to young, intermediate and old populations (x_Y, x_I, and x_O), defined as those with $t \leq 0.14$, $0.14 < t \leq 1.4$, and $t > 1.4$ Gyr, respectively. As usual, the choice of borderlines is somewhat subjective, constrained only by the underlying idea of grouping base elements covering relatively wide age ranges. For the base used in our   runs, the Y, I, and O bins contain 4×20, 4×10, and 4×9 SSPs, respectively (where the $4\times$ comes from the four metallicities).

The plots show that the spiral arms stand out more clearly in the x_Y map, specially in the western half of the galaxy, as also seen in the SDSS color composite (Fig. 1a). Very little of the light from $R < 1$ HLR comes from young stars. Intermediate age populations do contribute more, but the central ~0.5 HLR is completely dominated by old stars. Overall, however, despite the added informational content, these maps do not visibly add much to the $\langle \log t \rangle_L$ image (Fig. 6).

5.6. 2D maps: Star formation rates and IFS-based variations over Scalo's b parameter

The base used in our fits comprises instantaneous bursts (i.e., SSPs). Thus, despite the large number of ages considered, our SFHs are not continuous and hence not derivable. Nonetheless, there are ways of defining star formation rates (SFR).

The simplest way to estimate a SFR is to cumulate all the stellar mass formed since a lookback time of t_{SF} and perform a mass-over-time average:

$$\overline{\mathcal{SFR}}_{xy}(t_{SF}) = \frac{1}{t_{SF}} \sum_{t < t_{SF}} \mathcal{M}'_{txy}, \qquad (11)$$

where $\mathcal{M}'_{txy}$ is the mass (at xy and per unit area) of stars formed at lookback time t [5]. Equation (11) gives the *mean* SFR surface density since $t = t_{SF}$. One can tune t_{SF} to reach different depths in the past, but as t_{SF} increases this estimator becomes increasingly useless, converging to the mass density divided by $t_\infty \equiv 14$ Gyr (the largest age in the base).

It is often more useful to consider SFRs in relation to some fiducial value instead of absolute units. The classical example is Scalo's birthrate parameter, b, which measures the SFR in the recent past ($t < t_{SF}$) with respect to its average over the whole lifetime of the system [6]. This is trivially obtained dividing $\overline{\mathcal{SFR}}_{xy}(t_{SF})$ by its asymptotic value

$$b_{xy}^{loc}(t_{SF}) = \frac{\overline{\mathcal{SFR}}_{xy}(t_{SF})}{\overline{\mathcal{SFR}}_{xy}(t_\infty)} = \frac{t_\infty}{t_{SF}} \frac{\sum_{t < t_{SF}} \mathcal{M}'_{txy}}{\mathcal{M}'_{xy}}. \qquad (12)$$

The superscript "loc" is to emphasize that the reference lifetime average SFR is that of the same spatial location xy. One should recall that while young stars in a spaxel were probably born there (or near it), old ones may have migrated from different regions. Thus, despite the identical definitions, the physical meaning of b_{xy}^{loc} is not really the same as for galaxies as a whole.

The IFS data allow for other definitions of b. For instance, one might prefer to compare $\overline{\mathcal{SFR}}_{xy}(t_{SF})$ to the $\overline{\mathcal{SFR}}(t_\infty)$ of the galaxy as a whole, the bulge, the disk, or any general region. This variation measures the "present" ($t < t_{SF}$) "here" (at xy) to the "past" ($t \leq t_\infty$) in a spatial region $\mathcal{R}$:

$$b_{xy}^{\mathcal{R}}(t_{SF}) = \frac{\overline{\mathcal{SFR}}_{xy}(t_{SF})}{\overline{\mathcal{SFR}}_{\mathcal{R}}(t_\infty)}. \qquad (13)$$

A formally similar but conceptually different definition is obtained using for the reference value in the denominator the SFR surface density within the *same time-scale* but evaluated in a *different region*:

$$c_{xy}^{\mathcal{R}}(t_{SF}) = \frac{\overline{\mathcal{SFR}}_{xy}(t_{SF})}{\overline{\mathcal{SFR}}_{\mathcal{R}}(t_{SF})}, \qquad (14)$$

i.e., to compare not "now versus then" but "now here versus now there". Together with Eqs. (12) and (13), this definition covers

---

[5] The stellar mass in this equation differs from that in Eq. (7), Fig. 4, and the definitions of $\langle \log t \rangle_M$ and $\langle Z \rangle_M$. The latter are corrected by the mass returned to the medium by stars during their evolution (thus reflecting the mass currently in stars), while in the computation of SFRs this correction should not be applied. We distinguish the two types of stellar masses with the prime superscript ($\mathcal{M}$ versus $\mathcal{M}'$).

[6] A related index is the so-called specific SFR, which differs from b just by the t_∞ factor in Eq. (12).
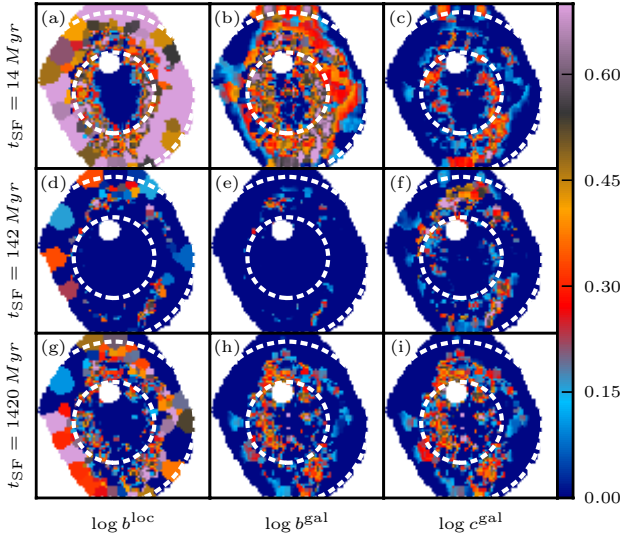
Fig. 9. Spatially resolved SFR surface density (Eq. (11)) on the last t_{SF} = 14 (*top*), 142 (*middle*), and 1420 (*bottom*) Myr in units of different reference values. The *left panels* compare $\overline{SFR}_{xy}(t_{SF})$ to $\overline{SFR}_{xy}(t_{\infty})$, i.e., the all-times average at xy, thus providing a local version of Scalo's b parameter (Eq. (12)). *Middle panels* compare the local $\overline{SFR}$ to the all-times average over the whole galaxy (Eq. (13)). *Panels on the right* compare $\overline{SFR}$ to that of the galaxy as a whole over *the same time scale* (Eq. (14)). All images are on log scale from log 1 to log 5, such that only $\overline{SFR}_{xy}(t_{SF})$ values above the corresponding reference value are visible.

the different combinations of time and space enabled by the application of fossil methods to IFS data.

Figure 9 shows maps of b^{loc} (left panels), $b^{\mathcal{R}}$ (middle panels), and $c^{\mathcal{R}}$ (right panels) for three values of t_{SF}: 14 (top), 142 (middle), and 1420 Myr (bottom). In all panels the color scale is deliberately saturated to highlight regions where $\overline{SFR}(t_{SF})$ is larger than the chosen reference value; the dynamical range of the images goes from 1 to 5 (0 to 0.7 in log) in the corresponding relative units.

Panel a shows that spaxels that have formed stars over the past 14 Myr at a larger rate than their respective past average are all located in the outer regions. Nowhere within $R \lesssim 0.5$ HLR does one find $b^{loc}(14$ Myr$) > 1$. Considering the past 142 Myr (panel d), the inner "deficit" covers as much as 1.2 HLR. On the longest time scale considered (g), one again sees that the inner spaxels have been less active than their lifelong average.

Maps look considerably different in the middle column of panels, where the local $\overline{SFR}$ is normalized to the past average over the *whole galaxy* (Eq. (13)). The spiral arms of CALIFA 277 appear better delineated in $b^{gal}(14$ Myr$)$ (panel b) than in any b^{loc} map. Interestingly, the b^{gal} map is practically featureless for t_{SF} = 142 Myr (e). This suggests that starformation is not continuous over this time scale but instead happens in a bursty mode. Over the past 1.4 Gyr (h), one again sees traces of the arms but with a lower amplitude than in panel b, which is qualitatively consistent with the cumulative effect of an intermittent sequence of short-duration bursts. (Due to the logarithmic age resolution of fossil methods, such short bursts can only be recognized as such at the very young ages sampled in panel b.)

The right column panels show our novel relative SFR index c (Eq. (14)), using the whole galaxy as reference region. Unlike Scalo's b, this index does not compare present to past, but present to present elsewhere. Its 2D maps can be understood as "snapshots" of the SFR in the galaxy taken with an

"exposure time" t_{SF}. Keeping the "diaphragm" open for only the last 14 Myr (panel c) highlights the ongoing starformation in the galaxy. The spiral arms are clearly visible, and the structures are more focused than in the $b^{gal}(14$ Myr$)$ map (panel b). Integrating for 142 Myr (f), the inner parts of the arms fade, but their outer ($R > 1$ HLR) parts brighten up in terms of c^{gal}. Over the past 142 Myr, these regions have formed more stars than anywhere else in the galaxy, even though a comparison with panel e shows that only parts of the $c^{gal} > 1$ regions are forming stars at a rate per unit area larger than that of the galaxy as a whole through its entire life (i.e., $b^{gal} > 1$). For t_{SF} = 1.4 Gyr (panel i) the image becomes more blurred. Because of the long time scale, the $c^{gal}(1.4$ Gyr$)$ map is nearly indistinguishable from that obtained with b^{gal} for the same t_{SF} (panel h).

One thus sees that, despite some degree of redundancy (the numerator is always the same), these definitions offer different and complementary views of star formation in a galaxy.

5.7. 1D spatial maps: radial profiles

The information contained in 2D maps like the ones shown above can sometimes be hard to absorb. Azimuthal averaging is a useful way to compress and help digest 2D data. PyCASSO provides both circular and elliptical xy-to-R conversion tensors. The examples below are based on a circular mapping.

For quantities like $\mathcal{M}$, one can think of two types of radial averaging. The first is to add up all the stellar mass in xy spaxels within a given R-bin and then divide by the bin area (counting only non-empty spaxels). The second is to average the surface density values for each spaxel directly. The same applies to, for instance, $\langle \log t \rangle_L$ (Eq. (9)): one can either add up the value of product $L_{txy} \times \log t$ for all spaxels at a given R and then divide by the corresponding $\sum L_{xy}$ or else simply average the $\langle \log t \rangle_L$ values for each spaxel in the R-bin. The first method, which we call *area averaging*, effectively collapses the galaxy to 1D, but this kind of averaging cannot be applied to quantities which do not involve light or mass, like A_V and $\sigma_\star$. For the sake of uniformity, in this subsection we chose the second type of radial averaging (henceforth *spaxel averaging*), noting that the two methods almost always give nearly identical results.

Figure 10 shows several PyCASSO products as a function of R. The grey points represent values for individual spaxels. The solid line and green circles show the mean value of the plotted quantity among the spaxels in the same R bin, and the error bars map the corresponding dispersion. (As discussed in Paper II, actual error bars in radial profiles are much smaller due to the large number statistics.) Several of the features discussed while describing the 2D images are clearly seen in these plots. The $\langle \log t \rangle$ and $\langle Z \rangle$ gradients, in particular, are cleanly depicted in these plots. As pointed out in Sect. 5.4, mean ages and metallicities increase ~simultaneously towards the nucleus, while A_V does not change much. This indicates that the classical degeneracies in stellar population studies do not play a strong role in shaping the results, with the possible exception of the central regions. As in Fig. 5, horizontal stripes of gray points in panels c, e, f, g, and h of Fig. 10 correspond to spaxels in the same Voronoi zones. The stripes disappear in panels a, b, and d because these extensive quantities were "dezonified" (cf. Eq. (7)).

5.8. 1D temporal maps: evolutionary curves

The main power of fossil record methods is to open the time domain, allowing evolutionary studies. The caveat is that it
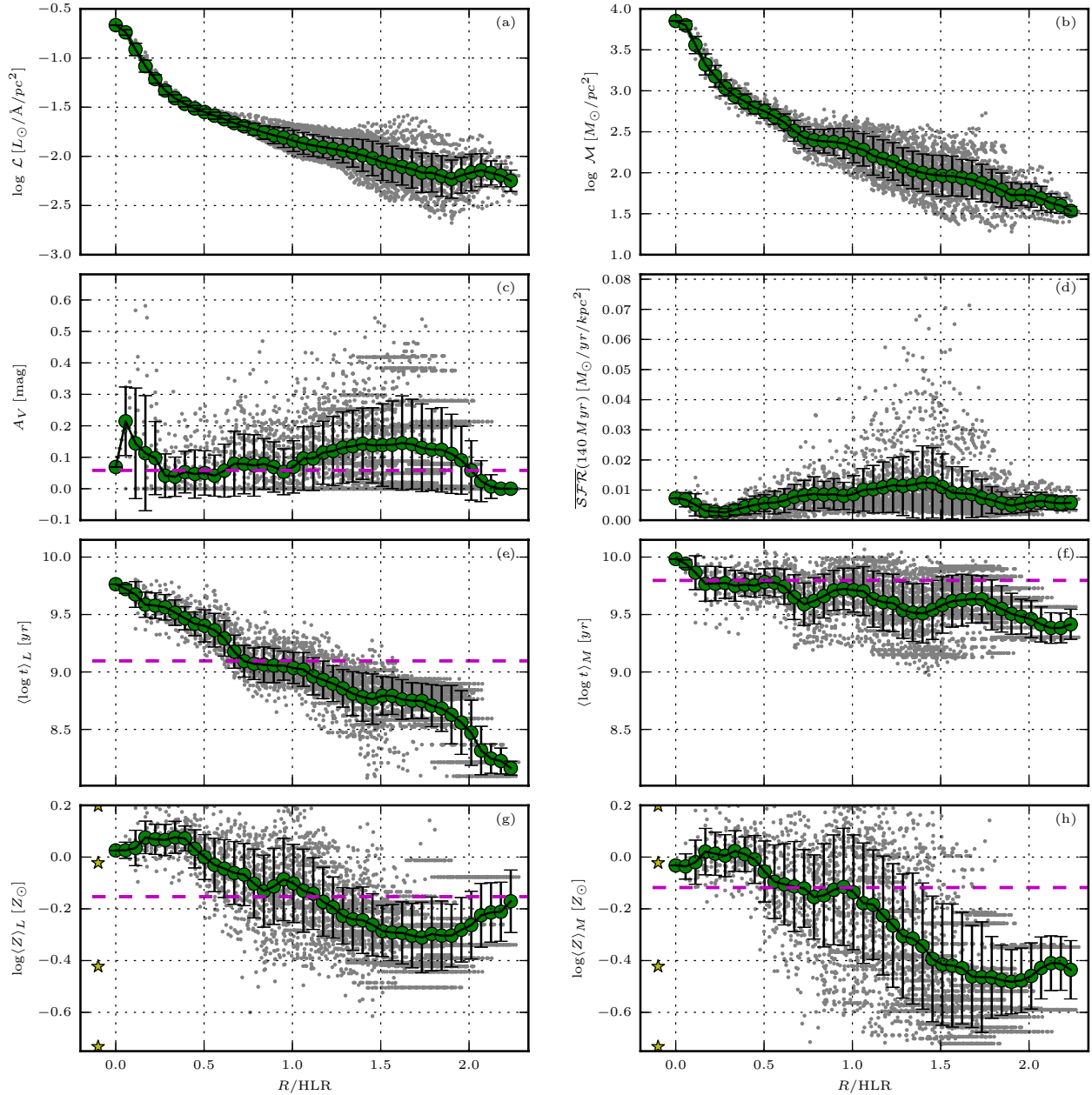
Fig. 10. Radial profiles of several properties. Grey points correspond to values in individual *xy* spaxels. The green circles and solid lines represent the average of the plotted quantity, while the error bars represent the dispersion in the *R*-bin. The dashed magenta horizontal line (only in the plots not involving surface densities) marks the value derived from the   analysis of the integrated spectrum, i.e., collapsing the *xy* dimensions of the datacube. The stars in the *bottom panels* mark the four metallicities in the base models.

does this with the typical logarithmic resolution inherent to stellar evolution, but several studies show that much can be learned about galaxy evolution despite this fundamental constraint. Because our 39 ages base is highly overdimensioned, some sort of SFH compression is necessary. As discussed by Asari et al. (2007), age resolutions between 0.5 and 1 dex are reasonable. We thus smooth the light and mass population vectors with a Gaussian of *FWHM* = 0.5 dex in log *t*.

Figure 11 plots a number of our synthesis products against age. To keep an at least partial representation of the spatial information, we plot evolutionary curves derived for different radial regions: the nucleus, defined as the central pixel (plotted in grey dashed lines), $R \leq 0.5$ (dashed green), ≤ 1 (solid red), and >1 HLR (solid blue).

The top panels show the growth of luminosity (Fig. 11a) and mass (b)[7]. Among other things, this plot illustrates the difference between light and mass, in the sense that regions inside and outside $R = 1$ HLR do not have the same mass, despite having (by definition) the same light. While HLR = 4.8 kpc, the radius containing half of the mass is 3.4 kpc. This is a direct consequence of the stellar population gradients in this galaxy. González Delgado et al. (in prep.) investigate the relation between light- and mass-based radii for different types of galaxies.

It is also seen that both light and mass grow at *different speeds for different regions*. This is better appreciated in panels c

---

[7] For clarity, the cumulative mass is computed with the total mass that has participated in star formation, instead of the one corrected for returned mass. In other words, we cumulate M' instead of M.
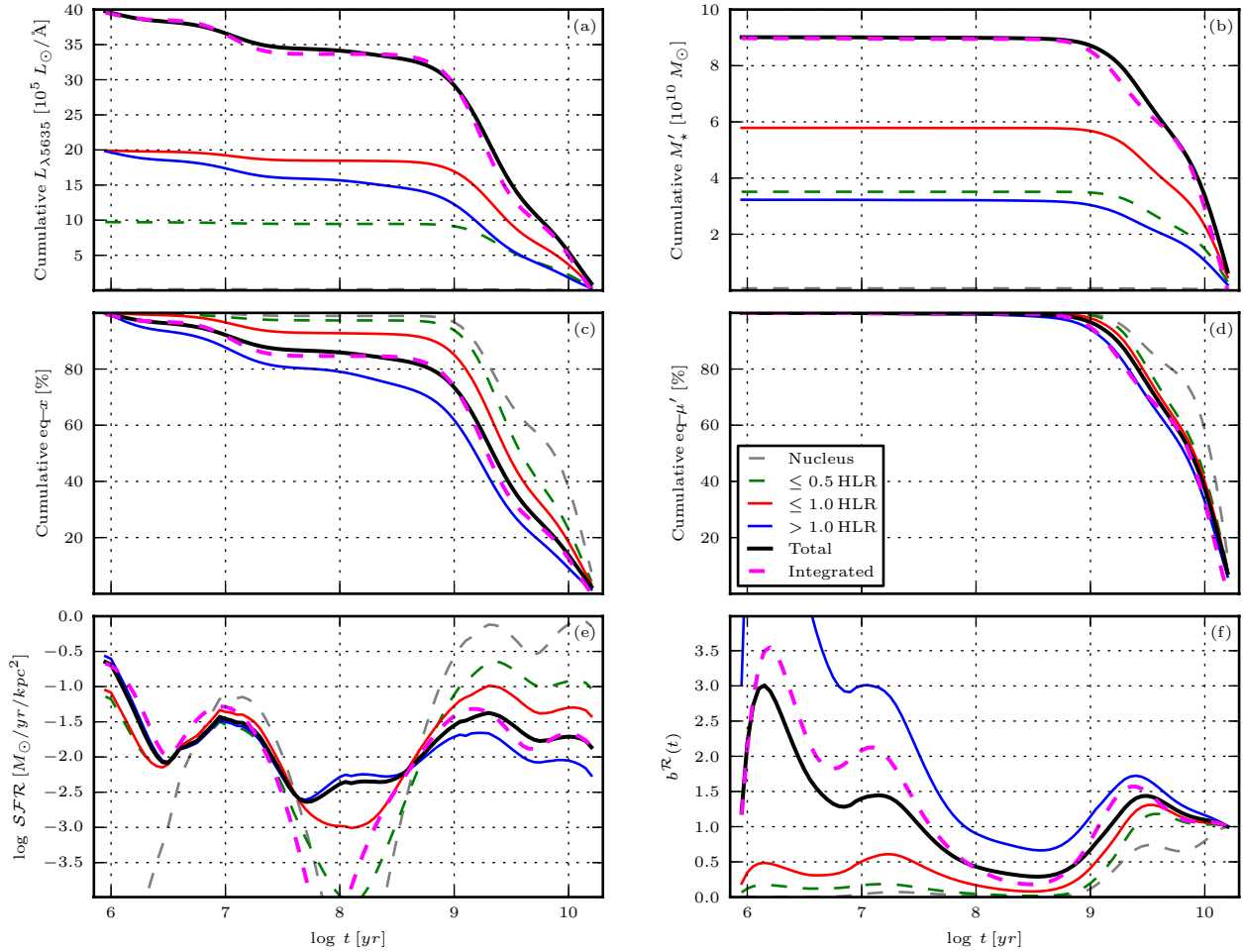
Fig. 11. Time evolution of light and mass representations of the SFH, as derived from the   fits. The discrete x_{tZxy} and μ'_{tZxy} population vectors involved in these curves were smoothed in $\log t$, marginalized in Z, and integrated over the spatial regions indicated. Dotted grey lines indicate the nucleus (central pixel). Green, red, and blue lines correspond to $R \leq 0.5$ HLR, $R \leq 1$ HLR, and $R > 1$ HLR regions, respectively. The black line represents the whole galaxy evolution as reconstructed from the sum of its parts, while (as in Fig. 10) the magenta dashed line is used to represent the results obtained for the spatially integrated spectrum.

and d, where each growth curve is plotted on a 0 to 1 scale, with 1 representing the present values (which tantamounts to cumulating the equivalent x_t and μ'_t vectors for each region). The nucleus reached 80% of its mass at $t = 8.5$ Gyr, while the $R > 1$ HLR region did so later, at $t = 1.9$ Gyr. As shown by Pérez et al. (2013), this inside-out ordering of the mass assembly history applies to essentially all massive galaxies.

Figure 11e shows $\mathcal{SFR}(t)$. The SFR per unit area decreases from the nucleus outwards most of the time, but the trend is reversed in the last ~500 Myr. Notice that, because of the smoothing, $\mathcal{SFR}(t)$ is now a continuous function of time, so that this panel represents the *instantaneous* SFR, as opposed to the mass-over-time definition in Eq. (11). Figure 11f shows Scalos's b parameter for each region, which does use the running mean $\overline{\mathcal{SFR}}(t)$ of Eq. (11). This plot helps interpret Fig. 9, which opens up the radial regions into full 2D maps but compress the time axis by stipulating fixed t_{SF} time scales.

5.9. The whole versus the sum of the parts

One of the applications of CALIFA is to assess the effects of the lack of spatially resolved information on the derivation of physical properties and SFHs from integrated-spectra surveys. The horizontal dashed magenta lines in Fig. 10 illustrate this point.

They represent the results obtained from the analysis of the spectrum of the datacube *as a whole*, that is, adding up all spaxels to emulate an integrated spectrum. Qualitatively, one expects that this should produce properties typical of the galaxy zones as a whole. This expectation is borne out in Fig. 10, where one sees that the extinction, mean ages, and metallicities marked by the dashed magenta line represent an overall average of the spatially resolved values. In this particular example, they all match quite well the values at 1 HLR. The stellar masses obtained from the whole and the sum of the parts are also in excellent agreement, differing by just 1%. Similarly, galaxy-wide luminosity and mass-weighted mean ages and metallicities computed in these two ways agree to within 0.05 dex.

But can one derive the SFH of a galaxy out of an integrated spectrum? Figure 11 says that, at least in CALIFA 277, the answer is yes. The dashed magenta and the black solid lines are very similar in all panels of this figure. As before, the former represents the results obtained from the analysis of the spatially compressed datacube, while the black curves are computed adding the   results for each spaxel. We are thus comparing the whole against the sum of the parts, and they match.

This may seem a trivial result, but it is not. Formally, one only expects this to happen if A_V is the same at all positions, a condition which is approximately met in CALIFA 277. In
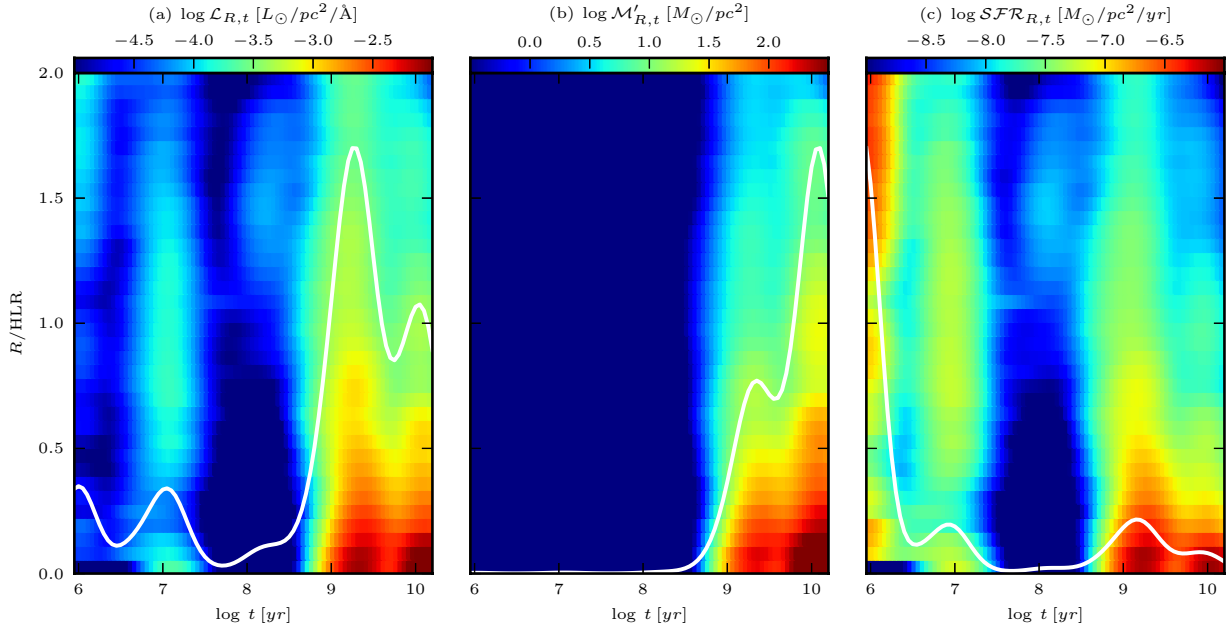
Fig. 12. R–t diagrams showing the radially averaged distribution of light, mass, and SFR as a function distance from the nucleus and age. *Left*: luminosity at $\lambda = 5635$ Å per unit area. ($\mathcal{L}_{R,t}$). *Middle*: stellar mass formed per unit area ($\mathcal{M}'_{R,t}$). *Right*: time-dependent SFR per unit area ($\mathcal{SFR}$). The solid (white) lines represent the sum over all spaxels for a given age.

objects where dust has strong spatial variations, the spectral fitting of the global spectrum with a single A_V will inevitably operate compensations among the parameters, like increasing the age to compensate for an underestimated A_V and viceversa. Also, the combined effects of population gradients and kinematics (e.g., disk population contributing more to the wings of absorption lines than the ones from the bulge) are hard to predict. Since we are presenting results for a single example galaxy, it remains to be seen how general this "coincidence" is.

5.10. Space × time diagrams: SFHs in 2D

One of the main challenges involved in the analysis of the multidimensional data built from the combination of the spatial dimensions with the t and Z dimensions opened by population synthesis is how to visualize the results. All examples shown so far project (or average over) two or more of these axes.

Figure 12 shows an attempt to visualize galaxy evolution as a function of both space and time. The trick is to compress xy into R and collapse the Z axis, producing a radially averaged SFH(R, t) map. The left panel shows the luminosity density $\mathcal{L}$ at each radial position R and for each age t. As for the other panels in this figure, the original $\mathcal{L}_{tZyx}$ array from which this map was derived was smoothed in $\log t$, marginalized over Z, and collapsed into one spatial dimension. Unlike in Fig. 10, we now use the area-averaging method discussed in Sect. 5.7, but the results do not depend strongly on this choice.

The $\mathcal{L}_{R,t}$ diagram shows that the light from old stars is concentrated in the bulge, while the youngest stars shine at all R. Also, $t \gtrsim 1$ Gyr stars are more smoothly distributed in age in the disk than in the bulge, where they are concentrated in two populations, one at ~2.5 Gyr and the other older than 10 Gyr. Figure 12b shows the formed stellar mass surface density as a function of R and t. As usual, due to the highly non-linear relation between light and mass in stars, the young populations that show up so well in light practically disappear when seen in mass. Young stars reappear in the right panel, which shows the

evolution in time and space of the SFR surface density. As in Fig. 11g, these are obtained from the instantaneous SFR at each spaxel, computed as in Asari et al. (2007):

$$SFR(t) = \frac{M'_t}{\Delta t} = \frac{\log e}{\Delta \log t} \frac{M'_t}{t}. \tag{15}$$

The age sampling is logarithmic ($\Delta \log t = $ const.), so that the SFR is proportional to the stellar mass formed at t divided by t. The $\mathcal{SFR}_{R,t}$ and $\mathcal{M}'_{R,t}$ diagrams therefore carry the same information; it is the t^{-1} factor that makes them look so different.

When interpreting these or any other plot involving age, one should always keep in mind the logarithmic age resolution. For instance, taken at face value, the spatially integrated SFR of CALIFA 277 in the last few Myr is almost equal to its historical peak, ~2.5 Gyr ago (solid line in Fig. 12c). However, these two peaks span *vastly different time intervals*, roughly by a factor of Gyr/Myr = a thousand. The peak SFR around 2.5 Gyr ago, and indeed even well before that (at >10 Gyr, when most of the mass was formed), were surely higher than the one we are now seeing at a few Myr but cannot be resolved in time. No fossil record method will ever be able to distinguish bursts much shorter than their current age. These limitations are well known in the field, but it is fit to recall them to avoid misinterpretation of the results.

Notwithstanding such age resolution issues, Fig. 12 represents a novel way of looking at galaxies both in time and space. It shows clear evidence in favor of an inside-out growth scenario in which the outer regions assemble their mass at a slower pace and over a more extended period. This behavior is not unique to this galaxy. Pérez et al. (2012) find just the same in a study of the first 105 galaxies observed by CALIFA.

5.11. Space vs. time "snapshots"

To go beyond the R–t diagrams of Fig. 12, one needs more dimensions than a sheet of paper can accommodate. An alternative is shown in Fig. 13, which shows t-slices through the cumulative $\mathcal{M}'_{xyt}$ cube. Unlike the previous diagrams, which compressed the
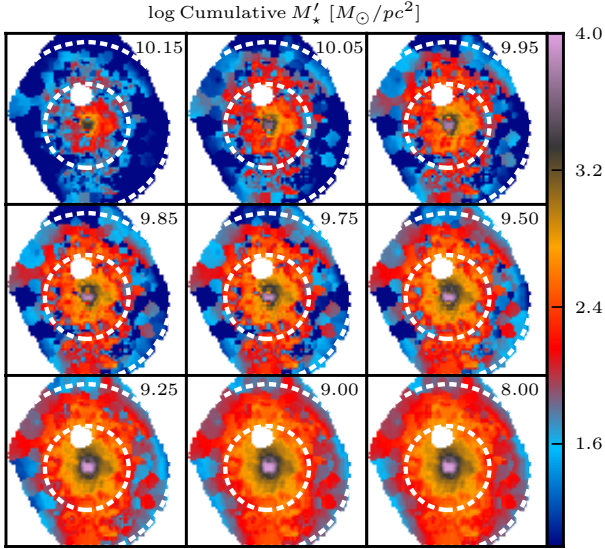
Fig. 13. "Pseudo snapshots" of the cumulative stellar mass surface density of CALIFA 277 at different ages: from $\log t$ [yr] $= 10.15$ to 8 (as labeled in *each panel*).

SFH in one way or another, these plots reveal the full 2D nature of the mass assembly history of CALIFA 277.

Age sequences like those in Fig. 13 can be constructed for several, but not all, properties inferred though   or any other fossil method. One can, for instance, replace mass by intrinsic luminosity, SFR, or stellar metallicity in cumulative or differential form, but it is obviously impossible to reconstruct maps of A_V, $\sigma_\star$, $v_\star$ as a function of t. It is also worth pointing out that the panels in Fig. 13 are *not* truly snapshots of a movie, that is, they are not pictures of the galaxy as it appeared at different look-back times. Instead, these are maps of where stars of a given age t are located nowadays.

Simulators should take notice of these simple facts. IFS data plus fossil methods provide a rich yet inevitably limited form of time travel. Illustrative and beautiful as they are, movies of stars and gas particles moving through time and space will never be directly compared to anything observational. In other words, simulations should be convolved through this "reality filter". The observationally relevant predictions are the distribution of stellar ages and metallicities as a function of xy.

5.12. Emission line maps

Independent of the stellar population applications described throughout this paper, the   fits provide a residual spectrum $R_\lambda = O_\lambda - M_\lambda$ that is, inasmuch as possible, free of stellar light. This is of great aid in the measurement of emission lines and hence in the derivation of a series of diagnostics of warm ISM properties, such as kinematics, nebular extinction, and chemical abundance. The complementarity of nebular and stellar analysis has been amply explored in studies of integrated spectra (e.g., Cid Fernandes et al. 2007; Asari et al. 2007; Pérez-Montero et al. 2010; García-Benito & Pérez-Montero 2012), and the addition of two spatial dimensions to this analysis holds great promise. Kehrig et al. (2012), for instance, combine   analysis and nebular emission to study the impact of post-AGB populations on the ionization of the ISM in early-type galaxies.

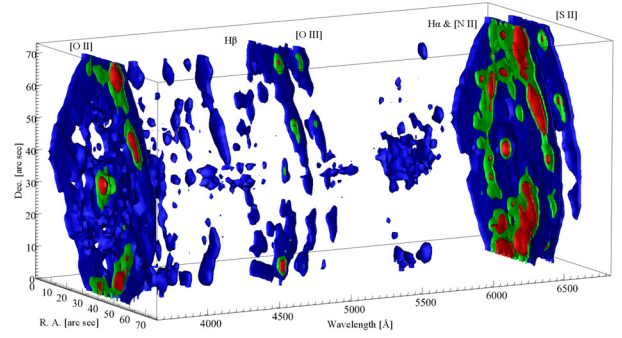Figure 14 shows a $R_{\lambda,xy}$ residuals cube with some of the main emission lines marked. The plot shows that emission lines are

Fig. 14. Residual spectral cube in a 3D rendering.

brighter towards the outside, in particular over the spiral arms, as could be guessed from the distribution of actively starforming regions traced by our SFH analysis (e.g., Fig. 9). Despite its active nucleus, the nuclear line fluxes are not particularly bright, implying a low-luminosity AGN.

6. Summary

This paper described a complete "analysis pipeline", which processes reduced IFS data through the   spectral synthesis code. Data for the spiral galaxy NGC 2916 (CALIFA 277) were used to illustrate the journey from (x, y, λ) datacubes to multidimensional maps of the synthesis products, focusing on the technical and methodological aspects. The three main steps in the analysis can be summarized as follows:

1. Pre-processing: this step comprises (a) construction of a spatial mask; (b) adjustments in the flag and error spectra; (c) rest-framing and resampling; (d) spatial binning. The last three stages were coded in a generic python package (   ), which can run in a fully automated fashion. Spatial binning was accomplished with a Voronoi tessellation scheme, which was tuned to produce zones with $S/N \geq 20$ spectra. In practice, because of the good quality of the data, no binning was necessary within $R \lesssim 1$ HLR. The issue of correlated errors in spatial binning was discussed and an empirical recipe to correct for it was presented. The output of these pre-processing steps are datacubes with fluxes, errors, and flags ready for a detailed λ-by-λ spectral analysis, as well as spatial masks, a zone map, and other ancillary products.

2.   fits and organization of the synthesis results: Spectral fits for all spatial zones were performed using a base of SSP spectra from a combination of MILES and Granada models, spanning ages from 1 Myr to 14 Gyr and four metallicities between 0.2 and 1.5 solar. The results were packed in a coherent multilayered FITS (or HDF5) file with the Python Califa Starlight Synthesis Organizer (PyCASSO).

3. Post-processing tools: PyCASSO includes a reader module and a series of analysis tools to perform operations like zone-to-pixel image reconstruction; mapping the spectral and stellar population properties derived by   into multidimensional time, metallicity, and spatial coordinates; averaging in spatial and temporal dimensions; manipulation of the stellar population arrays.

Some of the products of this whole analysis are standard in IFS work, like the kinematical field and emission line maps. The

real novelty resides in the spatially resolved stellar population products recovered from the fossil record of galaxy evolution encoded in the datacubes. The 2D products range from maps of the stellar extinction and surface densities of stellar mass to more elaborate products like mean ages and metallicities, time-averaged star formation rates, and b-parameters. These quantities are all normally used in the analysis of integrated spectra, but their application to IFS data raises some conceptual issues related to the unavoidable fact that not all stars in a given spaxel were born there. On the other hand, one can use spatially resolved data to construct diagnostics unapplicable to integrated data, such as indices comparing the present and past SFR in different regions or comparing the "present here" with the "present elsewhere". These IFS-based variations of the traditional b parameter were shown to be useful to highlight different aspects of the spatially resolved SFH.

1D profiles in temporal or radial coordinates helped interpret the results. In our example galaxy, these compressed views of the (t, Z, x, y) manifold reveal clear age and metallicity negative gradients, as well as spatially dependent mass growth speeds compatible with an inside-out formation scenario. Finally, radius-age diagrams and snapshot sequences were introduced as further means of visualization.

Clearly, the application of spectral synthesis methods to IFS datacubes offers new ways of studying galaxies and their evolution. Future communications will use the tools laid out in this paper to explore the astrophysical implications of the results for galaxies in the CALIFA survey.

References

Asari, N. V., Cid Fernandes, R., Stasińska, G., et al. 2007, MNRAS, 381, 263
Bell, E. F., Wolf, C., Meisenheimer, K., et al. 2004, ApJ, 608, 752
Bertin, E., & Arnouts, S. 1996, A&AS, 117, 393
Bica, E. 1988, A&A, 195, 76
Bica, E., Alloin, D., & Schmitt, H. R. 1994, A&A, 283, 805
Blanc, G. A., Gebhardt, K., Heiderman, A., et al. 2010, in New Horizons in Astronomy: Frank N. Bash Symposium 2009, 432, 180
Bruzual G., & Charlot S. 2003, MNRAS, 344, 1000
Cappellari, M., & Copin, Y. 2003, MNRAS, 342, 345
Cardelli, J. A., Clayton, G. C., & Mathis, J. S. 1989, ApJ, 345, 245
Charbonnel, C., Meynet, G., Maeder, A., Schaeller, G., & Schaerer, D. 1993, A&AS, 101, 415
Cid Fernandes, R. 2007, IAU Symp., 241, 461
Cid Fernandes, R., Mateus, A., Sodré L., Stasińska, G., & Gomes, J. M. 2005, MNRAS, 358, 363
Falcón-Barroso, J., Sánchez-Blázquez, P., Vazdekis, A., et al. 2011, A&A, 532, A95
Folkes, S., Ronen, S., Price, I., et al. 1999, MNRAS, 308, 459
García-Benito, R., & Pérez-Montero, E. 2012, MNRAS, 423, 406
González Delgado, R. M., Cerviño, M., Martins, L. P., Leitherer, C., & Hauschildt, P. H. 2005, MNRAS, 357, 945
Gutiérrez, C. M., Azzaro, M., & Prada, F. 2002, ApJS, 141, 61
Ilbert, O., Capak, P., Salvato, M., et al. 2009, ApJ, 690, 1236
Kehrig, C., Monreal-Ibero, A., Papaderos, P., et al. 2012, A&A, 540, A11
Kelz, A., Verheijen, M. A. W., Roth, M. M., et al. 2006, PASP, 118, 129
Koleva M., Prugniel P., & De Rijcke S. 2009, Astron. Nachr. 999, 1
Lilly, S. J., Le Fevre, O., Hammer, F., & Crampton, D. 1996, ApJ, 460, 1
MacArthur, L. A., González, J. J., & Courteau, S. 2009, MNRAS, 395, 28
Madau, P., Ferguson, H. C., Dickinson, M. E., et al. 1996, MNRAS, 283, 1388
Moles, M., Benítez, N., Aguerri, J. A. L., et al. 2008, AJ, 136, 1325
Moorthy, B. K., & Holtzman, J. A. 2006, MNRAS, 371, 538
Ocvirk, P., Pichon, C., Lançon, A., & Thiébaut, E. 2006, MNRAS, 365, 46
Panter, B., Heavens, A. F., & Jimenez, R. 2003, MNRAS, 343, 1145
Panter, B., Jimenez, R., Heavens, A. F., & Charlot, S. 2007, MNRAS, 378, 1550
Pérez, E., Cid Fernandes, R., González Delgado, R. M., et al. 2013, ApJ, 764, L1
Pérez-González, P. G., Rieke, G. H., Villar, V., et al. 2008, ApJ, 675, 234
Pérez-Montero, E., García-Benito, R., Hägele, G. F., & Díaz, Á. I. 2010, MNRAS, 404, 2037
Roth, M. M., Kelz, A., Fechner, T., et al. 2005, PASP, 117, 62
Rudnick, G., Rix, H.-W., Kennicutt, R. C., Jr. 2000, ApJ, 538, 569
Sánchez, S. F., Kennicutt, R. C., Gil de Paz, A., et al. 2012, A&A, 538, A8
Sánchez-Blázquez, P., Ocvirk, P., Gibson, B. K., Pérez, I., & Peletier, R. F. 2011, MNRAS, 415, 709
Schaerer, D., Charbonnel, C., Meynet, G., Maeder, A., & Schaller, G. 1993a, A&A, 102, 339
Schaerer, D., Meynet, G., Maeder, A., & Schaller, G. 1993b, A&AS, 98, 523
Schaller, G., Schaerer, D., Meynet, G., & Maeder, A. 1992, A&AS, 96, 269
Tojeiro, R., Heavens, A. F., Jimenez, R., & Panter, B. 2007, MNRAS, 381, 1252
Vazdekis, A., Sńchez-Blázquez, P., Falcón-Barroso, J., et al. 2010, MNRAS, 404, 1639
Verheijen, M. A. W., Bershady, M. A., Andersen, D. R., et al. 2004, Astron. Nachr., 325, 151
York, D. G., Adelman, J., Anderson, J. E., et al. 2000, AJ, 120, 1579
Walcher, J., Groves, B., Budavári, T., & Dale, D. 2011, Ap&SS, 331, 1

B.2 Resolving galaxies in time and space. II. Uncertainties in the spectral

134 **synthesis of datacubes**

B.2 Resolving galaxies in time and space. II. Uncertainties in the spectral synthesis of datacubes

Resolving galaxies in time and space: II:

Uncertainties in the spectral synthesis of datacubes

R. Cid Fernandes[1,2], R. M. González Delgado[2], R. García Benito[2], E. Pérez[2], A. L. de Amorim[1,2], S. F. Sánchez[2,3], B. Husemann[4], J. Falcón Barroso[5,6], R. López-Fernández[2], P. Sánchez-Blázquez[7], N. Vale Asari[1], A. Vazdekis[5,6], C. J. Walcher[4], and D. Mast[2,3]

[1] Departamento de Física, Universidade Federal de Santa Catarina, P.O. Box 476, 88040-900, Florianópolis, SC, Brazil
e-mail: cid@astro.ufsc.br
[2] Instituto de Astrofísica de Andalucía (CSIC), P.O. Box 3004, 18080 Granada, Spain
[3] Centro Astronómico Hispano Alemán, Calar Alto, (CSIC-MPG), C/Jesús Durbán Remón 2-2, E-04004 Almería, Spain
[4] Leibniz-Institut für Astrophysik Potsdam, innoFSPEC Potsdam, An der Sternwarte 16, 14482 Potsdam, Germany
[5] Instituto de Astrofísica de Canarias, Vía Lactea s/n, E-38200 La Laguna, Tenerife, Spain
[6] Departamento de Astrofísica, Universidad de La Laguna, E-38205, Tenerife, Spain
[7] Departamento de Física Teórica, Universidad Autónoma de Madrid, 28049 Madrid, Spain

ABSTRACT

Aims. In a companion paper we have presented many products derived from the application of the spectral synthesis code STARLIGHT to datacubes from the CALIFA survey, including 2D maps of stellar population properties (such as mean ages, mass, extinction) and 1D averages in the temporal and spatial dimensions. Our goal here is to assess the uncertainties in these products.
Methods. Uncertainties associated to noise and spectral shape calibration errors in the data and to the synthesis method are investigated by means of a suite of simulations, perturbing spectra and processing them through our analysis pipelines. The simulations use 1638 CALIFA spectra for NGC 2916, with perturbations amplitudes gauged in terms of the expected errors. A separate study was conducted to assess uncertainties related to the choice of evolutionary synthesis models, the key ingredient in the translation of spectroscopic information to stellar population properties. We compare results obtained with three different sets of models: the traditional Bruzual & Charlot models, a preliminary update of them, and a combination of spectra derived from the Granada and MILES models. About 10^5 spectra from over 100 CALIFA galaxies are used in this comparison.
Results. Noise and shape-related errors at the level expected for CALIFA propagate to uncertainties of 0.10–0.15 dex in stellar masses, mean ages and metallicities. Uncertainties in A_V increase from 0.06 mag in the case of random noise to 0.16 mag for spectral shape errors. Higher order products such as star formation histories are more uncertain than global properties, but still relatively stable. Due to the large number statistics of datacubes, spatial averaging reduces uncertainties while preserving information on the history and structure of stellar populations. Radial profiles of global properties, as well as star formation histories averaged over different regions are much more stable than those obtained for individual spaxels. Uncertainties related to the choice of base models are larger than those associated with data and method. Except for metallicities, which come out very different when fits are performed with Bruzual & Charlot models, differences in mean age, mass and metallicity are of the order of 0.15 to 0.25 dex, and 0.1 mag for A_V. Spectral residuals are of order of 1% on average, but with systematic features of up to 4% amplitude. The origin of these features, most of which are present in both in CALIFA and SDSS spectra, is discussed.

Key words. galaxies: evolution – galaxies:stellar content – galaxies: general– techniques: imaging spectroscopy

1. Introduction

Large optical spectroscopic surveys have dominated the panorama of extra-galactic astrophysics over the last decade. Stellar population analysis of these data has produced information on stellar masses, mean stellar ages, abundances, dust content and diagnostics of their star formation histories (SFHs), whose analysis per se and in relation to other properties (say, morphology or environment) has advanced the understanding of the physics of galaxies and their evolution through cosmic time. Yet, all this information is derived from spatially unresolved spectra, and thus reflect global averages over properties which are known to vary accross the face of galaxies. Integral field spectroscopy (IFS) is a natural next step to go from global properties to the internal physics of galaxies. Dissecting the different structural components should lead to a much more com-

plete picture of galaxies, as well as to a clearer understanding of the results already obtained in non-spatially resolved surveys. IFS has been around for over two decades, but has only recently been promoted to the scale of modern galaxy surveys. CALIFA, the Calar Alto Integral Field Area survey (Sánchez et al. 2012; Husemann et al. 2013), is a pioneer in this blooming field.

To harvest the full potential of IFS data one needs to adapt techniques developed for spatially unresolved galaxy spectra, folding in the information on the spatial structure. In a companion article (Cid Fernandes et al. 2013, hereafter Paper I) we have presented our method to extract stellar population properties out of CALIFA datacubes by means of the STARLIGHT spectral fitting software (Cid Fernandes et al. 2005). The packages developed to pre-process and partition the reduced datacubes (QBICK) and to

post-process the results of the spectral synthesis (pycasso[1]) were described in detail. The products of this work flow were exemplified using data for the nearby spiral NGC 2916 (CALIFA 277). Diagnostics such as 2D maps of physical properties (mean ages and metallicities, mass surface densities, star formation rates, etc.), 1D averages in the temporal and spatial dimensions, projections of the stellar light and mass growth onto radius-age diagrams, and cuts through the (x, y, age) cubes were presented to illustrate the potential of the combination of IFS data with spectral synthesis as a tool to study galaxy evolution in time and space simultaneously.

Uncertainties in this whole process stem from *(i)* noise and calibration of the data, *(ii)* limitations of our spectral synthesis method, and *(iii)* evolutionary synthesis models, the key ingredient in the mapping of observed spectra to astrophysical information. These different sources of uncertainty, each one comprising a large field of work by itself, intertwine and propagate in non trivial ways through our pipelines. Uncertainties in spectral synthesis products have been previously explored in the literature, like the noise-effect simulations in Cid Fernandes et al. (2005), the model-impact study of Panter el al. (2007), and the suite of tests presented by Tojeiro et al. (2007), but never in the context of IFS.

This article complements Paper I by addressing the effects of these uncertainties. Our central goal is to provide quantitative and qualitative guidelines to allow an assessment of the robustness of results produced with the methods and tools explained in Paper I, which are being used in a series of publications by our collaboration. Pérez et al. (2013), for instance, analysed the spatially resolved mass assembly history of 105 CALIFA galaxies, finding clear evidence for an inside-out growth for massive galaxies, and signs of outside-in growth for the less massive ones (see González Delgado et al. 2012a and 2012b for other results). Despite the focus on starlight and CALIFA, the results reported here are also useful in the broader context of stellar population analysis of IFS data; for instance, experimental datacubes recently obtained by MaNGA run through our qbick and pycasso pipelines without any modification.

The first part of this paper (§2 and §3) presents extensive simulations which explore effects of uncertainties related to the data and spectral synthesis method. Random noise and shape-changing perturbations are added to both observed and synthetic spectra of all zones of the same galaxy analysed in Paper I. These simulations are then used to evaluate uncertainties in global properties (mean ages, masses, etc.) and higher order products such as SFHs. This is done both at the level of individual spectra and for spatial regions cut out from the datacube.

The second part (§4) is dedicated to experiments carried out to evaluate how our results are affected by different choices of evolutionary synthesis models for the spectra of simple stellar populations (SSP). This study uses ~ 100 thousand spectra from 107 galaxies observed by CALIFA, all of which were processed with three sets of SSP models used in the current literature. An inspection of the quality of the spectral fits and a comparison with results obtained for SDSS galaxies is also presented.

§5 summarizes our main results. Throughout this paper the notation and definitions established in Paper I are followed.

---

[1] Python CALIFA Starlight Synthesis Organizer

2. Uncertainties associated to the data and the method: Description of the simulations

A drawback of starlight is that it provides no error estimate on its output. The most straightforward (albeit computationaly expensive) way to do so is to run the code several times, perturbing the input data according to some realistic prescription of the errors involved. This section describes a set of extensive simulations taylored to match the characteristics of CALIFA data. The simulations are designed to address the effects of

1. random noise,
2. shape-related calibration uncertainties, and
3. multiplicity of solutions

upon the physical properties derived with starlight. Throughout these experiments we keep the set of SSPs fixed at the same one used in Paper I and denoted "base *GM*" in §4, where the effects of this choice are investigated. This base comprises $N_\star = 156$ elements with 39 ages between $t = 1$ Myr and 14 Gyr, and 4 metallicities from $Z = 0.2$ to 1.5 solar. The simulations are based on the data and starlight fits of 1638 zone spectra[2] of CALIFA 277 studied in Paper I. Given the variety of properties found accross this galaxy and the fact that all other datacubes in CALIFA were processed in the same way, the uncertainty estimates presented here are representative of CALIFA data in general.

Each spectrum was perturbed 10 times for each of the R, C and E error prescriptions discussed below, and refitted. This data set is then used to evaluate uncertainties in the derived properties, both at the level of individual zones and for spatially averaged properties like those shown in Figs. 10 and 11 of Paper I. Both observed and synthetic spectra are perturbed in the simulations. The former represent real-life conditions, while the latter is essentially a theoretical exercise which explores the sensitivity of the starlight results to different kinds of perturbations.

2.1. Types of errors and simulations

The first type of error considered is that related to the variations on the derived properties induced by random fluctuations of the observed fluxes within the noise level. To study this, each zone spectrum was perturbed 10 times with gaussian noise with a λ-dependent amplitude given by the error spectrum ϵ_λ (hereafter OR1 runs, with "O" standing for observed, "R" for random, and 1 for the amplitude of the perturbation). Experiments were also conducted with pertubations of 2 and $3 \times \epsilon_\lambda$ (OR2 and OR3 runs, respectively) to emulate what would be obtained under considerably worse conditions than those in CALIFA.[3]

A second set of simulations was carried to address the issue of overall continuum shape calibration. starlight relies on flux calibrated input spectra, so it is relevant to access how much its solutions vary for spectra whose shape vary within expected uncertainty ranges. Husseman et al. (2013) find that CALIFA synthetic $g - r$ colors typically differ by 0.05 mag from those obtained by SDSS photometry. We use this value to gauge the

---

[2] 1527 of the spectra come from single spaxels, while the remaining 111 ones correspond to Voronoi zones comprising typically 10 spaxels.

[3] Note that these simulations add noise to observed spectra, which already contains it. Hence, OR1 spectra, which are nominaly meant to represent variations at the level of $1\epsilon_\lambda$, effectively have errors of $\sqrt{2}\epsilon_\lambda$, ie., 41% larger than intended. We will nevertheless pretend these runs correspond to 1σ perturbations, which gives a safety margin in our analysis. Similarlty, OR2 and OR3 runs have errors 2.23 and 3.16 times larger than the original ones, instead of factors of 2 and 3, respectively.

effects of continumm calibration uncertainty in each individual specrum of CALIFA 277. For simplicity, but with no loss of generality, these simulations keep the flux at $\lambda_r = 6231$ Å stable, such that the 0.05 mag variation in $g - r$ translates to a 0.02 dex uncertainty in the flux at $\lambda_g = 4770$ Å. To emulate the effects of such variations we have produced 10 versions of each spectrum by adding $A_g \times (\lambda_r - \lambda)/(\lambda_r - \lambda_g)$ to the original $\log F_\lambda$, with $A_g = \Delta \log F_{\lambda_g}$ sampled from a gaussian distribution of zero mean and dispersion $\sigma(\log F_{\lambda 4470}) = 0.02$ (OC002 runs, where "C" stands for color). This produces both redder and bluer versions of the original spectrum. Experiments were also carried out for $\sigma(\log F_{\lambda 4470}) = 0.01$, and 0.04 dex (OC001 and OC004, respectively). We take OC002 runs as default for CALIFA, even though the spaxel-to-spaxel variations in the continuum calibration for a single galaxy are probably smaller than the $g - r$ dispersion quoted by Husemann et al. (2013), which was derived from the 100 galaxies in the CALIFA DR1 sample.

Finally, fits were also conducted for no perturbation at all (OE0 runs), the motivation for which is to quantify a qualitatively different source of uncertainty, embedded in all other simulations. STARLIGHT provides a single best fit set of parameters, out of typically many millions tried out during its likelyhood-guided sampling of the parameter space. This single solution, however, is not meant to be mathematically unique. In fact, given the pseudo random nature of its Markov chains, STARLIGHT solutions depend on the input seed for the random number generator. For large samples, and each CALIFA datacube is a large sample in itself, these variations have no relevant effect on the overall results of the analysis. For individual spectra, however, the multiplicity of solutions leads to uncertainties in the derived properties. The OE0 runs quantify these uncertainties, which ultimately reflect an intrinsic limitation of our spectral synthesis method.

2.2. Simulations based on synthetic spectra

The OE0, OR* and OC* runs work upon the original observed spectra (hence the prefix "O"). A paralell set of simulations was carried out applying these same perturbation recipes to the synthetic spectra obtained in our STARLIGHT fits of CALIFA 277. We label these runs as SE0, SR1, SR2, SR3, SC001, SC002 and SC004 ("S" for synthetic).

The S runs use exactly the same sampling, masks, flags and ϵ_λ errors as in the O runs, thus following the pattern of CALIFA data in a realistic fashion. At the same time, these are idealistic simulations in the sense that the perturbations act upon "perfect" input spectra, instead of observed ones. This theoretical exercise therefore overlooks inadequacies in the SSP models (including issues like potential flux calibration problems in the libraries, limited coverage of the stellar parameter space, missing or incorrectly modeled evolutionary phases) and other assumptions involved in the modelling (namely, extinction and kinematics).

The purpose of these runs is to evaluate to which extent STARLIGHT recovers known input properties in the presence of perturbations. This kind of input versus output comparison is more commonly carried out feeding the spectral fitting code with data generated with ad hoc parametric descriptions of the SFH (eg, the so called "tau models"), while our theroretical SFHs are inspired in those derived from actual observations. A valid criticism of these simulations is that the same base is used to generate and fit spectra. The alternative would be to generate models with some other set of $t's$ and Z', but since our base is so large

Notation for the simulations				
Run	original spectra	type of perturbation	perturbation amplitude	comments
(1)	(2)	(3)	(4)	(5)
OR1	observed	noise	$1 \times \epsilon_\lambda$	gaussian
OR2	observed	noise	$2 \times \epsilon_\lambda$	gaussian
OR3	observed	noise	$3 \times \epsilon_\lambda$	gaussian
OC001	observed	color	0.01 dex	at λ_g
OC002	observed	color	0.02 dex	at λ_g
OC004	observed	color	0.04 dex	at λ_g
OE0	observed	none	0	
SR1	synthetic	noise	$1 \times \epsilon_\lambda$	gaussian
SR2	synthetic	noise	$2 \times \epsilon_\lambda$	gaussian
SR3	synthetic	noise	$3 \times \epsilon_\lambda$	gaussian
SC001	synthetic	color	0.01 dex	at λ_g
SC002	synthetic	color	0.02 dex	at λ_g
SC004	synthetic	color	0.04 dex	at λ_g
SE0	synthetic	none	0	

Table 1. (1) Nomenclature adopted to denote the different simulations. (2) The nature (observed versus synthetic) of the spectra which are perturbed. (3) Type of perturbation. (4) Amplitude of the perturbations. For C runs, we list the amplitude of the variations at λ_g. Each of the 1638 spectra from CALIFA 277 are perturbed 10 times according to each of these 14 recipes.

(39 ages and all 4 available metallicities), this would make very little difference in practice.

2.3. Notation

For clarity and quick reference, we summarize the notation and intended purpose of the simulations described above.

R runs (OR1, OR2, OR3, SR1, SR2 and SR3) explore the effect of noise by adding gaussian perturbations scaled to have amplitudes 1, 2 or 3 times the nominal error ϵ_λ. C runs perturb the input spectra in their global shape by multiplying the original F_λ by a power-law in λ, scaled such that the flux at λ_r remains fixed while that at λ_g differs by (on average over all realizations) 0.01 (OC001 and SC001), 0.02 (OC002 and SC002) and 0.04 (OC004 and SC004) dex with respect to the input flux. (In a $\log F_\lambda \times \lambda$ plot, these shape-pertubations correspond to straight lines anchored at λ_r and different slopes.) These runs are meant to emulate the effect of a flux calibration uncertainty in the data. E0 runs do nothing to the input spectra. They only differ in the random number seed feed to STARLIGHT. The variance among these fits reflects the multiplicity of SSP combinations leading to a similar total spectrum.

In all cases, a prefix "O" indicates that the perturbations act upon the observed spectra, while an "S" prefix means that synthetic spectra are perturbed. Table 1 summarizes the simulation-related nomenclature used thoughout the paper.

3. Results of the simulations

The simulations described in §2 provide the material to evaluate uncertainties associated with the data and spectral synthesis method. We split the presentation of this material into an assessement of the errors in global properties (§3.1), radial profiles (§3.2), and SFHs (§3.3). We conclude this part of our investigation with a summary of the results of the simulations (§3.4).
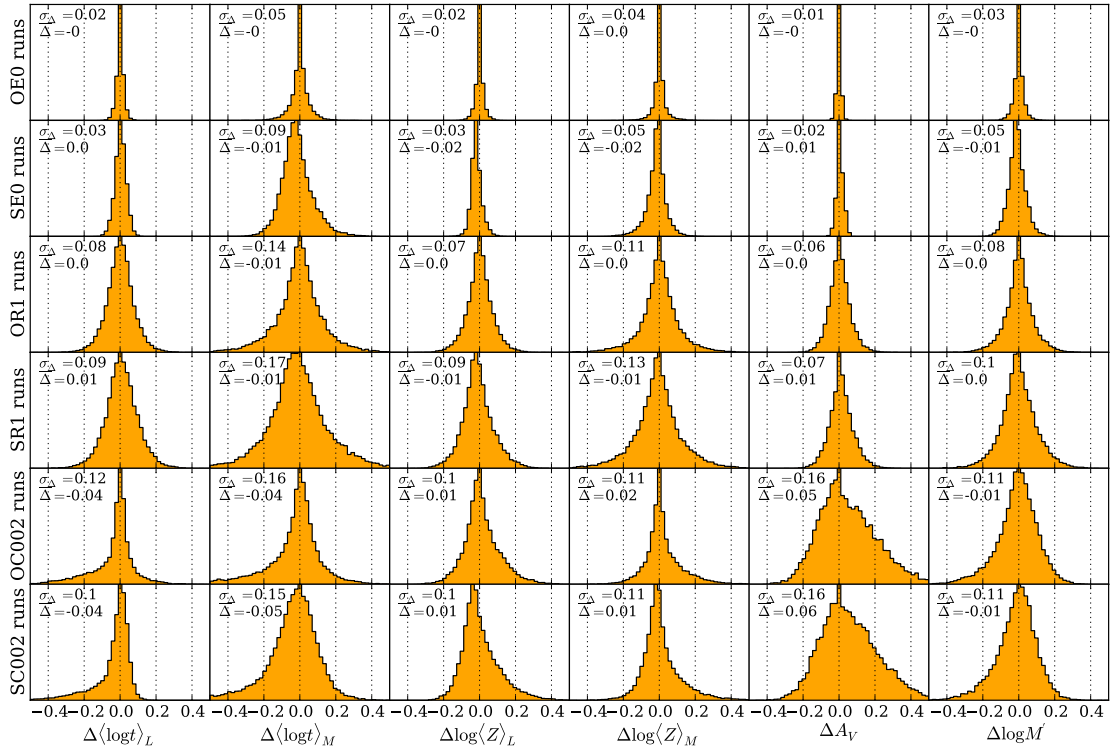
Fig. 1. Histograms of Δ ($\equiv$ Simulated minus Original value) for the main scalar properties derived from the spectral synthesis: $\langle \log t \rangle_L$, $\langle \log t \rangle_M$, $\log\langle Z \rangle_L$, $\log\langle Z \rangle_M$, A_V and the initial stellar mass formed ($\log M'$). Each row corresponds to one set of simulations, alternating S and O runs (as labeled in the y-axis). Mean Δ's and their σ's are labeled in each panel. Except for the A_V column, each histogram is based on 16380 values obtained from the 1638 zones in CALIFA 277 and 10 Monte Carlo realizations of the perturbation. For clarity, the A_V histograms were drawn excluding the many $\Delta A_V = 0$ cases, which occur due to the $A_V \geq 0$ physical limit imposed on the spectral fits. Noise-free simulations (OE0 and SE0), which trace intrinsic degeneracies in spectral fits of composite stellar populations, are show in the top two rows. Random-noise simulations (SR1 and OR1, central rows) map the uncertainties due to statistical fluctuations of the observed F_λ fluxes. C002-simulations, where the spectral-shape is changed to emulate calibration uncertainties, are shown on the bottom panels.

3.1. Uncertainties in global properties

The main scalar properties derived from the spectral synthesis are mean ages and metallicities (weighted by light or mass), extinction and stellar masses[4]. These 1st order products of the analysis convey enough information to draw a quite detailed sketch of the 2D distribution of stellar population properties in a galaxy. Before incorporating the spatial arrangement of the spectra, however, it is useful to assess uncertainties in the individual spectra, as if they came from different galaxies.

Fig. 1 shows histograms of the $\Delta \equiv$ Simulation $-$ Original value (ie., that obtained from the unperturbed spectrum) of each of these quantities, and for six different sets of simulations: E0, R1 and C002 runs, in both O and S versions. Statistics for all runs are listed in Table 2.

3.1.1. E runs: Noise-free simulations

The OE0 and SE0 panels show that variations due to the random number seed feed to STARLIGHT have a minute effect on the derived properties, with no bias ($\overline{\Delta} \sim 0$) and one σ uncertainties all in the second decimal place.

Intriguingly, SE0 runs have somewhat larger dispersions than OE0 runs. The mathematical reason for this behaviour is subtle, but simple to grasp with the concepts developed by Pelat (1997, 1998). By construction, SE0 spectra lie within the Synthetic Domain (SD), ie, the space generated by convex combinations of the base spectra[5]. A point inside this space can be exactly fitted by at least one set of parameters. Even if the solution is mathematically unique, a whole range of other solutions produce nearly identical spectra. Because of the limitations of evolutionary synthesis models, observed spectra cannot possibly be fitted exactly even in the ideal limit of perfect calibration and $S/N = \infty$, so OE0 spectra are inevitably *outside* the SD. Fits of OE0 spectra therefore have access to a smaller sub-space of acceptable solutions than fits of SE0 spectra, resulting in the

---

[4] Throughout this section we work with the initial stellar mass (M'), uncorrected for the mass expelled from stars back to the interstellar medium. Mass weighted ages and metallicities, however, do account for the returned mass.

[5] In the case of STARLIGHT and other full spectral fitting codes this space is further enlarged by the extinction and kinematical dimensions, but we leave this aside to simplify the argument.
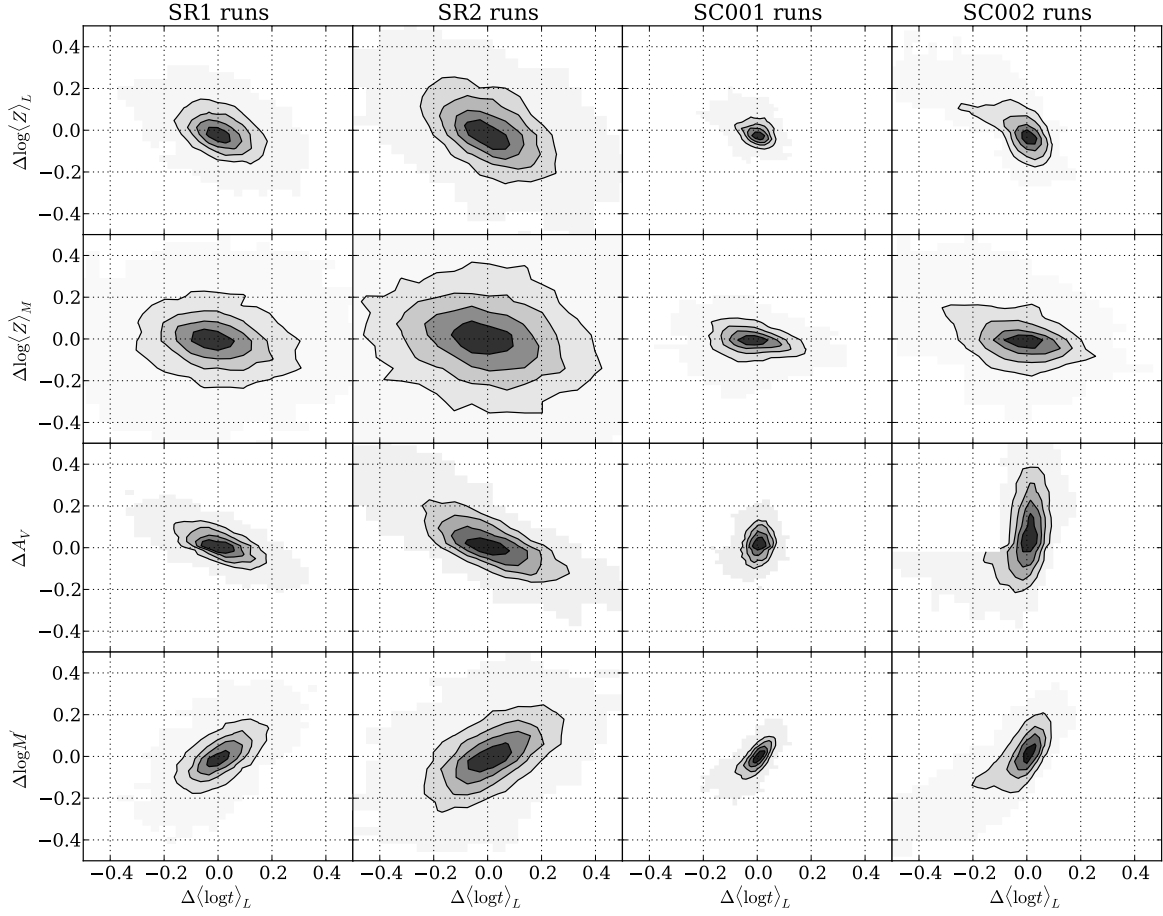
Fig. 2. Illustration of the correlated Δ variations of ages, metallicites, extincion, and masses. Each column corresponds to one set of simulations. Iso-density contours mark 20, 40, 60 and 80% of enclosed points.
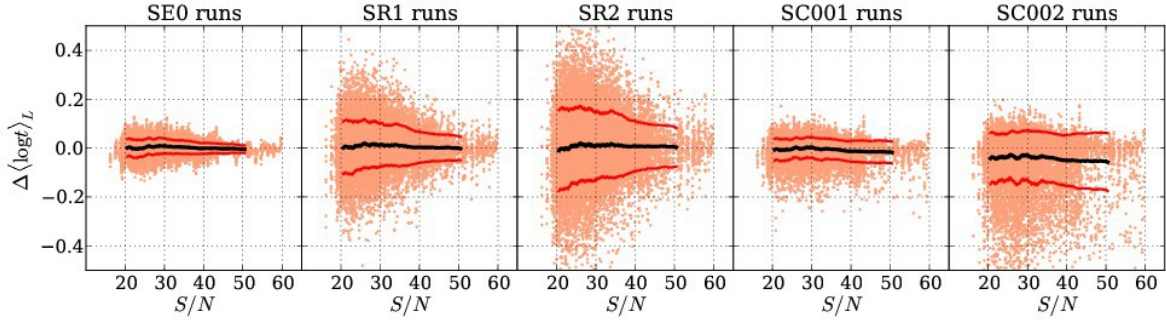
Fig. 3. $\Delta\langle\log t\rangle_L$ variations for all 1638 zones $\times$ 10 realizations plotted against the S/N of the corresponding original (observed) spectra. Different panels correspond to different sets of simulations, as labeled. The lines are running mean of $\Delta\langle\log t\rangle_L$ and the corresponding $\pm 1\sigma$ intervals.

smaller dispersions observed in Fig. 1. This same interpretation applies to other runs. Even when the synthetic spectra are perturbed (say, as in the SR1 simulations), they remain closer to the SD than the corresponding O spectra, thus reaching a larger region of the solutions space.

3.1.2. R runs: Random noise simulations

Random noise at the nominal level (OR1 and SR1 runs, middle rows in Fig. 1) lead to Δ-distributions with σ around 0.1 dex in ages, metallicities and masses, and 0.05 mag in A_V. As expected (and also seen in the E0 runs), mass-weighted ages and metallicities have broader Δ distributions than their luminosity

5

Summary of simulations: $\overline{\Delta} \pm \sigma_{\Delta}$

Property	OE0	OR1	OR2	OR3	OC001	OC002	OC004
$\langle \log t \rangle_L$	-0.00 ± **0.02**	0.00 ± **0.08**	0.01 ± **0.13**	0.01 ± **0.16**	-0.00 ± **0.05**	-0.04 ± **0.12**	-0.09 ± **0.20**
$\langle \log t \rangle_M$	-0.00 ± **0.05**	-0.01 ± **0.14**	-0.02 ± **0.21**	-0.03 ± **0.26**	-0.00 ± **0.08**	-0.04 ± **0.16**	-0.10 ± **0.28**
$\log \langle Z \rangle_L$	-0.00 ± **0.02**	0.00 ± **0.07**	-0.00 ± **0.12**	-0.00 ± **0.16**	0.00 ± **0.05**	0.01 ± **0.10**	0.03 ± **0.16**
$\log \langle Z \rangle_M$	0.00 ± **0.04**	0.00 ± **0.11**	-0.00 ± **0.18**	0.00 ± **0.22**	0.00 ± **0.05**	0.02 ± **0.11**	0.05 ± **0.18**
A_V	-0.00 ± **0.01**	0.00 ± **0.06**	0.01 ± **0.10**	0.02 ± **0.14**	0.01 ± **0.06**	0.05 ± **0.16**	0.14 ± **0.29**
$\log M'$	-0.00 ± **0.03**	0.00 ± **0.08**	-0.00 ± **0.13**	0.00 ± **0.15**	-0.00 ± **0.05**	-0.01 ± **0.11**	-0.02 ± **0.21**
Property	SE0	SR1	SR2	SR3	SC001	SC002	SC004
$\langle \log t \rangle_L$	0.00 ± **0.03**	0.01 ± **0.09**	0.01 ± **0.14**	0.01 ± **0.18**	-0.01 ± **0.04**	-0.04 ± **0.10**	-0.10 ± **0.19**
$\langle \log t \rangle_M$	-0.01 ± **0.09**	-0.01 ± **0.17**	-0.02 ± **0.23**	-0.03 ± **0.27**	-0.02 ± **0.10**	-0.05 ± **0.15**	-0.11 ± **0.26**
$\log \langle Z \rangle_L$	-0.02 ± **0.03**	-0.01 ± **0.09**	-0.01 ± **0.14**	-0.00 ± **0.18**	-0.01 ± **0.05**	0.01 ± **0.10**	0.02 ± **0.17**
$\log \langle Z \rangle_M$	-0.02 ± **0.05**	-0.01 ± **0.13**	-0.00 ± **0.20**	0.01 ± **0.24**	-0.01 ± **0.06**	0.01 ± **0.11**	0.04 ± **0.19**
A_V	0.01 ± **0.02**	0.01 ± **0.07**	0.02 ± **0.11**	0.03 ± **0.15**	0.02 ± **0.06**	0.06 ± **0.16**	0.15 ± **0.30**
$\log M'$	-0.01 ± **0.05**	0.00 ± **0.10**	0.00 ± **0.14**	0.00 ± **0.16**	-0.01 ± **0.06**	-0.01 ± **0.11**	-0.03 ± **0.20**

Table 2. Statistics of the simulations. For each global property the table lists the mean simulated minus original difference ($\overline{\Delta}$) and its standard deviation (σ_{Δ}). The latter, printed in bold, indicates the level of uncertaintites under different circunstances. Each column denotes one set of simulations. The upper half of the table shows results of simulations based on variations upon the original observed spectrum (O runs), whereas the bottom half corresponds to runs where the synthetic spectra were perturbed (S runs) and used as input.

weighted counterparts. In any case, these dispersions are all relatively small. Indeed, they are smaller than those induced by the use of different SSP models (§4, Fig. 11).

Table 2 reports results for simulations with noise levels 2 and 3 times worse than ϵ_λ. For the OR2 runs, for instance the the uncertainties in the properties ploted in Fig. 1 increase by roughly a factor of 2 with respect to those found in the OR1 simulations. The Δ distributions (not plotted) remain symmetric, with no significant biases. Recall, however, that there is no reason to believe that the ϵ_λ values produced by the CALIFA reduction pipeline are underestimated. On the contrary, Husemann et al. (2013) show that, if anything, they are slightly overestimated.

3.1.3. C runs: Shape perturbations

The bottom panels in Fig. 1 show the results for simulations where the continuum shape was perturbed to produce (on average) 0.02 dex variations in the flux at λ_g for a fixed flux at λ_r. The one σ variations in ages, metallicities and masses for OC002 runs are larger than those obtained with the OR1 runs, but not as large as in OR2 (Table 2). Similar conclusions apply to the corresponding S runs. Predictably, A_V is more severely affected by these global shape perturbations, with $\sigma(\Delta A_V) \sim 2.5$ times larger than those in the OR1 runs.

Unlike in other simulations, the Δ distributions are skewed, particularly the ones for A_V and $\langle \log t \rangle_L$. This is a by-product of the $A_V \geq 0$ limit imposed upon the fits. 582 of the 1638 zones of CALIFA 277 were fitted with $A_V = 0$ (see Fig. 4 in Paper I). About half of the shape-perturbed versions of these spectra are bluer than the original ones. Since STARLIGHT was not allowed to decrease A_V to fit them, it gets stuck at $A_V = 0$, compensating the extra blueness with younger populations, producing the tail towards negative $\Delta \langle \log t \rangle_L$ seen in the bottom rows of Fig. 1. This is also the reason why there are more instances of $\Delta A_V > 0$ than < 0, producing the positively skewed ΔA_V distributions.

Increasing the shape errors by a factor of 2 (C004 runs) leads to uncertainties roughly twice as large, biases of the order of −0.1 dex in ages and +0.15 mag in A_V (Table 2), as well as larger skewness of the Δ distributions. Conversely, C001 runs result in uncertainties ∼ 2 times smaller, with no bias nor much skewness.

3.1.4. Covariances

As usual in multivariate problems, variations in one property correlate with variations in others. In the context of spectral synthesis, such covariances are known as age-metallicity-extinction degeneracies: A_V affects colors while t and Z affects both absorption lines and colors. Previous work (e.g., Cid Fernandes et al. 2005; Sánchez-Blázquez et al. 2011) showed that λ-by-λ fits help reducing these degeneracies, but do not eliminate them.

Fig. 2 shows how the main scalar properies co-vary in our simulations. S runs are used in this plot—O runs produce similar plots, with slightly more compact contours. The first two columns (SR1 and SR2 runs) reveal the classical degeneracies of population synthesis, with mean ages increasing as mean metallicities decrease, and extinction variations also anti-correlated with variations in mean age. The bottom row shows how stellar masses increase as ages become older, and vice-versa.

In the R-runs, perturbations do not change the overall shape of the input spectrum. Hence, if a STARLIGHT solution turns out somewhat older than the original one, its extinction and/or metallicity will decrease to compensate the redder colors and stronger absorption lines of the older stars. C-runs, on the other hand, do change colors—that is, in fact, exactly what they are designed to do. This changes the nature of "degeneracies" a bit.

If the shape perturbation followed the same functional form of the extinction law, it would suffice to change A_V, leaving the population mixture essentially unchanged, varying t's and Z's at the level they would naturally vary without color perturbations (i.e, due to noise and the multiplicity of solutions). To first order, this is indeed what happens in the C-runs. Compare, for instance the (SR1, SR2) and (SC001, SC002) pairs of $\Delta A_V \times \Delta \langle \log t \rangle_L$ panels in Fig. 2. In both pairs of plots the corresponding type of error changes by a factor of 2 in amplitude, yet one sees that the ΔA_V contours grow more from SC001 to SC002 than from SR1 to SR2. Furthermore, the ΔA_V contours are nearly vertically oriented in the C-runs, while in R-runs the anti-correlation with $\Delta \langle \log t \rangle_L$ is clear (the age-extinction degeneracy). We thus confirm the expectation that, to first order, continuum shape uncertainties affect primarily the A_V estimates.

There are still two "second order" features to explain about the $\Delta A_V \times \Delta \langle \log t \rangle_L$ C-runs maps in Fig. 2. First, the inner contours have a slightly positive slope, opposite to that expected

from the age-extincion degeneracy (clearly seen in the SR1 and SR2 panels). This behaviour is due to the fact that, because of the different functional forms, our shape-perturbations (where $\Delta \log F_\lambda$ changes linearly with λ) cannot be fully absorbed by the reddening curve used in the fits. Since changing A_V alone is not quite enough to produce optimal spectral fits, STARLIGHT looks for other ways of making the synthetic spectrum redder or bluer (depending on the sign of the perturbation), and skewing the age mixture is the most effective one. In any case, the change in mean age is small: $\overline{\Delta}\langle \log t \rangle_L = -0.04$ for SC002 runs (Table 2). Secondly, for SC002 runs, the outer contours (containing about 20% of the points) are limited to $\Delta A_V \leq 0$ whenever simulated mean ages are more than 0.1 dex younger than the original ones ($\Delta \langle \log t \rangle_L < -0.1$). Spectra along this odd looking ridge were originally fitted with $A_V = 0$, and then perturbed to bluer colors. Since our fits do not allow $A_V < 0$, STARLIGHT fitted them with the same A_V (hence $\Delta A_V = 0$), but younger ages, leading to the pattern observed in this panel.

3.1.5. Checking the effects of imposing $A_V \geq 0$

As seen just above, the effects of a hypothetical systematic redness associated to spectroscopic calibration issues are almost entirely absorbed biasing A_V upwards, while an excessive blueness of the same nature stumbles upon the $A_V \geq 0$ constraint, leading to biases in the age mixture. An artificial way of fixing this assimetry is to allow for $A_V < 0$ in the spectral fits. A trivial statistical justification to allow for this unphysical possibility is that, when A_V is truly $= 0$, unbiased estimates should oscilate around 0, including both negative and positive values. We also note that completely independent studies (different methods, different data) also allow for or deduce negative extinctions (e.g. Kauffmann et al. 2003, their figure 11).

An extra set of OE0-like simulations, but imposing $A_V > -1$ was run to investigate this issue. In practice what happens is that only zones which were originally fitted with $A_V \sim 0$ are systematicaly refitted with negative A_V. The 591 zones which come out with $A_V < 0$ in these new fits include all the 582 for which we had originally found $A_V = 0$, and the remaining 9 had A_V very close to 0. The mean new A_V of these 591 zones was -0.12 mag, with a standard deviation of 0.08 mag. The minimum value reached was $A_V = -0.4$ mag, but in only 16% of the cases A_V went below -0.2 mag. The variations in other global properties (for these same 591 zones) were $\overline{\Delta}\langle \log t \rangle_L = +0.12$, $\overline{\Delta}\langle \log t \rangle_M = +0.12$, $\overline{\Delta} \log \langle Z \rangle_L = -0.07$, $\overline{\Delta} \log \langle Z \rangle_M = -0.04$, and $\overline{\Delta} \log M' = +0.03$ dex. Mean ages are the most affected property, but to an acceptably small degree, with biases of the same order as the one-σ variations produced by random and shape-related uncertainties at the nominal level (ie, R1 and C002 simulations).

Zones originally fitted with $A_V > 0$ did not show systematic variations in their global properties in these extra runs.

3.1.6. The effect of S/N

The Δ histograms in Fig. 1 and the statistics in Table 2 represent the uncertainties of the CALIFA 277 data set as a whole, including zones of different S/N. The general expectation is that smaller S/N leads to larger uncertainties, such that the tails of the Δ distributions in Fig. 1 are dominated by the noisier spectra, while the cores (small Δ values) correspond to higher S/N.

To verify this, Fig. 3 shows the $\Delta \langle \log t \rangle_L$ variations against the S/N of the original spectra. The lines represent the mean $\pm 1\sigma$ range. Uncertainties do decrease with increasing S/N in

the SE0, SR1 and SR2 runs, but not in the C-runs. This is in fact not surpising, since the shape perturbations have the same amplitude for all spectra, independent of their S/N. The rightmost panel illustrates the bias towards lower ages which results from the $A_V \geq 0$ barrier.

We note in passing that, as hinted in Fig. 3, the distribution of S/N values in CALIFA 277 is skewed towards the target minimum S/N of 20 stipulated in the spatial binning scheme explained in Paper I. This same threshold was applied to all other datacubes, so the uncertainty estimates presented here should be representative of the CALIFA data in general, even though they are based on a single galaxy.

3.2. Exploring the statistics in IFS data: Uncertainties in radial profiles

So far our error analysis has treated the datacube as a collection of unrelated spectra. Spectral synthesis does not care where a spectrum come from, so the positional information provided by IFS has no effect on the uncertainties for individual zones. However, averaging results obtained for different zones brings obvious statistical benefits, reducing uncertainties in properties derived from individual spectra.

Fig. 10 in Paper I shows azymuthally averaged profiles for a series of global properties. Despite the scatter at any given radius, gradients in age and metallicity were clearly detected in CALIFA 277. Fig. 4 in this paper repeats that plot, but now showing the radial profiles derived from the simulated spectra, so that we can evaluate the uncertainties in azymuthal averages. The original profiles are plotted in solid black, while colored shades represent the ranges spanned by OR1 (blue) and C002 (red) runs. Each panel also shows an (arbitrarely shifted) simulation minus original difference profile at its bottom.

As expected, random noise does not change the radial profiles significantly. A small bias of about 0.02 mag is seen in $\overline{A_V}(R)$ for radii beyond ~ 1 Half Light Radius (HLR). This is again a side effect of the $A_V \geq 0$ constraint: When a spectrum originally fitted with $A_V \sim 0$ is perturbed, some will be refitted with $A_V > 0$, but none will be refitted with $A_V < 0$. The resulting bias propagates to minor offsets in other properties, like slightly younger ages (panels e and f). Overall, however, these are all tiny effects.

Color perturbations (red shaded regions) produce larger effects. The main effect is on the $\overline{A_V}(R)$ profile (panel c), where the typical offset matches the expected $\overline{\Delta}(A_V) = 0.05$ mag reported in Table 2. Leaving aside this bias, the $\overline{A_V}(R)$ variations are much smaller than those in individuals zones. For instance, considering all radial bins and all 10×1638 versions of the OC002 spectra, the rms in $\Delta(\overline{A_V})$ is only 0.05 mag, while individual zones are subjected to uncertainties of $\sigma(A_V) = 0.16$ mag (Fig. 1).

Larger than typical variations occur in the nucleus for the trivial reason that it comprises a single spaxel, so no actual statistics is done. More robust results for "the nucleus" require extending its definition to include more spaxels. For instance, Pérez et al. (2013) define the nucleus as the inner 0.1 HLR, which in the case of CALIFA 277 comprises the central-most 9 spaxels. Uncertainties also increase in the outer regions ($R > 2$ HLR), induced by the smaller S/N of the spectra and by the decrease in the number of zones compared to intermediate radii.

Fig. 4 confirms the expected gain in dealing with averaged results. The simulations show that the uncertainties in the radial profiles are just too small to question the reality of the age and metallicity gradients in this galaxy. This conclusion holds
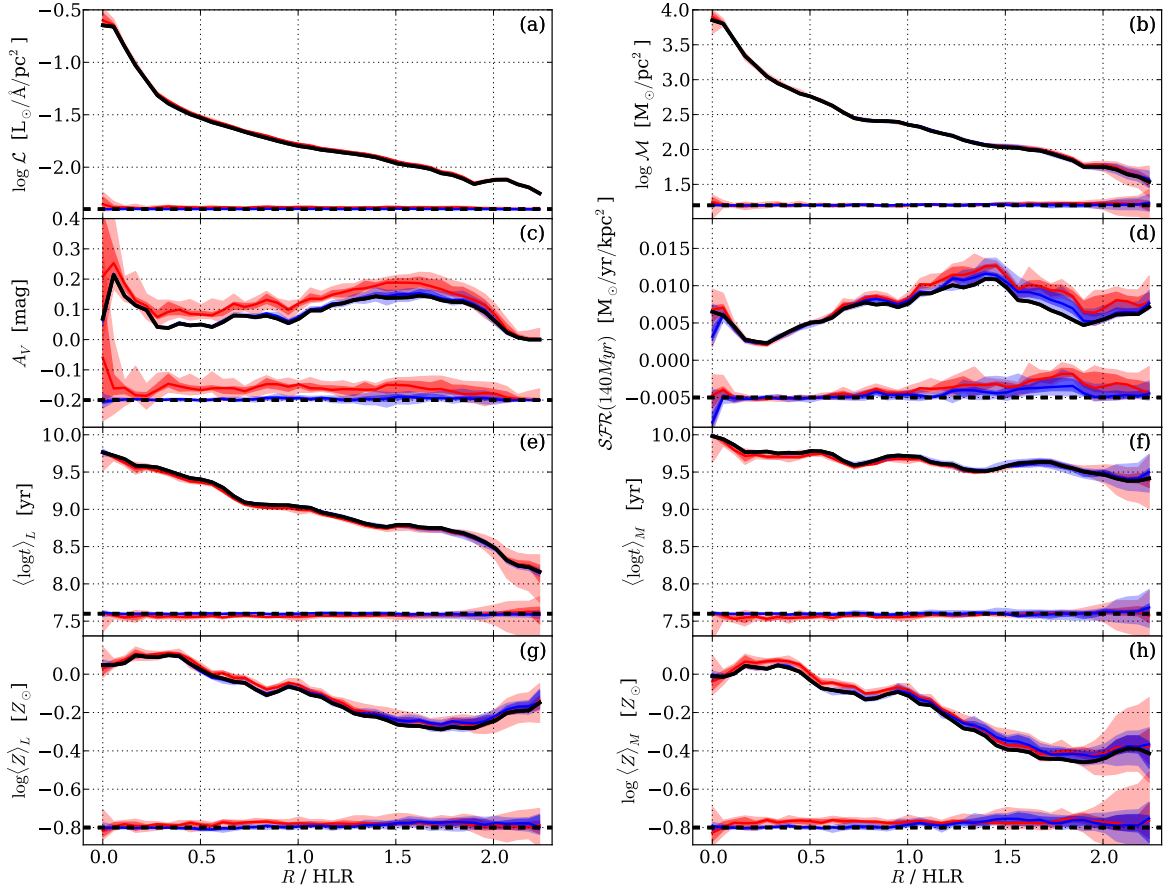
Fig. 4. Azymuthally averaged radial profiles of some global properties. (a) Dereddened luminosity surface density at 5635 Å; (b) stellar mass surface density; (c) extinction; (d) SFR surface density over the last 140 Myr; (e) luminosity and (f) mass weighted mean log ages; (g) luminosity and (h) mass weighted mean metallicities. The original solution is shown as the solid black line, while those obtained from simulations are shown in colored shades. Light blue shades show the full range of values found among the 10 realizations of random noise (OR1 runs). The darker blue bands mark the range spanned by the 6 values closer to the median (marked with the blue solid line). OC002 simulations of color-change effects are plotted in red. The differences between the simulations and original profiles are shown at the bottom of each panel, with the zero level indicated by the dashed black line. The dispersion and offsets along these difference profiles give a measure of the uncertainties and biases involved in the radial profiles.

even for our most pessimistic simulations (C004 and R3). This gain comes at the expense of a loss of spatial information—compressing the x, y plane to a single dimension (R) in the example presented here. Other forms of spatial averaging can be envisaged, like isolating structural components (bulge, disk, bar, arms, inter-arm regions). From the results above, it is easy to see that, as long as enough zones are involved in the statistics, any averaging scheme should lead to small uncertainties.

3.3. Uncertainties in Star Formation Histories

STARLIGHT outputs SFHs as population vectors: x and μ. The first gives the fractional contribution of each base element to the total flux at the chosen reference wavelength (5635 Å in our case), while the latter gives the corresponding mass fractions. The 39

ages in our base[6] sample the 1 Myr to 14 Gyr interval with a mean $\log t$ separation of just 0.1 dex. Individually, the strength of each component is not reliable (see Fig. 1 in Cid Fernandes et al. 2004 for an example), given the many ways that spectrally similar components can rearrange their x_j values to produce a similar total spectrum. Yet, their combination in indices such as $\langle \log t \rangle_L$ produces robust quantities, as shown by the simulations.

None of the properties studied in the previous sections relies heavily on the details of the spectral decomposition performed by STARLIGHT. Mean ages, for instance, are defined as the *first moment* of the age distributions encoded in x and μ. By construction, however, SFHs do rely on higher order descriptions of the age distribution. This section aims to evaluate the uncer-

---

[6] The base ages were chosen such that SSP spectra for ages in between t_j and t_{j+1} are adequately interpolated with the j and $j + 1$ SSPs (see Mateus et al. 2006 for further details).
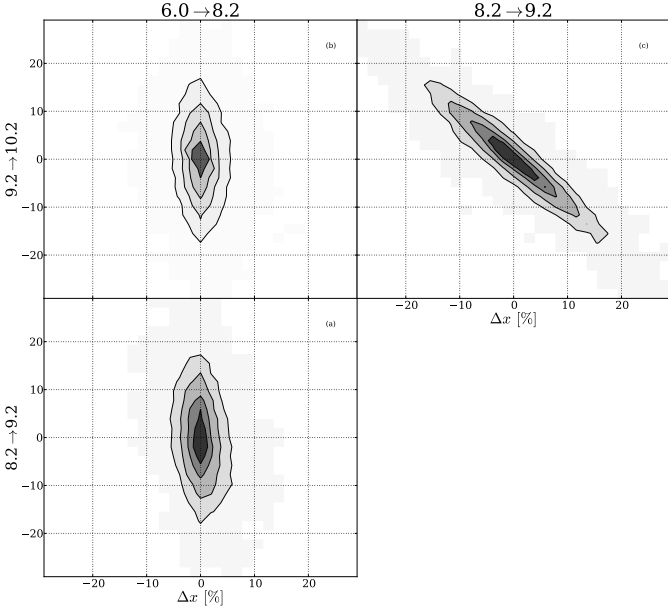
Fig. 5. Variations in the light fractions in Young, Intermediate and Old age groups (spanning $\log t = 6$–8.2, 8.2–9.2 and 9.2–10.2, respectively) for OR1 simulations. Contours are drawn at 20, 40, 60 and 80% of enclosed points.

Fig. 6. As Fig.5, but for a finer graded description of the SFH in terms of 5 age groups.

tainties in our SFHs. Before doing so, we digress on the actual meaning of the 'H' in SFH.

There is no standard semantics in what concerns the meaning of 'History' in spectral synthesis studies. On the contrary, the same term is used in very different ways in the literature, always qualitatively referring to some measure of the how star formation unfolded over time, but quantitatively varying from estimates of mean ages, to measures of the 'recent' star formation (where recent can mean anything between ~ 10 Myr and a few Gyr, depending on the tracers), and full t-by-t descriptions with varying age resolution. Besides different time scales, different metrics can be used to quantify the SFH, like luminosity or mass associated to stars in a given age range, in differential or cumulative forms, etc. This diversity is particularly natural in the case of non-parametric codes such as STARLIGHT. Because no pre-established functional forms for SFR(t) are imposed, one has plenty of freedom to design different indices and functions to characterize the SFH. Paper I is itself an example of this diversity. We have presented there a series of SFH diagnostics obtained by manipulating the x and μ vectors in different ways, always with the underlying philosophy of compressing the over-detailed output of STARLIGHT into coarser but more robust descriptions of the SFH.
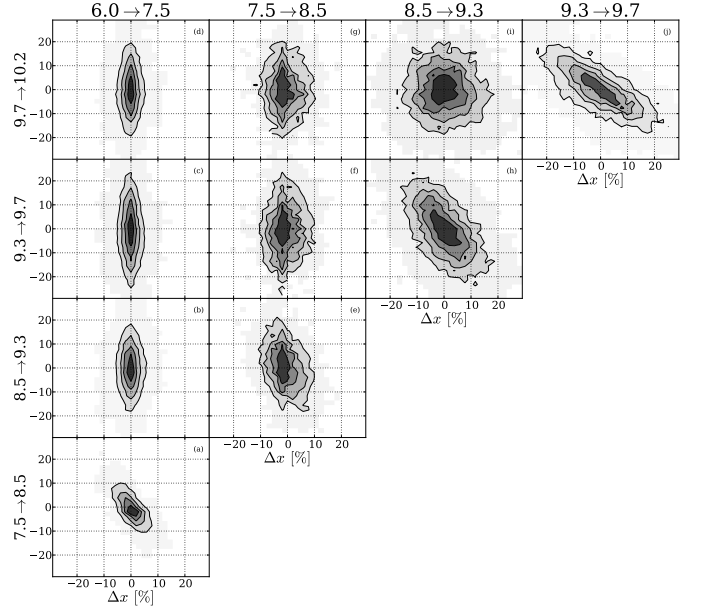
In short, there are numerous alternative ways to describe a SFH. In what follows we evaluate the uncertainties in a Paper I-inspired selection of SFH-descriptions. Following the sequence of our analysis of global properties, we first present results for uncertainties in individual zones (§3.3.1) and then for spatially averaged SFHs (§3.3.2).

3.3.1. SFHs for individual zones

One way to characterize SFHs is to compress the population vectors into age ranges, an approach which dates back to the early days of spectral synthesis (Bica 1988). In the context of STARLIGHT, Cid Fernandes et al. (2004 and 2005) showed that a robust summary of the SFH can be obtained by binning x into young (Y), intermediate (I) and old (O) groups. This $x \rightarrow (x_Y, x_I, x_O)$ compression scheme was employed to produce the maps shown in Figs. 8 and 9 of Paper I, where these age groups were separated by frontiers placed at $t = 0.14$ and 1.4 Gyr.

We have used our simulations to assess the uncertainties in these fractions. The top three rows in Table 3 list the O-runs statistics of Δx_Y, Δx_I and Δx_O, where, as before, $\Delta \equiv$ Simulated − Original value. The table shows that random noise at the one-σ level (R1 runs) induces uncertainties in x_Y, x_I and x_O of ~ 3, 9 and 9% respectively[7]. Larger uncertainties ($\sim 15\%$) in x_I and x_O apply for shape-changing perturbations at the level expected for CALIFA (OC002 runs). Part of this increase is due to aforementioned $A_V \geq 0$ effect, which forces low A_V zones which are perturbed to bluer spectra to become younger to compensate the inability to reduce A_V below 0. This is also reflected in the biases, with $\overline{\Delta}(x_I) \sim -\overline{\Delta}(x_O) \sim +5\%$. At any rate, comparing these uncertainties with $(\overline{x_Y}, \overline{x_I}, \overline{x_O}) = (15, 25, 60)\%$, the average values over all zones in CALIFA 277, one concludes that this compact description of the SFH is reasonably robust.

Fig. 5 show how the variations in these light fractions correlate with each other. Δx_O anti-correlates very strongly with Δx_I, which is not suprising given the $x_Y + x_I + x_O = 100\%$ constraint and the fact that these are the age groups which carry most of the light in CALIFA 277. The Y group, on the other hand, is roughly independent of the others.

---

[7] Notice that % here does *not* mean a relative deviation, but the very units of the x_Y, x_I and x_O fractions.

Uncertainties in light fraction in age groups: $\overline{\Delta x} \pm \sigma_{\Delta x}$ [%]

log t range	OE0	OR1	OR2	OR3	OC001	OC002	OC004
6.0→8.2	0.0 ± **1.9**	0.1 ± **3.3**	-0.0 ± **4.9**	-0.0 ± **6.0**	0.1 ± **2.2**	0.6 ± **2.7**	1.6 ± **4.2**
8.2→9.2	0.0 ± **4.5**	-0.1 ± **9.3**	0.7 ± **14.9**	1.2 ± **18.9**	0.7 ± **6.8**	4.3 ± **14.7**	9.4 ± **23.2**
9.2→10.2	-0.1 ± **4.0**	-0.2 ± **8.7**	-1.0 ± **14.0**	-1.7 ± **17.9**	-0.8 ± **6.4**	-5.0 ± **14.8**	-11.6 ± **23.9**
6.0→7.5	-0.0 ± **1.4**	-0.2 ± **3.0**	-0.4 ± **4.7**	-0.6 ± **5.8**	0.0 ± **1.6**	0.3 ± **2.4**	0.8 ± **4.0**
7.5→8.5	-0.4 ± **3.1**	-0.7 ± **5.9**	-1.3 ± **8.4**	-1.7 ± **10.1**	-0.4 ± **3.5**	-0.4 ± **4.8**	-0.1 ± **7.2**
8.5→9.3	0.0 ± **4.4**	0.0 ± **9.4**	0.6 ± **15.1**	1.2 ± **19.2**	0.7 ± **6.7**	4.5 ± **14.7**	9.8 ± **23.3**
9.3→9.7	-0.1 ± **5.5**	-0.7 ± **12.8**	-2.3 ± **19.6**	-4.0 ± **23.8**	-0.6 ± **7.7**	-3.2 ± **13.2**	-7.4 ± **18.2**
9.7→10.2	-0.1 ± **3.4**	0.1 ± **10.4**	0.4 ± **16.4**	1.0 ± **20.1**	-0.4 ± **5.6**	-2.3 ± **11.0**	-5.0 ± **15.4**

Table 3. As Table 2 but with the statistics of the light fractions in age groups for our different simulations. simulations. For each age group the table lists the mean simulated minus original difference ($\overline{\Delta}$) and its standard deviation (σ_Δ, in bold), both in percentages. The top part of the table corresponds to the Young, Intermediate and Old groups description discussed in the text and Fig. 5, while the bottom one is for 5-groups used in Fig. 6. The R1 and C002 columns are those applicable to CALIFA data.

Uncertainties in log mass in age groups: $\overline{\Delta \log M'} \pm \sigma_{\Delta \log M'}$ [dex]

log t range	OE0	OR1	OR2	OR3	OC001	OC002	OC004
6.0→8.2	0.00 ± **0.14**	-0.00 ± **0.21**	-0.02 ± **0.30**	-0.03 ± **0.37**	0.00 ± **0.16**	0.02 ± **0.20**	0.06 ± **0.29**
8.2→9.2	0.00 ± **0.12**	-0.01 ± **0.25**	-0.00 ± **0.37**	-0.00 ± **0.44**	0.01 ± **0.18**	0.08 ± **0.28**	0.15 ± **0.36**
9.2→10.2	-0.00 ± **0.05**	-0.00 ± **0.12**	-0.01 ± **0.19**	-0.02 ± **0.24**	-0.01 ± **0.08**	-0.04 ± **0.20**	-0.05 ± **0.33**
6.0→7.5	-0.00 ± **0.11**	-0.02 ± **0.18**	-0.05 ± **0.27**	-0.07 ± **0.32**	-0.00 ± **0.12**	0.01 ± **0.14**	0.02 ± **0.18**
7.5→8.5	-0.00 ± **0.22**	0.01 ± **0.35**	0.06 ± **0.43**	0.09 ± **0.49**	0.00 ± **0.24**	0.03 ± **0.29**	0.12 ± **0.39**
8.5→9.3	0.00 ± **0.12**	-0.00 ± **0.24**	0.01 ± **0.35**	0.03 ± **0.41**	0.01 ± **0.18**	0.08 ± **0.28**	0.16 ± **0.36**
9.3→9.7	0.00 ± **0.14**	-0.01 ± **0.25**	-0.02 ± **0.34**	-0.03 ± **0.39**	-0.01 ± **0.17**	-0.03 ± **0.24**	-0.04 ± **0.31**
9.7→10.2	-0.00 ± **0.11**	-0.01 ± **0.24**	-0.00 ± **0.34**	0.02 ± **0.38**	-0.01 ± **0.15**	-0.03 ± **0.27**	-0.00 ± **0.36**

Table 4. As Table 3 but for the (log) initial masses associated to stellar populations in different age groups.

Fig. 6 shows OR1-based results for a finer-graded description using 5 age groups, defined by log t [yr] = 6–7.5, 7.5–8.5, 8.5–9.3, 9.3–9.8 and 9.8–10.2. The anti-correlations among adjacent age groups are visible along the diagonal. The $\sigma_{\Delta x}$ values are 3, 6, 9, 13 and 10% (Table 3), for mean fractions of $\overline{x_t}$ = 13, 3, 24, 34 and 26%, respectively. This more detailed description shortens the difference between $\sigma_{\Delta x}$ values and the corresponding $\overline{x}$. The uncertainties are therefore larger, as expected, but these higher resolution SFHs are still useful, specially if used in a statistical way.

As the name implies, STARLIGHT fits light, so x-based SFH descriptions are the natural way to analyse its results. Yet, it is the stellar mass which carries the astrophysical information on the galaxy history. One can obviously group μ elements just as we did for x, but while light fractions in different age groups can be directly intercompared, mass fractions cannot. With a factor of ~ 1000 decrease in light-to-mass ratio from the youngest to the oldest elements in the base, wildly different mass fractions, say, $\mu_Y \sim 1\%$ and $\mu_O \sim 99\%$, can be equally relevant for the fits.

To evaluate uncertainties in the masses associated to different age groups it is better to use the masses themselves instead of mass-fractions. Table 4 reports the uncertainties in log M', where the prime denotes the initial stellar mass, uncorrected for the mass returned to the interstellar medium by stellar evolution. The table reports the results of the simulations for both the (Y,I,O) and the 5-age groups descriptions of the SFH discussed above. Again, the fact that we are now exploring higher moments of the age distribution implies larger uncertainties than for global properties. A column-by-column comparison with the $\Delta \log M'$ statistics in Table 2 confirms this. For instance, while the total masses have uncertainties of just 0.08 dex in OR1 runs, the masses in age-groups are typically 3 times more uncertain, an unavoidable but still reasonable price to pay for a time-resolved description of results of the spectral synthesis.

Further subdivisions lead to a quasi continuous regime which is better handled in ways other than age-binning, like cumulating x or μ. Fig. 7 illustrates this. The left panels show the cumulative light fraction, shown after a cosmetic smoothing by a FWHM = 0.2 dex gaussian in log t. Six individual zones, including the nucleus (top) and the last one (bottom), were chosen to exemplify this alternative description of SFHs and its uncertainties. The thick solid line traces the original STARLIGHT solution, while thin grey lines trace the solutions obtained for each of the 10 OR1 perturbations, whose median is drawn as a dashed line. The red-shaded bands mark the range spanned by the 6 SFHs closer to the median at each t. The right panels show the corresponding mass assembly histories, all scaled to 100% at $t = 0$. The six zones in Fig. 7 cover different distances from the nucleus, S/N and SFHs, thus providing representative examples of STARLIGHT results for CALIFA data.

Except for the nucleus, where the perturbed spectra and the associated SFHs are nearly indistinguishable from the original ones because of the very high S/N, there is a clear spread in cumulative light and mass distributions. The dispersion is larger for ages larger than a few Gyrs, which contain a substantial fraction of the light and most of the mass. The mild spectral evolution in this age range (Conroy 2013) explains the larger uncertainties, as components can be interchanged with relatively little variation in the total spectrum. Gauging the uncertainties in the cumulative SFHs by the width of the red band, we find it to be of the order of 10–20%, comparable to those reported in Tables 3 and 4 for age grouped quantities.

Despite uncertainties, the example SFHs in Fig. 7 reveal a gradual shift towards younger ages as one moves to larger radii. This trend is the higher order description of clear mean age radial gradients previously shown in panels e and f of Fig. 4, where results for individual zones at same R were averaged.
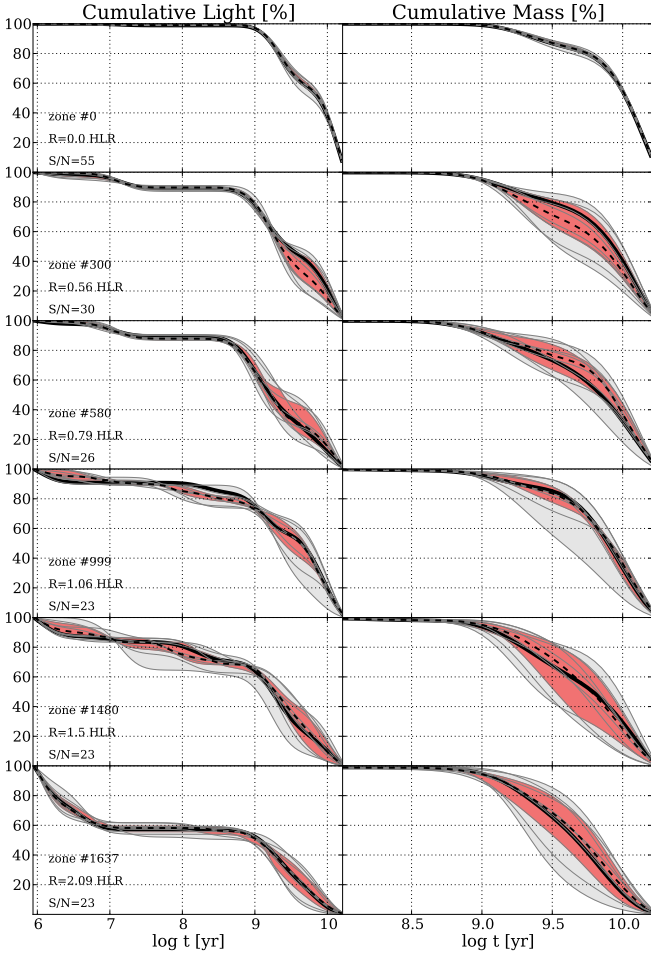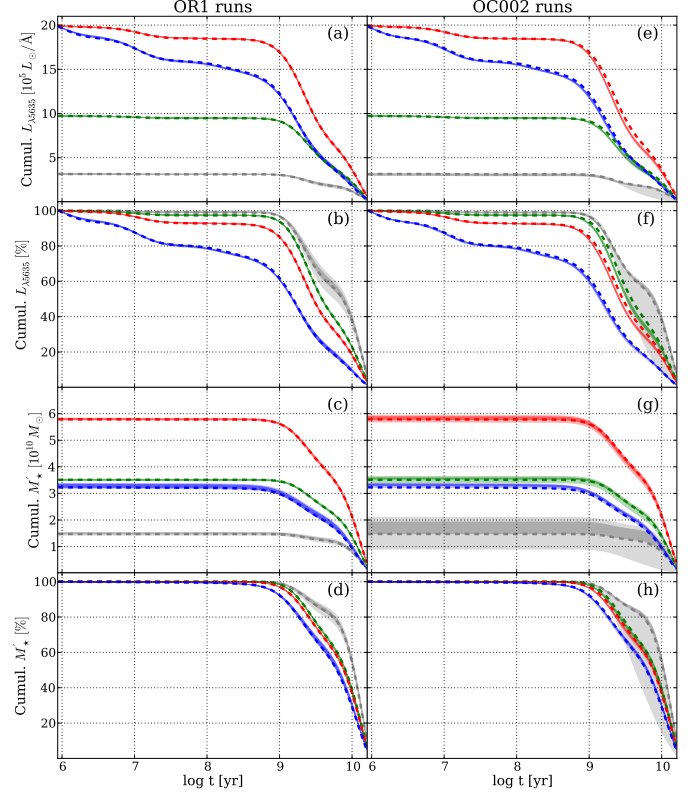
Fig. 7. SFHs of six different spatial zones, as represented by their cumulative light (left) and mass (right) distributions. Each panel shows 11 SFHs. The original one is plotted in thick black lines. Grey lines show the SFHs for the 10 realizations of OR1 simulations, with a grey shaded band tracing the full range of values. The median SFH is drawn as a dashed line, while the red band marks the range spanned by the 6 runs closer to the median. The zone number, distance to the nucleus and S/N are labeled in the left panels.

Fig. 8. Spatially averaged cumulative light and mass histories and their uncertainties for four regions: Red, blue, green and grey colors correspond to regions $R > 1$, $R < 1$, $R < 0.5$ HLR and the nucleus, respectively. Left and right panels show OR1 and OC002 simulations, respectively. The top four panels show cumulative light distributions, in both absolute (a, e) and relative (b, f) units. Similarly, the bottom four panels show the corresponding mass distributions. In each panel and for each radial region the original solution is drawn as a dashed line, while results of the simulations are shown with shaded bands, hardly visible except for the nuclear curves (grey). Light shaded bands show the ranges spanned by all 10 perturbations, and darker shades indicate the range spanned by the 6 versions closer to the median. The nuclear curves in panels a, c, e and g contain much less light and mass than the others, and so were multiplied by 20 for clarity.

3.3.2. Spatially averaged SFHs

In analogy with §3.2, uncertainties in the SFHs of individual zone spectra should be greatly reduced when averaging over spatial regions comprising many zones. This is confirmed in Fig. 8, which show cumulative light and mass distributions (in both absolute and relative units) for four spatial regions: The nucleus (grey), $R < 0.5$ (green), $R < 1$ (red) and $R > 1$ HLR (blue). The smoothing here is by FWHM = 0.5 dex in log t for compatibility with Fig. 11 of Paper I. OR1 runs are shown in the left panels, and OC002 on the right.

The statistical damping of the uncertainties is so strong that one can hardly notice that, as in Fig. 7, shaded bands are used to show the vertical ranges spanned by the simulations. The bands are so narrow that they look like thick lines. The "exception"

is the nucleus (grey), where the uncertainties are visible for the simple reason that, unlike for other regions, it does not involve any actual spatial averaging because it comprises a single spaxel.

Close inspection of the right panels reveals that the shape-changing simulations tend to have SFHs slightly skewed towards younger ages than SFHs inferred from spectral fits of the original data (marked by dashed lines). This is again the effect of some perturbations making low A_V zones too blue to be fitted with $A_V \geq 0$, so STARLIGHT compensates it with lower ages.

In conclusion, spatial averaging effectively eliminates the dispersions seen in the SFHs of individual zones. This remains valid even for simulations where the level of perturbations are higher than those expected for CALIFA spectra.

3.4. Summary of the simulations

The overall message from these experiments is that degeneracies inherent to stellar populations and uncertainties in the data have a limited impact upon our analysis. For the level of uncertainties expected in CALIFA, here represented by the R1 and C002 runs, the simulations yield acceptably small uncertainties in global properties. More precisely, mean ages and metallicities have one sigma variations of $\sim$ 0.1 dex when weighted in luminosity and $\sim$ 0.15 weighting by mass, while stellar masses are good to $\sim$ 0.1 dex (round numbers), with negligible biases. Uncertainties in A_V are $\sim$ 0.07 mag if only random noise is considered, increasing to 0.16 mag when shape-related uncertainties are accounted for. In the latter case, a bias of $\overline{\Delta A_V} \sim 0.06$ mag appears as a side-effect of forbidding negative A_V. Being a higher order product of the spectral synthesis, SFHs are naturally less strongly constrained than global properties, but the age-grouped and cumulative descriptions explored above were found to be relatively stable against random and spectral shape perturbations.

It is a consensus in the field of spectral synthesis that the results are best used in a statistical sense (e.g., Panter et al. 2006), and the present study endorses this view. First, averaging reduces uncertainties, as confirmed by our experiments with radial profiles (Fig. 4) and spatially averaged SFHs (Fig. 8), which showed that the results are stable against the kinds of uncertainties studied here. Second, and more importantly, large samples allow for *comparative* studies, which can reveal astrophysically valuable trends while mitigating worries about data or method related systematics affecting the absolute values. This point has been abundantly explored in spectral synthesis studies of SDSS galaxies, where inequivocal relations between, say, age, mass and metallicity, have been identified in spite of the uncertainties in the properties derived for individual galaxies. The analogy with IFS data is clear. In IFS each galaxy is a large sample by itself, and the very goal of IFS is to compare properties in one place against those somewhere else.

This concludes our study of data and method related uncertainties. This whole study was based on a single set of SSP models, a fundamental prior in the analysis. We now turn to the uncertainties resulting from this choice.

4. Uncertainties associated to evolutionary synthesis models: An empirical evaluation

SSP spectra are the key astrophysical ingredient in any spectral synthesis analysis, the dictionary which translates stellar properties to spectroscopic information, which can then be compared to data through different methods to extract physical properties and SFHs. The computation of model SSP spectra combines an assumed initial mass function (IMF) with stellar evolution theory (isochrones) and a library to provide the spectra of stars with temperature, gravity and chemical composition matching the values dictated by the evolutionary tracks. In practice, this algebric exercise stumbles upon a series of issues which directly affect the predicted SSP spectra.

First, despite its (well deserved) status as a founding stone of modern astrophysics, stellar evolution is still an open business. Rotation in massive stars (Levesque et al. 2012), rapid phases during the post main sequence evolution of intermediate mass stars (Maraston 2005), and binarity (Li et al. 2013) are examples of phenomena which affect the radiative output of stellar populations, but are still at the forefront of research, and thus prone to uncertainties. A practical example of how incomplete treatment of evolutionary phases affects spectral synthesis analysis is discussed by Koleva et al. (2008), Cid Fernandes & González Delgado (2010) and Ocvirk (2010). Using different codes, these studies find that spectral synthesis of old Milky Way and LMC globular clusters suggests the presence of very young stellar populations accounting for some 10–20% of the optical light, an astrophysically absurd result which also happens in some old, "red and dead" galaxies (Cid Fernandes et al. 2011). These "fake young bursts" (Ocvirk 2010) are in fact byproducts of inadequate modeling of the horizontal branch (and/or blue straglers, Cenarro et al. 2008). Seeking for a best match, the spectral synthesis uses young hot stars to replace the old hot ones missing in the models.

Secondly, spectral libraries, be they empirical or theoretical, have their own limitations (Martins & Coelho 2007). The widely used Bruzual & Charlot (2003; BC03) models, for instance, are based on the STELIB library (Le Borgne et al. 2003), a major advance in its days, but limited to 249 stars, some of which with severe spectral gaps. Its relatively poor coverage of the stellar parameter space propagates to the predicted SSP spectra, with collateral effects on the results of a spectral synthesis analysis. Koleva et al. (2008), for instance, noticed that, because of the lack of truly very metal rich stars in the library, BC03 spectra for $2.5 Z_\odot$ SSPs behave like $\sim Z_\odot$ models of larger age. In short, this too is an evolving field, undergoing constant revisions.

In this unstable scenario, it is relevant to evaluate to which extent the results of our spectral synthesis analysis depend on the choice of SSP models. To this end, we have performed spectral fits using three bases extracted from different sets of evolutionary synthesis models, listed in Table 5. We stress that this is by no means an exaustive exploration of this issue, but it suits our goal of estimating uncertainties related to this choice. §4.1 describes the sets of models to be compared. The CALIFA data used in this study are described in §4.2. Comparisons of the properties obtained with different sets of SSPs are presented in §4.3. Fit quality indicators and spectral residuals are discussed in §4.4, while §4.5 compares residuals in CALIFA and SDSS spectra.

4.1. SSP spectral models

Base *GM* is a combination of publicly available SSP spectra from Vazdekis et al. (2010)[8], which start at an age of 63 Myr, with the González Delgado et al. (2005)[9] models for younger ages. The former are based on stars from the MILES library (Sánchez-Blázquez et al. 2006), while the latter relies on the synthetic stellar spectra from the GRANADA library (Martins et al. 2005). Only minor adjustments were needed to match these two sets of models. First, we smoothed the GRANADA models to the spectral resolution of MILES (2.5 Å FWHM, cf. Beifiori et al. 2011 and Falcón-Barroso et al. 2011), and then multiplied them by a factor of 1.05, estimated from a direct comparison of the predicted spectra in the 63 Myr to 1 Gyr range, where these models agree very well in both continuum shape and absorption features. These independently derived SSP spectra complement each other, providing a base suitable for spectral fitting analysis of galaxies of all types.

The evolutionary tracks in base *GM* are those of Girardi et al. (2000), except for the youngest ages (1 and 3 Myr), which are based on Geneva tracks (Schaller et al. 1992; Schaerer et al. 1993a,b, Charbonnel et al. 1993). The specific subset of SSPs

---

[8] miles.iac.es

[9] www.iaa.csic.es/~mcs/sed@

Table 5. Sets of SSP models used for spectral fitting

Model-set	Code	Isochrones	IMF	Library	Metallicities	$N_Z \times N_t$	Ages [Gyr]
GM	SED@ + Vazdekis	Padova2000	Salpeter	GRANADA + MILES	0.004, 0.008, 0.019, 0.033	4×39	0.001–14
CB	Galaxev	Padova1994	Chabrier	GRANADA + MILES	0.004, 0.008, 0.02, 0.05	4×40	0.001–14
BC	Galaxev	Padova1994	Chabrier	STELIB	0.004, 0.008, 0.02, 0.05	4×40	0.001–14

used in the spectral fits comprises 39 ages between 1 Myr and 14 Gyr. Four metallicities are included: $Z = 0.2, 0.4, 1$ and 1.5 solar. The Salpeter IMF is adopted. Like the other bases discussed next, *GM* does not cover adequately the blue horizontal branch, both because it does not reach very low Z and because, as thoroughly discussed by Ocvirk (2010), these models perform poorly in this phase anyway.

Base *CB* is an updated version of the BC03 models (Charlot & Bruzual 2007, private communication), replacing STELIB by spectra from the MILES and GRANADA libraries. The IMF is that of Chabrier (2003), and the evolutionary tracks are those by Alongi et al. (1993), Bressan et al. (1993), Fagotto et al. (1994a, 1994b), and Girardi et al. (1996), collectively labeled 'Padova 1994' by BC03. $N_\star = 160$ SSPs comprising 40 ages in the 1 Myr to 14 Gyr range and 4 metallicities (0.2, 0.4, 1 and 2.5 $Z_\odot$) were chosen for the spectral fits.

Finally, base *BC* is built from the "standard" BC03 models, whose ingredients are identical to those of base *CB* except for the stellar library, which is STELIB. Base *BC* allows us to check if differences between results obtained with bases *GM* and *CB* are associated to isochrones and/or IMF instead of stellar libraries.

These three bases cover the same age range, and all have the same number of metallicities. All bases start at $Z = 0.004$ $(0.2Z_\odot)$[10], but *GM* stops at $1.5Z_\odot$, while both *CB* and *BC* go up to $2.5Z_\odot$. Because they are both based on stars not far from the Sun, neither MILES nor STELIB actually contain many stars as metal rich as $2.5Z_\odot$, so the latter models should be interpreted with care. On the other hand, the $Z \leq 1.5Z_\odot$ limit of base *GM* may be too low to accomodate the metal rich inner regions of galaxies, possibly leading to saturation effects. Base *GM* also differs from the others in IMF and isochrones. The differences in opacities and equation of state between Padova 2000 (*GM*) and 1994 (*CB* and *BC*) tracks produce somewhat warmer (hence bluer) stars in the red giant branch in the former than in the latter. In principle, one may thus expect to obtain older ages with *GM* than with *CB* and *BC*, but the diffences in color are very small in the spectral range of our data, only becoming noticeable at longer wavelengths (see Fig. 2 of BC03).

4.2. Data: 98291 spectra from 107 CALIFA datacubes

The experiments described below were based on data with the same characteristics and pre-processed in the exact same way as the data for CALIFA 277. The difference with respect to the simulations presented in the first part of this paper is that we now use 107 galaxies, out of which a total of 98291 spectra corresponding to individual spaxels (or Voronoi zones) were extracted following the methodology outlined in Paper I.

STARLIGHT fits of these spectra were carried out using the three bases described above. Our interest here is to identify and quantify differences in the results obtained with different model SSPs,

so we will overlook the spatial information and treat each spectrum as an individual. We now use this massive dataset to compare the results obtained with bases *GM*, *CB* and *BC*.

4.3. Comparison of global properties

Fig. 9 compares results obtained with bases *CB* (horizontal axis) and *GM* (vertical). The top panels compare values of $\langle \log t \rangle_L$, $\log \langle Z \rangle_M$, A_V and $\log M'$ for all 98921 individual zones, grayscale-coding by the density of points. Notice the wide ranges of values in all panels, illustrative of the diversity of properties spanned by the data. Each panel quotes the mean Δ and its standard deviation, where $\Delta = \text{property}(GM) - \text{property}(CB)$.

GM-based initial stellar masses are higher than *CB* ones by 0.14 dex on-average, reflecting their different IMFs.[11] Apart from this offset, the two masses agree to within 0.16 dex. Mean ages and extinctions are also in good agreement, with dispersions of 0.14 dex in $\langle \log t \rangle_L$ and 0.06 mag in A_V, and insignificant offsets. Metallicities are obviously related, but with a substantial scatter due to a combination of the difference in evolutionary tracks and IMF, coarse Z grids, intrinsic difficulties in estimating metallicities, and the aforementioned difference in maximum Z.

To estimate the effect of this in-built difference we have carried out experiments replacing the $2.5Z_\odot$ SSPs in *CB* by models interpolated to $1.5Z_\odot$, thus matching the Z's in *GM*. This modified *CB* base produces $\log \langle Z \rangle_M$ values which differ by $\sigma_\Delta \sim 0.15$ dex from the *GM*-based ones, slightly better than the 0.18 dex obtained with the original *CB*. Leaving aside caveats associated to the interpolation of SSP spectra, this result indicates that the difference in maximum Z between *GM* and *CB* has a relatively modest impact on the difference between $\log \langle Z \rangle_M$ values obtained with these two bases, so that differences in evolutionary tracks and IMF are also relevant.

The bottom panels repeat the comparison of the same four properties, but now for galaxy-wide values, so there are only 107 points.[12] These cleaner plots confirm the results from the zone-by-zone comparison. Naturally, galaxy-wide averages are much more robust than values for individual zones, so the σ_Δ dispersions are significantly smaller than those quoted in the top panels. $\langle Z \rangle_M$ estimates distribute around the identity line up to $Z_\odot$, where the relation bends down due to the differences in the maximum Z between the bases. In these cases all one can be sure of is that metalicities are over-solar.

Fig. 10 compares results for bases *BC* (vertical axis) with *CB* (horizontal). Masses, ages, and extinctions agree to within 0.15 dex, 0.16 dex and 0.09 mag respectively, with a tendency of A_V

---

[10] We exclude lower metallicity models to avoid SSPs that are not so well covered by the stellar libraries. Base *GM* base could include SSPs at $Z = 0.001$, but we do not do so because this metallicity is not available in the *CB* and *BC* models.

[11] Recall that M' refers to the initial stellar mass. The difference between *GM* and *CB* masses increases to 0.27 dex when stellar mass loss is accounted for.

[12] M' in this case is the sum of the M'_z values for each zone. The galaxy-wide $\langle \log t \rangle_L$ is obtained from $\sum_j \log t_j \sum_z L_{jz} / \sum_j \sum_z L_{jz}$, where j is the base age index and z is a zone index. $\langle Z \rangle_M$ is computed analogously. Lastly, the galaxy-wide A_V is defined as the mean A_{V_z} of all its zones.
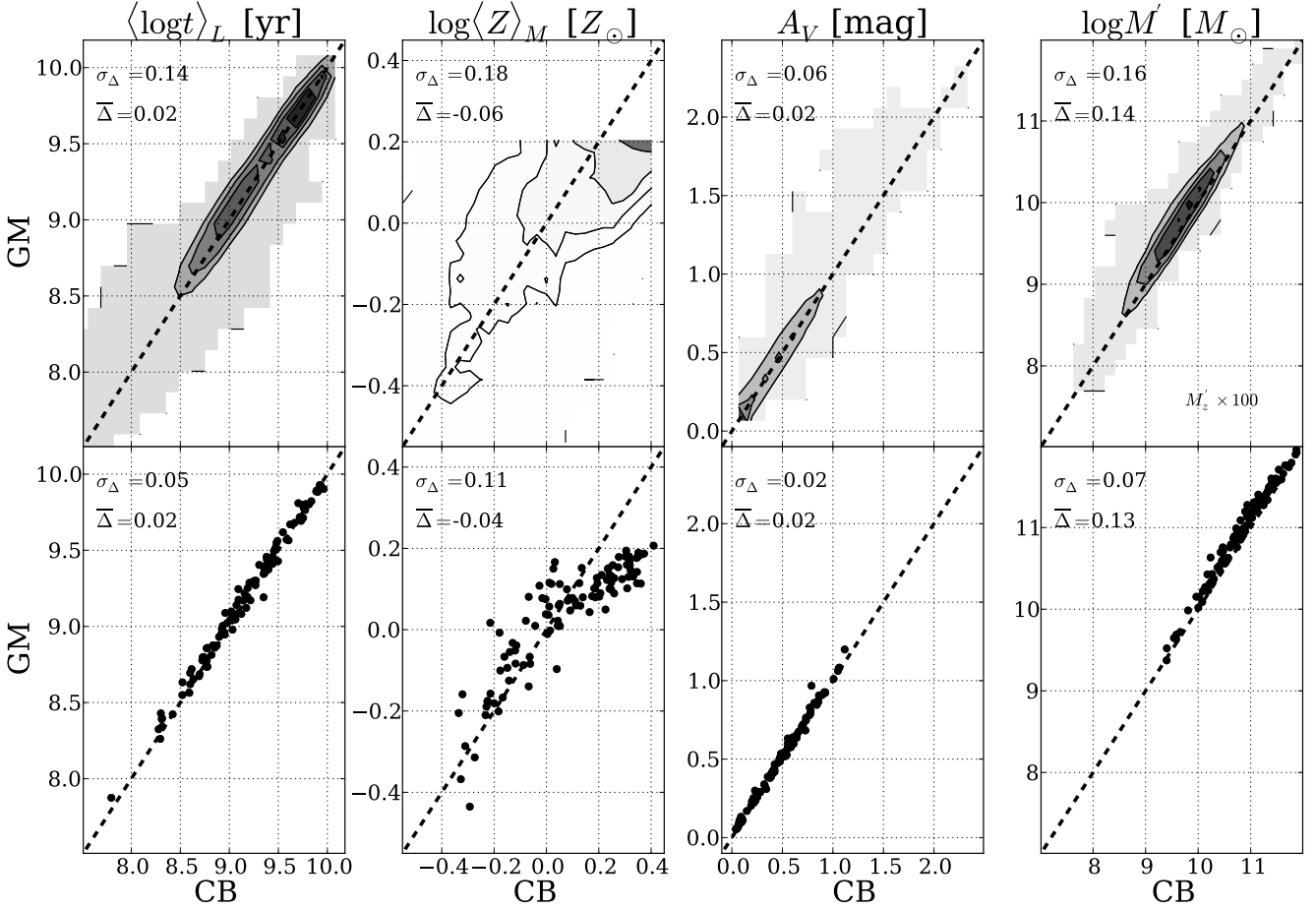
Fig. 9. Comparison of the global properties obtained with different bases *GM* (vertical axis) and *CB* (horizontal). The top panels compare luminosity weighted ages ($\langle \log t \rangle_L$), mass weighted metallicities ($\log \langle Z \rangle_M$), extinction (A_V) and initial stellar masses ($\log M'$) obtained for $\sim 10^5$ zones of 107 CALIFA galaxies, with contours drawn at every 20% of enclosed points. The bottom panels repeats the comparisons, but now for galaxy-wide values. A one-to-one line is drawn in all panels. Note that zone masses in the top right panel are multiplied by 100 to put them on the same scale as the bottom panel.

to be 0.04 mag smaller in *BC* fits. This relatively good level of agreement does not apply to mass weighted metallicities, which differ substantially. Given that these two sets of models coincide in isochrones, IMF and evolutionary synthesis code, this disagreement must be related to the stellar libraries. Because of the several improvements in MILES over STELIB (Sánchez-Blázquez et al. 2006), metallicities from the *CB* and *GM* bases should be considered more reliable than those obtained with *BC* (see also Koleva et al. 2008). This is in line with previous empirical tests by González Delgado & Cid Fernandes (2010), who showed that MILES based SSP spectra perform better than STELIB based ones in matching the metallicities of star clusters derived from spectroscopy of individual stars or CMD analysis of the same systems.

Fig. 11 shows histograms of the pair-wise Δ's: $GM - CB$ (top), $BC - CB$ (middle), $GM - BC$ (bottom). The width of these histograms (the σ_Δ values listed in each panel) gives a measure of the uncertainties related to the choice of evolutionary synthesis models for the spectral fits. As usual, mass weighted properties present larger uncertainties than luminosity-weighted ones. Metallicities, for instance, have dispersions in $\Delta \log \langle Z \rangle_L$ of 0.14

and 0.19 dex (*GM* versus *CB*, and *BC* versus *CB*, respectively), smaller than the 0.18 and 0.27 dex found for $\Delta \log \langle Z \rangle_M$.

The overal conclusion of these comparisons is that, from a statistical perspective, physical properties obtained from a spectral synthesis analysis do not depend strongly on the choice of SSP models. Mean ages and extinctions retrieved with the three models investigated here all agree to within relatively small margins, and the same is true for stellar masses once in-built differences in IMFs are accounted for. Metallicities are generally harder to estimate and our experiments confirm that. Unlike other properties mean Z's are sensitive to the choice of models. Base *BC* gives the most discrepant results, highlighting the influence of stellar libraries.

Rounding up numbers, we find that uncertainties related to the SSP models adopted in the analysis are of the order of 0.15 dex in $\langle \log t \rangle_L$, 0.23 dex in $\langle \log t \rangle_M$, 0.15 dex in $\log M'$ and 0.1 mag in A_V. Excluding *BC* models, $\log \langle Z \rangle_L$ and $\log \langle Z \rangle_M$ have uncertainties of 0.14 and 0.18 dex, respectively.
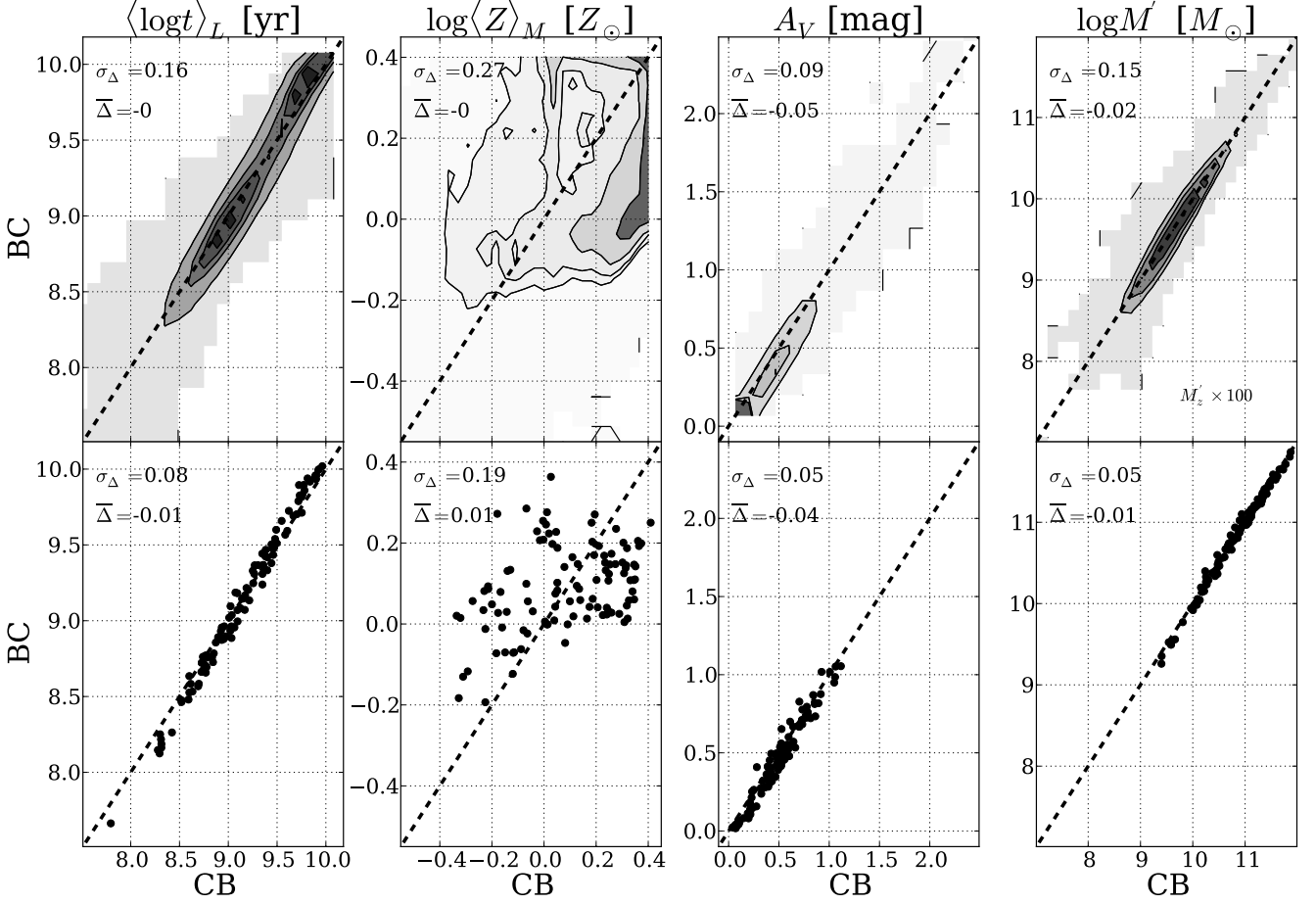
Fig. 10. As Fig. 9, but comparing results obtained with base *CB* (horizontal axis) and *BC* (vertical). Ages, extinction and masses agree well, but BC-based mean metallicities differ significantly from both *CB* and *GM*-based estimates.

4.3.1. Models versus data and method related uncertainties

How do these uncertainties compare with those related to the data and synthesis method, derived in the first part of this article?

To answer this, we focus on the OR1 and OC002 simulations described in §2.1, as they are the ones which represent random noise and shape-calibration errors in CALIFA. Comparing the σ_Δ values in Fig. 11 with those for the OR1 simulations in Fig. 1 we see that the former are roughly twice as large as the latter. In fact, the σ_Δ values in the top panels of Fig. 11 are closer to those obtained in the simulations where the noise was artificially amplified by a factor or 2 (OR2 runs in Table 2). Shape-related uncertainties also lead to uncertainties somewhat smaller than those found in this section, with the exception of A_V, whose uncertainty is 0.16 mag in the OC002 runs but 0.1 mag or less in ΔA_V histograms in Fig. 11. A visual comparison of Figs. 1 and 11 corroborates the conclusion that uncertainties related to differences among SSP models are larger than those related to data and method.

These comparisons, however, are not entirely fair, since model related uncertainties were evaluated from $\sim 10^5$ zones of 107 galaxies, while data + method related uncertainty estimates were based on 1638 zones of a single galaxy, perturbed 10 times in the simulations. Redoing Fig. 11 for CALIFA 277

alone we still find σ_Δ values higher than those found in §3, but by a smaller margin. The important message, therefore, is not so much that variance among current SSP spectral models leads to larger uncertainties than those related to data + method, but that both kinds of uncertainties are of the same order.

4.4. Quality of spectral fits

In principle one could use the quality of the spectral fits as a criterion to favor one base over another. In practice, however, all bases studied here provide $\sim$ equally good fits to the data. This is illustrated in Fig. 12, which shows the distributions of two figures of merit. Green, red and blue correspond to bases *GM*, *CB* and *BC*, respectively. The histograms are nearly identical. Considering all 98291 fits, the mean (median) values of the relative spectral deviation (eq. 6 of Paper I) are $\overline{\Delta}$ = 4.33 (3.92), 4.34 (3.93) and 4.37 (3.94) % for bases *GM*, *CB* and *BC* respectively, while the corresponding mean (median) χ^2 per fitted flux are 1.14 (0.96), 1.15 (0.97) and 1.18 (0.99). Formally, this puts base *GM* in 1st place, with *CB* in 2nd and *BC* in 3rd, but these statistics reveal that it is clearly not possible to favour one or another model in terms of fit quality. Because of their more complete spectral libraries, we favor bases *GM* and *CB* over *BC*.
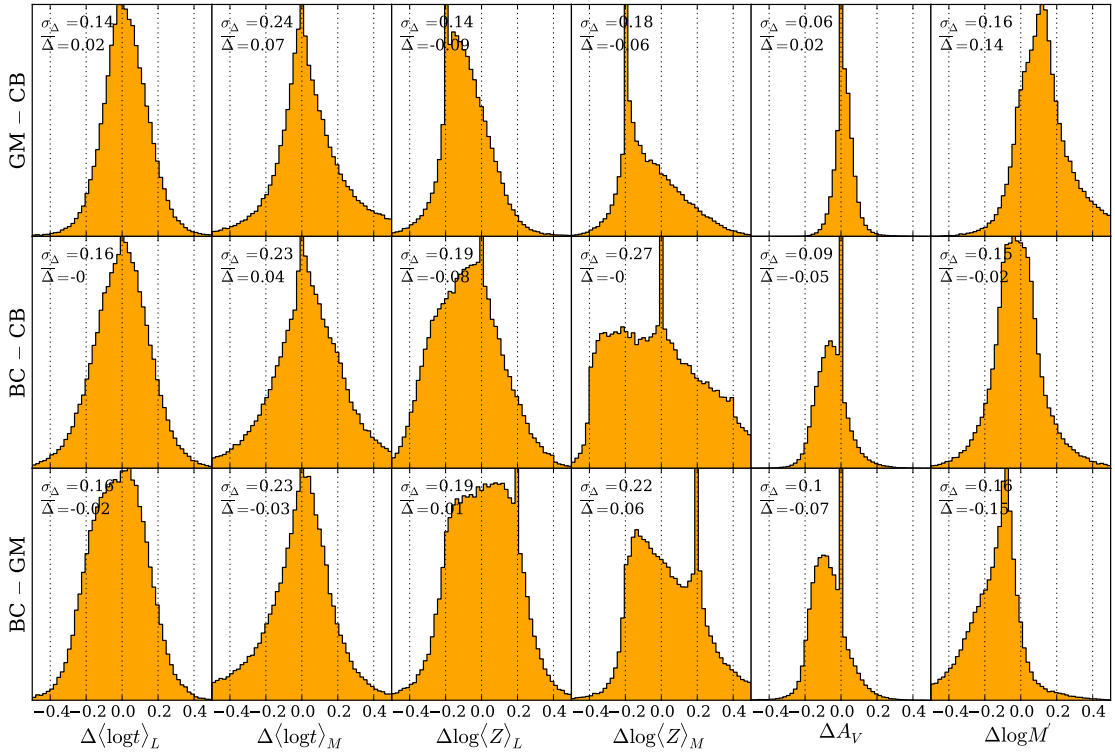
Fig. 11. Histograms of differences in global properties obtained with bases *GM*, *CB* and *BC*. Δ's are defined as *GM* − *CB* in the top panels, *BC* − *CB* in the middle, and *BC* − *GM* in the bottom ones. The horizontal scale is the same as in Fig. 1 to facilitate the comparison of data + method related uncertainties with the model related ones.

Fig. 13 provides a more direct visualization of the quality of the spectral fits. The top panel shows (in black) the average of all zone spectra (for examples of fits to individual zones see González Delgado et al., in prep.). Each spectrum is first divided by the median flux in the 5590–5680 Å normalization window, such that all zones weight equally in the average. The average synthetic spectra are shown in green, red and blue for fits with bases *GM*, *CB* and *BC*, respectively, vertically offset for clarity. The corresponding residual spectra are shown in the bottom of the same panel, but can hardly be distinguished on this scale. This similarity persists even after zooming in by a full order of magnitude in the flux scale, as shown in Fig. 13b. Gaps in this zoomed plot correspond to our generic emission line mask, ie., λ-windows which were ignored in the STARLIGHT fits. Notice that, because of bad pixel flags, augmented by windows around telluric features (Paper I), the number of specra involved in these averaged residuals varies for each λ, as shown in the bottom panel.

4.5. Spectral residuals and comparison with SDSS

Clearly, the amplitude of the average spectral residuals is very small. Whereas the typical relative deviation for fits of individual zones is $\overline{\Delta} \sim 4\%$ (Fig. 12), for the average spectra in Fig. 13 it is a tiny $\overline{\Delta} = 1\%$. This 4-fold reduction indicates that random noise is responsible for a large share of the residuals in spectral fits of individual zones. Yet, if the residuals were truly random, this

reduction should be by a factor of the order of $\sqrt{98291} \sim 300$, not just 4. Residuals may be small, but they are definitely real.

The systematics of the spectral residuals are visible in Fig. 13b. These deviations must be related to issues in the method, data and/or models.

The narrow positive peaks in the average residual spectrum are due to our fitting method. They are in fact emission lines not included in our generic emission line mask. [NeIII]λ3869, H8λ3889, [NI]λ5199 and [OI]λ6364 are the clearest ones in Fig. 13b, but weaker lines such as H9λ3835 and HeIλ6678 are identified upon closer inspection. The conservative clipping parameters adopted in the fits (see Paper I) prevent STARLIGHT from authomatically clipping these lines completely. Other STARLIGHT-based studies circumvent this problem by building emission line masks taylored for each spectrum individually (Mateus et al. 2006; Asari et al. 2007), a refinement which is yet to be implemented in our CALIFA pipelines.

The most noticeable features in Fig. 13b, however, are not the emission lines, but the broad $O_\lambda < M_\lambda$ trough around Hβ and the $O_\lambda > M_\lambda$ bumps in the 5800–6000 Å region. In order to understand whether these features are particular to CALIFA data we have compiled SDSS spectra for 50 galaxies in common with the current sample and analysed them using the same masks, wavelength range, sampling, and STARLIGHT configuration as used for CALIFA. These spectra were then averaged as in Fig. 13, and compared to the spectral statistics obtained from the nuclear CALIFA spectra of the same 50 galaxies. Fig. 14 shows the results of this comparison. The figure follows the same layout as Fig. 13, with spectral statistics for the 50 CALIFA nuclei and the
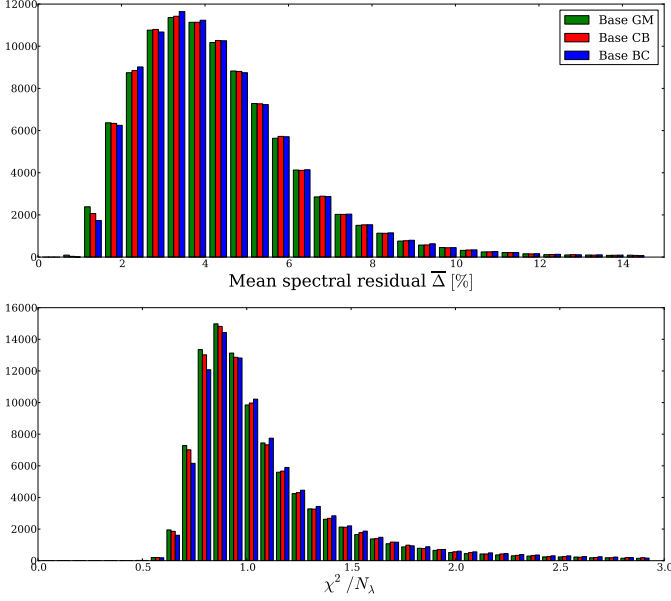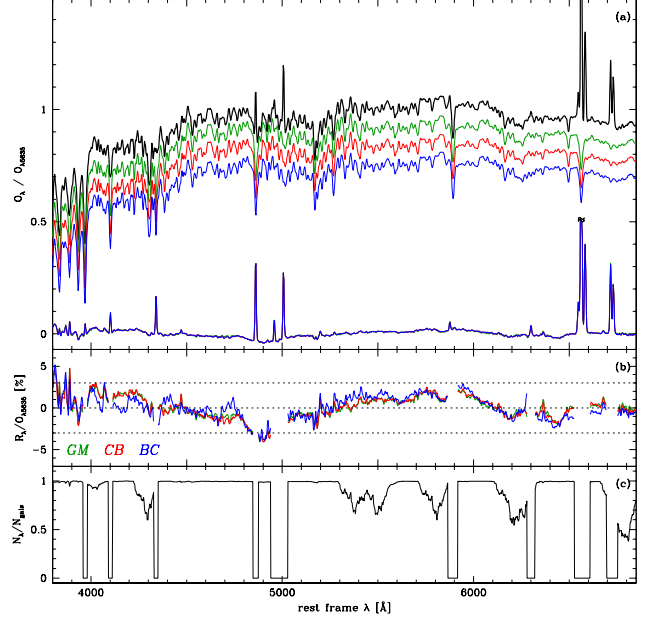
Fig. 12. *Top:* Distribution of the mean percentual spectral deviation for STARLIGHT fits with the *GM* (bars in green), *CB* (red) and *BC* (blue) bases. *Bottom:* As above, but for the distribution of χ^2 per fitted flux. In both cases the distributions are essentially identical, reflecting the fact that the three bases provide equally good spectral fits.

Fig. 13. *(a)* The black line shows the mean ("stacked") normalized spectrum of 98291 zones from 107 CALIFA galaxies, obtained by averaging $O_\lambda/O_{\lambda 5635}$. Green, red and blue lines (offset for clarity) show the mean synthetic spectra for bases *GM*, *CB* and *BC*, respectively. The corresponding $(O_\lambda - M_\lambda)/O_{\lambda 5635}$ residual spectra are shown with the same colors, but they are hardly distinguishable. *(b)* Zoom of the spectral residuals in the top panel, with emission lines removed for clarity. Dashed lines mark residuals of -3, 0 and $+3\%$. *(c)* Fraction of the 98291 zones contributing to the spectral statistics in the midde panel.

corresponding SDSS spectra plotted on the left and right panels, respectively. The spikier appearance of the SDSS residuals is due to its higher spectral resolution (3 versus 6 Å FWHM), but this is irrelevant for the broad residual features discussed above.

The humps around the ~ 5800 Å region of CALIFA residuals are clearly absent in the SDSS. These features are seen as shallow slanted bands in Fig. 16 of Husseman et al. (2013), where residuals for 100 galaxies are sorted by redshift. We have tracked the origin of this feature to an imperfect removal of telluric NaI bands around 5900 Å in the observed frame. In analogy with what happened with the SDSS data releases, as CALIFA data is used, imperfections like this will be identified and, when possible, corrected for in future updates of the data base.

The trough around Hβ, however, is present in both SDSS and CALIFA spectra. In fact, this problem has been noticed before (Cid Fernandes 2006; Panter et al. 2007; Walcher et al. 2009), but not satisfactorely explained to date. The fact that this feature appears in both data sets suggests that the models overpredict the continuum in a ~ 200 Å wide region centered around Hβ. On the other hand, the fact that the problem is present for both MILES and STELIB based models suggest that its origin is more likely related to data calibration issues. This latter view is supported by studies like Ferré-Mateu et al. (2012), where STARLIGHT fits of William Herschel Telescope long-slit spectra of massive compact galaxies with the Vazdekis et al. (2010) models (included in our *GM* base) do not reveal the Hβ trough seen in Fig. 13b. While a full investigation of this issue is beyond the scope of this paper, we note that the trough tends to be more pronounced in younger systems, as previously reported by Cid Fernandes (2006, see his Figure 5).

The negative residual seen in the region of Mg lines near 5175 Å is almost as strong as the Hβ trough. This deficit is due to differences in the abundances of α elements between galaxies (particular the central regions of massive ones) and stars in the stellar libraries. The fact that this residual is stronger in Fig. 14 (nuclear spectra) than in Fig. 13 (all zones) is likely due to α/Fe gradients. Walcher et al. (2009) report steps towards incorporating α/Fe in spectral synthesis analysis.

4.6. Public distribution of base GM spectra

Given the good performance of the *GM* base in the tests discussed in this section, we make these spectra available to the community in www.iaa.es/~rosa/AYA2010/AYA2010. We stress that these models were produced by González Delgado et al. (2005) and Vazdekis et al. (2010), to whom all credit should be given. Our distribution just puts these two sets of models together.

5. Summary

We have performed an extensive study of the uncertainties in the stellar population properties derived from STARLIGHT fits of optical integral field spectra from the CALIFA survey. In the first part of this investigation, Monte Carlo simulations were used to explore the effects of random noise, continuum shape calibration uncertainties and degeneracies in the spectral synthe-
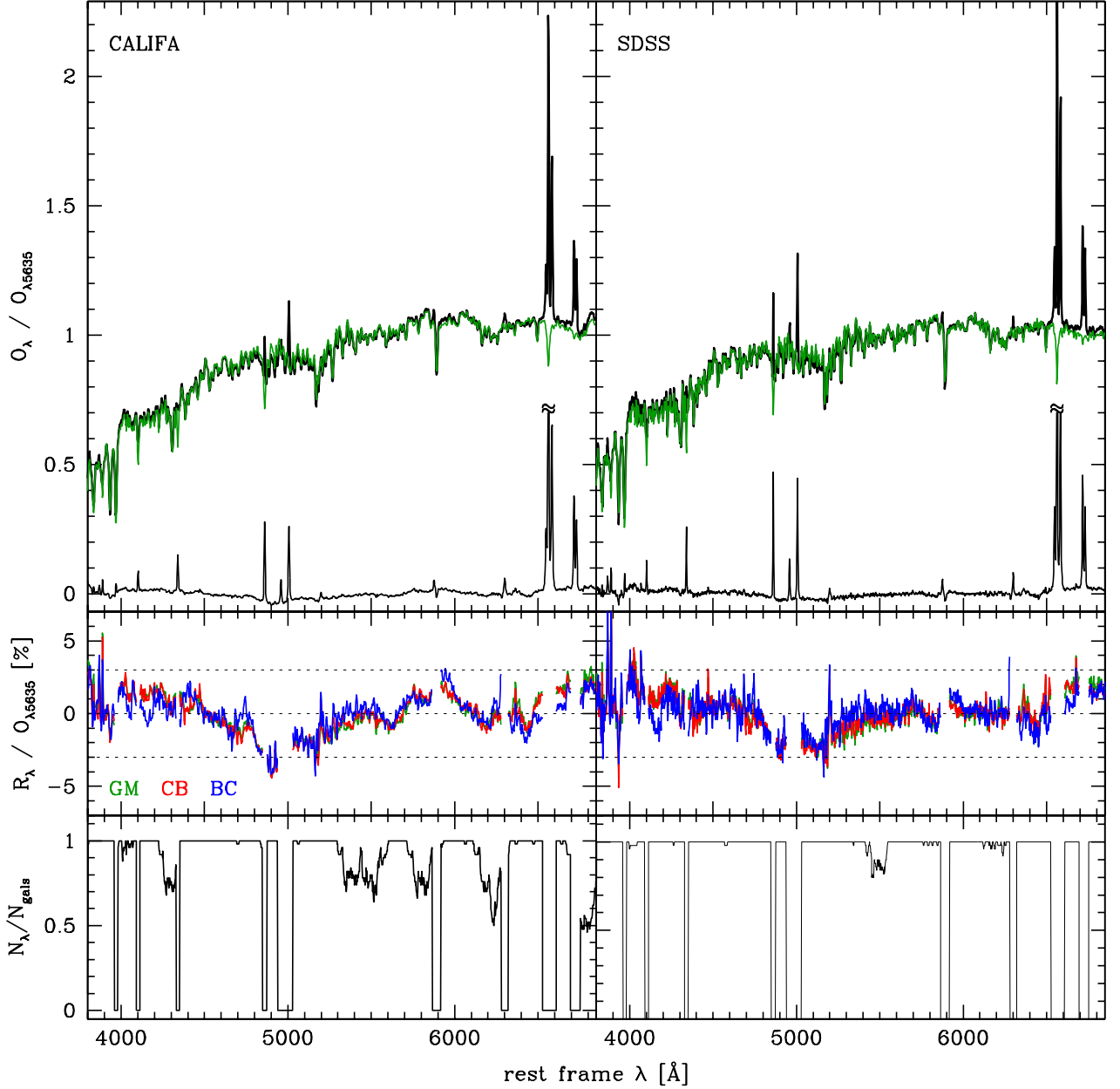
Fig. 14. As Fig. 13, but for a subset of 50 CALIFA galaxies for which SDSS spectra are available. Unlike in Fig. 13, however, the top panels show only results for *GM* based spectral fits. Left panels show the spectral statistics for the nuclear extractions of CALIFA datacubes, whereas those on the right show results obtained from STARLIGHT fits to the SDSS spectra.

sis. The simulations are based on the data and STARLIGHT fits of 1638 zone spectra of the Sb galaxy CALIFA 277 (NGC 2916). Uncertainties in mean age, metallicity, extincion, stellar mass and SFHs were evaluated both at the level individual zones (treating the datacube as a collection of unrelated spectra) and exploring the statistical power of IFS by means of radial profiles and other spatial averages. Second, we explore the variations in physical properties due to the use of different sets of models for SSP spectra. We compare physical properties and spectral residuals obtained from fits with three different SSP bases: (a) a combination of Gonzalez Delgado et al. (2005) and Vazdekis et al.

(2010) models (*GM*); (b) preliminary Charlot & Bruzual models using the GRANADA and MILES libraries (*CB*); (c) the standard Bruzual & Charlot (2003) models with STELIB (*BC*). This comparison employs $\sim 10^5$ spectra from 107 CALIFA galaxies.

Our main results can be summarized as follows:

1. The level of noise in CALIFA spectra leads to one-σ uncertainties in mean ages and metallicities of ~ 0.08 dex when weighting in luminosity and ~ 0.15 dex weighting by mass. Stellar masses are uncertain at the ~ 0.08 dex level, while $\sigma(A_V)$ is about 0.06 mag.

2. Shape-related calibration uncertainties of 0.05 mag in $g - r$ produce uncertainties of the same order of those induced by random noise, except for A_V, which becomes uncertain at the level of $\sigma \sim 0.16$ mag and biased by $+0.05$ mag.

3. Time resolved SFHs are higher order products of the spectral synthesis, inevitably subjected to larger uncertainties than global properties. For instance, we find that, for individual zones, stellar masses formed in broad age ranges have uncertainties about 3 times larger than those of the mass formed over all times. While SFHs of individual zones do carry useful information, a statistical approach is more advisable.

4. Spectral synthesis results are best used in comparative studies involving large samples, and IFS data fit this requirement perfectly. Spatial averaging reduces uncertainties while preserving enough information on the history and structure of stellar populations. Radial profiles of mean ages, metallicities, mass density and extincion are found to be very robust due to the large number statistics of datacubes. For instance, uncertainties in the data and limitations of the synthesis have a negligible impact upon the negative age and metallicity gradients detected in CALIFA 277. Similarly, SFHs averaged over different spatial regions are much more stable than those obtained for individual zones.

5. Mean ages, extinction and stellar masses obtained with *GM*, *CB* and *BC* models are reasonably consistent with one another, with one-σ differences in $\langle \log t \rangle_L$, $\langle \log t \rangle_M$, $\log M'$ and A_V of ~ 0.15, 0.24, 0.15 dex and 0.08 mag, respectively. *GM* and *CB* produce luminosity (mass) weighted metallicities consistent to within 0.14 (0.18) dex rms, while *BC*-based metallicities hardly correlate with the others.

   The variations induced by the use of different SSP models are larger than uncertainties due to data and method by roughly a factor of 2, highlighting the important role of this ingredient in the whole analysis.

6. The quality of the spectral fits is very nearly the same whichever set of SSP models is used. Spectral residuals are of the order of 4% for individual zones and 1% when averaged over all zones and galaxies. The strongest feature in the residual spectra is a broad but shallow ($\sim 3\%$) trough around Hβ, also present in SDSS spectra, and its origin remains unidentified. Other systematic features in the residual spectra were tracked to incomplete masking of weak emission lines, imperfect removal of telluric features and the lack of α enhanced models in the base.

These results, along with the tables and figures in this paper, fulfill our goal of assessing the uncertainties on the several products of STARLIGHT applied to CALIFA datacubes presented in Paper I. The combination of these spatial and temporal diagnostics of stellar populations with the diversity of galaxy types in the CALIFA survey offers new ways to study galaxy evolution, which shall be explored in other publications by our collaboration, and this paper provides quantitative and qualitative guidelines on how to interpret them appropriately.

References

Alongi M., Bertelli G., Bressan A., Chiosi C., Fagotto F., Greggio L., Nasi E., 1993, A&AS, 97, 851

Asari, N.V., Cid Fernandes, R., Stasińska, G., Torres-Papaqui, J.P., Mateus, A., Sodré, L., Schoenell, W., Gomes, J. M., 2007, MNRAS, 381,

Beifiori, A., Maraston, C., Thomas, D., & Johansson, J. 2011, A&A, 531, A109

Bica E., 1988, A&A, 195, 76

Bressan A., Fagotto F., Bertelli G., Chiosi C., 1993, A&AS, 100, 647

Cenarro, A. J., Cervantes, J. L., Beasley, M. A., Marín-Franch, A., & Vazdekis, A. 2008, ApJ, 689, L29

Charbonnel, C., Meynet, G., Maeder, A., Schaeller, G., Schaerer, D., 1993, A&AS, 101, 415

Chabrier G., 2003, PASP, 115, 763

Charlot, Bruzual, 2007, private communication

Cid Fernandes R., Gu Q., Melnick J., Terlevich E., Terlevich R., Kunth D., Rodrigues Lacerda R., Joguet B., 2004, MNRAS, 355, 273

Cid Fernandes R., Mateus A., Sodré L., Stasińska G., Gomes J. M., 2005, MNRAS, 358, 363

Cid Fernandes R., 2006, BAAA, 49, 228

Cid Fernandes R., González Delgado R. M., 2010, MNRAS, 403, 780

Cid Fernandes R., Stasińska G., Mateus A., Vale Asari N., 2011, MNRAS, 413, 1687

Conroy C., 2013, arXiv, arXiv:1301.7095

Fagotto F., Bressan A., Bertelli G., Chiosi C., 1994a, A&AS, 104, 365

Fagotto F., Bressan A., Bertelli G., Chiosi C., 1994b, A&AS, 105, 29

Falcón-Barroso, J., Sánchez-Blázquez, P., Vazdekis, A., et al. 2011, A&A, 532, A95

Ferré-Mateu, A., Vazdekis, A., Trujillo, I., et al. 2012, MNRAS, 423, 632

Girardi L., Bressan A., Chiosi C., Bertelli G., Nasi E., 1996, A&AS, 117, 113

Girardi L., Bressan A., Bertelli G., Chiosi C., 2000, A&AS, 141, 371

González Delgado , R. M.; Cerviño, M., Martins, L. P., Leitherer, C.; Hauschildt, P. H., 2005, MNRAS, 357, 945

González Delgado R. M., Cid Fernandes R., 2010, MNRAS, 403, 797

Gonzlez Delgado et al., 2012, Highlights Of Astronomy, Volume 15. XXVIIIth IAU General Assembly

Gonzlez Delgado et al., 2012, The intringuing life of massive galaxies. Proceedings IAU Symposium No. 295

Gonzlez Delgado et al., in prep.

Husemann B., et al., 2013, A&A, 549, A87

Kauffmann G., et al., 2003, MNRAS, 341, 33

Koleva M., Prugniel P., Ocvirk P., Le Borgne D., Soubiran C., 2008, MNRAS, 385, 1998

Le Borgne J.-F., et al., 2003, A&A, 402, 433

Levesque E. M., Leitherer C., Ekstrom S., Meynet G., Schaerer D., 2012, ApJ, 751, 67

Li Z., Mao C., Chen L., Zhang Q., Li M. 2013, arXiv, arXiv:1302.0927

Maraston, C. 2005, MNRAS, 362, 799

Martins L. P., González Delgado R. M., Leitherer C., Cerviño M., Hauschildt P., 2005, MNRAS, 358, 49

Martins L. P., Coelho P., 2007, MNRAS, 381, 1329

Mateus A., Sodré L., Cid Fernandes R., Stasińska G., Schoenell W., Gomes J. M., 2006, MNRAS, 370, 721

Ocvirk P., 2010, ApJ, 709, 88

Panter B., Heavens A. F., Jimenez R., 2003, MNRAS, 343, 1145

Panter, B., Jimenez, R., Heavens, A. F., & Charlot, S. 2007, MNRAS, 378, 1550

Pérez E., et al., 2013, ApJ, 764, L1

Sánchez S. F., et al., 2012, A&A, 538, A8

Sánchez-Blázquez P., et al., 2006, MNRAS, 371, 703

Sánchez-Blázquez, P., Ocvirk, P., Gibson, B. K., Pérez, I., & Peletier, R. F. 2011, MNRAS, 415, 709

Schaerer, D., Charbonnel, C., Meynet, G., Maeder, A., Schaller, G., 1993a, A&A, 102, 339

Schaerer, D., Meynet, G., Maeder, A., Schaller, G., 1993b, A&AS, 98, 523

Schaller, G., Schaerer, D., Meynet, G., Maeder, A., 1992, A&AS, 96, 269

Tojeiro, R., Heavens, A. F., Jimenez, R., & Panter, B. 2007, MNRAS, 381, 1252

Vazdekis, A., Sánchez-Blázquez, P.; Falcón-Barroso, J.; Cenarro, A. J.; Beasley, M. A.; Cardiel, N.; Gorgas, J.; Peletier, R. F., 2010, MNRAS, 404, 1639

Walcher C. J., Coelho P., Gallazzi A., Charlot S., 2009, MNRAS, 398, L44

B.3 The Evolution of Galaxies Resolved in Space and Time: A View of Inside-out Growth from the CALIFA Survey

Artigo por Pérez et al. (2013) (`doi:10.1088/2041-8205/764/1/L1`). Também disponível em *preprint* (`arXiv:1301.1679`).

THE EVOLUTION OF GALAXIES RESOLVED IN SPACE AND TIME: A VIEW OF INSIDE-OUT GROWTH FROM THE CALIFA SURVEY

E. Pérez[1], R. Cid Fernandes[1,2], R. M. González Delgado[1], R. García-Benito[1], S. F. Sánchez[1,3], B. Husemann[4],
D. Mast[1,3], J. R. Rodón[1], D. Kupko[4], N. Backsmann[4], A. L. de Amorim[2], G. van de Ven[5], J. Walcher[4],
L. Wisotzki[4], C. Cortijo-Ferrero[1], and CALIFA collaboration[6]
[1] Instituto de Astrofísica de Andalucía (CSIC), Glorieta de la Astronomía s/n, E-18008 Granada, Spain; eperez@iaa.es
[2] Departamento de Física, Universidade Federal de Santa Catarina, Florianópolis, Brazil
[3] Centro Astronómico Hispano Alemán, Calar Alto, (CSIC-MPG), Jesús Durbán Remón 2-2, E-04004 Almería, Spain
[4] Leibniz-Institut für Astrophysik Potsdam, An der Sternwarte 16, D-14482 Potsdam, Germany
[5] Max-Planck-Institut für Astronomie, Königstuhl 17, D-69117 Heidelberg, Germany
[6] CALIFA International Collaboration; http://calIfa.caha.es

ABSTRACT

The growth of galaxies is one of the key problems in understanding the structure and evolution of the universe and its constituents. Galaxies can grow their stellar mass by accretion of halo or intergalactic gas clouds, or by merging with smaller or similar mass galaxies. The gas available translates into a rate of star formation, which controls the generation of metals in the universe. The spatially resolved history of their stellar mass assembly has not been obtained so far for any given galaxy beyond the Local Group. Here we demonstrate how massive galaxies grow their stellar mass inside-out. We report the results from the analysis of the first 105 galaxies of the largest three-dimensional spectroscopic survey to date of galaxies in the local universe (CALIFA). We apply the fossil record method of stellar population spectral synthesis to recover the spatially and time resolved star formation history of each galaxy. We show, for the first time, that the signal of downsizing is spatially preserved, with both inner and outer regions growing faster for more massive galaxies. Further, we show that the relative growth rate of the spheroidal component, nucleus, and inner galaxy, which happened 5–7 Gyr ago, shows a maximum at a critical stellar mass $\sim 7 \times 10^{10}\,M_\odot$. We also find that galaxies less massive than $\sim 10^{10}\,M_\odot$ show a transition to outside-in growth, thus connecting with results from resolved studies of the growth of low-mass galaxies.

Key words: galaxies: bulges – galaxies: evolution – galaxies: fundamental parameters – galaxies: stellar content – galaxies: structure

Online-only material: color figures

1. INTRODUCTION

The stellar mass of a galaxy, $M_\star$, is one of its most fundamental properties as it provides a measure of the galaxy evolution process. Elucidating how it evolves in space and time, and in relation to other galaxies is central to understanding the processes that govern the efficiency and timing of star formation in galaxies. Look-back time studies of galaxy evolution determine the spatially resolved star formation rate (SFR) at a range of redshifts as a proxy for the average history of a particular type of galaxy (Lilly et al. 1996; Madau et al. 1996; Folkes et al. 1999; York et al. 2000; Bell et al. 2004; Moles et al. 2008; Ilbert et al. 2009; Pérez-González et al. 2008; Nelson et al. 2012). A major handicap of this approach is the inability to follow the evolution of any one galaxy over time (Faber et al. 2007). In this work we follow an alternative approach. For a new set of integral field spectroscopic data of a large sample of galaxies in the local universe, we recover their spatially resolved individual star formation histories (SFH) by means of stellar population spectral synthesis.

Beyond the Local Group, where individual stars are not resolved, a powerful method to reverse engineer the SFH of a galaxy is to find the most plausible combination of evolved single stellar populations (SSPs) that matches its spectrum (Walcher et al. 2011 and references therein). This fossil record method has been applied to images (e.g., Brinchmann & Ellis 2000; Bell & de Jong 2000; Pérez-González et al. 2008; Hansson et al. 2012) with good spatial coverage but poor spectral resolution. It has also been applied to Sloan Digital Sky Survey (SDSS) spectra of many galaxies (Heavens et al. 2004; Brinchmann et al. 2004; Gallazzi et al. 2005; Cid Fernandes et al. 2005, 2011; Panter et al. 2007), although SDSS provides just a single spectrum per galaxy with varying spatial coverage with redshift. The CALIFA survey (Sánchez et al. 2012) provides a set of spectra that covers the extent of each galaxy with good spatial and spectral sampling. Here we report on the spatially resolved growth with cosmic time for 105 galaxies, which sample a wide range of properties in the color–magnitude diagram (CMD), drawn from the full CALIFA survey of 600 galaxies.

2. SAMPLE AND METHODS

Details of the CALIFA survey, sample selection, reduction and calibration methods, and analysis pipeline are provided by Sánchez et al. (2012), Husemann et al. (2012, 2013, CALIFA first public data release DR1), Cid Fernandes et al. (2013), and J. Walcher et al. (2013, in preparation). Here we use the spectral data cubes combining both setups, V500 and V1200 gratings, with median limiting sensitivity 1.0 and 2.2 × 10^{-18} erg s^{-1} cm^2 Å^{-1} arcsec^{-2}, spectral resolution ~ 6 Å in the range ~ 3650–7500 Å, median spatial resolution 3″.7, and spectrophotometric calibration better than 15%.
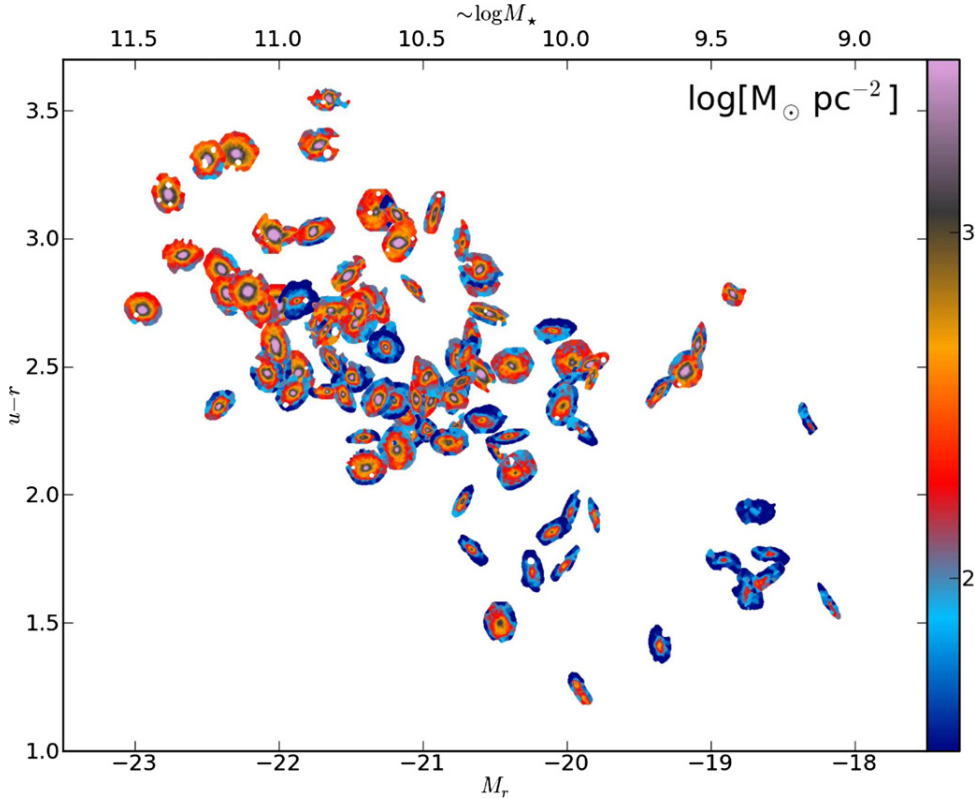
Figure 1. Stellar mass surface density ($M_\odot$ pc^{-2}) in the galaxies CMD. Absolute magnitude in SDSS r, M_r, vs. SDSS $u - r$ color, where each galaxy is represented with its present-day stellar mass density distribution. Holes in some galaxies result from removing foreground stars. The upper horizontal axis indicates approximate values of the stellar mass, from a linear fit to the M_r–log($M_\star$) relation. The time evolution of the stellar mass buildup of each galaxy in this diagram can be seen in http://www.iaa.es/~eperez/CALIFA/CMD.

(A color version of this figure is available in the online journal.)

For each galaxy the data are spatially rebinned to a minimum signal-to-noise ratio of 20 in a continuum band at 5635 ± 40 Å (Cid Fernandes et al. 2013). The stellar spectral synthesis code STARLIGHT (Cid Fernandes et al. 2005) is then used to recover the SFH, including a value for the stellar extinction, from each spectrum. Here we use a set of SSPs sampling the 1 Myr–14 Gyr age range with 40 age bins and four metallicities between 0.2 and 2.5 solar (S. Charlot & G. Bruzual 2007, private communication), assuming a Chabrier initial mass function. This method provides spatially resolved SFHs for ~200–2000 regions per galaxy, which we use to derive a three-dimensional buildup of mass (with two spatial and one temporal coordinates).

3. RESULTS

Figure 1 shows the (M_r, $u - r$) CMD, where each galaxy is represented with its present-day distribution of stellar mass density (in logarithmic units of $M_\odot$ pc^{-2}). Since the absolute magnitude M_r of galaxies is roughly proportional to their total log($M_\star$) (a main driver of galaxy physics) and the $u - r$ color works as a rough evolutionary clock, the CMD encapsulates galaxy evolution and the diversity of galaxies in a simple and observationally convenient form. Furthermore, given its widespread use in the literature (Faber et al. 2007; Blanton & Moustakas 2009) and the fact the CALIFA sample was defined to cover it as uniformly as possible, the CMD provides a natural framework to present and analyze our results. The general trend in Figure 1 shows more luminous galaxies to be redder, while the color coded mass density image of each galaxy shows that more

luminous ones have a higher central stellar surface density and steeper gradients;[7] we now see these trends spatially resolved over a five magnitude range in M_r.

Spatially resolved mass distributions have been computed for some galaxies from broadband imaging (e.g., Zibetti et al. 2009; Wuyts et al. 2012). Since we have the spatially resolved SFH for each galaxy, we can also see the time evolution of the CMD. This is shown in the animation http://www.iaa.es/~eperez/CALIFA/CMD, with the 10,000–250 Myr age plotted in the top right-hand corner, stopping at a time when galaxies have most of their $M_\star$ in place. For clarity, and to emphasize the way $M_\star$ grows, galaxies are kept at their present location in the CMD, even though their luminosities and colors would actually change with time. The most luminous, redder, massive galaxies have transformed an important part of their mass into stars already 10 Gyr ago (e.g., Pérez-González et al. 2008), particularly in their central regions, while many of the less massive galaxies show a lower stellar surface density.

Although we can derive the time evolution of the stellar populations at their present-day location, it is not feasible to trace their spatial location at earlier epochs, i.e., we cannot follow the evolution of their motions. If the stars undergo major spatial shuffling over their lives, then our analysis would be hampered. Breaks in the exponential distribution of disk outer regions (e.g., Pohlen & Trujillo 2006; Erwin et al. 2008) have

---

[7] With few exceptions, such as the outstanding low surface brightness galaxy at (-21.87, 2.76).
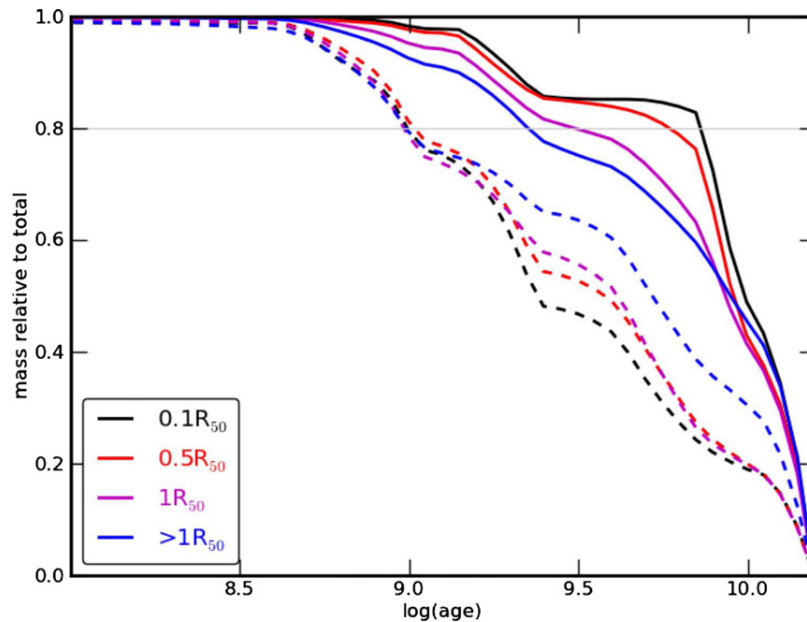
Figure 2. Relative stellar mass growth of four main spatial components (nucleus, inner 0.5 R_{50} and 1 R_{50}, and outer >1 R_{50}) for two galaxy mass bins, the lowest (dashed, log $M_\star$ [$M_\odot$] ∼ 9.58) and an intermediate (full line, log $M_\star$ [$M_\odot$] ∼ 10.83). Each component is normalized to its final $M_\star$. To compute a growth rate, a horizontal gray line at 0.8 marks when each component achieves 80% of its final $M_\star$. At the lowest mass, galaxies' outskirts grow faster (dashed blue line steeper), but at higher masses the growth proceeds inside-out (full black line steeper).

(A color version of this figure is available in the online journal.)

been interpreted as evidence of radial migration, although there is no general consensus. Numerical simulations show that, for secular evolution, the consequences of radial migration are only significant in the outer parts of galaxies, beyond about 2–3 scale lengths (Figure 2 in Roškar et al. 2008; Figures 15 and 16 in Sánchez-Blázquez et al. 2009; Behroozi et al. 2012). Here we partition galaxies into four radial zones to compare their histories, so that the outer regions (at several effective radii) where radial migration may have an impact on the SFH do not have a significant contribution to the results in the analysis that follows.

3.1. Spatially Resolved Growth of Stellar Mass $M_\star$

The animated CMD is a visually compelling tool, but lacks the quantitative information needed to probe the spatial growth of the stellar mass assembly. A more quantitative analysis in Figures 2–5 show the time evolution for four galaxy regions: the nucleus (left, defined as the central 0.1 R_{50}[8]), the region inside 0.5 R_{50}, the region inside 1 R_{50}, and the region outside 1 R_{50}. To make the growth of $M_\star$ more visible, galaxies are normalized to a common radial scale in units of R_{50}, and then stacked in seven equally populated bins (15 galaxies each) of increasing present-day galaxy $M_\star$. Figure 2 shows the relative growth of the four spatial components for two $M_\star$ bins, the lowest (dashed, log $M_\star$ [$M_\odot$] ∼ 9.58) and an intermediate mass (full line, log $M_\star$ [$M_\odot$] ∼ 10.83). To compute the $M_\star$ growth rate, a gray line marks when each component achieves 80% of its final $M_\star$. Clearly, at higher $M_\star$ the growth proceeds inside-out, while at the lowest $M_\star$ galaxies' outskirts grow faster than their inner parts.

Figure 3 shows at a glance the trends for all mass bins. The horizontal axis represents log time (bottom) or redshift (top; $H_0 = 71$, $\Omega_M = 0.27$, $\Omega_\Lambda = 0.73$); the vertical axis

represents the present-day total $M_\star$. Panels show gray scale coded the relative growth of each of the four spatial components, normalized to its final stellar mass, so that all components grow up to mass unity (i.e., gray scale and contours in Figure 3 represent for all mass bins the growth curves shown for two example mass bins in Figure 2; the black contour line in each panel marks 0.8 $M_\star$). Thus, the relative growth of different parts of the galaxy can be assessed. Three $M_\star$ growth cuts are plotted corresponding to three mass bins (lowest, intermediate, and highest in blue, green, and red, as colored in their axis mass value). The right-hand side panel shows that outer reaches (>1 R_{50}) of less massive galaxies (log mass[$M_\odot$] ∼ 9.58, in the lower part of the plot) achieve 0.8 $M_\star$ about 1 Gyr ago, while more massive ones (log mass[$M_\odot$] ∼ 11.26) had 0.8 $M_\star$ already ∼5 Gyr ago. The systematics of this outer galaxy $M_\star$ growth is clearly seen from the less massive up to the most massive galaxies in the sample. The central panels show a similar behavior for the inner regions (1 R_{50} and 0.5 R_{50}), but with a steeper growth at higher galaxy masses. The left panel shows a similar behavior for the nuclei, with an even steeper slope for galaxies more massive than log mass[$M_\odot$] ∼10.5. Thus there is a clear systematic sequence of $M_\star$ growth from the inside-out, where the mass is transformed into stars much earlier within 0.5 R_{50}.

3.2. Spatially Resolved Mean Age of the Stellar Populations

To better understand this result, for each of the spatial regions we compute the age at 0.8 $M_\star$ (as indicated in Figures 2 and 3). These are represented color coded in Figure 4 (in Gyr, also shown in each box), with the present-day stellar mass of the galaxy in the vertical axis and the spatial zone in the horizontal. Arising from the number of galaxies, statistical errors in the age for each box amount to 0.23 dex, while systematic errors introduced by the choice of other SSP basis (González Delgado et al. 2005) are 0.05 dex (R. M. González Delgado et al. 2013, in

---

[8] R_{50} is the circular half-light radius in 5635 ± 40 Å.
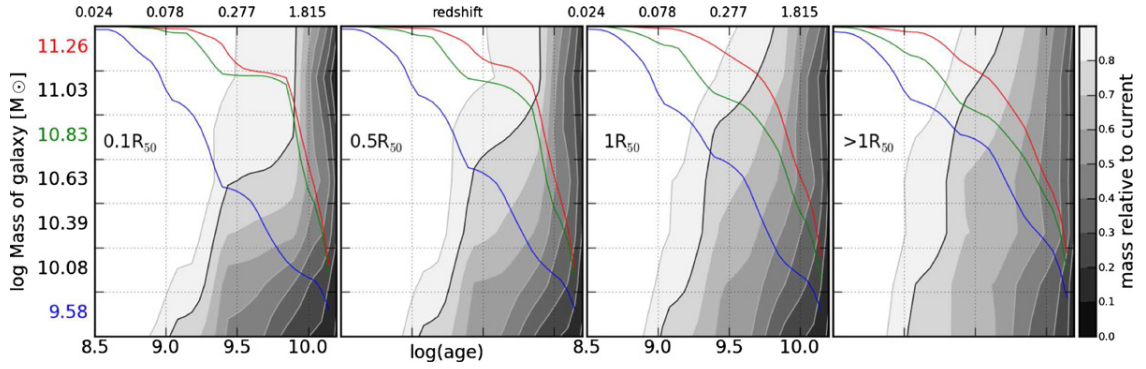
Figure 3. Inside-out stellar mass growth and spatially resolved downsizing. Panels show the normalized growth (gray scale in 10 intervals of 10%, with the 80% contour in black) in time in the four zones of Figure 2. To avoid number statistics biases, the galaxies are stacked in seven equally populated bins of 15 galaxies each, sorted by present-day total stellar mass; this implies that the vertical axis in Figures 3–5 is not uniform in log mass. For each spatial component, the growth is normalized to its total final stellar mass (i.e., the growth curves of Figure 2 are cuts for two of the mass bins through the gray scale and contours). For each zone, three example mass bins growth curves are plotted (lowest, intermediate, and highest in blue, green and red, respectively) showing how the signal of downsizing is spatially preserved (the four blue lines here correspond to the four dashed lines in Figure 2, while the four green lines here correspond to the four full lines in Figure 2); the axis corresponding to these cuts is the same as the gray scale, i.e., the scale 0.0–1.0 on the right-hand side. For a given galaxy mass, the progressive steepening of the growth from the outer ($>1\,R_{50}$) toward the nucleus shows the inside-out growth trend with the total mass of the galaxy. At the same time, for a given galaxy region, more massive galaxies grow faster than less massive ones, and this is sustained systematically from the inner to the outer zones.

(A color version of this figure is available in the online journal.)
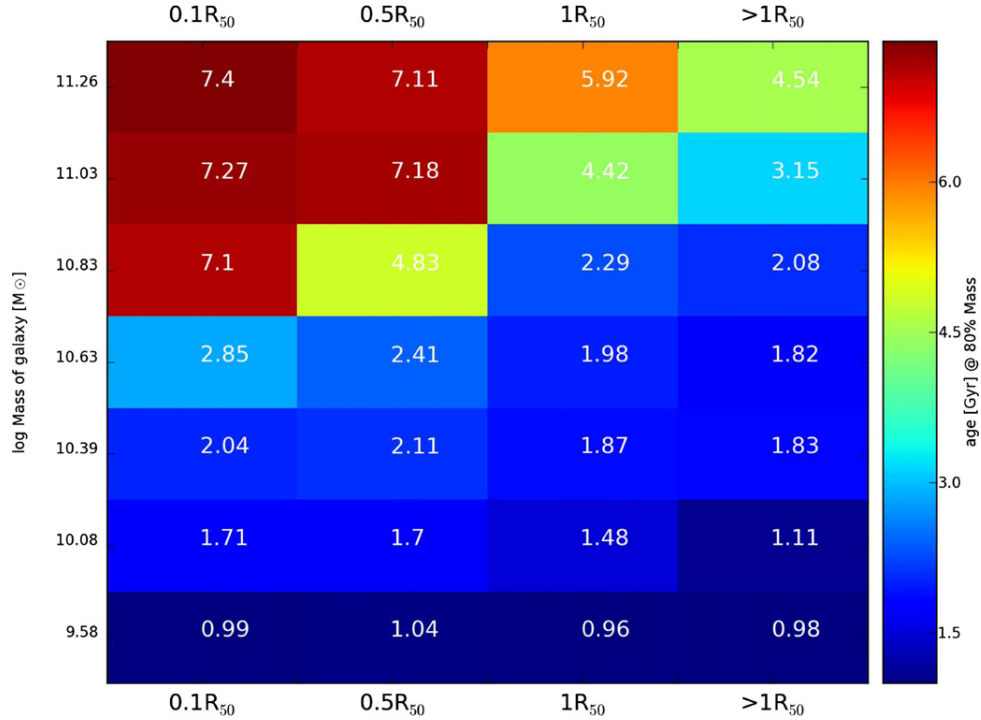
Figure 4. Inside-out stellar mass growth: ages. Using the same vertical axis as in Figure 3, this figure color codes the age at which each spatial component grows to 80% of its final stellar mass; the age (in Gyr) is shown within each box. For a given mass, the horizontal run of color gives the systematic aging from the outer (right) to the inner regions (left). Conversely, for a given galaxy region, the vertical run gives the systematic aging of that zone with increasing galaxy total stellar mass. There is a systematic change with both mass and location for all cases, with the exception of the very low mass galaxies (bottom row) for which there is no inside-out growth (the age at 80% growth is approximately the same in all four spatial components). These diagrams show clearly the differential inside-out growth and its explicit dependence on galaxy mass and galactocentric radius.

(A color version of this figure is available in the online journal.)

preparation). At a glance, it is clear that (1) running vertically for a given galaxy zone, older ages (red) correspond to more massive galaxies, and (2) running horizontally for a given galaxy mass, older ages (red) correspond to the central zones. The trends are clear for all masses and spatial regions, except for the lower mass bin, where there is no evidence of inside-out growth. In fact, the evidence at the lower masses is that galaxies do grow outside-in

(Figure 2), connecting with the behavior seen in studies of dwarf galaxies (e.g., Gallart et al. 2008; Zhang et al. 2012 and references therein).

The increase in mean stellar ages with increasing $M_\star$ reflects the downsizing phenomenon previously established on the basis of fossil record analyses of spatially unresolved data (Heavens et al. 2004; Pérez-González et al. 2008). Figures 3 and 4 show,
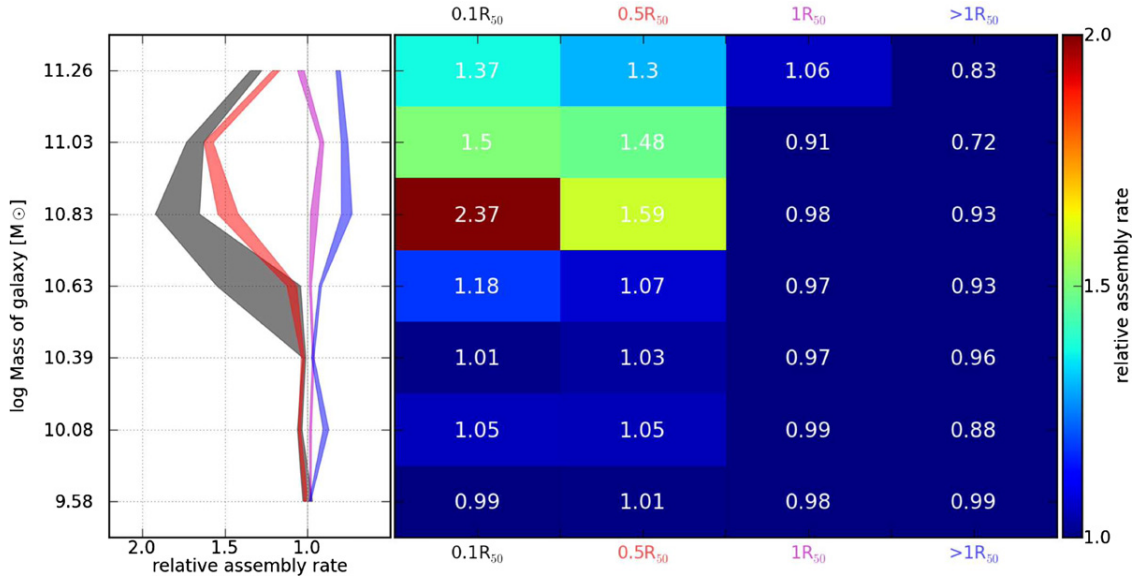
Figure 5. Stellar mass assembly rate. With the same axes of Figure 4, the right panel color codes the relative growth rate at 80% mass, for a given galaxy mass and zone, normalized to the total galaxy growth rate at 80%. The result indicates that for most of the galaxies, on average, the relative rate (within each galaxy) of transforming gas into stars is similar in all parts, except for the central regions ($<0.5\,R_{50}$) of galaxies more massive than $\sim 5 \times 10^{10}\,M_\odot$, which are up to a factor of ~ 2 faster. The left panel shows vertical cuts through the four zones, including uncertainty bands computed in 1000 iterations of randomly removing five different galaxies at a time. (A color version of this figure is available in the online journal.)

for the first time, that the signal of downsizing is preserved in a radial fashion, with both inner and outer regions growing faster for more massive galaxies. At the same time, these figures show that different spatial regions in a galaxy grow at different paces.

3.3. Spatially Resolved Growth Rate of the Stellar Populations

To examine the relative growth of inner and outer regions more closely, we compute growth rates from the inverse of the cosmic time span corresponding to the buildup of $0.8\,M_\star$. This is done for each spatial component of each galaxy, and the resulting rates expressed in units of the growth rate of the galaxy as a whole, obtained by integrating over its full spatial extent. Thus we derive the relative growth rates shown in Figure 5. The right panel, with coordinates as in Figure 4, codes in color this relative growth rate. The left panel plots vertical cuts through the four locations within the galaxy, as a function of total present-day stellar mass. This figure shows at once that not only the inner parts of more massive galaxies grew $M_\star$ faster (as in Figure 4), but also that in galaxies more massive than $5 \times 10^{10}\,M_\odot$ the inner regions grew as much as 50%–100% faster than the galaxy-wide average. The relative growth rate for $1\,R_{50}$ (magenta line) is close to unity, meaning that R_{50} best represents the stellar mass growth in the galaxy as a whole.

Although we have grouped 105 galaxies (105,123 spectra in total) in just a few mass bins to obtain robust results, when the complete CALIFA sample of 600 galaxies is observed and analyzed, these results will be established with a finer detail. The most striking aspect of Figure 5 is the peak at $M_\star \sim 6\text{--}7 \times 10^{10}\,M_\odot$. At masses below this, the relative growth rates of inner and outer regions slowly converge to the galaxy average, becoming essentially indistinguishable at the lowest galaxy masses sampled. A convergence toward spatially uniform histories is also seen at masses above the critical mass, but the inner regions still grow faster than the outer ones at the highest

masses. The largest differences peak at $\sim 6\text{--}7 \times 10^{10}\,M_\odot$, where the nucleus grows about twice faster than the outer regions.

4. DISCUSSION AND SUMMARY

Previous studies have revealed a special mass or mass range (referred to as critical or pivotal) around $M_\star \sim 6 \times 10^{10}\,M_\odot$ (Kauffmann et al. 2003; Mateus et al. 2006; Leauthaud et al. 2012, and references therein). Leauthaud et al. study the stellar-to-halo mass relation (SHMR) using COSMOS data and find that this mass marks where the accumulated stellar growth of the central galaxy has been the most efficient. On the modeling side, Shankar et al. (2006) discuss the shape of the SHMR as a change of dominance of two feedback mechanisms, with stellar winds and supernova (SN) efficiently removing the gas and quenching the star formation at lower galaxy masses, while active galactic nucleus (AGN) winds become more powerful in massive galaxies thus lowering star formation efficiency at higher masses. There is still much to be understood about the self-consistent combined effects of AGN and SN feedback (Stinson et al. 2013; Booth & Schaye 2012). Recent papers try to reproduce the observed SHMR from cosmological simulations (cf. Figure 14 in Behroozi et al. 2012), with values of $\sim 2\text{--}10 \times 10^{10}\,M_\odot$ in the peak efficiency of conversion of halo gas into stellar mass. Cosmological models of star formation with negative feedback do not allow yet for a more precise value of this critical mass for optimal growth (De Lucia & Borgani 2012).

In short, there is clear mounting evidence from a series of independent studies, both observationally and from numerical simulations, of a special galaxy mass range where the SFR reaches higher values faster. Our results, Figure 5, show that the physical process(es) responsible for this peak efficiency also leave a strong imprint in the *spatial* assembly of stars in galaxies. From our spatially resolved study, we can see that this is restricted to the inner reaches of galaxies with this pivotal mass. This would imply that the effect is seen in the spheroidal

component, which dominates the central mass distribution of galaxies at this stellar mass range, and that this happened 5–7 Gyr ago (a redshift ∼0.5–1; Figure 4).

We can also tentatively frame our results in the context of secular versus merger driven evolution. A possible scenario to interpret our findings is that galaxies with $M_\star \gtrsim 5 \times 10^{10}\ M_\odot$ have grown quickly their inner part by means of a merger at ages 5–9 Gyr ago (such as M31), while lower mass galaxies are dominated by secular evolution (such as the Milky Way). Although we do not have the means to test this, it is compatible with the results obtained by Puech et al. (2012), and with the studies of M31 and the Milky Way (Hammer et al. 2007, 2010; Cignoni et al. 2006; Vergely et al. 2002; McMillan 2011).

Our analysis of the SFHs in 105 galaxies of the CALIFA survey provides a direct powerful probe of the rates and efficiency of spatially resolved stellar mass growth in galaxies, as derived from the information encoded in their present-day spectra. We demonstrate spatially resolved downsizing, with galaxies more massive than $M_\star \sim 5 \times 10^9\ M_\odot$ growing inside-out while lower mass galaxies grow outside-in. We find an optimal growth for the galaxy stellar mass around $\sim 7 \times 10^{10}\ M_\odot$.

REFERENCES

Behroozi, P. S., Wechsler, R. H., & Conroy, C. 2012, ApJ (arXiv:1207.6105v1)
Bell, E. F., & de Jong, R. S. 2000, MNRAS, 312, 497
Bell, E. F., Wolf, C., Meisenheimer, K., et al. 2004, ApJ, 608, 752
Blanton, M. R., & Moustakas, J. 2009, ARA&A, 47, 159
Booth, C. M., & Schaye, J. 2012, MNRAS (arXiv:1203.3802v1)
Brinchmann, J., Charlot, S., White, S. D. M., et al. 2004, MNRAS, 351, 1151
Brinchmann, J., & Ellis, R. 2000, ApJL, 536, 77
Cid Fernandes, R., Mateus, A., Sodré, L., et al. 2005, MNRAS, 358, 363
Cid Fernandes, R., Stasińska, G., Mateus, A., et al. 2011, MNRAS, 413, 1687
Cid Fernandes, R., et al. 2012, A&A, submitted
Cignoni, M., Degl'Innocenti, S., Prada Moroni, P. G., & Shore, S. N. 2006, A&A, 459, 783
De Lucia, G., & Borgani, S. 2012, MNRAS, 426, L61
Erwin, P., Pohlen, M., & Beckman, J. E. 2008, AJ, 135, 20
Faber, S., Willmer, C. N. A., Wolf, C., et al. 2007, ApJ, 665, 265
Folkes, S., Ronen, S., Price, I., et al. 1999, MNRAS, 308, 459
Gallart, C., Stetson, P. B., Meschin, I. P., et al. 2008, ApJL, 682, 89
Gallazzi, A., Charlot, S., Brinchmann, J., et al. 2005, MNRAS, 362, 41
González Delgado, R. M., Cerviño, M., Martins, L. P., et al. 2005, MNRAS, 357, 945
Hammer, F., Puech, M., Chemin, L., Flores, H., & Lehnert, M. D. 2007, ApJ, 662, 322
Hammer, F., Yang, Y. B., Wang, J. L., et al. 2010, ApJ, 725, 542
Hansson, K. S. A., Lisker, T., & Grebel, E. K. 2012, MNRAS, 427, 2376
Heavens, A., Panter, B., Jimenez, R., & Dunlop, J. 2004, Natur, 428, 625
Husemann, B., Kamann, S., Sandin, C., et al. 2012a, A&A, 545, 137
Husemann, B., et al. 2012b, A&A, 549, A87, CALIFA Data Release 1 (DR1)
Ilbert, O., Capak, P., Salvato, M., et al. 2009, ApJ, 690, 1236
Kauffmann, G., Heckman, T. M., White, S. D. M., et al. 2003, MNRAS, 341, 54
Leauthaud, A., Tinker, J., Bundy, K., et al. 2012, ApJ, 744, 159
Lilly, S., Le Fevre, O., Hammer, F., & Crampton, D. 1996, ApJL, 460, 1
Madau, P., Ferguson, H. C., Dickinson, M. E., et al. 1996, MNRAS, 283, 1388
Mateus, A., Sodré, L., Cid Fernandes, R., et al. 2006, MNRAS, 370, 721
McMillan, P. J. 2011, MNRAS, 414, 2446
Moles, M., Benítez, N., Aguerri, J. A. L., et al. 2008, AJ, 136, 1325
Nelson, E. J., van Dokkum, P. G., Brammer, G., et al. 2012, ApJL, 747, 28
Panter, B., Jimenez, R., Heavens, A. F., & Charlot, S. 2007, MNRAS, 378, 1550
Pérez-González, P., Rieke, G. H., Villar, V., et al. 2008, ApJ, 675, 234
Pohlen, M., & Trujillo, I. 2006, A&A, 454, 759
Puech, M., Hammer, F., Hopkins, P. F., et al. 2012, ApJ, 753, 128
Roškar, R., Debattista, V. P., Stinson, G. S., et al. 2008, ApJL, 675, 65
Sánchez, S. F., Kennicutt, R. C., Gilde Paz, A., et al. 2012, A&A, 538, 1
Sánchez-Blázquez, P., Courty, S., Gibson, B. K., & Brook, C. B. 2009, MNRAS, 398, 591
Shankar, F., Lapi, A., Salucci, P., De Zotti, G., & Danese, L. 2006, ApJ, 643, 14
Stinson, G. S., Brook, C., Macciò, A. V., et al. 2013, MNRAS, 428, 129
Vergely, J.-L., Köppen, J., Egret, D., & Bienaymé, O. l. 2002, A&A, 390, 917
Walcher, J., Groves, B., Budavári, T., & Dale, D. 2011, Ap&SS, 331, 1
Wuyts, S., Förster Schreiber, N. M., Genzel, R., et al. 2012, ApJ, 753, 114
York, D. G., Adelman, J., Anderson, J. E., Jr., et al. 2000, AJ, 120, 1579
Zhang, H.-X., Hunter, D., Elmegreen, B. G., Gao, Y., & Schruba, A. 2012, AJ, 143, 47
Zibetti, S., Charlot, S., & Rix, H. W. 2009, MNRAS, 400, 1191

B.4   The star formation history of CALIFA galaxies: Radial structures

Artigo por González Delgado et al. (2013), disponível em *preprint* (`arXiv:1310.5517`). Aceito para publicação no A&A.

The star formation history of CALIFA galaxies: Radial structures

R. M. González Delgado[1], E. Pérez[1], R. Cid Fernandes[1,2], R. García-Benito[1], A. L. de Amorim[2], S. F. Sánchez[1,3], B. Husemann[4], C. Cortijo-Ferrero[1], R. López Fernández[1], P. Sánchez-Blázquez[5], S. Bekeraite[4], C. J. Walcher[4], J. Falcón-Barroso[6,7], A. Gallazzi[8,16], G. van de Ven[9], J. Alves[10], J. Bland-Hawthorn[11], R. C. Kennicutt, Jr.[12] D. Kupko[4], M. Lyubenova[9], D. Mast[1,3], M. Mollá[13], R. A. Marino[14], A. Quirrenbach[15], J. M. Vílchez[1], L. Wisotzki[4], and CALIFA collaboration

[1] Instituto de Astrofísica de Andalucía (CSIC), P.O. Box 3004, 18080 Granada, Spain
e-mail: `rosa@iaa.es`
[2] Departamento de Física, Universidade Federal de Santa Catarina, P.O. Box 476, 88040-900, Florianópolis, SC, Brazil
[3] Centro Astronómico Hispano Alemán, Calar Alto, (CSIC-MPG), C/ Jesús Durbán Remón 2-2, E-04004 Almería, Spain
[4] Leibniz-Institut für Astrophysik Potsdam, innoFSPEC Potsdam, An der Sternwarte 16, 14482 Potsdam, Germany
[5] Depto. de Física Teórica, Universidad Autnoma de Madrid, 28049 Madrid, Spain
[6] Instituto de Astrofísica de Canarias (IAC), E-38205 La Laguna, Tenerife, Spain
[7] Depto. Astrofísica, Universidad de La Laguna (ULL), E-38206 La Laguna, Tenerife, Spain
[8] INAF − Osservatorio Astrofisico di Arcetri, Largo Enrico Fermi 5, 50125 Firenze, Italy
[9] Max Planck Institute for Astronomy, Königstuhl 17, 69117 Heidelberg, Germany
[10] University of Vienna, Turkenschanzstrasse 17, 1180, Vienna, Austria
[11] Sydney Institute for Astronomy, The University of Sydney, NSW 2006, Australia
[12] University of Cambridge, Institute of Astronomy, Madingley Road, Cambridge, CB3 0HA, United Kingdom
[13] Departamento de Investigación Básica, CIEMAT, Avda. Complutense 40, E-28040 Madrid, Spain
[14] CEI Campus Moncloa, UCM-UPM, Departamento de Astrofísica y CC. de la Atmósfera, Facultad de CC. Físicas, Universidad Complutense de Madrid, Avda. Complutense s/n, 28040 Madrid, Spain
[15] Landessternwarte, Zentrum fur Astronomie der Universitat Heidelberg, Königstuhl 12, D-69117 Heidelberg, Germany
[16] Dark Cosmology Centre, Niels Bohr Institute, University of Copenhagen, Juliane Mariesvej 30, 2100 Copenhagen, Denmark
[17] http://califa.caha.es

ABSTRACT

We study the radial structure of the stellar mass surface density (μ_*) and stellar population age as a function of the total stellar mass and morphology for a sample of 107 galaxies from the CALIFA survey. We apply the fossil record method based on spectral synthesis techniques to recover the star formation history (SFH), resolved in space and time, in spheroidal and disk dominated galaxies with masses from 10^9 to 10^{12} M$_\odot$. We derive the half mass radius, and we find that galaxies are on average 15% more compact in mass than in light. The ratio of half mass radius to half light radius (HLR) shows a dual dependence with galaxy stellar mass; it decreases with increasing mass for disk galaxies, but is almost constant in spheroidal galaxies. In terms of integrated versus spatially resolved properties, we find that the galaxy-averaged stellar population age, stellar extinction, and μ_* are well represented by their values at 1 HLR. Negative radial gradients of the stellar population ages are present in most of the galaxies, supporting an inside-out formation. The larger inner ($\leq$ 1 HLR) age gradients occur in the most massive (10^{11} M$_\odot$) disk galaxies that have the most prominent bulges; shallower age gradients are obtained in spheroids of similar mass. Disk and spheroidal galaxies show negative μ_* gradients that steepen with stellar mass. In spheroidal galaxies μ_* saturates at a critical value ($\sim 7 \times 10^2 M_\odot/\mathrm{pc}^2$ at 1 HLR) that is independent of the galaxy mass. Thus, all the massive spheroidal galaxies have similar local μ_* at the same distance (in HLR units) from the nucleus. The SFH of the regions beyond 1 HLR are well correlated with their local μ_*, and follow the same relation as the galaxy-averaged age and μ_*; this suggests that local stellar mass surface density preserves the SFH of disks. The SFH of bulges are, however, more fundamentally related to the total stellar mass, since the radial structure of the stellar age changes with galaxy mass even though all the spheroid dominated galaxies have similar radial structure in μ_*. Thus, galaxy mass is a more fundamental property in spheroidal systems while the local stellar mass surface density is more important in disks.

Key words. Galaxies: evolution, stellar content; Techniques: Integral Field Spectroscopy

1. Introduction

The separation of galaxies in a red sequence and a blue cloud according to their location in the color-magnitude diagram (CMD) is well established since the work of Strateva et al (2001). This location correlates with stellar population properties (Kauffmann et al. 2003a,b; Baldry et al. 2004; Bell et al. 2004; Brinchmann et al. 2004; Gallazzi et al. 2005; Mateus et al. 2006, 2007; Blanton & Moustakas 2009). Red galaxies are usually made of metal rich

and old stars, and have very little gas and recent star formation. In contrast, galaxies in the blue cloud are actively forming stars, have a large gas fraction, a metal poor and young stellar population. This bimodal distribution of galaxy properties reflects the Hubble sequence, because red galaxies are mainly spheroidal dominated systems, while blue galaxies are disk dominated systems. This distribution also depends on the galaxy stellar mass (M_*) which has become the most important parameter for galaxy evolution studies (e.g. Brinchmann & Ellis 2000; Dickinson et

1

al. 2003; Fontana et al. 2006; Pérez-González et al. 2008), although environment can play also a relevant role (e.g. Peng et al. 2010).

In fact, sorting galaxies by their stellar mass is a way to start to classify galaxies and to check if their properties scale among the different subsamples. Earlier results from the analysis of Sloan Digital Sky Survey (SDSS) data (Strateva et al. 2001) have reported the existence of a critical mass, $\sim 3 \times 10^{10} M_\odot$, that divides the local population of galaxies in two distinct families: lower-mass galaxies with young stellar populations, low mass surface density and low concentration index typical of disks, and higher-mass galaxies with old stellar populations, high mass surface density and concentration index typical of bulges (Kauffmann et al. 2003a,b). This dependence of the galaxy properties with the stellar mass distribution points to morphology as a secondary parameter (Balogh et al. 2001; Boselli et al. 2001). Later works have also pointed out that μ_* is a more fundamental parameter than M_*. Kauffmann et al. (2006) found that there is also a critical $\mu_* \sim 3 \times 10^8 M_\odot$ kpc^{-2} that divide galaxies in disk-dominated and bulge-dominated systems. Below this critical surface density, μ_* scales with the stellar mass, while above it μ_* is almost constant. These results suggest that the conversion of baryons into stars in low mass galaxies increases with their halo mass, but in massive galaxies the star formation efficiency decreases in the highest mass haloes, with little star formation occurring in massive galaxies after they have assembled.

These SDSS results were obtained analyzing a single central spectrum per galaxy, with 3 arcsec diameter covering from just nuclear regions to typically not more than 70% of the total galaxy light depending on distance. Due to the radial structure of galaxy properties, such as the mass-to-light (M/L) ratio, results based on SDSS spectroscopy can be grossly affected by aperture losses and fiber location within the galaxy (Ellis et al. 2005; Iglesias-Páramo et al. 2013).

Based on spatially resolved surface photometry, Bell & de Jong (2000) found that μ_* is a more fundamental parameter than M_* in driving the SFH. They analyzed a sample of 121 nearby S0–Sd galaxies, and concluded that the SFH of a disk galaxy is primarily driven by its local surface density, with the total stellar mass as secondary parameter that correlates with metallicity, but not with age. This suggests that galaxy mass dependent feedback is an important process in the chemical evolution of galaxies, as it has been suggested also by the mass–metallicity relation (Tremonti et al. 2004), although recent works point out that this relation is a scaled-up integrated effect of a local μ_* – oxygen abundance relation (Rosales Ortega et al. 2012; Sánchez, et al. 2013). Note, however, that Bell & de Jong (2000) use K band surface brightness as a proxy of the stellar mass surface density, and their results are based on color gradients, which can be affected by spatially variation of the extinction, and even by emission lines contributing to optical bands.

In a pioneering work, Zibetti et al. (2009) carried out a detailed analysis of nine nearby galaxies using SDSS *ugriz* plus J, H, K images, devising a method to derive the spatially resolved H band M/L ratio as a function of the $g - i$ color. Comparing the total stellar mass obtained from the spatially resolved μ_* map with the mass inferred from the integrated photometry, they find that the former can be up to 0.2 dex larger. However, due to the limited number of galaxies in their sample, they could not study how the radial structure of μ_* changes with M_* or with galaxy type.

More recently, μ_* profiles have been obtained for individual galaxies at different redshifts, made possible by the high spatial resolution provided by WFC3 on board HST. Now it is possible to measure the rest frame optical emission of galaxies at redshift $z \sim 2$, and to obtain spatially resolved maps of the stellar mass by fitting the SED in each individual pixel (Wuyts et al. 2012), or simply using an empirical relation between the rest-frame color and stellar M/L ratio (Szomoru et al. 2012). Stellar mass surface density radial profiles have been used to trace the mass distribution, concluding that galaxies at $z \sim 2$ are growing inside-out.

Note, however that these works estimate not only μ_* but also the average age of the stellar population based on broad band photometry. The average age is a crude but robust way to represent the SFH of galaxies, and rest-frame optical colors are used extensively to obtain ages. Radial gradients of colors have been detected in bulges (Peletier et al. 1990; Silva & Bothun 1998; La Barbera et al. 2004; Menanteau et al. 2004; Wu et al. 2005; Moorthy & Holtzman, 2006; Roche et al. 2010) and disks (Peletier & Balcells 1996; de Jong 1996; Peletier & de Grijs 1998; Bell & de Jong 2000; MacArthur et al. 2004; Muñoz-Mateos et al. 2007; Tortora et al. 2010; Bakos et al. 2008). Usually, a color gradient is interpreted as due to radial variations in age or metallicity, but due to the age-metallicity-extinction degeneracy, color gradients can also be related to metallicity and/or extinction gradients that are certainly present in the disks and central regions of massive galaxies.

Spectroscopic data and measured line-strength stellar indices can help to break these degeneracies (Trager et al. 2000; Proctor & Sansom 2002; Sánchez-Blázquez et al. 2007; MacArthur et al. 2009). Pioneering three-dimensional spectroscopic surveys like SAURON (Bacon et al. 2001; de Zeeuw et al. 2002), and ATLAS3D (Capellari et al. 2011) have taken this approach to spatially resolve the stellar population properties of mainly early type galaxies (Peletier et al. 1997; McDermid et al. 2006; Chilingarian 2009; Kuntschner et al. 2010; see also Ganda et al. 2007 for a few spiral galaxies). Unfortunately, the short spectral range in these works limits the analysis to a few spectral indices, with little leverage to trace extinction effects and to use long range continuum shape to further constrain stellar populations properties. Surveys covering a larger spectral range exist (e.g. Chilingarian 2009; Blanc et al. 2013; Yoachim et al. 2012; Greene et al. 2012; Sil'chenko et al. 2012), but they are still based on a small number of galaxies.

It is clear from this summary that spatially resolved spectroscopy covering the whole optical wavelengths for a large homogenous sample is needed to better map the radial structure of the stellar population properties, and to ascertain the roles that μ_* and M_* play in the SFH of galaxies. The Calar Alto Integral Field Area (CALIFA, Sánchez et al. 2012; Husemann et al. 2013) is the largest 3D spectroscopic survey to date of galaxies in the local Universe, providing a unique set of data for galaxies covering a large range of masses ($10^{9-12} M_\odot$) and morphological types (from E to Sc), spatially resolved up to three half light radii.

We have already obtained the spatially resolved history of the stellar mass assembly for the first 105 galaxies of CALIFA. In Pérez et al. (2013) we applied the fossil record method of spectral synthesis to recover the spatially and time resolved SFH of each galaxy, finding that galaxies more massive than $10^{10} M_\odot$ grow inside-out. We also show that the signal of downsizing is spatially preserved, with both inner and outer regions growing faster for more massive galaxies. Further, we show that the relative growth rate of the spheroidal component, nucleus, and inner galaxy, which happened 5–7 Gyr ago, shows a maximum at a critical stellar mass of $\sim 7 \times 10^{10} M_\odot$.

We use the full spectral fitting technique because it has been proven to reduce the age-metallicity degeneracy (Sánchez-Blázquez et al. 2011). Further, this technique, that has been ex-

tensively applied to single SDSS spectra of galaxies (e.g. Cid Fernandes et al. 2005, 2007; Asari et al. 2007), successfully produces the 2D distribution of the stellar population properties when applied to CALIFA data cubes (Cid Fernandes et al. 2013a). Additionally, the uncertainties associated to the estimation of the radial distribution of the stellar population properties have been extensively studied by us (Cid Fernandes et al. 2013b).

In this paper we extend our study of the spatially resolved stellar population properties of galaxies in the CALIFA survey; we obtain the radial structure of the stellar mass surface density and ages of the stellar population and their dependence on the galaxy stellar mass and morphology; we compare the averaged and integrated properties of the galaxies, and find out where and in which galaxies the total stellar mass and/or the local stellar mass surface density is more connected to their history.

This paper is organized as follows. Section 2 describes the observations and summarizes the properties of CALIFA galaxies and of the subsample studied here. In Section 3 we summarize the fossil record method to extract the SFH, and the single stellar population models used as ingredients for the full spectral fitting. Section 4 presents the 2D maps of μ_* and age, as well as their radial structures. Section 5 deals with the total stellar mass. Section 6 compares the galaxy averaged with the integrated stellar population properties, and links them with their values at one HLR. In Section 7 we obtain the mass weighted size, and we discuss the ratio of half-mass to half-light radii as a function of galaxy mass and the spatial variation of the M/L ratio. Section 8 presents the radial structures of age and μ_* stacking galaxies according to their M_*, and concentration index, we discuss the roles of M_* and μ_* in the history of disk and spheroidal galaxies. Finally, Section 9 summarizes the results obtained and presents our conclusions. Throughout we adopt a Salpeter IMF (Salpeter 1955), resulting in stellar masses a factor 1.78 larger than in case of a Chabrier IMF (Chabrier 2003).

2. Observations, data reduction, and sample

2.1. Observations and Data reduction

The observations were carried out with Potsdam Multi-Aperture Spectrophotometer (PMAS, Roth et al. 2005) in the PPak mode (Verheijen et al. 2004) at the 3.5m telescope of the Calar Alto Observatory (CAHA). PPak is a fiber bundle of 382 fibers of 2.7″ diameter each, covering a 74″ × 64″ Field of View (FoV, Kelz et al. 2006).

Observations for CALIFA are obtained in two different spectral settings using the V500 and V1200 gratings. The V500 grating achieves a spectral resolution of ∼ 6 Å (FWHM) with a nominal wavelength coverage from 3745–7300 Å, while the V1200 achieves a higher spectral resolution of ∼ 2.3 Å, covering the 3650–4840 Å range. However, the useful wavelength range is reduced by vignetting of the CCD corners which cannot be fully compensated with the three dithering scheme. More extended explanations on the observational strategy, effects of vignetting, the reduction pipeline and data quality can be found in Sánchez et al. (2012) and Husemann et al. (2013).

In order to reduce the effects of the vignetting on the data, we combine the observations in both setups such that they fully cover the optical range from [OII] λ3727 to [SII] $\lambda\lambda$6717,6732. To combine both spectral setups we first degraded the spectral resolution of the V1200 data set to match the V500 data. This is done within the standard CALIFA pipeline to ensure that the data handling and error propagation matches that of the V500

data. Spatial alignment of the V500 and V1200 datacubes requires only full pixel shifts because both datacubes have been reconstructed during the correction for differential atmospheric refraction such that the central surface brightness peak is centered on a certain pixel. The V500 and V1200 data are always observed under different observing conditions, so that the difference in the seeing will slightly affect the observed surface brightness for each spaxel. Thus, we scale all individual spectra of the V1200 data such they match with surface brightness of the corresponding V500 data within the unvignetted wavelength range from 4500–4600 Å. Finally, a combined V1200 + V500 datacube is produced where wavelength range short-ward of 4600 Å is taken from matched V1200 datacube and long-ward of 4600 Å is taken from the original V500 datacube.

The combined V1200 + V500 datacubes were processed as described in Cid Fernandes et al. (2013a). Briefly, spectra adequate for a full spectral synthesis analysis of the stellar population content were extracted in a way that ensures a signal-to-noise ratio $S/N \geq 20$ in a 90 Å wide region centered at 5635 Å (in the rest-frame). When individual spaxels do not meet this S/N threshold (typically beyond a couple of half light radii from the nucleus), they were coadded into Voronoi zones (Cappellari & Copin 2003). On average, we analyze ∼ 1000 zones per galaxy (to be precise, the 107 galaxies studied in this paper were segmented into 98291 zones). Pre-processing steps further include spatial masking of foreground/background sources and very low S/N spaxels, rest-framing and spectral resampling. The whole process takes spectrophotometric errors (ϵ_λ) and bad pixel flags (b_λ) into account. The spectra were then processed through PYCASSO (the Python CALIFA STARLIGHT Synthesis Organizer), producing the results discussed throughout this paper.

2.2. The parent sample and the first 107 galaxies

A detailed characterization of the CALIFA sample will be presented by Walcher et al. (in preparation). Here we summarize its main properties and compare it to the subsample studied in this paper.

CALIFA's mother sample contains 939 galaxies selected from the SDSS DR7 photometric catalog (Abazajian et al. 2009). In addition to the restriction in declination to ensure good visibility from CAHA, the main selection criteria are: a) angular isophotal diameter in the SDSS r-band in the range $D_{25} = 45$–80 arcsec, to ensure that objects fill well the PPak FoV; b) redshift range $z = 0.005$–0.03, guaranteeing that all relevant optical emission lines are covered. The sample includes a significant number of galaxies in the different areas across the CMD, ensuring that CALIFA spans a wide and representative range of galaxy types.

In this paper we present the results of the analysis of the first 107 galaxies observed by CALIFA. The observing order selection is random, but is this subset representative of the mother sample as a whole? To answer this question, Fig. 1 compares the distributions of galaxy properties in the mother sample (empty bars) and in our subsample. The plots show (scaled) histograms of the absolute magnitude, the ratio of the isophotal major-axis to minor-axis diameters, colors, the Petrosian radius, and concentration index (defined as the ratio of Petrosian radii r_{90}^P/r_{50}^P), as well as the $u - r$ versus M$_r$ CMD. All data were extracted from the SDSS photometric catalog for the CALIFA mother sample. The histograms are normalized to form a probability density, i.e. each bar scales with the ratio of the number of galaxy in each bin and the total number of galaxies multiply by the bin width. A
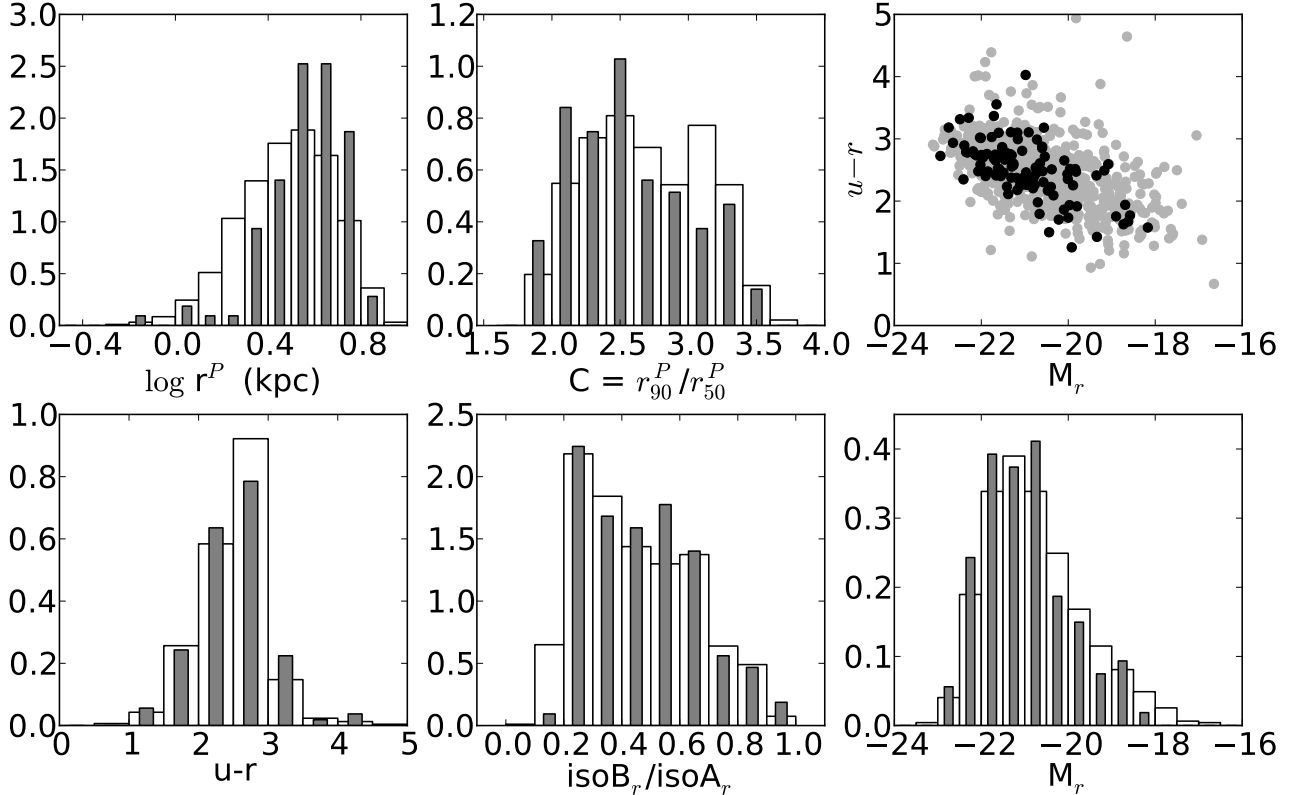
Fig. 1. Comparison of the distributions of the CALIFA mother sample (empty bars) and the 107 galaxies analyzed here (filled bars). From bottom up, and from left to right, we show the distributions of: $u - r$ color, the ratio between the semi-minor and semi-major axis, the absolute magnitude, the Petrosian 50% radius, r_{50}^P, and the concentration index (measured at the SDSS r band). The histograms are normalized to form a probability density, i.e. each bar scales with the ratio of the number of galaxies in each bin and the total number of galaxies × bin width, so that we can directly compare the two distributions. The upper right panel shows the CMD where galaxies of the mother sample are the grey points and the 107 galaxies analyzed here are marked as black points.

simple visual inspection shows that our subsample of 107 galaxies represents well the CALIFA sample. We thus expect that the results reported in this paper remain valid once the full sample is observed. Note however, that without applying a volume correction, these distributions do not represent the local galaxy population.

3. Methods, ingredients and uncertainties

Our method to extract stellar population information from the CALIFA data cubes is based on the full spectral synthesis approach. This section presents a summary of the method, ingredients and tests that we have carried out (see also Appendix B).

3.1. The spectral synthesis method

Methods to extract information on stellar populations encoded in galaxy spectra split into two broad categories: Those which focus on spectral indices like equivalent widths and/or colors (Bica 1988; Proctor et al. 2004 ; Gallazzi et al. 2005, 2006), and those which use the whole spectrum (Heavens et al. 2004; Cid Fernandes et al. 2005; Ocvirk et al. 2006; Koleva et al. 2009 ; Tojeiro et al. 2007; MacArthur et al. 2009). Both have prons and cons. The full spectral synthesis approach has boomed since the first generation of medium spectral resolution evolutionary syn-

thesis calculations became available with the paper by Bruzual & Charlot (2003), and was one of the main tools employed in the mining of the SDSS spectroscopic database, leading to the derivation of physical properties and SFHs of galaxies (e.g.; Panter et al. 2003, 2007; Mateus et al. 2007; Vale Asari et al. 2009; Tojeiro et al. 2009). Here, we use the full spectral fitting approach.

We analyze the stellar population properties of CALIFA galaxies with the STARLIGHT[1] code (Cid Fernandes et al. 2005), which fits an observed spectrum (O_λ) in terms of a model (M_λ) built by a non-parametric linear combination of $N_\star$ Simple Stellar Populations (SSPs) from a base spanning different ages (t) and metallicities (Z). Dust effects are modeled as a foreground screen with a Cardelli et al. (1989) reddening law with $R_V = 3.1$. Kinematical effects are also accounted for assuming a gaussian line-of-sight velocity distribution. The fits were carried out in the rest-frame 3800–6850 Å interval, with a $\Delta\lambda = 2$ Å sampling. Windows around the main optical emission lines of [OI], [OII] and [OIII], [NII], HeI and the Balmer series from Hα to Hϵ were masked in all fits. Because of its interstellar absorption component, the NaI D doublet was also masked. A more detailed ac-

---

[1] Available at www.starlight.ufsc.br. The version of STARLIGHT used in this work differs from the publicly available one, but mostly in aspects not related to the analysis performed here.
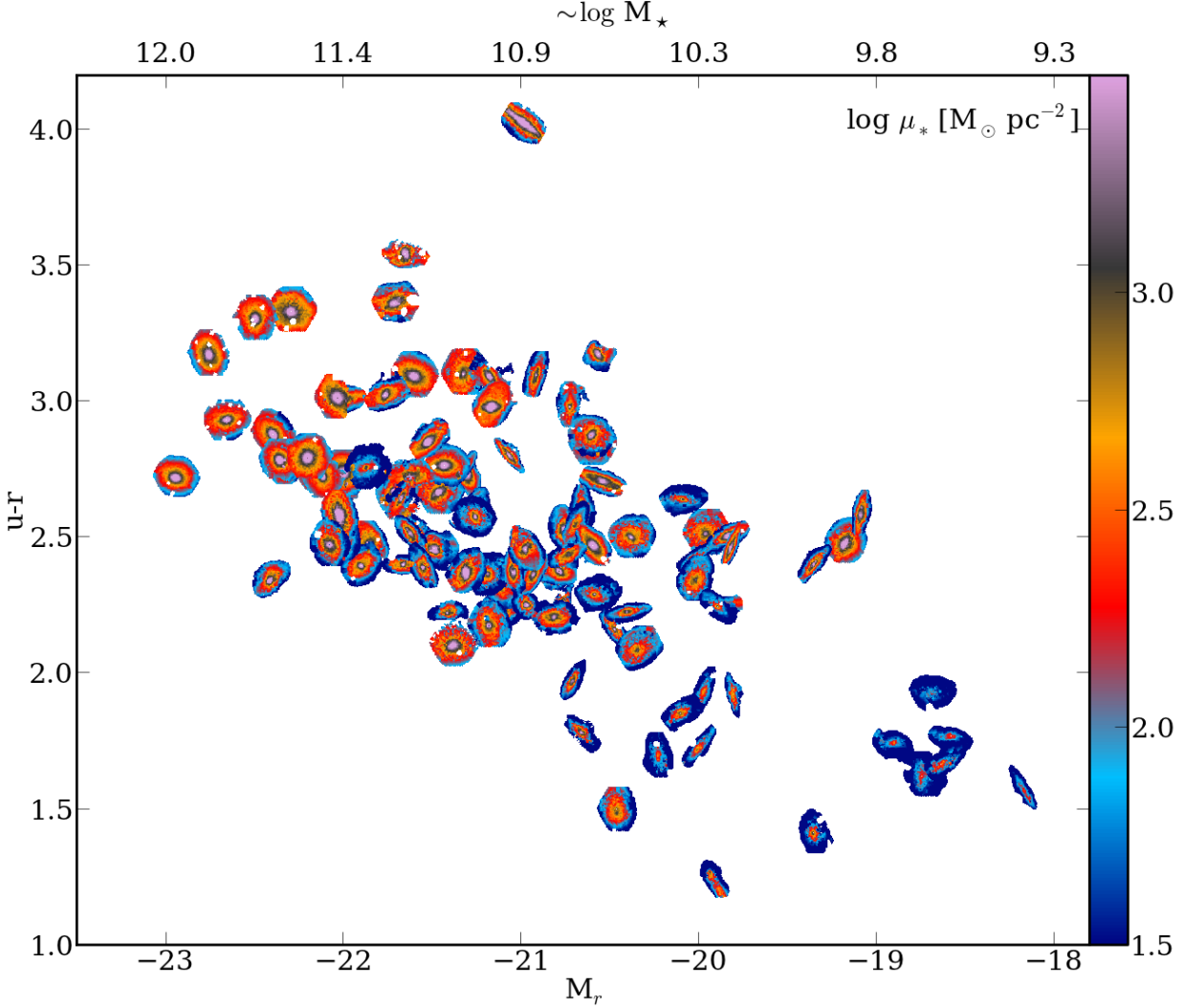
Fig. 2. 2D maps of the stellar mass density μ_*. Each galaxy is placed in its location in the $u - r$ vs. M_r diagram, where color and magnitude correspond to its global values. The stellar mass corresponding to M_r is shown in the top horizontal axis, following the fit $\log M_* = -0.45 - 0.54 M_r$ (Fig. 5b). The 2D maps are shown with North up and East to the left.

count on how we process CALIFA data cubes through STARLIGHT is given in Cid Fernandes et al. (2013a,b).

All spectral fits were performed using the cluster Grid-CSIC at the Instituto de Astrofísica de Andalucía. Example spectral fits are presented in Appendix B.

3.2. SSP spectral models

SSP models are the key ingredient in any spectral synthesis analysis, as it is through them that one transforms observed quantities to physical properties of the stellar populations in galaxies. SSP spectra result from the combination of an initial mass function (IMF) with stellar isochrones and libraries that provide the spectra of stars with temperature, gravity and metallicity demanded by the evolutionary tracks (e.g., Tinsley 1980; Bruzual & Charlot 1993; Leitherer et al. 1999; Walcher et al. 2011; Conroy 2013).

All these ingredients involve choices among different options (different IMFs, different tracks, different libraries, and differ-

ent codes to put them all together), and for this reason we have performed spectral fits using three different sets of SSPs: (a) The *GM* base is a combination of the SSP spectra provided by Vazdekis et al. (2010) for populations older than 63 Myr and the González Delgado et al. (2005) models for younger ages. (b) Base *CB* is an updated version of the Bruzual & Charlot (2003) models that replaces STELIB (Le Borgne et al. 2003) with a combination of the MILES (Sánchez-Blázquez et al. 2006; Falcón-Barroso et al. 2011) and GRANADA (Martins et al. 2005) spectral libraries. (c) Base *BC* comprises the standard Bruzual & Charlot (2003) models.

In Cid Fernandes et al. (2013b) we have compared the results of fitting the same 98291 spectra studied here, and the main conclusions are: masses (or mass surface density), mean ages and extinction are in very good agreement. Some discrepancies are, however, found in metallicity. Comparing *GM* and *CB*, the dispersion in luminosity weighted ages is 0.14 dex and the dispersion in A_V is 0.06 dex. *GM* stellar masses are 0.27 dex higher than *CB* due to the different IMFs (Salpeter vs. Chabrier), but apart from this offset, the two masses agree to within a disper-
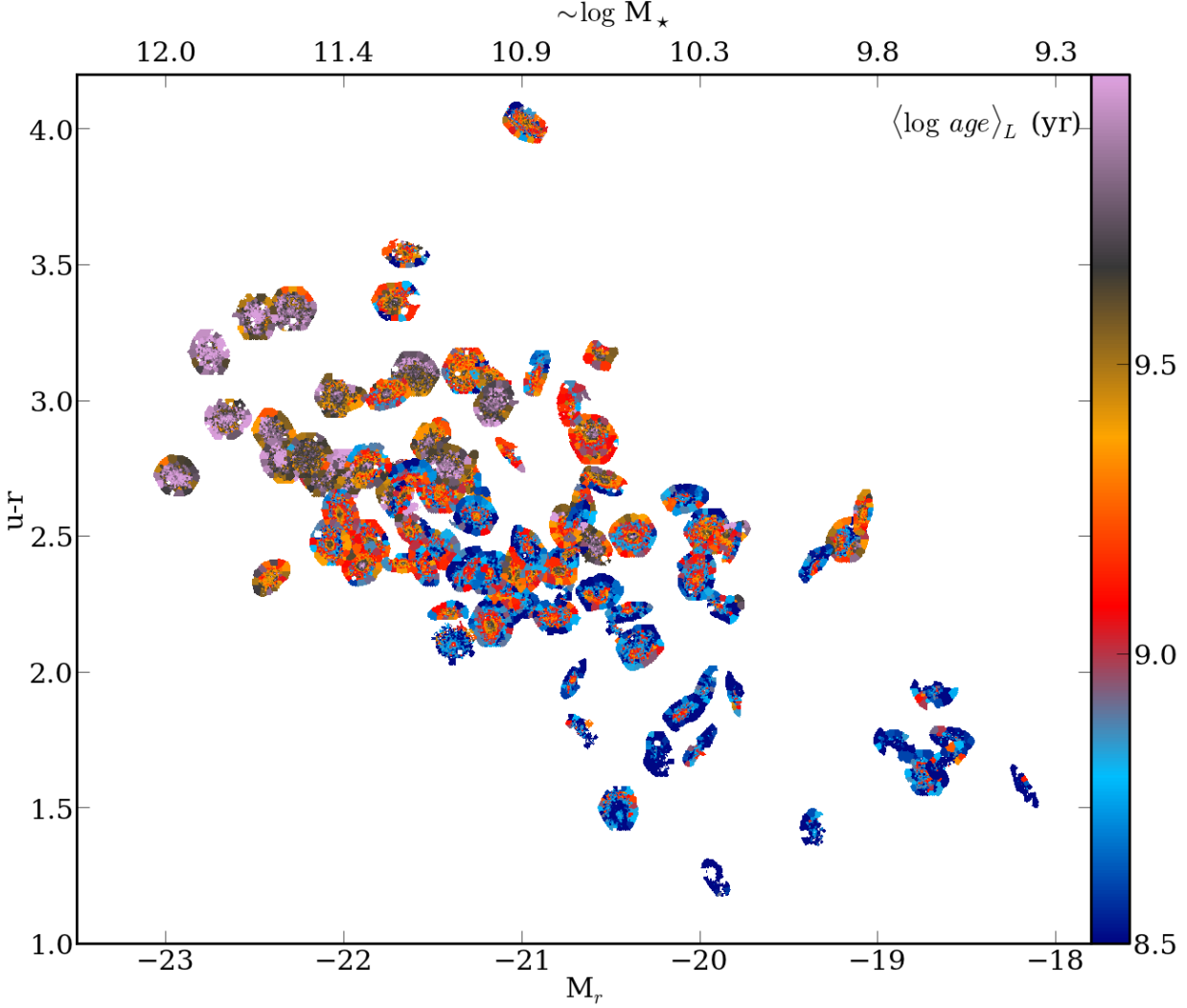
Fig. 3. As Fig. 2, but for images of the luminosity weighted mean age, $\langle \log age \rangle_L$ (in yr). Radial age gradients are visible in galaxies in the green valley ($-22 < M_r < -20$ and $2 < u - r < 3.5$), but not in the blue cloud or red sequence. Note that CALIFA 853 ($u - r = 4.02$, $M_r = -20.98$) has ages similar to other galaxies of similar M_r, and its red color is mainly due to extinction ($A_V(1HLR) = 1.2$).

sion of 0.16 dex. Similar conclusions are obtained when *GM* and *BC* results are compared. In short, the differences in mass, age and extinction obtained with these three sets of SSP models are all relatively small. Uncertainties due to random noise variations and continuum shape errors associated to flux calibration were evaluated through simulations and found to be somewhat smaller than, but of the same order as those associated with the choice of SSP models.

For these reasons, here we present the results obtained with only one set of SSP models. We have chosen base *GM*, but a comparison of the results obtained with other bases for the most relevant galaxy properties analyzed here is presented in the Appendix B. The *GM* base spans 39 ages from 1 Myr to 14 Gyr, and four metallicities ($Z = 0.2, 0.4, 1, 1.5\,Z_\odot$). They are built with the Girardi et al. (2000) evolutionary tracks, except for the youngest ages (1 and 3 Myr), which are based on the Geneva tracks (Schaeller et al. 1992; Schaerer et al. 1993a,b; Charbonnel et al. 1993). We adopt a Salpeter initial mass function throughout.

4. Spatially resolved properties of the stellar population in galaxies

The spatial distributions of μ_* and the luminosity weighted mean stellar age ($\langle \log age \rangle_L$, defined in equation 9 of Cid Fernandes et al. 2013a) are at the heart of the analysis carried out in this paper. For this analysis we prefer to use luminosity weighted ages for two reasons: first because luminosity is more sensitive than mass to age variations and thus provides a wider range of ages; second, because after comparing for several galaxies the ages estimated by STARLIGHT with ages estimated using Lick indices, we find that luminosity weighted ages are more in accord with Lick ages than mass weighted ones, so this choice facilitates comparison with this more traditional school of stellar population analysis in galaxies. This section presents the 2D maps and radial profiles of μ_* and $\langle \log age \rangle_L$. The results are presented in the framework of the CMD. Because absolute magnitude is related to M_* and color is a proxy for the stellar population age, the CMD is a
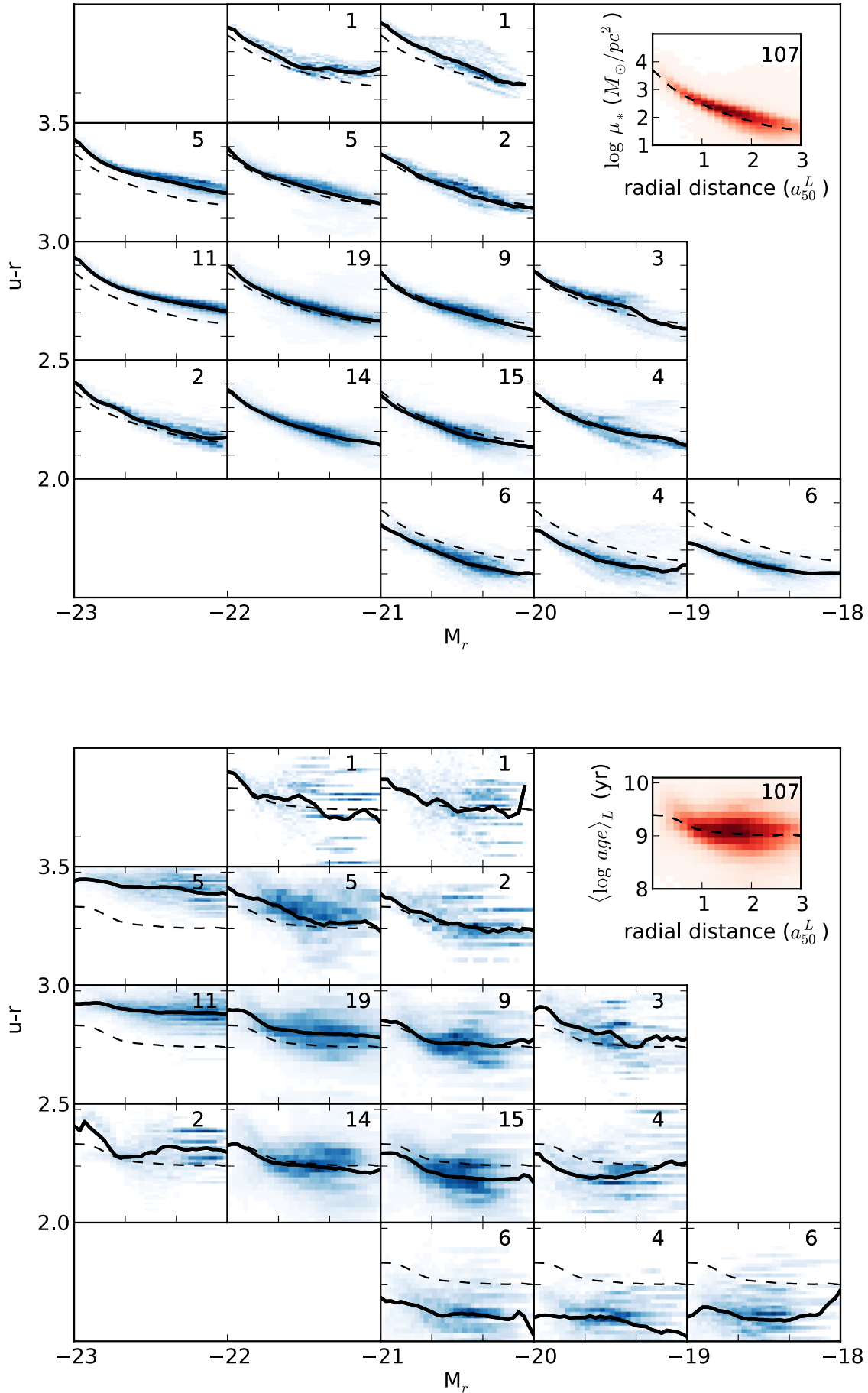
Fig. 4. Radial profiles (in units of HLR) of the stellar mass surface density ($\log \mu_*$, upper panel), and luminosity weighted mean age, ($\langle \log age \rangle_L$, bottom panel). Results are stacked in each CMD bin. Individual spaxels are shown in blue, while the mean profile in each CMD box is traced by a solid line. The dashed line is the averaged profile obtained with the 107 galaxies. This profile is also shown in the upper right inset box that contains the whole spaxel distribution (in red). The number of galaxies in each bin is indicated in each panel.

convenient observational framework to study the properties of different types of galaxies.

4.1. 2D maps: Stellar mass surface density and age

Figs. 2 and 3 both show the M_r vs. $(u - r)$ CMD for our sample[2]. Each galaxy is represented by its 2D map of μ_* (Fig. 2) and $\langle \log age \rangle_L$ (Fig. 3), located at the position of their integrated M_r and $(u - r)$ values. In these plots the SFH of each galaxy is compressed into μ_* and $\langle \log age \rangle_L$, with μ_* representing the end product of the SFH and $\langle \log age \rangle_L$ a measure of the pace with which this end product was achieved.

Cid Fernandes et al. (2013a) explain the processes that we follow to convert light into mass and the determination of the ages through the spatially resolved SFH, all included in our analysis pipeline PYCASSO. Effects of the spatial binning are visible in the mean age maps, where all pixels in a Voronoi zone have the same value. These effects are not noticeable in the μ_* images because the zoning effect was softened by scaling the value at each pixel by its fractional contribution to the total flux in the zone, thus producing smoother images.

Figures 2 and 3 show the results obtained with the *GM* template library. Note that our spectral synthesis analysis accounts for extinction, thus, to the extent that the simple foreground dust screen model works, our μ_* values and their radial variation are free of dust effects. This is an improvement with respect to most works based on photometry, which estimate μ_* from the surface brightness, typically assuming that color variations are entirely due to changes in M/L, and dust effects on colors compensate those on luminosity.

Fig. 2 shows the stellar mass surface density maps of each of our 107 galaxies. One sees that spheroids are one or two orders of magnitude denser than disks. The gradient is steeper in the luminous and red galaxies than in faint and blue ones. The disk μ_* scales well with the luminosity of the galaxy.

Fig. 3 shows that $\langle \log age \rangle_L$ is correlated both with color (as expected) and luminosity (due to the downsizing effect). Larger age gradients are seen in the galaxies in the green valley than in the more massive red galaxies. The fainter and bluer galaxies either do not show a clear age gradient or seem to have more of an inverted gradient, being younger in the center than in the outskirts.

4.2. Radial profiles of μ_* and $\langle \log age \rangle_L$

In order to study the radial variations with galaxy type, we compress the 2D maps of μ_* and $\langle \log age \rangle_L$ in azimuthally averaged radial profiles. A common metric is needed to compare (and stack) the radial profiles, so we express the radial distance in units of the half light radius (HLR). Appendix A explains how we have derived a_{50}^L, defined as the semimajor axis length of the elliptical aperture containing 50% of the light at 5635 Å. There we also compare a_{50}^L with the Petrosian radius (r_{50}^P) and with the half light radius obtained with circular apertures (R_{50}^L).

PYCASSO provides with two methods to compute radial profiles: area or spaxel averaging (Cid Fernandes et al. 2013a). The latter method, which averages a property among all values in the same radial bin, is used here for both μ_* and $\langle \log age \rangle_L$, but we note that area averaging yields very similar results.

We divide the CMD into 5×5 bins, covering the whole range in absolute magnitude ($-23 \leq M_r \leq -18$) and color ($1.25 \leq u - r \leq 4.25$). The individual radial profiles of galaxies located in the same bin are stacked, limiting the radial range to $R \leq 3$ HLR. The number of galaxies is shown in the top-right corner in each box.

Fig. 4 shows the stacking results for $\log \mu_*$ and $\langle \log age \rangle_L$ as solid lines. Values for individual spaxel are shown in blue, intensity coded by the density of points. Note that, unlike for μ_*, $\langle \log age \rangle_L$ images cannot be softened by the zone effects, so we assign the same age to all the spaxels that belong to a given Voronoi zone. Because these spaxels are at different distances within the galaxy, the radial structure of $\langle \log age \rangle_L$ shows horizontal stripes that are not seen in the radial profiles of $\log \mu_*$. The consequence is that the dispersion in $\langle \log age \rangle_L$ profiles is higher than in $\log \mu_*$, and the radial structure of $\langle \log age \rangle_L$ is more uncertain than that of $\log \mu_*$ beyond 2 HLR (where spatial binning becomes prevalent).

The mean stacked profile for all 107 galaxies is shown as the inset in the top-right of each figure. The horizontal and vertical scales of all panels is the same used in this plot. In addition to the mean stacked profile (solid line) in each CMD bin, we plot for reference the mean stacked profile of the 107 galaxies (dashed line), so that systematic trends in the radial structure are more clearly seen.

As expected, μ_* exhibits negative radial gradients in all cases. In the nuclei $2.5 \leq \log \mu_* (M_\odot pc^{-2}) \leq 4.5$, while in the outer radii $1.5 \leq \log \mu_* (M_\odot pc^{-2}) \leq 3$. A trend of $\log \mu_*$ with the magnitude and the color of the galaxy is found: Red and luminous galaxies are denser than blue and faint galaxies throughout their extent. Disk galaxies show $\log \mu_*$ profiles that scale with M_r. A general trend is also found between the central value of $\log \mu_*$ of each galaxy (or the average $\log \mu_*$) and M_r, as expected since the magnitude correlates with the total mass.

Similarly, $\langle \log age \rangle_L$ shows negative gradients, but not for all CMD bins. A strong gradient is found for most of the disk galaxies in the green valley ($-22 \leq M_r \leq -19$ and $2 \leq u - r \leq 3.5$), with mean ages ranging from 5–6 Gyr at the galaxy center to 1 Gyr at $R = 1$ HLR in the disk. Galaxies in the blue cloud ($M_r \geq -20$ and $u - r \leq 2$) show less age gradient, with flat radial profiles at an age ≤ 1 Gyr beyond 1 HLR. Red galaxies are the oldest (~ 10 Gyr) not only at the core but also in the extended envelope, and they also show $\sim$ flat age gradients.

CALIFA sample was chosen to cover most of the FoV of PPaK, which corresponds to sizes between 2 and 5 HLR, being the typical size 3 HLR. This is why the radial profiles in Fig. 4 are represented up to 3 HLR, but the 2D maps in Figure 3, are plotted up the maximum radius observed for each galaxy.

5. Stellar masses

The stellar mass is one of the most important physical properties for galaxy evolution. Armed with the results from our spectral synthesis analysis, we now present total stellar masses derived for the CALIFA subsample of 107 galaxies.

These masses are obtained by adding, for each galaxy, the masses of each zone, hence taking into account spatial variations of the stellar populations and extinction across the face of the galaxies. We take into account areas that were masked in the data cubes (cf. Appendix A), replacing the missing spaxels by the average of μ_* values at the same radial distance. On average, this correction amounts to just $\sim 5\%$, and for only 3% of the galaxies the correction reaches 0.05–0.1 dex in $\log M_*$. We have further verified that light outside the PPak FoV does not add much to

---

[2] they are from SDSS tables and have been corrected for Galactic extinction
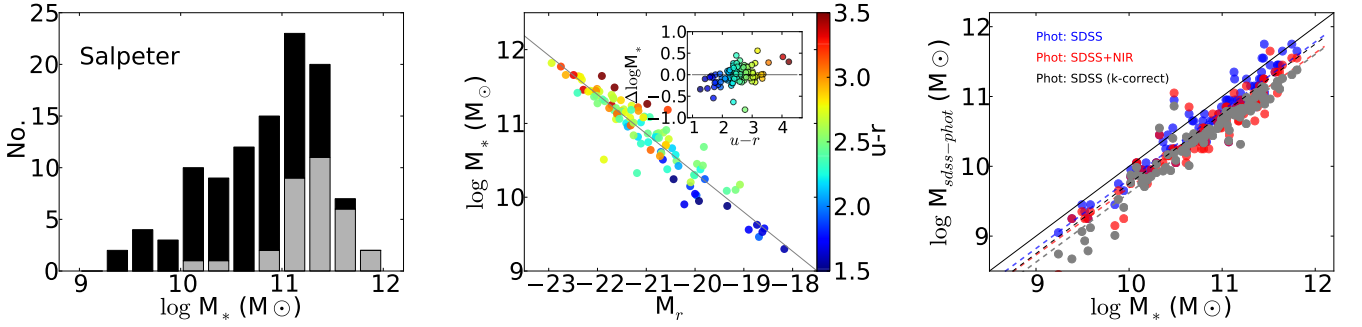
Fig. 5. a) Distribution of total stellar masses obtained from the spatially resolved spectral fits of each galaxy. Black bars mark galaxies with $C < 2.8$, while grey bars denote those with $C \geq 2.8$. b) Correlation between the total stellar mass and SDSS r-band total magnitude. c) Comparison of the masses estimated from our analysis (horizontal axis) and from SED fitting of integrated SDSS photometry (blue circles) and SDSS+2MASS (red) bands using the code explained in Walcher et al. (in prep.) Grey points show the comparison with masses obtained fitting the SDSS photometry with the k-correct routine of Blanton & Roweis (2007). Note that photo-SED masses are obtained assuming a Chabrier IMF, while the STARLIGHT masses are for a Salpeter IMF. The dashed (blue, red and grey) lines show the best linear fits, while the solid black line is the one-to-one relation. The dashed black line is the one-to-one relation shifted by 0.25 dex to account for the expected offset due to IMF.

the stellar masses computed here. As explained in Appendix C, correcting for this effect would increase our masses by $\sim 8\%$ on average.

Fig. 5a shows the distribution of M_*. The masses range between 10^9 and $10^{12} M_\odot$, with the peak at $\sim 10^{11} M_\odot$. Overall, our sample is dominated by galaxies in the 10^{10}–$3 \times 10^{11} M_\odot$ range, so CALIFA is sampling well Milky Way and M31 like galaxies. Using the concentration index, $C = r_{90}^P / r_{50}^P$, to divide the sample in spheroidal ($C \geq 2.8$) or disk ($C < 2.8$) dominated galaxies, we find a clear segregation in mass: galaxies with $C \geq 2.8$ are dominated by the most massive ones ($\geq 10^{11} M_\odot$), while disk galaxies are well distributed over all the CALIFA mass range, with the peak at $10^{11} M_\odot$. Note that this distribution in mass is not meant to be representative of the local universe, since the CALIFA sample is not complete for $M_r \geq -19.5$. Dwarf elliptical or irregular galaxies, for instance, are not sampled.

In the previous section the spatially resolved properties of galaxies were presented as a function of their location in the $(M_r, u-r)$ CMD (Figs. 2–4), where the absolute magnitude plays the qualitative role of galaxy mass. To calibrate this relation in quantitative terms, Fig. 5b shows our stellar masses against M_r. Results are shown for base GM, as results obtained with this set of SSP models are adopted throughout this paper. As expected, a good correlation is found, but the dispersion in mass is ~ 0.19 dex with respect to a linear fit. The inset in Fig. 5b shows that residuals correlate with color, revealing the well known relation between stellar mass and stellar population properties, with massive galaxies being older (and thus having larger M/L) than less massive ones, as previously shown in Fig. 4.

Fig. 5c compares the masses estimated from our spatially resolved spectroscopic analysis with those obtained by Walcher et al. (in prep.) through SED fitting using just SDSS photometry (blue symbols) or 2MASS plus SDSS bands (red). Grey points represent photo-masses obtained by fitting the SDSS bands with the KCORRECT code (Blanton & Roweis 2007). Our STARLIGHT-based masses correlate well with the photometric masses, but with systematic offsets: Red, blue and grey points in Fig. 5c are shifted from the one-to-one line by -0.20, -0.33 and -0.39 dex, respectively. Of this offset, a factor of -0.25 dex can be accounted for by the Salpeter IMF used in our spectral fits with base GM versus the Chabrier IMF adopted in the photo-masses. Also, the photo-masses are not corrected for extinction, so they

are expected to be a factor 0.16–0.2 dex lower than the STARLIGHT values if we assume an average $A_V = 0.4$–0.5 mag. Alternatively, the spectroscopic and photometric methods are obtaining SFHs that weight the contribution of old stellar population in different ways, resulting on M/L ratios larger in STARLIGHT than obtained with SED fitting. The dispersion around the best linear fits (dashed lines in Fig. 5c) are 0.16–0.19 dex, which is of the same order as the dispersion between different photo-masses.

Table 1 lists the masses for all 107 galaxies obtained for the base GM. Fig. B.2 in the Appendix shows the comparison of mass distributions for other SSP bases.

6. Spatially resolved vs. galaxy averaged and integrated stellar population properties

In this section we take advantage of our spatially resolved information to address two inter-related questions: *(a)* What radial location can be considered typical of a galaxy as a whole in terms of its stellar population properties? *(b)* How do properties derived from an integrated spectrum (obtained from the spatially collapsed data cube) relate to the typical (spatially averaged) properties within a galaxy?

The relevance of these questions resides on the fact that spatially unresolved spectra of galaxies will forever be more abundant than IFS data like CALIFA. It is therefore important to understand precisely what is it that an integrated spectrum represents.

6.1. Galaxy averaged stellar population properties

Let us define galaxy-wide average values for $\langle \log age \rangle_L$ and μ_* as follows:

– *Galaxy-averaged age*: The luminosity weighted mean value of $\langle \log age_{xy} \rangle_L$ over all spaxels, computed as

$$\langle \log age \rangle_L^{galaxy} = \frac{\sum_{xy} L_{xy} \langle \log age_{xy} \rangle_L}{\sum_{xy} L_{xy}} \qquad (1)$$

where L_{xy} is evaluated at our reference wavelength 5635 Å.
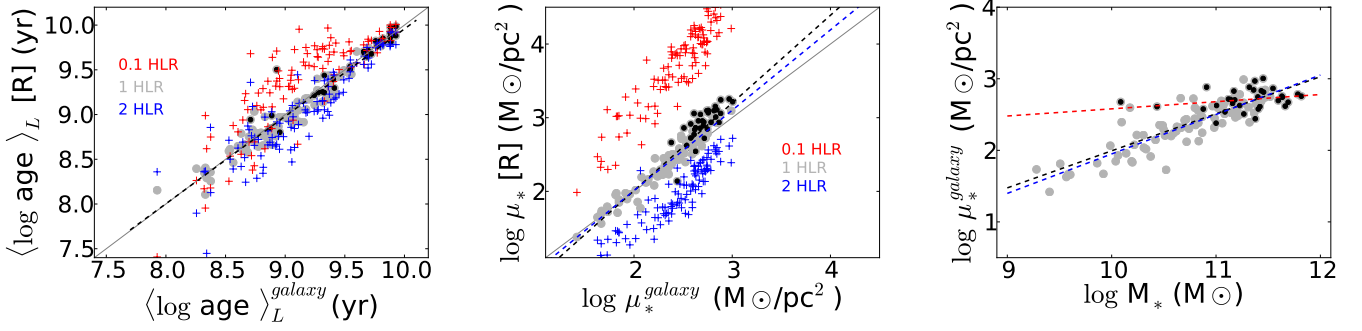
Fig. 6. Left: Correlation between $\langle \log age \rangle_L$ at 1 HLR and the galaxy-averaged age $\langle \log age \rangle_L^{galaxy}$. Black dashed line shows the fit, which is almost equal to the one-to-one line. Black dots mark spheroidal galaxies, $C \geq 2.8$. Red and blue plus signs establish the relation between the nuclear (inner 0.1 HLR) and outer disk (2 HLR) ages as a function of $\langle \log age \rangle_L^{galaxy}$. Center: Correlation between the stellar mass surface density at 1 HLR (gray circles) and $\log \mu_*^{galaxy}$. Black dashed line shows the fit to all the points, and dashed blue line the fit to the disk galaxies; plus signs like in the left plot. Right: Correlation between the galaxy averaged stellar mass surface density and galaxy stellar mass. Black points are spheroidal galaxies, $C \geq 2.8$. The dashed lines show the fits, for disk (blue) dominated galaxies and spheroidals (red). Black dashed line is the fit to all the galaxies.
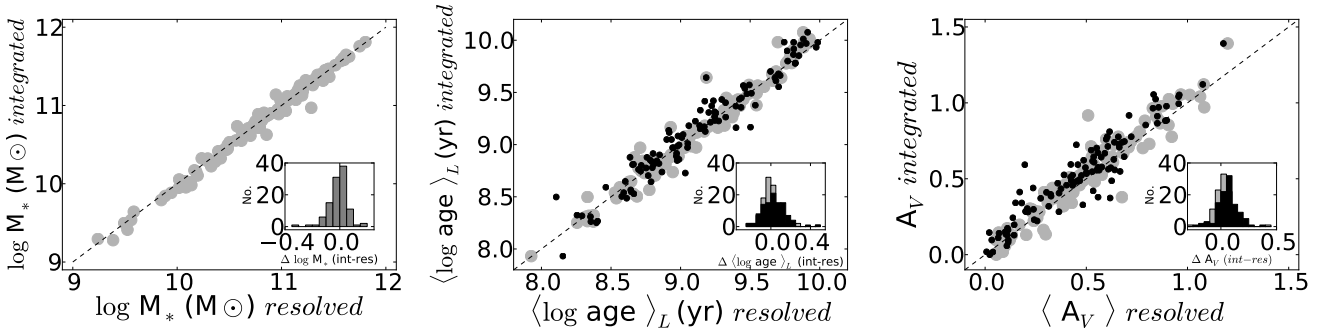
Fig. 7. Comparison of the averaged stellar population properties derived from the spatially resolved star formation history and the integrated properties derived from fitting the total galaxy spectrum: a) total stellar mass; b) luminosity weighted age; c) stellar extinction. The histograms in the insets show the distribution of the difference between the integrated and resolved properties. Black dots show the comparison between the integrated property and the value of the property at 1 HLR.

– *Galaxy-averaged stellar mass surface density:* We simply divide the total mass (summing the contributions from all the spaxels) by the total area of these spaxels to obtain the galaxy averaged stellar mass density

$$\mu_*^{galaxy} = \frac{\sum_{xy} M_{xy}}{\sum_{xy} A_{xy}} \qquad (2)$$

Fig. 6 compares these galaxy-wide averages with the corresponding values at $R = 0.1$ (red crosses), 1 (grey circles) and 2 HLR (blue crosses).

The left panel shows a very good agreement between $\langle \log age \rangle_L$ at 1 HLR and the galaxy-wide average. The relations for other radii exihibit offsets and larger dispersions. As expected (see Fig. 4), the nuclei are older by (on average) 0.2 dex with respect to the galaxy averaged age (red crosses). Note that due to the variation of the age gradient with the galaxy mass and Hubble type, the nuclei of spheroidal galaxies ($C \geq 2.8$) are (on average) only 0.16 dex older than $\langle \log age \rangle_L^{galaxy}$, whereas for disk galaxies this difference increases to 0.23 dex. On the other hand, the outer 1–3 HLR of either disk or spheroidal galaxies are more similar to the average galaxy age (blue crosses), with an average offset of -0.08 dex.

Fig. 6b repeats these comparisons, but now for the stellar mass surface density. Again, the galaxy-averaged values are well matched by the μ_* values at $R = 1$ HLR. For spheroidal galaxies

(marked with black dots), μ_*^{galaxy} is slightly smaller than μ_* at 1 HLR, coinciding better with μ_* at 1.2 HLR. In nuclei μ_* is significantly larger than μ_*^{galaxy}, by typically 1.25 dex in disk galaxies and 1.43 for spheroidal galaxies.

In summary, the values of $\langle \log age \rangle_L$ and μ_* at 1 HLR represent remarkably well the galaxy-averaged age and stellar mass surface density, except that spheroidal galaxies are slightly denser at $R = 1$ HLR than their spatially averaged value.

Both $\langle \log age \rangle_L^{galaxy}$ and μ_*^{galaxy} correlate with the total stellar mass. The latter relation is shown in the right panel of Fig. 6, where one sees μ_*^{galaxy} increasing from $\sim 10^{1.5} M_\odot/pc^2$ for $M_* \sim 10^9 M_\odot$ to $\sim 10^3 M_\odot/pc^2$ for the most massive galaxies in the sample. The points are well fitted by a power law, $\mu_*^{galaxy} \propto M_*^{0.52 \pm 0.04}$. This relation was reported before by Kauffmann et al. (2003b) from the analysis of a much larger SDSS sample. They also report a sharp change in the slope in the μ_*–M_* relation at a stellar mass of $\sim 3 \times 10^{10} M_\odot$, finding that below this mass μ_* increases as $M_*^{0.54}$, while above it μ_* is constant. Even though Fig. 6c does not show a clear change in slope, we can confirm that in the disk galaxies of our sample, $\mu_*^{galaxy} \propto M_*^{0.55 \pm 0.04}$, and in spheroid dominated galaxies (black symbols) the relation follows a much flatter slope, with $\mu_*^{galaxy} \propto M_*^{0.1 \pm 0.07}$. Similar results are obtained if we repeat the analysis replacing μ_*^{galaxy} by the surface density at 1 HLR, except that in this case the slope for

early type galaxies is 0.02 ± 0.11, much closer to the Kauffmann et al. (2003) fit. The transition mass of $\sim 3 \times 10^{10} M_\odot$ reported by Kauffmann et al. (2003) corresponds to ~ 5–$6 \times 10^{10} M_\odot$ for our IMF. Our sample does not yet allow us to precisely pinpoint a transition mass. Nonetheless, we will see below that all the spheroid dominated galaxies in our sample with $M_* \geq 10^{11} M_\odot$ show radial variations of μ_* that are independent of the stellar mass.

6.2. Integrated vs. galaxy averaged

Besides the 98291 spectra of all zones of all galaxies, we have also used STARLIGHT to fit the 107 total spectra obtained by collapsing the data cube to a single spectrum per galaxy. These integrated spectra, which emulates the situation in integrated spectroscopy surveys, are fitted in the same way as the individual ones, adopting identical assumptions regarding the SSP templates, masks, etc. It is instructive to compare properties derived from the integrated spectrum with those derived from our spatially resolved analysis.

Fig. 7a compares the total stellar masses derived from the integrated spectra (on the vertical axis) with those obtained by adding the zone masses (horizontal). The two values agree very well. The mean difference in $\log M_*$ is in fact 0.00, and the dispersion is ± 0.07 dex.

Fig. 7b compares the $\langle \log age \rangle_L$ values from the integrated spectra to the galaxy-average age (eq. 1, grey circles). Again, the two values match each other, with no mean offset and a dispersion ± 0.1 dex. Extinction values also agree, as shown in Fig. 7c. The A_V values obtained from spectral fits of integrated spectra are on average only 0.02 mag larger than the mean A_V over all zones, with a dispersion of just ± 0.03 mag. The black symbols in Figs. 7b and c compare integrated ages and extinctions to those at 1 HLR. The integrated minus 1 HLR differences are 0.02 ± 0.12 dex for $\langle \log age \rangle_L$ and 0.06 ± 0.09 mag for A_V, only slightly worse than for galaxy-wide averages.

Overall, the total stellar mass, age and extinction estimated from integrated spectroscopy are remarkably robust when compared with those obtained from a spatially resolved analysis.

7. Mass weighted size: The half mass radius and its relation to the half light radius

While evolution of galaxies is nowadays characterized by their stellar mass more than their luminosity, galaxy sizes are still estimated from the way light, not mass, is distributed. Just as the stellar mass of a galaxy is a more fundamental property than its luminosity, at least when one considers galaxy evolution, the Half Mass Radius (HMR) is a more physical metric than the HLR. These two radii are only equivalent in the idealized case of a spatially uniform M_*/L ratio. Variations of the SFH and/or extinction within a galaxy produce a spatially dependent M/L ratio, and hence differences in their sizes estimated from mass and from light.

We take advantage of our spatially resolved SFH and extinction maps to investigate the relation between HLR and HMR. We use the 2D distribution of μ_* to define the HMR, for both circular (R_{50}^M) and elliptical (a_{50}^M) apertures, as the radius at which the mass curve of growth reaches 50% of its asymptote. Fig. 8a shows how a_{50}^M and R_{50}^M relate to their luminosity based counterparts a_{50}^L and R_{50}^L. The following equations express the best fit relations between these radii (in kpc):

$$\log a_{50}^M = (0.90 \pm 0.04) \times \log a_{50}^L - (0.03 \pm 0.03) \qquad (3)$$

$$\log R_{50}^M = (0.87 \pm 0.04) \times \log R_{50}^L - (0.02 \pm 0.03) \qquad (4)$$

These fits and Fig. 8a show that the HMR is generally smaller than the HLR. The histogram of a_{50}^M/a_{50}^L for our 107 galaxies is shown in Fig. 8c (black bars). On average, $a_{50}^M/a_{50}^L = 0.80$ (std = 0.13), so galaxies are typically 20% smaller in mass than how they appear in optical light.

This number is only slightly smaller than the 25% reported by Szomoru et al. (2012) for a sample of high-redshift galaxies analyzed with multi-band photometry. This agreement gives us a preliminary indication that there is no significant cosmic evolution of the HMR/HLR ratio.

7.1. The relative roles of SFH and extinction gradients

Both SFH and extinction gradients induce differences between HMR and HLR. Our analysis provides a means to disentangle the relative roles of these two effects.

Unlike the HMR, the HLR is sensitive to extinction variations. When A_V increases inwards, which is generally the case, the excess dimming of the central regions with respect to outer ones produces HLR values larger than those which would be measured in the absence of extinction gradients. We use our STARLIGHT-derived A_V maps to "dust off" the $L_{\lambda 5635}$ images and re-evaluate the HLR from the extinction corrected curve of growth, obtaining $a_{50}^{L_{intrin}}$. This allows us to quantify the role of dust in the observed difference between HMR and HLR.

Fig. 8b compares a_{50}^M to both a_{50}^L (crosses) and $a_{50}^{L_{intrin}}$ (circles). Besides a slightly smaller scatter, the extinction correction brings the irregular galaxy NGC 3991 (CALIFA 475, the outlier cross with $a_{50}^M/a_{50}^L > 1$) to the one-to-one line. On average, however, $a_{50}^M/a_{50}^{L_{intrin}} = 0.85$ (std = 0.11) (Fig. 8c, grey histogram), corresponding to HMR 15% smaller than the extinction corrected HLR. Compared to the 20% difference found without this corrections, we conclude that dust gradients play a relatively small role in explaining the difference between mass and light based sizes.

The main reason why HMR < HLR is thus that stellar populations produce less light per unit mass in the center than outside. This is explicitly confirmed in Fig. 9, where $a_{50}^M/a_{50}^{L_{intrin}}$ is plotted against the difference in $\log M/L_{\lambda 5635}^{intrin}$ (i.e., the extinction-corrected M/L ratio) between $R = 1$ HLR and the nucleus. Galaxies with small M_*/L gradients have $a_{50}^M/a_{50}^{L_{intrin}} \sim 1$, while those with the largest gradients can be up to a factor of two more compact in mass than in light. Points in Fig. 9 are color-coded by the corresponding $\nabla \langle \log age \rangle_L$, showing that age variations are the main factor behind the difference between HMR and HLR.

Therefore HMR < HLR is ultimately a fingerprint of inside-out growth, previously found for this sample by Pérez et al. (2013). This result explains why effective radii derived in the near infrared are in general smaller than those obtained in optical bands (La Barbera et al. 2004, 2010; Falcón Barroso et al. 2011). Besides being less sensitive to extinction effects, the near infrared is a better tracer of stellar mass than the optical.

7.2. Relation with galaxy properties

The dispersion in the HMR/HLR ratio is significant (Fig. 8c), which prompts the question of whether it correlates with some global galaxy property. Szomoru et al. (2012) were unable to identify any significant dependence with a series of galaxy properties.
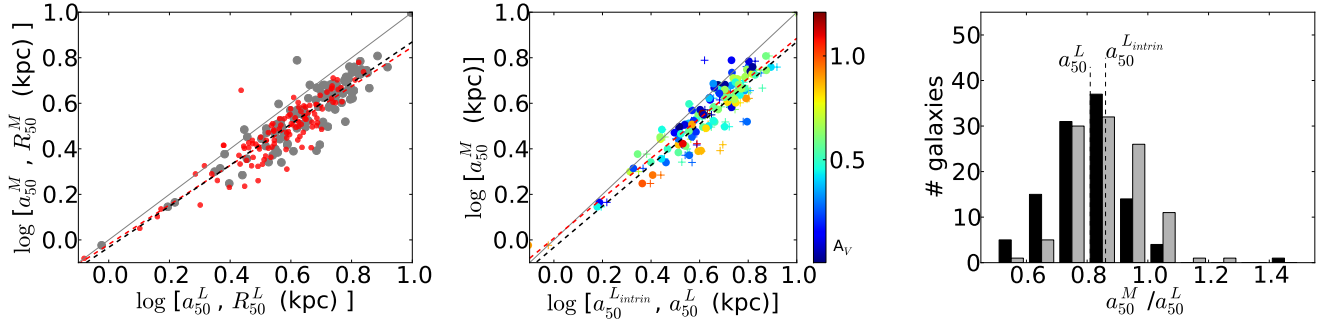
Fig. 8. a) The a_{50}^M (grey points) vs. a_{50}^L and R_{50}^M (red points) vs. R_{50}^L estimated from the stellar mass integrating the stellar mass surface density profiles. Grey and red dashed lines show the fits. b) Relation between a_{50}^M and $a_{50}^{L_{intrin}}$ (dots) and a_{50}^L (cross). Color bar codes A_V at a_{50}^L. c) Distribution of the ratio between half mass and half light ratio, corrected (grey bars) and un-corrected (black bars) by extinction. The dashed lines mark the averaged values of the distributions, $\log a_{50}^M / a_{50}^L$ = -0.096 (std= 0.07) and $\log a_{50}^M / a_{50}^{L_{intrin}}$ = -0.071 (std=0.06).

We investigate this issue examining correlations between a_{50}^M / a_{50}^L (and $a_{50}^M / a_{50}^{L_{intrin}}$) with galaxy mass, luminosity, age, color, concentration index, central surface brightness, and size. Two distinct behaviours are identified: a_{50}^M / a_{50}^L decreases with color, surface brightness, central stellar age and stellar mass surface density in galaxies that are bluer than $u - r \sim 2.5$, fainter than $M_r \sim -20.5$, younger than $\sim$ 1–3 Gyr, and less dense than $\log \mu_* \leq 3.5$ M$_\odot$/pc^2 at their core. This trend is appreciated in the relation between a_{50}^M / a_{50}^L and the stellar mass shown in Fig. 10. For galaxies with $M_* \lesssim 10^{11}$ M$_\odot$ one sees a_{50}^M / a_{50}^L decreasing with increasing stellar mass, whereas this ratio is almost constant for more massive galaxies. This reflects the bimodal distribution of galaxies found in SDSS (Strateva et al. 2001): for spheroid dominated ($C \geq 2.8$), red, old massive galaxies, the ratio is almost constant, independent of the stellar mass, but for disk galaxies, the ratio changes significantly from 1 to 0.5 as galaxies go from the blue cloud to the red sequence through the green valley.

Galaxies with lower $a_{50}^M / a_{50}^{L_{intrin}}$ are those with larger M/L gradients and age gradients. These are galaxies dominated by a large central bulge surrounded by an extended luminous blue disk. These results point to the same conclusions obtained in Pérez et al. (2013), where we find that galaxies with $M_* \geq 10^{10} M_\odot$ grow their mass inside-out, and galaxies with a critical mass $\sim$ 6–8 $\times 10^{10} M_\odot$ have been relatively more efficient growing their central regions. If galaxies grow inside-out, we expect that $a_{50}^M / a_{50}^L < 1$. In the proposed scenario by van Dokkum et al. (2010), galaxies more massive than $10^{10} M_\odot$ build their core via short violent bursts at high-redshift, and their envelope via accretion of material since $z = 2$. The SFH in the core, where half of the galaxy mass formed, results in a stellar population that is quite different from that of the extended envelope, giving $a_{50}^M / a_{50}^L < 1$. At intermediate masses, $\sim 10^{11} M_\odot$, disk galaxies have the lowest a_{50}^M / a_{50}^L, as expected if these galaxies were growing their central mass at a rate which is significantly larger than their extended envelope. Note, however, that for low mass galaxies ($M_* \leq 10^{10} M_\odot$), $a_{50}^M / a_{50}^L \sim 1$, as expected if they are not growing their mass inside-out, and the build up of their central mass is likely dominated by secular processes. Thus, HMR/HLR is a good probe of the variation of the star formation history in the core with respect to extended envelope in galaxies.
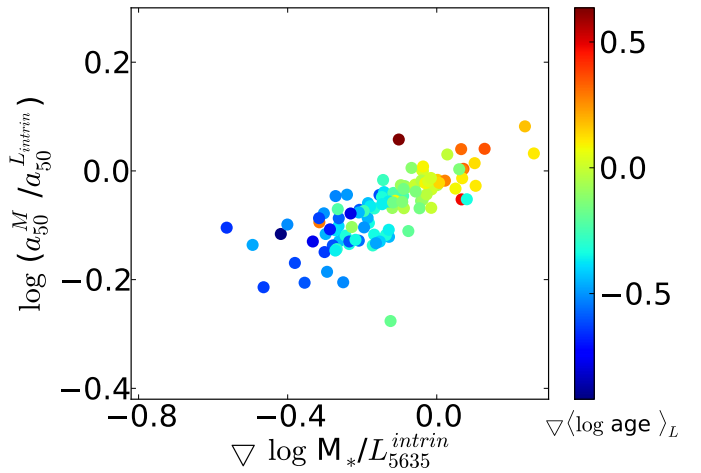
Fig. 9. Correlation between the $a_{50}^M / a_{50}^{L_{intrin}}$ and gradient of the M/L ratio. Color bar codes the gradient of the age of the stellar population in the inner 1 HLR.

8. Star formation histories in terms of stellar mass, surface density and morphology

We now explore the dependence of the SFH (represented by the first moment of the age distribution, $\langle \log age \rangle_L$) with the total stellar mass (M_*), surface density (μ_*), and morphology (as encoded by the concentration index C). We inspect how the radial structure of $\langle \log age \rangle_L$ and μ_* varies with M_* and C. We discuss first the relation resulting from our spatially resolved analysis between μ_* and $\langle \log age \rangle_L$, then their gradients in the inner HLR, and radial profiles. The goal is to ascertain whether galaxies dominated by the spheroid or by the disk are well separated in their spatially resolved stellar population properties, where and which, stellar mass or stellar mass surface density, is the main independent parameter that preserves the SFH of galaxies.

8.1. Stellar mass surface density - age relation

In a pioneering work, Bell & de Jong (2000) correlate the local surface brightness in the K band of a sample of spirals with the age of each region, derived from optical and near-infrared
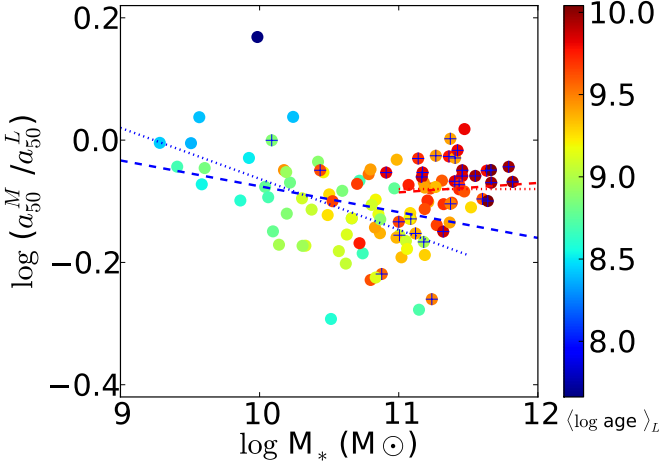
Fig. 10. Relation between a_{50}^M/a_{50}^L and the total stellar mass. Points are colored according to the luminosity weighted age of the stellar population at $R = 0.5a_{50}^L$. Galaxies with concentration index $C \geq 2.8$ are marked with a cross. Dashed blue line show the fit for all the galaxies with $\log M_*$ ($M_\odot$) ≤ 11, dashed red for $\log M_*$ ($M_\odot$) > 11, and dotted blue and red lines are the fit for disk dominated galaxies and spheroidal galaxies, respectively.

Fig. 11. The stellar mass surface density – age relationship resulting from fitting the 98291 spectra of 107 galaxies. The color bar shows the density of spectra per plotted point (red-orange are a few tens of spectra). Also plotted (as larger circles) are the averaged values for each galaxy, obtained as explained in Section 6. The colors of these circles code the galaxy mass (orange-red are galaxies more massive than $10^{11} M_\odot$) dashed line marks $\mu_* = 7 \times 10^2$ $M_\odot/pc^2$.

colors. They find that ages are much better correlated with their local surface brightness than with the galaxy absolute magnitude in the K band, and conclude that the surface density plays a more fundamental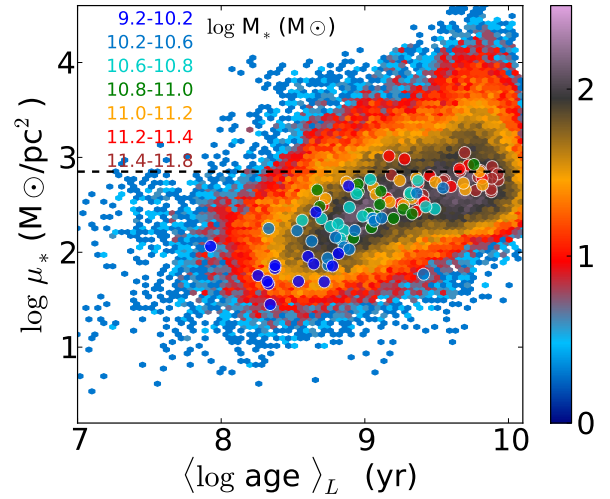 role in the SFH of disks than the mass of the galaxy. They suggest that the correlation can be explained through a dependence of the star formation law on the local density (see also Bell & Bowen 2000; Boissier & Prantzos 2000). Note that they assume that colors trace age, and use surface brightness and total luminosity as proxies for μ_* and M_* respectively. Furthermore, this conclusion was obtained only for spiral galaxies. In the light of this result, and armed with our spectroscopically derived properties, we ask whether this conclusion holds for all types of galaxies, and for all regions within galaxies.

We start by exploring the age-density relation for all regions of all galaxies in our sample. Fig. 11 plots μ_* as a function of $\langle \log age \rangle_L$ for all our 98291 individual spectra, color coded by the log density of points in the diagram. Large circles overplotted represent the galaxy averaged $\langle \log age \rangle_L$ and $\log \mu_*$ obtained as explained in Section 6 (equations 1 and 2). The color of these circles code M_* (as labeled on the left-hand side legend). In this plane, our galaxies are well divided into two distinct families that break at a stellar mass of ~ 6–$8 \times 10^{10} M_\odot$. Galaxies below this critical mass show a correlation between $\log \mu_*$ and $\langle \log age \rangle_L$, and are usually young disk galaxies. Above the critical mass, the relation is significantly flatter, and galaxies there are increasingly dominated by a spheroidal component. A similar result is found by Kauffmann et al. (2003b, 2006) analyzing galaxy averaged $\langle \log age \rangle_L$ and μ_* for 122808 SDSS galaxies. The critical mass reported by these works ($\sim 3 \times 10^{10} M_\odot$), is close to the one we find here once the differences in IMF are accounted for.

Note that galaxy-averaged values fall where a large fraction of the individual zone results are located. This is because $\log \mu_*^{galaxy}$ and $\langle \log age \rangle_L^{galaxy}$ are well represented by values around 1 HLR, and most of the single spaxel zones are located between 1–1.5 HLR. In fact, Fig. 11 shows that most of the individual zones follow the same general trend followed by the galaxy averaged properties. Thus, local ages correlate strongly

with local surface density. This distribution also shows that there is a critical value of $\mu_* \sim 7 \times 10^2 M_\odot/pc^2$ (similar to the value found by Kauffmann et al. 2006 once differences in IMF are factored in). Below this critical density μ_* increases with age, such that regions of low density formed later (are younger) than the regions of higher surface density, while above this critical density the dependence of μ_* on age is very shallow or altogether absent.

Since $\langle \log age \rangle_L$ reflects the SFH and it correlates with μ_*, the general distribution of galaxy zones in Fig. 11 suggests that the local mass density is linked to the local SFH, at least when $\mu_* \leq 7 \times 10^2 M_\odot/pc^2$. Since these densities are typical of disks (Fig. 7), this result is in agreement with the findings of Bell & de Jong (2000) that explain the correlation through a local density dependence in the star formation law. Note, however, that there is a large dispersion in the distribution for individual regions, caused mainly by the radial structure of the age and of the stellar mass surface density.

8.2. Radial gradients of stellar mass surface density and age

We now investigate inner gradients in age and μ_*, and their relation with M_*. The gradient of $\log \mu_*$ in the inner HLR of each galaxy was computed as $\nabla \log \mu_* = \log \mu_*[1 \text{ HLR}] - \log \mu_*[0]$, and similarly for $\nabla \langle \log age \rangle_L$. Fig. 12 shows these gradients as a function of the galaxy mass. Grey dots denote disk dominated galaxies ($C < 2.8$) and black dots mark spheroid dominated galaxies ($C \geq 2.8$). Coloured symbols show mean values in eight equally populated mass bins[3], with circles and stars representing spheroid and disk dominated systems, respectively.

A clear anti-correlation exists between $\nabla \log \mu_*$ and M_*. The stellar mass surface density profile becomes steeper with increasing galaxy mass. There does not seem to be a dependence

---

[3] 15 galaxies per bin, except in the two bins with largest mass (log $M_\odot > 11.4$) that add up to 17 galaxies

13
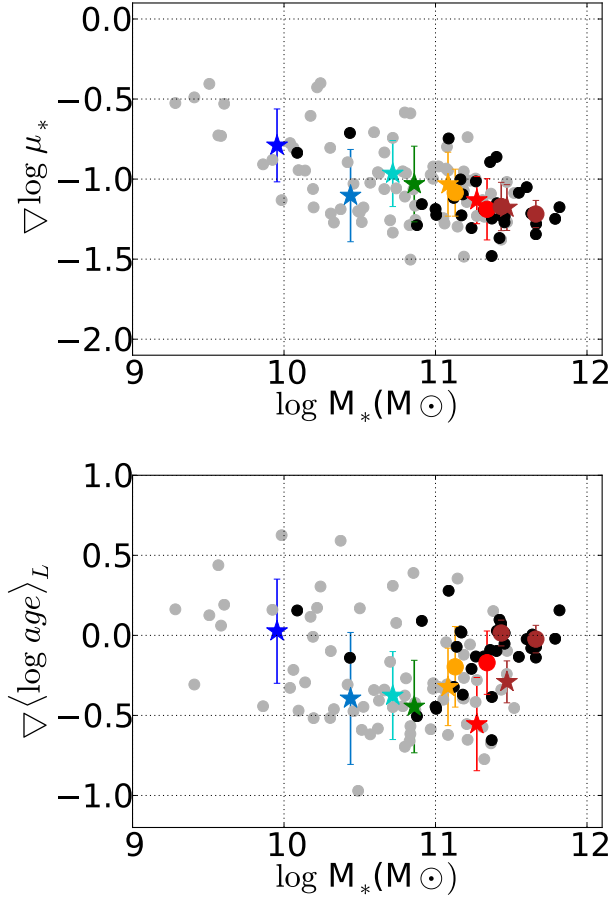
Fig. 12. Correlation between the inner gradient (calculated between the galaxy nucleus and at HLR) of $\log \mu_*$ (upper panel) and ages (bottom panel) and galaxy stellar mass. Black and grey points are galaxies with concentration index above (early type galaxies) and below (late type galaxies) 2.8, respectively. Median gradient value for different mass bins ($\log M_*$ ($M_\odot$) = 9.2–10.2, 10.2–10.6, 10.6–10.8, 10.8–11.0, 11.0–11.2, 11.2–11.4, and 11.4–11.6, 11.6–12.0) for early (dots) and late (stars) type galaxies are shown. Stars and large color dots are located at the mean value of $\log M_*$ of the galaxies that belong to corresponding the mass bin.

on morphology, with both disk and spheroid dominated galaxies of similar mass having similar gradients $\triangledown \log \mu_*$. Thus, at least for galaxies of $M_* \geq 10^{11} M_\odot$, $\triangledown \log \mu_*$ is independent of the galaxy morphology. We note that this anti-correlation between $\triangledown \log \mu_*$ and M_* holds only when the gradient is measured between the galaxy center ($\log \mu_*[0]$) and the galaxy averaged stellar mass density ($\log \mu_*[1 \, HLR]$), but that this result does not hold if the gradient is measured between the center and a fixed physical distance (e.g. 3 kpc) because a fixed distance represents a different position in each galaxy.

Age gradients show a different behavior with galaxy mass. While there is no correlation between $\triangledown \langle \log age \rangle_L$ and M_* for the sample as a whole, a clear trend emerges when galaxies are separated by their concentration index (colored stars for disks and circles for spheroids). Overall, negative age gradients are detected, but low mass disk dominated galaxies (dark blue star) and high mass spheroidal galaxies (brown circles) have flat age profiles. High M_* disk galaxies show negative age gradients

that steepen with increasing galaxy mass up to −0.5 dex/HLR for galaxies of $10^{11} M_\odot$, and then flatten towards the values of spheroidal galaxies of similar mass.

For early type galaxies, we obtain an average $\triangledown \langle \log age \rangle_L$ of −0.11 and a dispersion ±0.21 dex/HLR. Restricting to the more massive ones even smaller gradients are obtained: $\triangledown \langle \log age \rangle_L$ = −0.02 ± 0.08 dex/HLR for $M_* > 2.5 \times 10^{10} M_\odot$. These values are in good agreement with the results obtained by fitting stellar indices of several small samples of ellipticals observed with long-slit (eg. Sánchez-Blázquez et al. 2007; Mehlert et al. 2003), or IFU data (eg., Rawler et al. 2010; Kuntschner et al. 2006). These authors measure age gradients compatible with zero, ranging from −0.09 to 0.02 dex per effective radius, also in agreement with some of the results obtained from color gradients (Wu et al. 2005). Some of the CALIFA spheroidal galaxies show a positive central gradient (cf. Fig. 13), but these are certainly smaller than those derived from color gradients recently reported (e.g. Tortora et al. 2010; La Barbera et al. 2012) or from stellar indices (Greene et al. 2012).

For spirals we find that age gradients become increasingly negative for masses up to ∼ $10^{11} M_\odot$. In amplitude, these $\triangledown \langle \log age \rangle_L$ values are in agreement with results previously reported by MacArthur et al. (2004) based on color maps of several samples of spiral galaxies. However, our trend with M_* and the age-gradient values are not in agreement with those reported by Tortora el al. (2010). They use SDSS radial color profiles to find a bimodal distribution with galaxy mass, negative gradients of ∼ −0.2 dex per effective radius for galaxies less massive than $10^{10} M_\odot$, going through 0 and turning positive for high mass ($10^{11} M_\odot$) spirals. There are several possible reasons for this discrepancy, one of which is dust, which is not considered in their analysis. Furthermore, their fits compare colors of galaxy disks to single SSPs, an unrealistic approximation for the SFH of spirals, which are better represented by composite stellar population models such as those we use, or by τ models as in MacArthur et al. (2004).

In summary, we find that there is a good correlation between the μ_* gradient and M_*, and a trend of the age gradient with the mass that breaks at $M_* \sim 10^{11} M_\odot$, which is also approximately where the M_*-μ_* correlation breaks (Fig. 7c; Kauffmann et al. 2003b). In the next section we inspect if the trend of the age gradient with stellar mass is a consequence of the M_*-μ_* relation.

8.3. Radial profiles as a function of stellar mass and concentration index

A first glance at how the radial profiles of μ_* and $\langle \log age \rangle_L$ change with stellar mass is shown in Fig. 4 since M_r scales with the galaxy mass. In more detail, Fig. 13 shows the result of stacking $\log \mu_*$ (left column) and $\langle \log age \rangle_L$ (right column) radial profiles sorting the galaxies in seven M_* bins, chosen so as to have a similar number of 15 galaxies in each one. The mean radial profiles are obtained co-adding $\log \mu_*$, or $\langle \log age \rangle_L$, in each of the following intervals in $\log M_*(M_\odot)$: 9.2–10.2, 10.2–10.6, 10.6–10.8, 10.8–11.0, 11.0–11.2, 11.2–11.4, and 11.4–11.8.

The top row in Fig. 13 shows that the radial profiles of $\log \mu_*$ and $\langle \log age \rangle_L$ scale well with the total stellar mass. Both $\log \mu_*$ and $\langle \log age \rangle_L$ show negative gradients, which are flatter in the outskirts, except for the galaxies in the lowest mass bin (blue) which have a flatter $\langle \log age \rangle_L$ gradient also in the inner 1 HLR. These negative gradients are also observed if mass weighted age is used instead of luminosity weighted age. This trend confirms again that galaxies more massive than ∼ $10^{10} M_\odot$ grow inside-out (Pérez et al. 2013). More massive galaxies are denser than lower
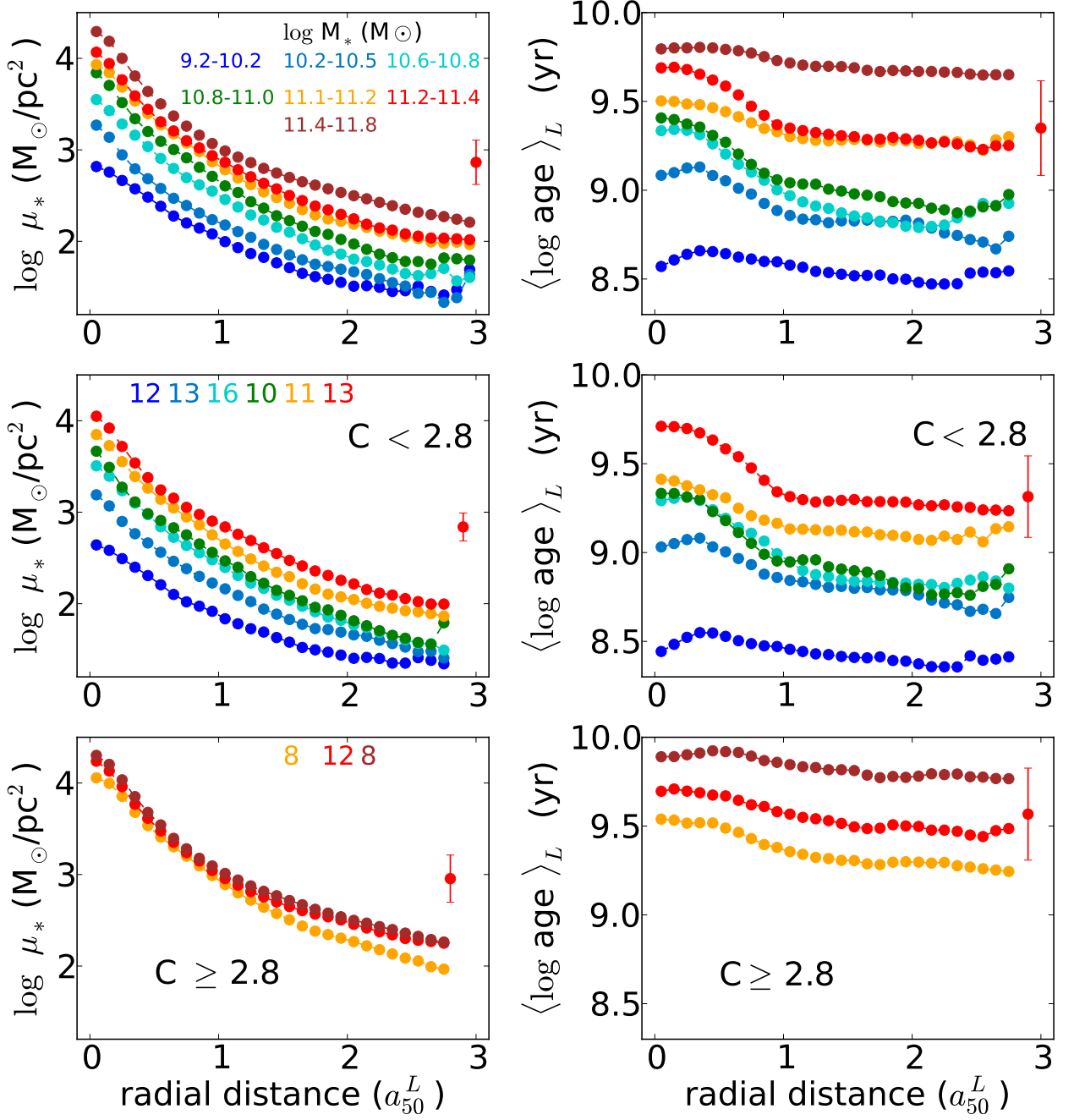
Fig. 13. The radial profiles of the stellar mass surface density and ages stacked in seven bins of galaxy stellar mass. In each bin log $M(M_\odot)$ is: 9.2–10.2, 10.2–10.6, 10.6–10.8, 10.8–11.0, 11.0–11.2, 11.2–11.4, and 11.4–11.8. Upper panel: All the galaxies. Middle panel: Disk dominated galaxies. Lower panel: spheroidal dominated galaxies ($C \geq 2.8$). Here, we are showing only the profiles in the mass bins with at least two galaxies. Numbers in the middle and lower panel indicate the number of galaxies in each bin. In the upper panel the number of galaxies in each mass bin is 15, except in the highest mass bin that has 17 galaxies. The error bars in all panels indicate the typical dispersion at any given distance in the mass bin log M ($M_\odot$) = 11.2–11.4; it is similar for other mass bins and radial distances.

mass ones, not only in their core but all along their extent. There is also a clear trend of the age profile with the mass. More massive galaxies are older along most of their radial extent. There is some overlapping in the ages at radii between 1 and 2 HLR in galaxies of few $10^{11} M_\odot$ (red and orange). The mean age shows radial structure, with a generally steeper gradient in the inner

HLR. This depends on M_*, with the largest inner gradient occurring in galaxies of intermediate mass (light blue to red curves). The most massive galaxies of the sample studied here (brown) show also negative age gradient but flatter than that of galaxies that belong to the intermediate mass bins, even though they have

the largest $\log \mu_*$ gradient. Thus, the age gradient does not seem to be correlated with the central stellar mass surface density.

In order to check whether M_* is the only galaxy property that determines the radial structures of age and μ_*, or whether these depend on structural properties like the morphological type, we divide the sample in two subclasses according with the galaxy concentration index.

First, we divide the sample in spheroidal ($C \geq 2.8$) and disk ($C < 2.8$) dominated galaxies, and then co-add the radial profiles of galaxies in the same M_* bin. The central and bottom rows of Fig. 13 show the results. Note that now the number of galaxies in each mass bin is smaller and uneven (there is not the same number of galaxies in each mass bin), and that the highest M_* bin (brown) is not populated by disk galaxies. Conversely, there are no spheroidals in the low mass bins (see also Fig. 5a)[4]. The $\log \mu_*$ and $\langle \log age \rangle_L$ radial structure of disk galaxies (central panels in Fig. 13) is similar to that for the whole sample for galaxies with mass below $10^{11} M_\odot$. There is a steep age gradient in the inner part of disk galaxies more massive than few $10^{10} M_\odot$ (cyan to red), and $\log \mu_*$ scales with the galaxy mass. The difference in the $\log \mu_*$ radial structure of galaxies with $M \geq 10^{11} M_\odot$ (orange and red) is very small in comparison with the difference in the $\langle \log age \rangle_L$ radial structure between these same two mass bins. Thus, for similar μ_*, the more massive disk galaxies have older disks and bulges. Note also that the difference in bulge ages is larger than the difference between disk ages for these two high mass bins. This is also clearly shown in Fig.12, where the largest mass bins show age gradients larger for the late than for the early type galaxies.

Spheroidal galaxies (bottom panels in Fig. 13) show $\langle \log age \rangle_L$ and $\log \mu_*$ profiles that clearly differ from disk galaxies. Because low mass bins are not well populated, we concentrate first in comparing the three highest mass bins. The most remarkable result is that, as seen in the bottom right panel, the SFH of spheroidal galaxies changes with stellar mass, while $\log \mu_*$ shows little variation[5]. Also, for the same galaxy mass, the extended envelopes of early type galaxies are denser than in disk galaxies, and formed earlier than the disks, although the bulge of the most massive disk galaxies can be as old as the core of spheroids. In fact, it is not only that the average μ_* of early type galaxies is almost constant, but also that the inner gradient of $\log \mu_*$ is independent of the stellar mass (see also Fig. 12).

In summary, we see that we see that stellar mass surface density and total stellar mass play a significant role in determining the ages, and their radial variations, but for most of the early type galaxies, the age at the core, as well as the galaxy averaged age, change with the total stellar mass, even though they have similar stellar mass surface density, and similar μ_* gradient in the inner HLR. These empirical results imply that, for early type galaxies, total mass is a more important property than mass surface density to shape the age radial profiles, which in principle reflect the spatial variation of the star formation history of galaxies.

8.4. The role of stellar mass in the inner regions of galaxies

Throughout this section we showed a series of relations between stellar age and mass density, local or galaxy-wide averaged, and their mass stacked radial dependencies, as illustrated in Figs.

---

[4] Note that the CALIFA mother sample does not include dwarf ellipticals, so this analysis lacks low mass spheroids.

[5] Note that the coincidence of the radial profiles for early type galaxies is a consequence of combining the radial profiles scaled in HLR units.
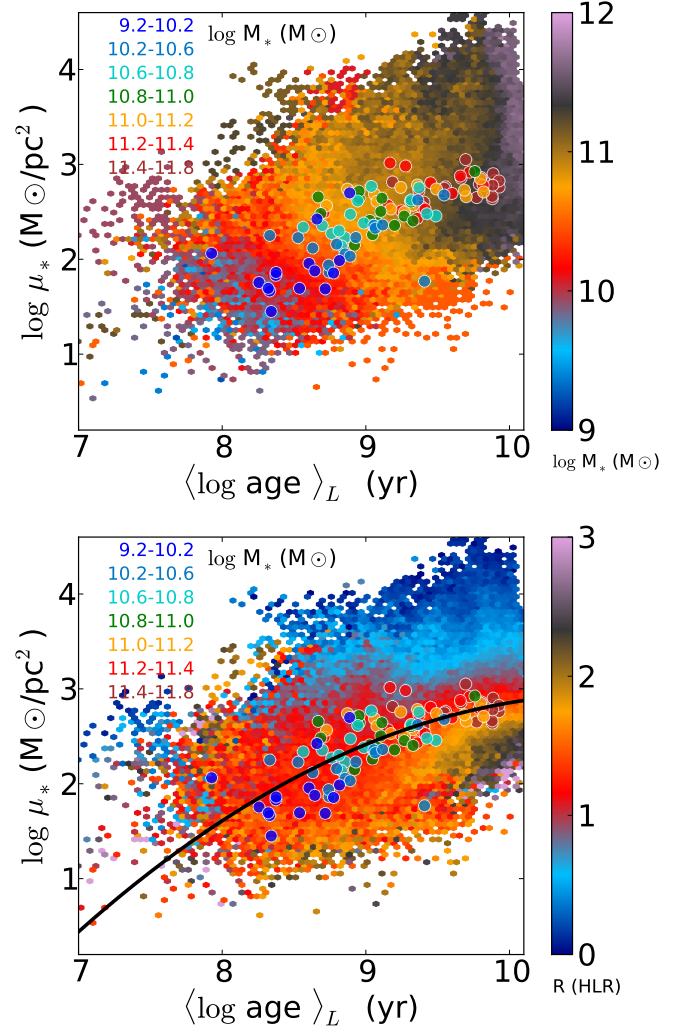
Fig. 14. Stellar mass surface density – age relationship for all the 98291 individual zones in the 107 galaxies. Small points are color coded by the stellar mass of the galaxy to which they belong (upper panel) and by the distance of each zone to the nucleus of the galaxy in units of HLR (bottom panel). The (color coded by galaxy mass) circles represent the global μ_*^{galaxy} and $\langle \log age \rangle_L^{galaxy}$ relation. The line in the bottom panel shows the result of a second order polynomial fit.

11–13. These results show that in early type galaxies $\langle \log age \rangle_L$ scales with M_* but *not* with μ_*, while in disk dominated systems $\langle \log age \rangle_L$ scales with μ_* as well as with M_*. Furthermore, we found that μ_* and $\langle \log age \rangle_L$ for many of the individual regions in the galaxies follow the same relation found for the galaxy averaged age and mass density (Fig. 11). These findings indicate that μ_* is correlated with the stellar ages, and thus linked to the SFH. Yet, the apparent disconnection between μ_* and age at high masses, coupled to the $\langle \log age \rangle_L$-$M_*$ relation (implicit in the right panels of Fig. 13) suggests that M_* is more related to the SFH than μ_*.

If μ_* is the main parameter defining the mean stellar population age, one would expect that the relation between them holds for any region of any galaxy. However, Fig. 11 shows that there is a large dispersion around the global $\log \mu_*^{galaxy}$-$\langle \log age \rangle_L^{galaxy}$ relation, a dispersion that reflects the spatial variations of μ_* and $\langle \log age \rangle_L$ withing galaxies. In fact, the scatter is larger for ages

older than 2–3 Gyr, which is where the global relation between $\log \mu_*^{galaxy}$ and $\langle \log age \rangle_L^{galaxy}$ starts to flatten. Fig. 14 sheds light on the nature of this dispersion. The figure is analogous to Fig. 11, except that now the color of the small dots indicates M_* (upper panel) or the distance to the nucleus (lower panel). As in Fig. 11, the large circles plot the global $\log \mu_*^{galaxy}$ – $\langle \log age \rangle_L^{galaxy}$ relation, and their colors code for M_*. These plots show that regions that are older than a few Gyr belong to massive galaxies ($M_* \geq 7 \times 10^{10} M_\odot$) and/or they are located in the inner 1 HLR of the galaxies. These inner regions are denser than those at 1 HLR (which approximately represent the galaxy wide average) and outer ones, even though they all formed in a similar epoch (bottom panel of Fig. 14).

To quantify how much the inner regions are overdense with respect to the galaxy-averaged μ_* we have fitted a second order polynomial to the $\log \mu_*^{galaxy}$ – $\langle \log age \rangle_L^{galaxy}$ relation[6], shown as a black line in the bottom panel of Fig. 14. If μ_* is the main property that determines the local SFH, this fit predicts the expected stellar mass density given the age. Deviations from the relation trace deviations from this assumption, so it is interesting to correlate the residuals with other properties, M_* being the obvious contender.

This is done in Fig. 15, where we plot the difference with respect to the fit ($\Delta \log \mu_*$) as a function of M_*. The plot contains two sets of 107 points each. The grey points and their error bars represent the mean and ± 1 sigma values of $\Delta \log \mu_*$ for all zones located at $R \geq 1.5$ HLR in each of the 107 galaxies in our sample. These points are scattered around $\Delta \log \mu_* = 0$, with a small shift towards a negative residual. This residual would be even smaller if we used only points around 1 HLR (which, as shown in Fig. 6, match the galaxy-averaged properties very well). More importantly, the residuals show little, if any, correlation with M_*. Black points, however, do correlate strongly with M_*. These are obtained considering only regions inside $R = 0.5$ HLR, where (as seen in the bottom panel of Fig. 14) μ_* values are generally well above the critical μ_* of $\sim 7 \times 10^2 M_\odot / pc^2$. The inner regions show an excess μ_* which grows for increasing M_*, particularly so for galaxies more massive than $10^{10} M_\odot$. In the inner regions of the most massive systems the $\log \mu_*^{galaxy}$ – $\langle \log age \rangle_L^{galaxy}$ relation fails by about an order of magnitude, confirming our earlier conclusion that μ_* is basically unrelated to the stellar population age in these cases.

To sum up, we find that *the ages and their spatial variation in the inner parts (< 1 HLR) of galaxies more massive than $10^{10} M_\odot$ are primarily related to the total stellar mass, and to the mass surface density in the outer parts (> 1 HLR)*.

9. Summary

We have analyzed the stellar population properties of the first 107 galaxies observed by CALIFA with the V500 and V1200 gratings to investigate the trends in the star formation history with radial distance as a function of the galaxy stellar mass and morphology, as traced by the concentration index. This CALIFA sub-sample is well distributed in the CMD ($-23 \leq M_r \leq -18$) covering from the blue cloud to the red sequence. In terms of concentration index, our sample contains a fair representation of early type (spheroidal) dominated galaxies and late type (disk) dominated galaxies. A full spectral fitting analysis was performed comparing combinations of SSP spectra with those of our sample galaxies using the STARLIGHT code. The fitting results

---

[6] $\log \mu_*^{galaxy}$ = -0.18×($\langle \log age \rangle_L^{galaxy}$)^2 + 3.9×$\langle \log age \rangle_L^{galaxy}$ −17.94
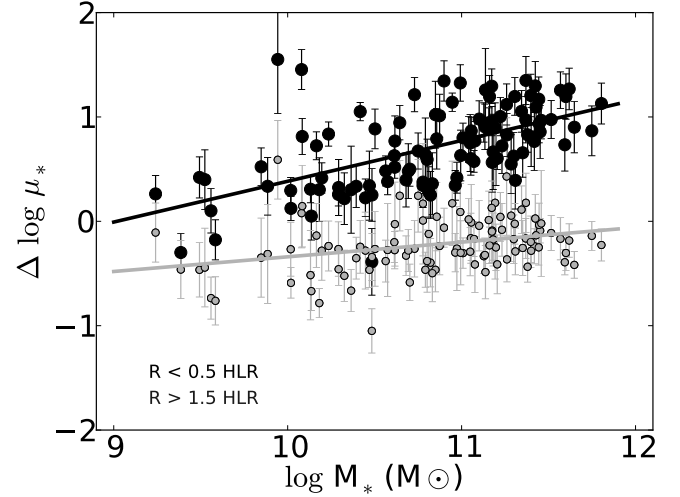
Fig. 15. The stellar mass surface density excess ($\Delta \log \mu_*$, see text) as a function of the galaxy stellar mass. Gray points and "error" bars are galaxy-by-galaxy averages and dispersions obtained for points located outside $R = 1.5$ HLR, while black points are for inner regions ($R < 0.5$ HLR).

are processed with our pipeline PYCASSO allowing us to resolve the galaxies in time and space. Here, the time information is collapsed to produce 2D maps of the stellar mass surface density and light weighted ages, azimuthally averaged to produce radial profiles. Throughout we adopt a Salpeter IMF, resulting in stellar masses a factor 1.78 (0.25 dex) larger than in case of a Chabrier IMF.

Our main conclusions are:

1. *Total stellar mass:* The sample is distributed between 10^9 – $10^{12} M_\odot$ with a peak $\sim 10^{11} M_\odot$ similar to MW and M31. Masses obtained from the integrated spectra match well those obtained from the spatially resolved SFH. This makes integrated masses a robust result. SDSS photometric masses are also well correlated with spectroscopic masses, but the former can be underestimated if the photo-SED fit does not account for stellar extinction.

2. *Spatially averaged vs. integrated galaxy properties:* The luminosity weighted age, $\langle \log age \rangle_L$, and the stellar surface mass density, μ_*, averaged over the whole galaxy, as well as from integrated spectra, correlate well with the age and local surface density measured at 1 HLR. These results show that the properties of a galaxy at 1 HLR are representative of the integrated and of the averaged galaxy properties.

3. *Mass weighted size:* Half Mass Radii are on average 20% smaller than the Half Light Radii, with spatial variations in the extinction accounting only for 1/4 of this difference. Thus, galaxies are intrinsically more compact in mass than in light. This average size difference shows a dual dependence with stellar mass, in the sense that in disk dominated galaxies the ratio of the half mass to half light radii decreases with stellar mass, but in spheroidal systems, the ratio is independent of total stellar mass. Differences between HLR and HMR arise because of radial variations in the SFHs, reflected in M/L gradients. In spheroidal systems and low mass spirals, were the spatial variation of the SFH are small, the ratio is smaller than in massive spirals. These massive spirals, that are mainly disk-like systems with large central bulges, can be up to a factor 2 more compact in mass than in luminosity.

4. *Stellar mass surface density:* The local stellar mass surface density scales with the total mass in disk dominated galaxies; the more massive galaxies are more compact than galaxies of lower mass, and this result is preserved radially at any given distance. Spheroidal systems saturate at a critical stellar mass surface density of $\sim 7 \times 10^2 M_{\odot}/pc^2$ (measured at 1 HLR) which is almost independent of the galaxy stellar mass.

5. *Luminosity weighted age:* The radial run of $\langle \log age \rangle_L$ shows inner regions older than outer ones, changing with the galaxy stellar mass and with concentration index. There is no *correlation* between the gradient and the total stellar mass, but there is a clear trend with galaxy mass when they are separated in early and late type systems. Low mass disk galaxies (usually the galaxies with lowest galaxy mass) and high mass spheroidals (usually galaxies in the highest mass bins) have relatively flat age profiles. The larger inner gradients are detected in massive disk galaxies. The presence of a massive bulge in spirals imprints a large spatial variation of the age in the inner HLR. This suggests that the SFH of building a massive bulge is quite different to the process in low mass disk dominated galaxies.

6. *Stellar local mass surface age–density relation:* The SFH of the regions located beyond 0.5-1 HLR are well correlated with their local μ_*. They follow the same relation as the galaxy averaged age and μ_*. This suggests that it is the local stellar mass surface density that preserves the SFH in disks. However, the radial structure of the age in spheroidal galaxies change significantly with galaxy mass even if all these galaxies show a similar radial structure in μ_*. This implies that the SFH of spheroids is more fundamentally related to the stellar mass. Thus, *galaxy mass is a more fundamental property in spheroidal systems while the local stellar mass surface density is more important in disks.*

References

Abazajian, K. N., Adelman-McCarthy, J. K., Agüeros, M. A., et al. 2009, ApJS, 182, 543

Asari, N. V., Cid Fernandes, R., Stasińska, G., et al. 2007, MNRAS, 381, 263

Baldry, I. K., Balogh, M. L., Bower, R., Glazebrook, K., & Nichol, R. C. 2004, AIPC, 743, 106

Balogh, M. L., Christlein, D., Zabludoff, A. I., & Zaritsky, D. 2001, ApJ, 557, 117

Bacon, R., Copin, Y., Monnet, G., et al. 2001, MNRAS, 326, 23

Bakos, J., Trujillo, I., & Pohlen, M. 2008, ApJL, 683, 103

Bell, E. F., & de Jong, R. S. 2000, MNRAS, 312, 497

Bell, E. F., & Bowen, R. G. 2000, MNRAS, 319, 235

Bell, E. F., Wolf, C., Meisenheimer, K., et al. 2004, ApJ, 608, 752

Bica, E. 1988, A&A, 195, 76

Blanc, G. A., Weinzirl, T., Song, M., et al. 2013, AJ, 145, 138

Blanton, M. R., & Roweis, S. 2007, AJ, 133, 734

Blanton, M. R., & Moustakas, J. 2009, ARA&A, 47, 159

Boissier, S., & Prantzos, N. 2000, MNRAS, 312, 398

Boselli, A., Gavazzi, G., Donas, J., & Scodeggio, M. 2001, AJ, 121, 753

Brinchmann, J., & Ellis, R. S. 2000, ApJ, 536, 77

Brinchmann, J., Charlot, S., Heckman, T. M., Kauffmann, G., Tremonti, C., & White, S. D. M. 2004, astro, arXiv:astro-ph/0406220

Bruzual, G., & Charlot, S. 1993, ApJ, 405, 538

Bruzual, G., & Charlot, S. 2003, MNRAS, 344, 1000

Cappellari, M., & Copin, Y. 2003, MNRAS, 342, 345

Cappellari, M., Emsellem, E., Krajnovic, D., et al. 2011, MNRAS, 413, 813

Cardelli, J. A., Clayton, G. C., & Mathis, J. S. 1989, ApJ, 345, 245

Chabrier, G. 2003, PASP, 115, 763

Charbonnel, C., Meynet, G., Maeder, A., Schaeller, G., & Schaerer, D. 1993, A&AS, 101, 415

Charlot, S., & Bruzual, G. 2007, private communication

Chilingarian, I. V. 2009, MNRAS, 394, 1229

Cid Fernandes, R., Mateus, A., Sodré, L., Stasińska, G., & Gomes, J. M. 2005, MNRAS, 358, 363

Cid Fernandes, R. 2007, IAU Symposium, 241, 461

Cid Fernandes, R., Pérez, E., García Benito, R., et al. 2013a, A&A, arXiv1304.5788

Cid Fernandes, R., González Delgado, R. M., Pérez, E., et al. 2013b, A&A, submitted

Conroy, C. 2013, ARAA, arXiv:1301.7095

de Jong, R. S. 1996, A&A, 313, 377

de Zeeuw, P. T., Bureau, M., Emsellem, E., et al. 2002, MNRAS, 329, 513

Dickinson, M., Papovich, C., Ferguson, H. C., & Budavári, T. 2003, ApJ, 587, 25

Ellis, S. C., Driver, S. P., Allen, P. D., Liske, J., & Bland-Hawthorn, J. 2005, MNRAS, 363, 1257

Falcón-Barroso, J., Sánchez-Blázquez, P., Vazdekis, A., et al. 2011a, A&A, 532, 95

Falcón-Barroso, J., van den Ven, G., Peletier, R. F., et al. 2011b, MNRAS, 417, 1787

Fontana, A., Salimbeni, S., Grazian, A., et al. 2006, A&A, 459, 745

Gallazzi, A., Charlot, S., Brinchmann, J., White, S. D. M., & Tremonti C. A. 2005, MNRAS, 362, 41

Gallazzi, A., Charlot, S., Brinchmann, J., & White, S. D. M. 2006, MNRAS, 370, 1106

Ganda, K., Peletier, R. F., & McDermid, R. M. 2007, MNRAS, 380, 506

Girardi, L., Bressan, A., Bertelli, G., & Chiosi, C. 2000, A&AS, 141, 371

González Delgado, R. M., Cerviño, M., Martins, L. P., Leitherer, C., & Hauschildt, P. H. 2005, MNRAS, 357, 945

Greene, J. E., Murphy, J. D., Comerford, J. M., Gebhardt, K., & Adams, J. J. 2012, ApJ, 750, 32

Heavens, A., Panter, B., Jimenez, R., & Dunlop, J. 2004, Nature, 428, 625

Husemann, B., Jahnke, K., Sánchez, S. F., et al. 2013, A&A, 549, A87

Iglesias-Páramo, J., Vílchez, J. M., Galbany, L., et al. 2011, A&A, 553, L7

Kauffmann, G., Heckman, T. M., White, S. D. M., et al. 2003, MNRAS, 341, 33

Kauffmann, G., Heckman, T. M., White, S. D. M., et al. 2003, MNRAS, 341, 54

Kauffmann, G., Heckman, T. M., De Lucia, G., Brinchmann, J., Charlot, S., Tremonti, C., White, S. D. M., & Brinkmann, J. 2006, MNRAS, 367, 1394

Kelz, A., Verheijen, M. A. W., Roth, M. M., et al. 2006, PASP, 118, 129

Koleva, M., Prugniel, P., & De Rijcke, S., et al. 2009, Astron. Nachr. 330, 960

Kuntschner, H., Emsellem, E., Bacon, R., et al. 2006, MNRAS, 369, 497

Kuntschner, H., Emsellem, E., Bacon, R., et al. 2010, MNRAS, 408, 97

La Barbera, F., Merluzzi, P., Busarello, G., Massarotti, M., & Mercurio, A. 2004, A&A, 425, 797

La Barbera, F., de Carvalho, R. R., de la Rosa, I. G., Lopes, P. A. A., Kohl-Moreira, J. L., & Capelato, H. V. 2010, MNRAS, 408, 1313

La Barbera, F., ferreras, I., de Carvalho, R. R., Bruzual, G., Charlot, S., Pasquali, A., & Merlin, E. 2012, MNRAS, 426, 2300

Le Borgne, J. F., Bruzual, G., Pelló, R., et al. 2003, A&A, 402, 433

Leitherer, C., Schaerer, D., Goldader, J.D., et al., 1999, ApJS, 123, 3

MacArthur, L. A., Courteau, S., Bell, E., & Holtzman, J. A. 2004, ApJS, 152, 175

MacArthur, L. A., González, J. J., & Courteau, S. 2009, MNRAS, 395, 28

Martins, L. P., González Delgado, R. M., Leitherer, C., Cerviño, M., & Hauschildt, P. 2005, MNRAS, 358, 49

Mateus, A., Sodré, L., Cid Fernandes, R., Stasińska, G., Schoenell, W., & Gomes, J. M. 2006, MNRAS, 370, 721

Mateus, A., Sodré, L., Cid Fernandes, R., & Stasińska, G. 2007, MNRAS, 374, 1457

McDermid, R. M., Emsellem, E., Shapiro, K. L., et al. 2006, MNRAS, 373, 906

Menanteau, F., Ford, H. C., Illingworth, G. D., et al. 2004, ApJ, 612, 202

Mehlert, D., Thomas, D., Saglia, R. P., Bender, R., & Wegner, G. 2003, A&A, 407, 423

Moorthy, B. K., & Holtzman, J. A. 2006, MNRAS, 371, 538

Muñoz-Mateos, J. C., Gil de Paz, A., Boissier, S., Zamorano, J., Jarrett, T., Gallego, J., & Madore, B. F. 2007, ApJ, 658, 1006

Ocvirk, P., Pichon, C., Lançon, A., & Thiébaut, E. 2006, MNRAS, 365, 46

Panter, B., Heavens, A. F., & Jimenez, R. 2003, MNRAS, 343, 1145

Panter, B., Jimenez, R., Heavens, A. F., & Charlot, S. 2007, MNRAS, 378, 1550

Peletier, R., Davies, R. L., & Illingworth, G. 1990, dig..book, 267

Peletier, R. F., & Balcells, M. 1996, AJ, 111, 2238

Peletier, R. F., Prada, F., Arribas, S., Mediavilla, E., Del Burgo, C., Guttiérez, C., Garcia-Lorenzo, B., & Vazdekis, A. 1997, IEEES, 15, 16

Peletier, R. F., & de Grijs, R. 1998, MNRAS, 300, L3

Peng, Y., Lilliy, S. J., Kovac, K., et al. 2010, ApJ, 721, 193

Pérez, E., Cid Fernandes, R., González Delgado, R. M., et al. 2013, ApJ, 764, 1L

Pérez-González, P. G., Rieke, G. H., Villar, V., et al. 2008, ApJ, 675, 234

Proctor, R. N., & Sansom A. E. 2002, MNRAS, 333, 517

Proctor, R. N., Forbes, D. A., & Beasley, M. A. 2004, MNRAS, 355, 1327

Rawler, T. D., Smith, R. J., & Lucey, J. R. 2010, MNRAS, 401, 852

Roche, N., Bernardi, M., & Hyde, J. 2010, MNRAS, 407, 1231

Rosales-Ortega, F. F., Sánchez, S. F., Iglesias-Páramo, J., Díaz, A. I., Vílchez, J. M., Bland-Hawthorn, J., Husemann, B., & Mast, D. 2012, ApJL, 756, 31

Roth, M. M., Kelz, A., Fechner, T., et al. 2005, PASP, 117, 62

Salpeter, E. E. 1955, ApJ, 121, 161

Sánchez, S. F., Kennicutt, R. C., Gil de Paz, A., et al. 2012, A&A, 538, 8

Sánchez, S. F., Rosales-Ortega, F. F., Jungwiert, B., et al. 2013, A&A, arXiv1304.2158S

Sánchez-Blázquez, P., Peletier, R. F., Jiménez-Vicente, J., et al. 2006, MNRAS, 371, 703

Sánchez-Blázquez, P., Forbes, D. A., Strader, J., Brodie, J., & Proctor, R. 2007, MNRAS, 377, 759

Sánchez-Blázquez, P., Ocvirk, P., Gibson, B. K., Pérez, I., & Peletier, R. F. 2011, MNRAS, 415, 709

Schaerer, D., Charbonnel, C., Meynet, G., Maeder, A., & Schaller, G. 1993a, A&A, 102, 339

Schaerer, D., Meynet, G., Maeder, A., & Schaller, G. 1993b, A&AS, 98, 523

Schaller, G., Schaerer, D., Meynet, G., & Maeder, A. 1992, A&AS, 96, 269

Sil'chenko, O. K., Proshina, I. S., Shulga, A. P., & Koposov, S. E. 2012, MNRAS, 427, 790

Silva, D. R., & Bothun, G. D. 1998, AJ, 116, 2793

Stoughton, C., Lupton, R. H., Bernardi, M., et al. 2002, AJ, 123, 485

Strateva, I., Ivvezic, Z., Knapp, G. R., et al. 2001, AJ, 122, 1861

Szomoru, D., Franx, M., & van Dokkum, P. G. 2012, ApJ, 749, 121

Tinsley, B., 1980, FCPh, 5, 287

Tojeiro, R., Heavens, A. F., Jimenez, R., & Panter, B. 2007, MNRAS, 381, 1252

Tojeiro, R., Wilkins, S., Heavens, A. F., Panter, B., & Jimenez, R. 2009, ApJS, 185, 1

Tortora, C., Napolitano, N. R., Cardone, V. F., Capaccioli, M., Jetzer, Ph., & Molinaro, R. 2010, MNRAS, 407, 144

Trager, S. C., Faber, S. M., Worthey, G., & González, J. J. 2000, AJ, 119, 1645

Tremonti, C. A., Heckman, T. M., Kauffmann, G., et al. 2004, ApJ, 613, 898

Vale Asari, N., Stasińska, G., Cid Fernandes, R., Gomes, J. M., Schlickmann, M., Mateus, A., & Schoenell, W. 2009, MNRAS, 396, L71

van Dokkum, P. G., Whitaker, K. E., Brammer, G., et al. 2010, ApJ, 709, 1018

Vazdekis, A., Sánchez-Blázquez, P., Falcón-Barroso, J., et al. 2010, MNRAS, 404, 1639

Verheijen, M. A. W., Bershady, M. A., Andersen, D. R., et al. 2004, Astron. Nachr., 325, 151

Walcher, J., Groves, B., Budavári, T., & Dale, D. 2011, Ap&SS, 331, 1

Walcher, J., et al., in prep.

Wu, H., Shao, Z., Mo, H. J., Xia, X., & Deng, Z. 2005, ApJ, 622, 244

Wuyts, S., Forster Schreiber, N. M., Genzel, R., et al. 2012, ApJ, 753, 114

Yoachim, P., Roskar, R., & Debattista, V. P. 2012, ApJ, 752, 97

Zibetti, S., Charlot, S., & Rix, H. W. 2009, MNRAS, 400, 1181

Appendix A: Structural parameters: Half light radius

In order to compare the spatial distribution of any given property in galaxies which are at different distances, the 2D maps need to be expressed in a common metric. We chose the half light radius (HLR). To compute the HLR, we collapse the spectral cubes in the (rest-frame) window 5635 ± 45Å, derive the isophotal ellipticity and position angle, and then integrate a curve of growth from which we derive the HLR. In some galaxies, the integrated image may contain masked regions at the position where the original cube contains foreground stars or some other artifacts (see Cid Fernandes et al. 2013a for further explanations) which may affect the estimation of the different parameters, including the HLR. In order to correct for these missing data, we build an average surface brightness radial profile for each galaxy using circular apertures. This profile is used to estimate the surface brightness of the spaxels masked in the original cube, assuming a smooth change of surface brightness between the missing data and the averaged values of their near neighbours at the same distance. This re-constructed flux image is used to derive the ellipticity and position angle of the aperture, and to obtain the average azimuthal radial profiles of the stellar population properties. These structural parameters are defined and obtained as follows:

- *Galaxy center:* We take as the galaxy center the peak flux position. This definition results to be correct for most of the galaxies, except for the irregular galaxy CALIFA 475 (NGC 3991), where the maximum flux is well outside of the morphological center.

- *Ellipticity and position angle:* The flux-weighted moments of the 5635 Å image are used define the ellipticity and position angle (Stoughton et al. 2002). The re-constructed flux image is used to calculate the so called Stokes parameters in order to obtain the ellipticity and position angle at each radial distance. The values, however, are kept constant beyond 2 HLR, which are taken to define a unique elliptical aperture for each galaxy. The final values do not change significantly after an iteration, filling the missing data with the surface brightness profile resulting from adding the flux with the derived elliptical aperture, and then estimating again the Stokes parameters.

- *Half light radius (HLR):* For each galaxy, the re-constructed flux image is used to build the flux curve of growth and to obtain the half light radius. The flux is integrated in elliptical apertures with a position angle and ellipticity defined as explained above. The semimajor axis length at which the curve of growth reaches 50% of its maximum value is defined as the half light radius, a_{50}^L.

For the sample analyzed here, $1 \leq a_{50}^L \leq 8$ kpc, with a mean value of 4.6 kpc. These values are higher than the Petrosian radius r_{50}^P (obtained from the SDSS data archive), as shown in Fig. A.1. However the circularized size, defined as $a_{50}^L \times \epsilon^{1/2}$, where ϵ is the ellipticity, follows well the one-to-one line, as does the HLR obtained through curve of growth integrating in circular rings, R_{50}^L. The linear fit, in fact, deviates from the one-to-one line, giving circular HLR that are on average 5% lower than r_{50}^P. The outlier in the correlation is CALIFA 886 (NGC 7311), the central galaxy of a compact group. Given the morphology of the system, r_{50}^P is probably overestimated.

Table 1 lists a_{50}^L values obtained for our sample. In this paper we will use "HLR" to refer generally to this metric, indepen-
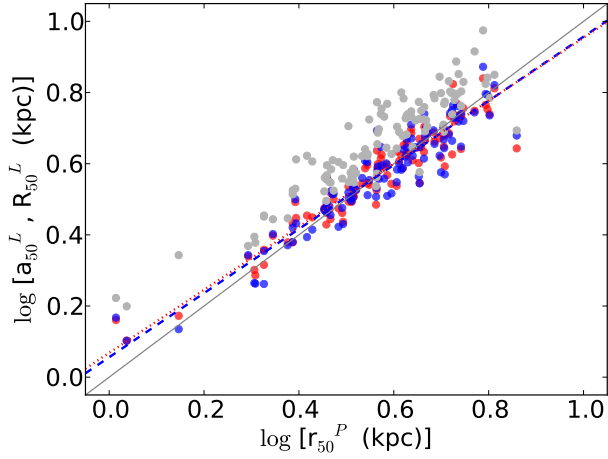
Fig. A.1. The Petrosian radius r_{50}^P versus a_{50}^L (gray) the semima-jor axis length of the ellipse that contains half of flux estimated from the CALIFA data cube through the curve of growth at 5635 Å; the radius ($a_{50}^L \times \epsilon^{1/2}$) of the circle with equivalent flux to the ellipse (blue points); the half light radius, R_{50}^L (red points). The black line is the one-to-one line, while the dotted blue line is the fit to ($a_{50}^L \times \epsilon^{1/2}$) and r_{50}^P, and dashed red line the fit to R_{50}^L.

Fig. B.2. The galaxy stellar mass distributions obtained from the spatially resolved star formation history. The histograms show the results obtained with the bases GM, CB and BC, from the left to right upper panels. Lower panels shows the comparison of the galaxy stellar mass obtained with *GM* (vertical axis) and *CB* or *BC* (horizontal axis) for the 107 CALIFA galaxies. A one-to-one line is drawn in all the panels, and the best fit (dashed lines). The histogram inserted in each panel shows the differences in the log M_* obtained with the base *CB* or *BC* with respect to *GM*. On the top-left corner of the panel, Δ's are defined as *CB - GM* or *BC - GM*, and their dispersion are labeled.

dently of whether it is computed in circular or elliptical geome-try, unless the specific results depend on the actual definition (as in Section 7).
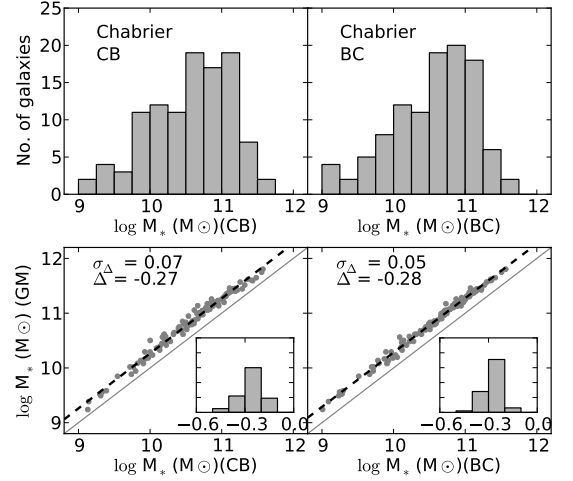
Appendix B: Quality of the spectral fits and uncertainties associated to evolutionary synthesis models

B.1. Quality of the spectral fits

All stellar population information used throughout this work comes from the STARLIGHT fits of the 98291 individual spectra from 107 CALIFA data cubes. Here we illustrate these spectral fits with example spectra extracted from the nucleus and from a spaxel at 1 HLR for three different galaxies.

The top panels in Fig. B.1 show the nuclear spectra (black) of CALIFA 001 (IC 5376), CALIFA 073 (NGC 776) and CALIFA 014 (UGC 00312). The respective STARLIGHT fits are shown by the red line. Each panel shows also the $O_\lambda - M_\lambda$ residual spectrum. Examples of fits for regions 1 HLR away from the nucleus are shown in the bottom panels.

As customary in full spectral fitting work, the fits look very good. In these particular examples the figure of merit $\overline{\Delta}$, defined as the mean value of $|O_\lambda - M_\lambda|/M_\lambda$ (eq. 6 in Cid Fernandes et al. 2013a), is $\overline{\Delta} = 1.3\%$ (5.8%) for the nucleus (at 1 HLR) of IC5376, 1.3% (5.8%) for NGC776 and 1.6% (5.0%) for UGC00312. The median values for the 107 galaxies are $\overline{\Delta} = 1.6\%$ at the nucleus and 5.1% at $R = 1$ HLR. The SSP models used in these examples are from the *GM* base, built from evolu-tionary synthesis models by González Delgado et al. (2005) and Vazdekis et al. (2010), as summarized in Section 3. Very similar results are obtained with bases *CB* and *BC*.

B.2. Uncertainties associated to using different SSP models

To evaluate to which extent the results of our spectral synthe-sis analysis depend on the choice of SSP models, we now com-pare properties derived with bases *GM*, *CB* and *BC*. Since Cid Fernandes et al. (2013b) has already performed such a compar-ison for the same data analysed here, we focus on comparisons related to specific points addressed in this paper.

First, we compare the results obtained for M_*. Fig. B.2 shows the galaxy stellar mass distribution obtained with the *CB* and *BC* bases. The *GM* mass distribution (see Fig. 5a) is shifted to higher masses than *CB* and *BC* by ∼ 0.27 dex, as expected be-cause of the different IMFs (Salpeter in *GM* and Chabrier in *CB* and *BC*). The Salpeter IMF used in *GM* models has more low mass stars than the Chabrier function used in *CB* and *BC*, im-plying larger initial masses for the same luminosity. In addition, for the Salpeter IMF about 30% of this mass is returned to the ISM through stellar winds and SNe, while for a Chabrier IMF this fraction is 45%. These effects end up producing differences of a factor of ∼ 1.8 in the total mass currently in stars.

In the context of this paper, it is useful to compare the results for μ_* and $\langle \log age \rangle_L$ at the nucleus and at 1 HLR, as these allow us to estimate the uncertainties associated to the stellar mass sur-face density and age gradient due to the choice of SSP models. This is done in the top two rows of Fig. B.3, where values ob-tained with bases *GM* are plotted in the vertical axis, while *CB* and *BC*-based estimates are in horizontal. In all panels the labels Δ and σ_Δ denote the mean and rms of the difference of values in the y and x axis, and the histogram of these differences is shown in the inset panels.

The $\mu_*(0)$ and $\mu_*(1$ HLR) values show the same 0.27 dex IMF-induced systematic differences seen in Fig. B.2. The dis-persions in log μ_* values are ∼ 0.1 dex, much smaller than the
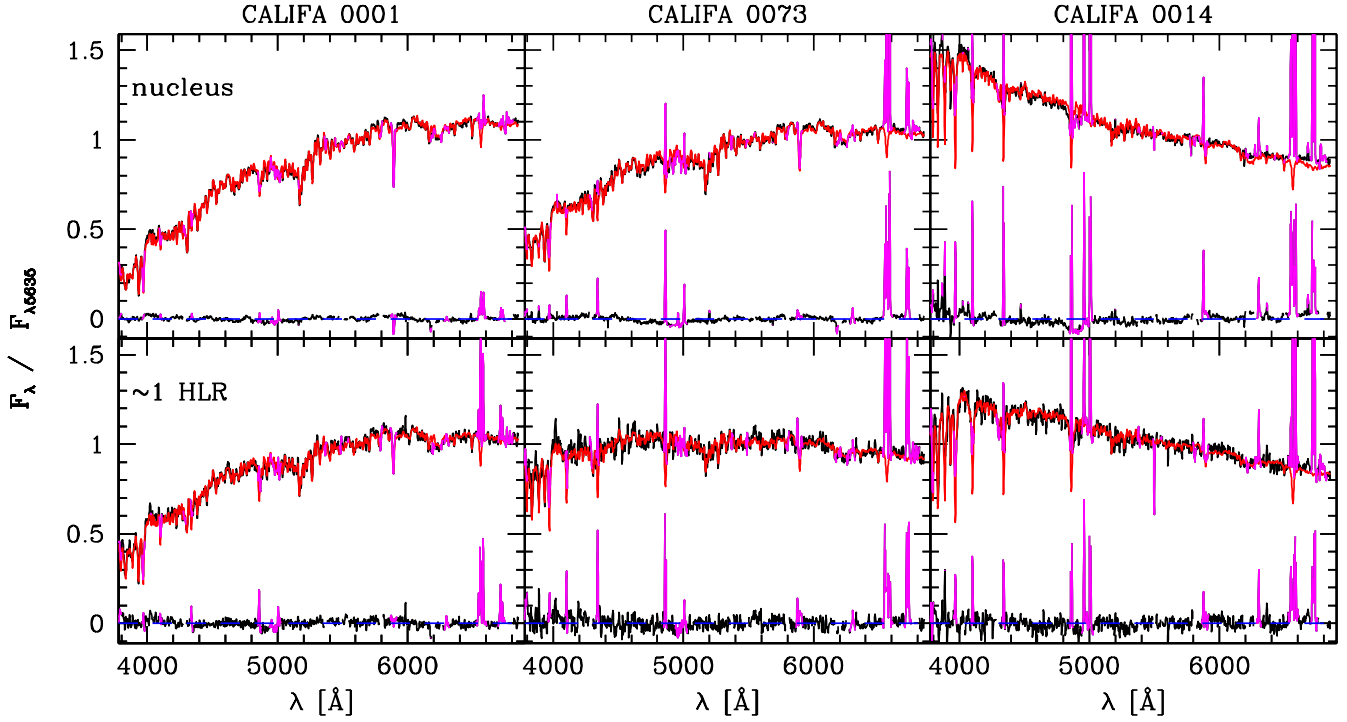
Fig. B.1. Example STARLIGHT fits for IC5376 (CALIFA 001, left), NGC776 (CALIFA 073, middle) and UGC00312 (CALIFA 014, right). The top panels show the nuclear spectrum, while the bottom ones are for spaxels located at 1 HLR from the nucleus. Observed and synthetic spectra are shown in black and red lines, respectively. Masked regions (mostly emission lines) are plotted in magenta, and bad pixels are not plotted. Emission lines peaks in the resdiual spectra were clipped for clarity.

$\triangledown \log \mu_*$ gradients seen in Fig. 12. Note also that IMF factors shift $\log \mu_*(0)$ and $\log \mu_*(1\,\text{HLR})$ by the same amount. We thus conclude that SSP model choice has no significant impact on the μ_* gradients discussed in this work.

Dispersions in the $\langle \log age \rangle_L$ values are also of the order of 0.1 dex. One sees a small bias whereby the nuclei of (mainly low mass) galaxies are older with *GM* than *CB* by 0.05 dex, whereas the difference at 1 HLR is 0.02 dex. This would make $\triangledown \langle \log age \rangle_L \sim 0.03$ larger (smaller gradient) with *CB* than with *GM*, a small effect which does not impact our conclusion that low mass galaxies show flat age radial profiles. The same small effect is found comparing *GM* and *BC* ages.

Finally, we evaluate the effect of SSP choice on the half mass and half light radii dicussed in Section 7. Note that a_{50}^M depends on the spatial variation of the SFH (through the M/L ratio), while $a_{50}^{L^{intrin}}$ further depends on the radial variation of the stellar extinction. The bottom panels of Fig. B.2 shows that the choice of SSP base has no significant impact upon the estimates of either HLR or HMR. Light based sizes derived from *GM*, *CB* and *BC* fits agree with each other to within ±0.01 dex, while HMR have dispersion of 0.05 dex or less.

Appendix C: Missing mass in the CALIFA FoV

The main constraint in the sample selection for the CALIFA survey is a size[7] isoA$_r$ < 79.2", only a 7% larger than the PPAK FoV of 74". This implies that while some galaxies are completely enclosed within the FoV, others are somewhat larger. The question arises of how much stellar mass is left out of our stellar

population synthesis analysis because it is out of the FoV. In order to estimate this "missing mass", we proceed in the following manner, depicted in figure C.1 for the case of CALIFA 003. We use a $3' \times 3'$ copy of the SDSS *r* band image to compute and subtract the background around the galaxy; the distribution of the background residual is used to compute the edge of the galaxy as that enclosed above 1σ of the background (red contour in the figure). The missing flux (light blue in the top-right panel) is that contained within this contour and outside the CALIFA image; the points corresponding to this missing flux are represented in green in the radial profile in the bottom-left panel. From our population synthesis analysis of the CALIFA data cube, we compute the M/L ratio as a function of distance from the center of the galaxy (grey points in the bottom-right panel of the figure). The mean M/L value between 1.5 and 2.5 HLR is then used together with the missing flux to compute the missing mass outside the PPaK FoV. Note that this is an approximate method, because we assume a constant value for the M/L in the outer parts of the CALIFA FoV, but the results are quite reliable, given that M/L has generally little or no gradient in these outer reaches, as can be seen in the bottom panels for the case of CALIFA 003.

The overall results for the missing mass are shown in the histogram of figure C.2, with a mean value of 8.63%, it shows a shape of the type lognormal with the peak at $\sim 5\%$.

---

[7] The semimajor axis length corresponding to the isophote 25 mag/arcsec^2 in the *r* band.
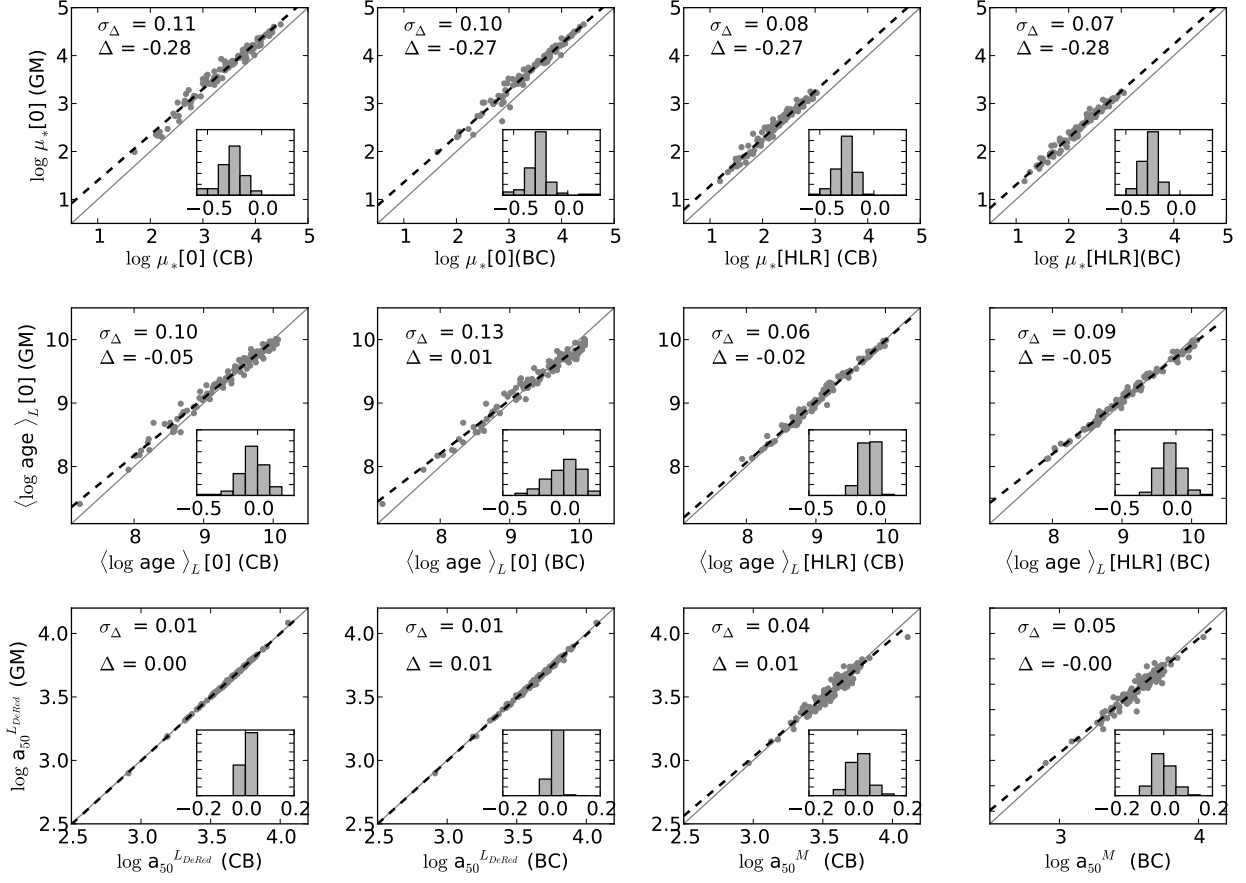
Fig. B.3. Comparison of stellar population properties obtained with bases *GM* (vertical axis) and *CB* or *BC* (horizontal axis) for the 107 CALIFA galaxies. A one-to-one line is drawn in all the panels, and the best fit (dashed lines). The histogram inserted in each panel shows the differences in the property obtained with the base *CB* or *BC* with respect to *GM*. On the top-left corner of each panel, Δ's are defined as the mean $CB - GM$ (or $BC - GM$) difference, and σ_Δ is the corresponding standard deviation.
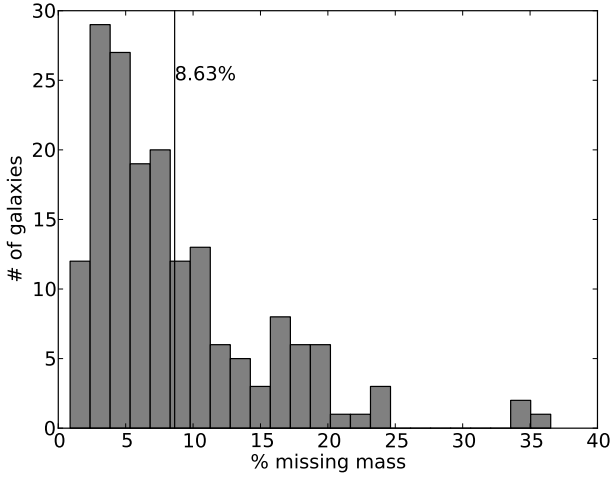
Fig. C.2. Histogram of the fraction of mass that is outside of the CALIFA FoV. The average value is marked by a vertical line.
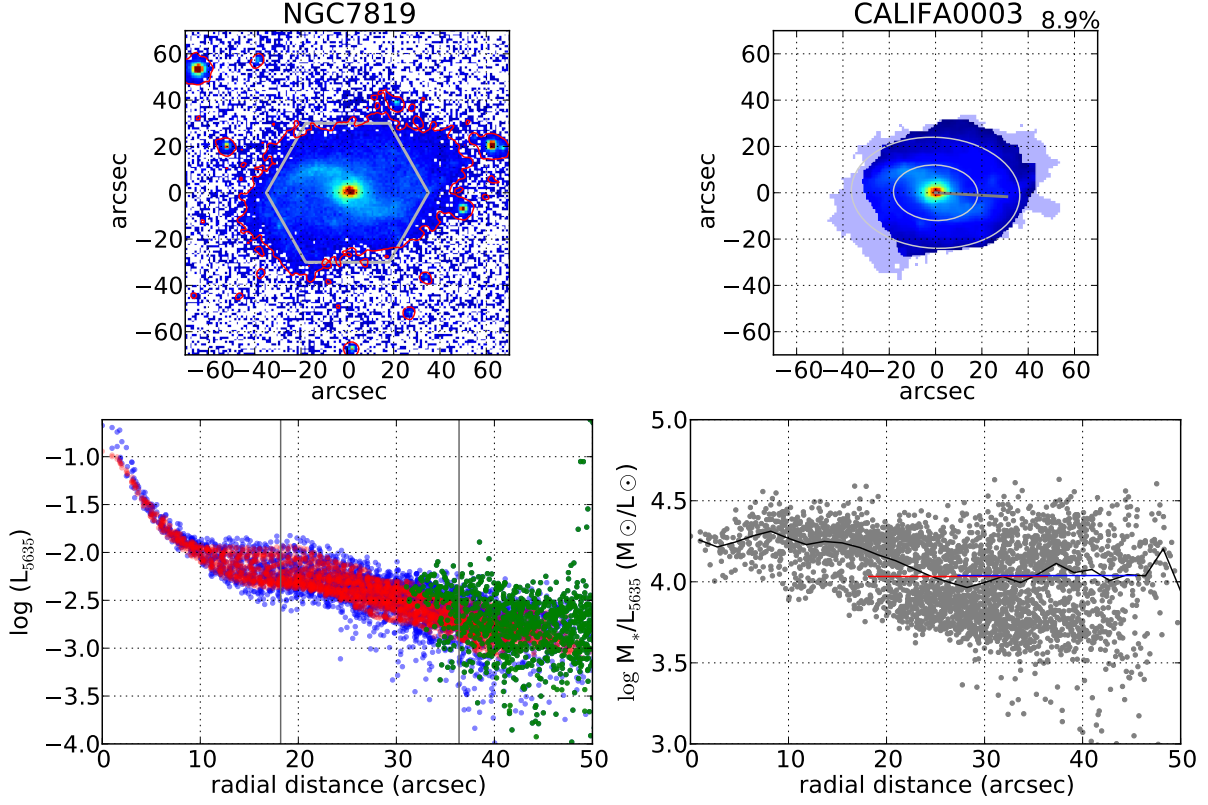
Fig. C.1. Upper-left panel: *r* band SDSS image of NGC 7819 (CALIFA 003); an hexagon indicates the PPaK FoV, and a red contour shows the 1σ background. Upper-right panel: CALIFA image at 5635Å; light blue shows the area of the galaxy outside the PPaK FoV, taken as that enclosed within the red contour in the left image minus the CALIFA image. The ellipses show the positions of 1 HLR and 2 HLR (a_{50}^L), and the gray line shows r_{90}^P. Bottom-left panel: (blue points) SDSS *r* band surface brightness profiles scaled to (red points) CALIFA surface brightness profiles at 5635Å; the green points are those red points that fall outside PPaK FoV, and are the ones used for the computation of the 'missing stellar mass'. The position of 1 HLR and 2 HLR are marked by vertical lines. Bottom-right panel: Mass-Luminosity ratio derived from our spectral fits obtained pixel to pixel (grey points) and the averaged radial profile (black line). Horizontal lines are the mass-to-luminosity ratio averaged for points that are between 1 and 2 HLR (red) and 1.5-2.5 HLR (blue).

Table 1. Stellar population properties

CALIFA ID#	Name NED	log Mass $M_\odot$	$\log \mu_*[0]$ $M_\odot/pc^2$	$\log \mu_*[HLR]$ $M_\odot/pc^2$	$\langle \log age[0] \rangle_L$ (yr)	$\langle \log age[HLR] \rangle_L$ (yr)	HLR pc	HLR^{DeRed} pc	HMR pc
001	IC5376	10.88	4.10	2.72	9.76	9.25	4039	3938	2441
003	NGC7819	10.37	3.28	1.98	8.43	9.03	5612	4902	4305
004	UGC00029	11.40	3.87	2.85	9.85	9.81	4897	4509	4141
007	UGC00036	11.23	4.18	3.05	9.50	9.42	4071	3885	3402
008	NGC0001	11.00	4.17	2.86	9.31	8.80	2778	2594	1945
010	NGC0036	11.31	3.95	2.72	9.74	9.14	6010	6103	5117
014	UGC00312	9.92	2.74	1.73	8.17	8.35	5298	4931	4937
039	NGC0444	10.04	2.74	1.85	8.94	8.60	5937	5597	4939
042	NGC0477	10.87	3.51	2.21	9.38	8.93	6242	5942	4415
043	IC1683	10.85	3.93	2.75	8.67	9.14	3636	2747	2755
045	NGC0496	10.72	2.99	2.12	8.62	8.98	6354	5458	5460
053	UGC01057	10.62	3.38	2.29	9.29	8.65	4979	4336	3135
073	NGC0776	11.19	4.14	2.50	9.29	8.98	5062	4598	3293
088	UGC01938	10.83	3.47	2.64	9.49	8.87	5687	5067	4546
100	NGC1056	10.09	4.01	3.05	8.84	8.98	955	791	954
119	NGC1167	11.47	4.32	2.93	9.81	9.77	4433	4555	4634
127	NGC1349	11.43	4.22	2.76	9.81	9.46	5126	5326	4215

Table 1. continued.

CALIFA ID#	Name NED	log Mass M$_\odot$	log μ_*[0] M$_\odot$/pc^2	log μ_*[HLR] M$_\odot$/pc^2	$\langle$log age[0]$\rangle_L$ (yr)	$\langle$log age[HLR]$\rangle_L$ (yr)	HLR pc	HLR^{DeRed} pc	HMR pc
133	UGC03107	11.02	3.71	2.59	9.39	9.05	6989	5957	4509
146	UGC03253	10.80	3.88	2.61	9.52	9.14	3656	2754	2149
147	NGC2253	10.33	3.39	2.02	9.09	8.66	3606	3280	2422
151	NGC2410	11.12	4.03	2.72	9.54	9.21	4392	4097	3085
152	UGC03944	10.14	3.03	1.96	9.08	8.77	3853	3430	2611
155	UGC03995	11.26	4.22	2.77	9.67	9.32	5479	5488	4021
156	NGC2449	11.18	4.04	2.88	9.59	9.24	4181	3941	3570
208	UGC04461	10.51	3.52	2.09	8.99	8.12	4766	3978	2430
213	NGC2623	10.74	3.67	2.44	8.69	8.75	3385	2520	2204
273	IC2487	10.63	3.41	2.31	9.44	8.99	6283	5591	4392
274	IC0540	10.18	3.53	2.82	9.31	9.43	2202	2061	1981
277	NGC2916	10.83	3.81	2.37	9.73	9.02	5398	5488	3903
306	UGC05358	9.58	2.41	1.57	8.54	8.60	4093	3772	3571
307	UGC05359	10.98	3.42	2.27	9.55	9.17	8231	7855	5692
309	UGC05396	10.59	3.06	2.20	9.10	8.79	6077	5584	5042
319	NGC3160	11.07	3.75	2.68	9.82	9.74	5303	4807	4480
326	UGC05598	10.67	3.51	2.37	8.88	8.48	5056	4912	3837
364	UGC06036	11.36	4.10	3.11	9.78	9.70	5076	5439	4771
387	NGC3615	11.63	4.44	3.10	9.93	9.81	4167	4034	3728
388	NGC3614	10.46	3.42	2.23	9.50	9.01	3652	3583	3240
475	NGC3991	9.99	2.99	1.77	7.41	8.13	3946	5140	5843
479	NGC4003	11.38	4.09	2.76	9.58	9.70	5269	4381	4141
486	UGC07012	9.86	3.02	1.98	8.75	8.26	2847	2785	2252
489	NGC4047	10.97	3.81	2.71	9.23	8.64	3534	3292	2938
500	UGC07145	11.08	3.56	2.52	9.75	9.07	7107	6578	5363
515	NGC4185	10.99	3.48	2.43	9.72	9.40	6088	6213	5657
518	NGC4210	10.49	3.69	2.32	9.95	8.92	3749	3696	2813
528	IC0776	9.40	1.99	1.38	8.62	8.29	3615	3719	3260
548	NGC4470	10.24	2.92	2.45	8.25	8.59	2795	2793	3063
577	NGC4676	11.09	3.49	2.63	9.15	9.43	6073	4707	4515
607	UGC08234	11.40	4.19	2.92	9.37	9.40	3940	3737	3685
609	UGC08250	10.22	2.63	2.19	8.56	8.79	5866	5477	5091
610	UGC08267	11.07	3.60	2.67	9.28	8.90	5862	5093	4377
657	UGC08733	9.60	2.33	1.69	8.54	8.71	3522	3410	3151
663	IC0944	11.47	4.02	2.85	9.71	9.45	6792	6294	5631
676	NGC5378	10.70	3.86	2.44	9.69	9.47	3441	3798	2932
758	NGC5682	9.51	2.35	1.95	8.18	8.36	2387	2211	2362
764	NGC5720	11.32	3.85	2.50	9.97	9.17	7079	7536	5510
769	UGC09476	10.42	3.15	2.17	9.05	8.79	4413	4236	4071
783	UGC09665	10.10	3.55	2.47	9.16	8.66	2481	2315	1762
797	UGC09873	10.31	3.20	1.86	8.86	8.81	5489	4665	3725
798	UGC09892	10.57	3.42	2.27	9.37	8.72	6313	6140	4164
802	ARP220	11.15	3.88	2.40	8.38	8.83	4906	3252	2603
806	NGC5966	11.16	4.10	2.96	9.82	9.85	3693	3483	3247
820	NGC6032	10.50	3.51	2.22	8.94	9.05	5947	5486	4822
821	NGC6060	11.05	3.99	2.61	9.40	8.97	5787	5576	3971
823	NGC6063	10.30	3.16	2.23	9.37	8.85	3757	3617	3021
826	NGC6081	11.32	4.37	3.06	9.83	9.68	3539	2968	2507
828	UGC10331	10.06	2.79	1.90	8.81	8.65	4239	4046	3460
829	NGC6125	11.46	4.41	3.10	9.91	9.90	3343	3168	2974
832	NGC6146	11.82	4.39	3.07	9.83	9.98	5586	5057	4788
845	UGC10693	11.66	4.22	2.84	9.93	9.86	6347	6362	5469
847	UGC10710	11.38	3.85	2.13	9.68	8.97	9430	12147	9366
848	NGC6310	10.78	3.89	2.85	9.77	9.32	4025	4057	3538
850	NGC6314	11.27	3.98	2.86	9.44	9.30	4867	4601	4593
851	NGC6338	11.78	4.30	2.94	9.92	9.88	6948	6574	6248
852	UGC10796	9.57	2.47	1.64	7.95	8.39	3352	3345	3715
853	NGC6361	11.26	4.21	3.08	9.55	9.18	4237	4062	3522
854	UGC10811	11.19	3.71	2.58	9.65	9.28	7712	7482	6407
856	IC1256	10.80	3.58	2.49	9.18	8.97	4885	4536	3815

Table 1. continued.

CALIFA ID#	Name NED	log Mass M$_\odot$	log μ_*[0] M$_\odot$/pc^2	log μ_*[HLR] M$_\odot$/pc^2	$\langle$log age[0] $\rangle_L$ (yr)	$\langle$log age[HLR] $\rangle_L$ (yr)	HLR pc	HLR^{DeRed} pc	HMR pc
857	NGC6394	11.21	3.53	2.71	9.77	9.11	6759	6575	5331
858	UGC10905	11.60	4.19	2.96	9.52	9.51	5489	5011	4453
859	NGC6411	11.14	4.08	2.94	9.72	9.64	3328	3308	3093
860	NGC6427	10.91	4.53	3.24	9.75	9.82	1669	1551	1463
863	NGC6497	11.21	3.93	2.65	9.86	9.20	5435	5853	4330
864	NGC6515	11.42	4.25	2.77	9.69	9.77	4811	4586	4645
866	UGC11262	10.20	3.02	1.71	9.24	8.65	5315	5062	4054
867	NGC6762	10.43	3.87	3.06	9.70	9.54	1581	1538	1411
869	NGC6941	10.52	3.11	1.80	9.70	9.24	6675	6787	5329
872	UGC11649	10.72	3.88	2.43	9.80	9.22	3524	3665	2373
873	UGC11680NED01	11.52	4.03	2.78	9.68	9.18	5744	5338	4369
874	NGC7025	11.45	4.65	3.22	9.84	9.72	3131	3223	2739
877	UGC11717	11.23	4.12	2.54	9.71	9.50	5929	6137	3263
878	MCG-01-54-016	9.28	2.30	1.70	8.26	8.40	2827	2719	2800
879	UGC11740	10.80	3.15	2.51	9.64	8.78	5341	5718	4746
880	UGC11792	10.66	3.71	2.72	9.31	8.98	4190	3684	3200
881	NGC7194	11.64	4.48	3.10	10.01	9.99	4372	4113	3409
883	UGC11958	11.55	4.15	2.94	9.97	9.81	4936	4772	4367
886	NGC7311	11.37	4.60	3.25	9.64	9.25	3268	3491	2580
887	NGC7321	11.37	3.99	2.69	9.59	8.91	6275	5914	4580
888	UGC12127	11.69	4.20	2.84	10.00	9.91	6285	6378	5498
890	UGC12185	11.00	3.96	2.66	9.73	9.24	4516	4540	3312
896	NGC7466	11.06	3.89	2.44	9.31	8.95	6212	5505	4093
900	NGC7550	11.43	4.36	3.01	9.56	9.69	3732	3305	3170
901	NGC7549	10.87	3.84	2.44	9.06	8.58	4182	4288	3102
902	NGC7563	11.17	4.50	3.15	9.81	9.83	2338	2141	2073
904	NGC7591	11.18	4.12	2.89	9.24	8.84	3838	3398	2639
935	UGC12864	10.19	3.03	1.89	8.69	8.70	5396	4466	4752
938	NGC5947	10.83	3.78	2.12	9.32	8.76	5280	5076	3143
939	NGC4676B	11.19	3.99	2.89	9.66	9.49	3769	3305	2918

Referências Bibliográficas

Abazajian, K. N., Adelman-McCarthy, J. K., Agüeros, M. A., Allam, S. S., Allende Prieto, C., An, D., Anderson, K. S. J., Anderson, S. F. et al. 2009, ApJS, 182, 543

Asari, N. V., Cid Fernandes, R., Stasińska, G., Torres-Papaqui, J. P., Mateus, A., Sodré, L., Schoenell, W., & Gomes, J. M. 2007, MNRAS, 381, 263

Bershady, M. A., Verheijen, M. A. W., Swaters, R. A., Andersen, D. R., Westfall, K. B., & Martinsson, T. 2010, ApJ, 716, 198

Bian, W., Gu, Q., Zhao, Y., Chao, L., & Cui, Q. 2006, MNRAS, 372, 876

Binney, J. & Tremaine, S. 2011, Galactic Dynamics: (Second Edition), Princeton Series in Astrophysics (Princeton University Press)

Bruzual, G. & Charlot, S. 2003, MNRAS, 344, 1000

Bryant, J. J., Owers, M. S., Robotham, A. S. G., Croom, S. M., Driver, S. P., Drinkwater, M. J., Lorente, N. P. F., Cortese, L. et al. 2015, MNRAS, 447, 2857

Bundy, K., Bershady, M. A., Law, D. R., Yan, R., Drory, N., MacDonald, N., Wake, D. A., Cherinka, B. et al. 2015, ApJ, 798, 7

Calzetti, D., Kinney, A. L., & Storchi-Bergmann, T. 1994, ApJ, 429, 582

Cappellari, M. & Copin, Y. 2003, MNRAS, 342, 345

Cappellari, M., Emsellem, E., Krajnović, D., McDermid, R. M., Scott, N., Verdoes Kleijn, G. A., Young, L. M., Alatalo, K. et al. 2011, MNRAS, 413, 813

Cardelli, J. A., Clayton, G. C., & Mathis, J. S. 1989, ApJ, 345, 245

Cid Fernandes, R., Gonzalez Delgado, R. M., Garcia Benito, R., Perez, E., de Amorim, A. L., Sanchez, S. F., Husemann, B., Falcon Barroso, J. et al. 2013a, ArXiv e-prints

I

Cid Fernandes, R., Mateus, A., Sodré, L., Stasińska, G., & Gomes, J. M. 2005, MNRAS, 358, 363

Cid Fernandes, R., Pérez, E., García Benito, R., González Delgado, R. M., de Amorim, A. L., Sánchez, S. F., Husemann, B., Falcón Barroso, J. et al. 2013b, A&A, 557, A86

Croom, S. M., Lawrence, J. S., Bland-Hawthorn, J., Bryant, J. J., Fogarty, L., Richards, S., Goodwin, M., Farrell, T. et al. 2012, MNRAS, 421, 872

Curtis, H. D. 1918, Publications of Lick Observatory, 13, 9

de Souza, R. E., Gadotti, D. A., & dos Anjos, S. 2004, ApJS, 153, 411

de Vaucouleurs, G. 1948, Annales d'Astrophysique, 11, 247

de Vaucouleurs, G. 1977, in Evolution of Galaxies and Stellar Populations, ed. B. M. Tinsley & R. B. G. Larson, D. Campbell, 43

Driver, S. P., Norberg, P., Baldry, I. K., Bamford, S. P., Hopkins, A. M., Liske, J., Loveday, J., Peacock, J. A. et al. 2009, Astronomy and Geophysics, 50, 12

Erwin, P. 2015, ApJ, 799, 226

Freeman, K. C. 1970, ApJ, 160, 811

García-Benito, R., Zibetti, S., Sánchez, S. F., Husemann, B., de Amorim, A. L., Castillo-Morales, A., Cid Fernandes, R., Ellis, S. C. et al. 2015, A&A, 576, A135

González Delgado, R. M., Pérez, E., Cid Fernandes, R., García-Benito, R., de Amorim, A. L., Sánchez, S. F., Husemann, B., Cortijo-Ferrero, C. et al. 2013, ArXiv e-prints

Häußler, B., Bamford, S. P., Vika, M., Rojas, A. L., Barden, M., Kelvin, L. S., Alpaslan, M., Robotham, A. S. G. et al. 2013, MNRAS, 430, 330

Hubble, E. 1926, Contributions from the Mount Wilson Observatory / Carnegie Institution of Washington, 324, 1

Hubble, E. 1936, The Realm of the Nebulae, Mrs. Hepsa Ely Silliman memorial lectures (Yale University Press)

Hubble, E. P. 1927, The Observatory, 50, 276

Husemann, B., Jahnke, K., Sánchez, S. F., Barrado, D., Bekerait*error*ė, S., Bomans, D. J., Castillo-Morales, A., Catalán-Torrecilla, C. et al. 2013, A&A, 549, A87

Iglesias-Páramo, J., Vílchez, J. M., Galbany, L., Sánchez, S. F., Rosales-Ortega, F. F., Mast, D., García-Benito, R., Husemann, B. et al. 2013, A&A, 553, L7

Johnston, E. J., Aragón-Salamanca, A., Merrifield, M. R., & Bedregal, A. G. 2012, MNRAS, 422, 2590

Kauffmann, G., Heckman, T. M., White, S. D. M., Charlot, S., Tremonti, C., Peng, E. W., Seibert, M., Brinkmann, J. et al. 2003, MNRAS, 341, 54

Kelvin, L. S., Driver, S. P., Robotham, A. S. G., Hill, D. T., Alpaslan, M., Baldry, I. K., Bamford, S. P., Bland-Hawthorn, J. et al. 2012, MNRAS, 421, 1007

Kelz, A., Verheijen, M. A. W., Roth, M. M., Bauer, S. M., Becker, T., Paschke, J., Popow, E., Sánchez, S. F. et al. 2006, PASP, 118, 129

King, I. R. 1966, AJ, 71, 64

Knox-Shaw, H. 1915, Helwan Institute of Astronomy and Geophysics Bulletins, 15, 129

La Barbera, F. & de Carvalho, R. R. 2009, ApJ, 699, L76

Lara-López, M. A., Bongiovanni, A., Cepa, J., Pérez García, A. M., Sánchez-Portal, M., Castañeda, H. O., Fernández Lorenzo, M., & Pović, M. 2010, A&A, 519, A31

Lara-López, M. A., Cepa, J., Bongiovanni, A., Pérez García, A. M., Castañeda, H., Fernández Lorenzo, M., Pović, M., & Sánchez-Portal, M. 2009, A&A, 505, 529

Lawrence, A., Warren, S. J., Almaini, O., Edge, A. C., Hambly, N. C., Jameson, R. F., Lucas, P., Casali, M. et al. 2007, MNRAS, 379, 1599

Levenberg, K. 1944, Quart. Applied Math., 2, 164

Liang, Y. C., Hammer, F., Yin, S. Y., Flores, H., Rodrigues, M., & Yang, Y. B. 2007, A&A, 473, 411

Lintott, C. J., Schawinski, K., Slosar, A., Land, K., Bamford, S., Thomas, D., Raddick, M. J., Nichol, R. C. et al. 2008, MNRAS, 389, 1179

Marquardt, D. W. 1963, Journal of the Society for Industrial and Applied Mathematics, 11, 431

Méndez-Abreu, J., Aguerri, J. A. L., Corsini, E. M., & Simonneau, E. 2008, A&A, 478, 353

Metropolis, N., Rosenbluth, A. W., Rosenbluth, M. N., Teller, A. H., & Teller, E. 1953, J. Chem. Phys., 21, 1087

Moffat, A. F. J. 1969, A&A, 3, 455

Moles, M., Benítez, N., Aguerri, J. A. L., Alfaro, E. J., Broadhurst, T., Cabrera-Caño, J., Castander, F. J., Cepa, J. et al. 2008, AJ, 136, 1325

Möllenhoff, C., Popescu, C. C., & Tuffs, R. J. 2006, A&A, 456, 941

Nelder, J. A. & Mead, R. 1965, The Computer Journal, 7, 308

Peeples, M. S., Pogge, R. W., & Stanek, K. Z. 2009, ApJ, 695, 259

Peng, C. Y., Ho, L. C., Impey, C. D., & Rix, H.-W. 2002, AJ, 124, 266

—. 2010, AJ, 139, 2097

Pérez, E., Cid Fernandes, R., González Delgado, R. M., García-Benito, R., Sánchez, S. F., Husemann, B., Mast, D., Rodón, J. R. et al. 2013, ApJ, 764, L1

Racine, R. 1996, PASP, 108, 699

Roth, M. M., Fechner, T., Wolter, D., Sandin, C., Kelz, A., Bauer, S. M., Popow, E., Monreal-Ibero, A. et al. 2010, Commissioning of the CCD231 4Kó4K detector for PMAS

Roth, M. M., Kelz, A., Fechner, T., Hahn, T., Bauer, S.-M., Becker, T., Böhm, P., Christensen, L. et al. 2005, PASP, 117, 620

Saha, P. & Williams, T. B. 1994, AJ, 107, 1295

Sánchez, S. F., Kennicutt, R. C., Gil de Paz, A., van de Ven, G., Vílchez, J. M., Wisotzki, L., Walcher, C. J., Mast, D. et al. 2012, A&A, 538, A8

Sandage, A., Sandage, M., & Kristian, J. 1975, Galaxies and the universe, Stars Stellar Syst. (Chicago, IL: Chicago Univ. Press)

Scoville, N., Aussel, H., Brusa, M., Capak, P., Carollo, C. M., Elvis, M., Giavalisco, M., Guzzo, L. et al. 2007, ApJS, 172, 1

Sérsic, J. L. 1963, Boletin de la Asociacion Argentina de Astronomia La Plata Argentina, 6, 41

Simard, L., Willmer, C. N. A., Vogt, N. P., Sarajedini, V. L., Phillips, A. C., Weiner, B. J., Koo, D. C., Im, M. et al. 2002, VizieR Online Data Catalog, 214, 20001

Storn, R. & Price, K. 1997, J. of Global Optimization, 11, 341

Tatarskii, V. I. 1961, Wave Propagation in Turbulent Medium (McGraw-Hill)

Vika, M., Bamford, S. P., Häußler, B., Rojas, A. L., Borch, A., & Nichol, R. C. 2013, MNRAS, 435, 623

Walcher, C. J., Wisotzki, L., Bekeraité, S., Husemann, B., Iglesias-Páramo, J., Backsmann, N., Barrera Ballesteros, J., Catalán-Torrecilla, C. et al. 2014, A&A, 569, A1

Willett, K. W., Lintott, C. J., Bamford, S. P., Masters, K. L., Simmons, B. D., Casteels, K. R. V., Edmondson, E. M., Fortson, L. F. et al. 2013, MNRAS, 435, 2835

Wolf, M. 1908, Publikationen des Astrophysikalischen Instituts Koenigstuhl-Heidelberg, 3, 109

York, D. G., Adelman, J., Anderson, Jr., J. E., Anderson, S. F., Annis, J., Bahcall, N. A., Bakken, J. A., Barkhouser, R. et al. 2000, AJ, 120, 1579